

THÈSE DE DOCTORAT
de l'Université Sorbonne Paris Cité



Préparée à l'Université Paris Diderot

École doctorale des Sciences de la Terre et de l'Environnement et Physique de l'Univers, Paris -
ED 560

Laboratoire AstroParticule et Cosmologie (APC)

PHYSIQUE THÉORIQUE

**Theoretical and phenomenological aspects of
non-singular black holes**

Frédéric Lamy

Thèse dirigée par Pierre Binétruy[†] et David Langlois,

présentée et soutenue publiquement le 21 septembre 2018
devant un jury composé de :

Dr. Alessandro Fabbri	(Enrico Fermi Ctr. (Rome), LPT Orsay)	<i>Examineur</i>
Dr. Eric Gourgoulhon	(CNRS, LUTH)	<i>Examineur</i>
Pr. Ruth Gregory	(Durham University)	<i>Rapporteure</i>
Pr. Carlos Herdeiro	(Universidade de Aveiro)	<i>Rapporteur</i>
Dr. David Langlois	(CNRS, APC)	<i>Directeur de thèse</i>
Pr. Danièle Steer	(Université Paris-Diderot, APC)	<i>Présidente du jury</i>

À Pierre.

À Michel et Bernard.

REMERCIEMENTS

La thèse est une aventure à au moins trois égards, en ce qu'elle est un pari scientifique, un défi personnel et un labyrinthe administratif. Sans toutes les personnes qui m'ont apporté leur soutien ou leur concours, tout au long de ces trois années ou simplement à des moments décisifs, rien n'aurait été possible. Je tiens ici à les en remercier.

Mes premières pensées vont à Pierre Binétruy, qui a fini par m'accepter comme doctorant à l'APC à force de me voir camper devant son bureau. A l'instar de ses autres doctorants, j'ai développé au cours de la thèse un sixième sens pour déceler sa présence au laboratoire. De tous nos échanges je retiendrai une profondeur de vue, une pédagogie et une patience remarquables, ainsi qu'un engagement inextinguible pour la diffusion des savoirs. Mais c'est avant tout son humanité rare que je garderai en mémoire.

Je tiens ensuite à remercier chaleureusement David Langlois, qui a accepté de reprendre la direction de ma thèse au pied levé en avril 2017. Bien que nous n'ayons pas développé de projet en commun, son aide et sa disponibilité ont été cruciales pour établir de nouvelles collaborations et mener à bien mon projet initial. Je lui suis reconnaissant pour toutes nos discussions, qu'elles aient eu trait à la physique, la géopolitique ou à mon avenir professionnel.

Je remercie les membres du jury, Alessandro Fabbri, Ericourgoulhon, et Danièle Steer pour leur présence à ma soutenance. Mes remerciements tout particuliers vont aux rapporteurs Ruth Gregory et Carlos Herdeiro, qui ont accepté sans ciller cette mission chronophage. Je suis également reconnaissant à Christos Charmoussis et Danièle Steer pour leurs conseils dans le cadre de mon comité de suivi de thèse.

Un immense merci également à mes compagnons de route du PCCP, Alexis Helou et Marie Verleure. Alexis, bien qu'en fin de troisième année alors que j'arrivais en stage de pré-thèse à l'APC, a pris le temps de m'initier aux subtilités des horizons de piégeage. Notre collaboration n'a pas cessé depuis, et s'est muée en une amitié scellée par de passionnantes discussions sur l'histoire des langues anciennes et l'archéologie. Marie a été d'un soutien constant et a réussi, contre vents et marées, à faire éditer le livre de Pierre.

Ma thèse doit énormément à Ericourgoulhon et Karim Noui qui m'ont introduit, avec bienveillance et patience, à leurs domaines de recherche et ont su créer des opportunités pour que j'y contribue. Merci à Frédéric Vincent et Thibaut Paumard, grands manitouts de GYOTO qui ont patiemment répondu à toutes mes questions sur le sujet, ainsi qu'à Jibril Ben Achour

pour nos discussions.

Ces trois années se sont déroulées dans le cadre privilégié du groupe Théorie de l'APC et ont été grandement facilitées par la gentillesse et l'efficacité des chercheurs et personnels administratifs du laboratoire. Je remercie ainsi Cristina Volpe pour son implication dans la recherche de nouveaux projets pour la suite de ma thèse, Nathalie Deruelle pour ses conseils et nos discussions, ainsi que Yannick Giraud-Héraud et Antoine Kouchner pour leur soutien. Je remercie enfin Martine Piochaud et Béatrice Silva pour l'organisation de mes voyages, et Céline Benoit pour la recherche d'articles soviétiques introuvables.

Merci à mes amis de bureau pour les moments partagés, et plus généralement la QPUC Team intergénérationnelle qui a connu quelques heures de gloire au 424A. Merci également aux doctorants élus au conseil d'UFR pour toutes nos discussions, ainsi que pour le partage des séances. Merci surtout à Carole, qui a été d'un soutien total aux moments critiques.

Merci également à mes amis de la Croix-Rouge du 5^{ème} pour les parties de baby-foot, et en particulier à Antoine Le Roy d'avoir repris le poste de responsable maraudes alors que la rédaction de thèse approchait dangereusement.

Avant de conclure, j'ai une pensée toute particulière pour les professeurs de Physique et de Mathématiques qui m'ont mis sur la voie de la recherche il y a plus de 10 ans: Ghislain Polin, Marie-Christine Duchemin, Yves Chevalier et Christophe Poupon.

Enfin, ces quelques mots seraient vides de sens si je ne remerciais pas ma famille, et en particulier mes parents qui m'ont appris à apprendre et me soutiennent dans mes choix depuis le début.

Merci à Julia pour ces derniers mois, et pour les années à venir.

ABSTRACT

The issue of singularities in General Relativity dates back to the very first solution to the equations of the theory, namely Schwarzschild's 1915 black hole. Whether they be of coordinate or curvature nature, these singularities have long puzzled physicists, who managed to better characterize them in the late 60's. This led to the famous singularity theorems applying both to cosmology and black holes, and which assume a classical behaviour of the matter content of spacetime summarized in the so-called energy conditions. The violation of these conditions by quantum phenomena supports the idea that singularities are to be seen as a limitation of General Relativity, and would be cured in a more general theory of quantum gravity. In this thesis, pending for such a theory, we aim at investigating black hole spacetimes deprived of any singularity as well as their observational consequences. To that purpose, we consider both modifications of General Relativity and the coupling of Einstein's theory to exotic matter contents. In the first case, we show that one can recover known static spherically symmetric non-singular black holes in principle in the tensor-scalar theory of mimetic gravity, and implicitly by a deformation of General Relativity's hamiltonian constraint in an approach based on loop quantum gravity techniques. In the second case, we stay inside the framework of General Relativity and consider effective energy-momentum tensors associated first with a regular rotating model à la Hayward, reducing in some regime to the first example of fully regular rotating black hole, and then with a dynamical spacetime describing the formation and evaporation of a non-singular black hole. For the latter, we show that all models based on the collapse of ingoing null shells and willing to describe Hawking's evaporation are doomed to violate the energy conditions in a non-compact region of spacetime. Lastly, the theoretical study of the rotating Hayward metric comes with numerical simulations of such an object at the center of the Milky Way, using the ray-tracing code GYOTO and mimicking the known properties of the accretion structure of the presumed black hole Sgr A*. These simulations allow exhibiting the two very different regimes of the metric, with or without horizon, and emphasize the difficulty of asserting the presence of a horizon from strong-field images as the ones provided by the Event Horizon Telescope.

Le problème des singularités en relativité générale remonte à la première solution exacte de la théorie obtenue en 1915, à savoir celle du trou noir de Schwarzschild. Qu'elles soient de coordonnée ou de courbure, ces singularités ont longtemps questionné les physiciens qui parvinrent à mieux les caractériser à la fin des années 1960. Cela conduisit aux fameux théorèmes sur les singularités, s'appliquant à la fois aux trous noirs et en cosmologie, basés sur un comportement classique du contenu en matière de l'espace-temps résumé par des conditions d'énergie. La violation de ces conditions dans les processus quantiques pourrait indiquer que les singularités doivent être vues comme des limitations de la relativité générale, pouvant ainsi disparaître dans une théorie plus générale de la gravité quantique. Dans l'attente d'une telle théorie, nous avons pour objectif dans cette thèse d'étudier les espaces-temps de trous noirs dépourvus de toute singularité ainsi que leurs conséquences observationnelles. A cette fin, nous considérons à la fois des modifications de la relativité générale et le couplage de la théorie à des contenus en matière exotiques. Dans le premier cas nous montrons qu'il est possible de retrouver des trous noirs réguliers à symétrie sphérique connus, tout d'abord en principe avec la théorie tenseur-scalaire de gravité mimétique, puis implicitement par le biais d'une déformation de la contrainte hamiltonienne en relativité générale inspirée des techniques de gravitation quantique à boucles. Dans le second cas nous restons dans le cadre de la relativité générale, et considérons des tenseurs énergie-impulsion effectifs. Ils sont en premier lieu associés à un modèle régulier à la Hayward en rotation fournissant dans un certain régime un premier exemple de trou noir en rotation exempt de toute singularité, puis à un espace-temps dynamique décrivant la formation et l'évaporation d'un trou noir sans singularité. Pour ce dernier, nous montrons que tout modèle basé sur l'effondrement gravitationnel de coquilles de genre lumière visant à décrire l'évaporation de Hawking est voué à violer les conditions sur l'énergie dans une région non compacte de l'espace-temps. Enfin, l'étude théorique de la métrique de Hayward en rotation est accompagnée de simulations numériques d'un tel objet au centre de la Voie Lactée, obtenues à l'aide du code de calcul de trajectoires de particules GYOTO en reproduisant les propriétés connues de la structure d'accrétion du trou noir présumé Sgr A*. Ces simulations permettent d'illustrer deux régimes très différents de la métrique, avec ou sans horizon, et soulignent la difficulté d'affirmer avec certitude la présence d'un horizon à partir d'images en champ fort telles que celles obtenues par l'instrument Event Horizon Telescope.

LIST OF PUBLICATIONS

- **Imaging a non-singular rotating black hole at the center of the Galaxy,**
F. Lamy, E.ourgoulhon, T. Paumard and F. Vincent,
Class. Quantum Grav. **35** (2018) 115009,
DOI: [10.1088/1361-6382/aabd97](https://doi.org/10.1088/1361-6382/aabd97).
- **Non-singular black holes and the limiting curvature mechanism: a Hamiltonian perspective,**
J. Ben Achour, F. Lamy, H. Liu and K. Noui,
JCAP 05 (2018) 072,
DOI: [10.1088/1475-7516/2018/05/072](https://doi.org/10.1088/1475-7516/2018/05/072).
- **Polymer Schwarzschild black hole: An effective metric,**
J. Ben Achour, F. Lamy, H. Liu and K. Noui,
EPL (Europhysics Letters) **123** (2018) 20006,
DOI: [10.1209/0295-5075/123/20006](https://doi.org/10.1209/0295-5075/123/20006).
- **Closed trapping horizons without singularity,**
P. Binétruy, A. Helou and F. Lamy,
Phys. Rev. D **98** (2018) 064058,
DOI: [10.1103/PhysRevD.98.064058](https://doi.org/10.1103/PhysRevD.98.064058).

NOTATION

The following notation will be used throughout this dissertation.

- The spacetimes we consider are four-dimensional, with metric signature $(-+++)$.
- Most of tensorial objects are written in bold. In particular, the vectors of the natural basis are denoted $(\boldsymbol{\partial}_t, \boldsymbol{\partial}_r, \boldsymbol{\partial}_\theta, \boldsymbol{\partial}_\phi)$ while the 1-forms associated with the dual basis read $(\mathbf{d}t, \mathbf{d}r, \mathbf{d}\theta, \mathbf{d}\phi)$.
- When a tensorial object is not written in bold, Wald's abstract index notation applies (exclusively with indices a, b, c, d, e).
- The components of tensorial objects are denoted with Greek indices ranging from 0 to 3. When dealing with spatial components only, we use Latin indices i, j, k, l ranging from 1 to 3.
- Einstein's summation conventions are used. For instance,

$$g_{\mu\nu} \mathrm{d}x^\mu \mathrm{d}x^\nu \equiv \sum_{\mu,\nu=0}^3 g_{\mu\nu} \mathrm{d}x^\mu \mathrm{d}x^\nu .$$

- 3-vectors are denoted by an arrow (e.g., \vec{v}).
- Unless explicitly mentioned, we use the natural units $G = c = 1$.

TABLE OF CONTENTS

	Page
Introduction	1
1 Fundamentals of General Relativity	5
1 Space, time and gravitation: from Galileo to Einstein	6
1.1 The fruitful union of space and time	6
1.1.1 Emergence of the notion of spacetime	6
1.1.2 The spacetime of special relativity	8
1.2 Gravitation enters the game	10
1.2.1 Equivalence principles	10
1.2.2 Gravity as a curvature of spacetime	11
2 Spacetime in General Relativity	12
2.1 Manifolds and tensors	13
2.1.1 Manifolds	13
2.1.2 Tensors on manifolds	13
2.1.3 The metric tensor	15
2.2 Curvature	17
2.2.1 Levi-Civita connection on a manifold	17
2.2.2 Riemann and Ricci tensors	19
2.3 Geodesics	20
2.3.1 Geodesics' equation	20
2.3.2 Congruences of geodesics	21
2.4 Causal structure	22
2.4.1 Basic definitions	22
2.4.2 Black holes: a first approach	24
3 Einstein's equations	27
3.1 Formulation of the equations	27
3.1.1 Energy-momentum tensor	27
3.1.2 The equations	29
3.2 Lagrangian formulation: Einstein-Hilbert's action	30
4 Singularity theorems	31
4.1 What is a singularity?	31
4.2 Penrose's singularity theorem (1965)	32
4.2.1 Notion of trapped surface	32
4.2.2 Formulation and proof	33

4.2.3	Circumventing the theorem	37
4.3	Hawking & Penrose’s singularity theorem (1970)	38
2	Black hole solutions in General Relativity	41
1	Schwarzschild’s solution	42
1.1	Solving Einstein’s equations in vacuum	42
1.2	Crossing the horizon	43
1.3	Maximal extension of the Schwarzschild spacetime	46
2	Reissner-Nordström solution	50
2.1	Properties	50
2.2	Maximal extension of Reissner-Nordström spacetime	52
3	Kerr’s solution	57
3.1	Properties of the Kerr spacetime	57
3.1.1	Metric of a rotating black hole	57
3.1.2	Ergosphere	57
3.1.3	Trapping horizons	58
3.1.4	The ring singularity	60
3.2	Maximal extension of the Kerr spacetime	60
3.3	Deriving Kerr’s solution from the Newman-Janis algorithm	64
4	Vaidya’s solution and gravitational collapse	66
4.1	An exact dynamical solution to Einstein’s equations	66
4.2	Gravitational collapse of ingoing null dust	68
3	Static non-singular black holes	71
1	Examples of static non-singular black holes	72
1.1	Bardeen’s spacetime	72
1.1.1	Metric and horizons	72
1.1.2	Avoiding singularities	72
1.2	Hayward’s spacetime	73
1.2.1	Metric and horizons	73
1.2.2	Avoiding singularities	75
1.3	Energy-momentum tensor from non-linear electrodynamics	75
1.3.1	General static case in spherical symmetry	75
1.3.2	Recovering Bardeen’s mass function	78
1.3.3	Recovering Hayward’s mass function	79
2	Static non-singular black holes from mimetic gravity	80
2.1	Mimetic gravity	80
2.1.1	Original theory	80
2.1.2	Extended mimetic gravity	82

2.2	General construction of static spherically symmetric spacetimes in mimetic gravity	83
2.2.1	Solving the mimetic condition	83
2.2.2	Solving the modified Einstein equations	84
2.3	Application to non-singular black holes	85
2.3.1	A non-singular black hole from limiting curvature mechanism . .	85
2.3.2	Recovering known static non-singular black holes	87
3	Loop quantum deformation of Schwarzschild's black hole	89
3.1	Introduction to canonical gravity	89
3.1.1	3 + 1 decomposition of Einstein-Hilbert action	89
3.1.2	Hamiltonian formulation of General Relativity	90
3.1.3	Ashtekar variables in spherical symmetry	93
3.2	Deforming the constraint algebra	94
3.2.1	Effective Einstein's equations for a general deformation	94
3.2.2	Solving effective Einstein's equations in the static case	99
3.2.3	The standard LQG deformation	100
3.3	Recovering known static spherically symmetric non-singular black holes .	101
4	Rotating non-singular black holes	103
1	Rotating Hawyard's black hole: a first attempt by Bambi and Modesto	104
1.1	Applying the Newman-Janis algorithm to Hayward's spacetime	104
1.2	Presence of a singularity in Bambi-Modesto's spacetime	106
2	A non-singular model of rotating black hole	108
2.1	Regular extension to $r < 0$	108
2.1.1	Metric	108
2.1.2	Regularity	109
2.2	The two regimes of the model	110
2.2.1	Presence of horizons	110
2.2.2	Regular rotating Hawyard black hole	111
2.2.3	Naked rotating wormhole	112
2.3	Causality	113
2.4	Energy conditions	114
3	Energy-momentum tensor of the non-singular model	116
3.1	Results of Toshmatov et al.	116
3.1.1	A nonlinear electrodynamical source	116
3.1.2	Issues in the derivation of the "solution"	116
3.2	Exact solutions	117
3.2.1	Magnetic source	117
3.2.2	Electromagnetic source	119

4	Analytical study of geodesics	122
4.1	Circular orbits in the equatorial plane	122
4.1.1	Energy and angular momentum of a massive particle	122
4.1.2	Influence of the spin	123
4.1.3	Influence of the parameter b	125
4.1.4	Innermost stable circular orbit (ISCO)	125
4.2	Null geodesics	127
5	Simulating a rotating non-singular black hole at the center of the Galaxy	131
1	General features of black hole images	132
1.1	First approach	132
1.2	Photon region	132
1.2.1	Definition	132
1.2.2	Stability of photon orbits	135
1.3	Structure of a typical black hole image	138
1.3.1	The Kerr shadow	138
1.3.2	Main features of a typical black hole image	140
2	Astrophysical and numerical set-up	141
2.1	Implementing regular black holes metrics in the ray-tracing code GYOTO .	142
2.2	Mimicking an observation of Sagittarius A* in the simulations	144
2.2.1	Features of Sgr A*	144
2.2.2	Observations with the Event Horizon Telescope	145
2.2.3	Accretion model used in the simulations	146
3	Images of the regular rotating Hayward model	149
3.1	Regular rotating Hayward black hole	149
3.2	Naked rotating wormhole	151
3.2.1	Ray-traced images	151
3.2.2	A glimpse at $r < 0$	152
3.2.3	Following 3 typical geodesics	153
3.3	Low resolution images as seen by the Event Horizon Telescope	154
6	Dynamical non-singular black holes	157
1	Non-singular spacetimes with closed trapping horizons	158
1.1	Motivations	158
1.2	Existence of non-singular spacetimes with closed trapping horizons	159
1.2.1	Conditions for the existence of closed trapping horizons	160
1.2.2	Conditions for the absence of singularities	161
1.2.3	Minimal form of F	161
2	Examples of closed trapping horizons: properties and limits	162

2.1	Location of the trapping horizons	162
2.2	Hayward-like model	163
2.3	Frolov's model	164
2.4	Bardeen-like model	164
3	Behaviour of null geodesics in models with closed trapping horizons	166
3.1	Null geodesic flow	166
3.2	Frolov's separatrix and quasi-horizon	167
3.3	Relevant null geodesics for closed trapping horizons	168
4	Towards a model for the formation and evaporation of a non-singular trapped region	170
4.1	A form of the metric constrained by the energy-momentum tensor	171
4.2	Explicit energy-momentum tensor	172
4.2.1	Conditions on the energy-momentum tensor	172
4.2.2	Generating a Hawking flux on \mathcal{I}^+	173
4.2.3	Avoiding the NEC violation on \mathcal{I}^-	174
	Conclusion	177
A	Typology of horizons	179
1	Killing horizon	179
2	Event horizon	180
3	Trapping and apparent horizons	180
3.1	Definition	180
3.2	Dynamical spherically symmetric metric	181
3.3	Stationary axisymmetric metric	182
4	Cauchy horizon	183
B	Tensorial computations	185
1	General spherically symmetric metric	185
2	Regular rotating black hole	186
C	Sagemath worksheets	189
1	Rotating non-singular black holes	189
1.1	Curvature	189
1.2	Null energy condition	189
1.3	Geodesics	189
1.4	Energy-momentum tensor from nonlinear electrodynamics	190
	Bibliography	191

INTRODUCTION

A century after their discovery as a solution to Einstein's equations, black holes are still at the heart of modern research in General Relativity. The seminal paper [104] by Karl Schwarzschild, providing the first vacuum solution to the equations of Einstein's theory [49], does not explicitly mention the term "black hole" but paves the way for their explicit description as regions of spacetime from which neither matter nor light can escape. In light of the recent experimental evidence in favor of their existence obtained thanks to the detection of gravitational waves [3], achieving a full grasp of the nature of these objects becomes an even more pressing matter.

Among the various fields of research dealing with black holes, the one we have explored in this thesis consists in better understanding the persistent question of the singularity lying at their center. The notion of singularity in gravitational physics has little to do with the meaning of the original Latin word *singularitas*, translating into "the fact of being unique". However, the gravitational singularities we will be dealing with in this thesis do display a unique feature, as they appear to be predictions by General Relativity of its own limitations. One is for instance confronted with the presence of a singularity at the center of Schwarzschild's black hole, where the curvature of spacetime diverges, which amounts to saying that spacetime itself cannot be defined there.

Singularity theorems, due to Penrose and Hawking [68, 94], developed in the late 60's and shed some light on the assumptions needed for the existence of such singularities, both for black holes and cosmology (in which one has to deal with the Big-Bang singularity). One of the key assumptions of these theorems is that matter should be well-behaved, in the sense that it oughts to satisfy some energy conditions. These conditions, and particularly the weakest of all, the null energy condition, can be violated when dealing with quantum phenomena. This fact tends to enforce the generally believed idea that a quantum theory of gravity would be able to cure singularities.

Since this theory has not yet been found, one is led to follow other approaches in order to study non-singular black holes reproducing Schwarzschild's metric at large distance. The very first example of such model dates back to Bardeen's black hole, proposed in 1968 [11]. Since then various other models have followed, among which some possessing a de Sitter core (Dymnikova [48] and Hayward [71]), and others inspired by non-commutative geometry (Nicolini [91]). These models all share a common feature: they introduce a new parameter in the black hole's metric, preventing the curvature from diverging as $r \rightarrow 0$. This might seem in contradiction with the no-hair theorem,

stating that the unique solution for a steady isolated black hole in four-dimensional vacuum general relativity is the Kerr-Newman black hole, which depends on only three parameters: the mass M , the reduced angular momentum $a = J/M$ and the electric charge Q . Actually, there is no contradiction since the non-singular models are not solutions of vacuum Einstein's equations.

As regards the approaches chosen to study non-singular black holes, pending for a theory of quantum gravity, this thesis aims at exploring two different ones. The first consists in considering modified theories of gravity. Starting from the Hamiltonian formulation of General Relativity, one can for instance add quantum corrections to it by hand (technically, by deforming the constraint algebra) in order to obtain effective Einstein's equations, which might be a limit of the quantum Einstein's equations from the fully quantized theory. Another option would be to work with modified theories of gravity aiming at explaining the structure of the universe at large scale, in particular dark matter and dark energy, such as some scalar-tensor theories. We will show how one of these theories, namely mimetic gravity, could in principle allow recovering known non-singular black hole metrics.

The second approach assumes to stay inside the framework of General Relativity, but to match non-singular black hole metrics with exotic energy-momentum tensors. Non-linear electrodynamics, for instance, has been shown to be a potential source for some famous non-singular static black holes, such as Bardeen's and Hayward's. After constructing explicitly a regular rotating Hayward model, reducing to a regular rotating Hayward black hole in some regime and to Hayward's static black hole in the absence of rotation, we will show that non-linear electrodynamics does not provide an adequate energy-momentum tensor anymore in this case. Finally, we will attempt to build a dynamical model for the formation and the evaporation of a non-singular black hole with an exotic energy-momentum tensor reducing to Vaidya's solution in some regimes only.

In this thesis non-singular black holes are studied from quite various perspectives, ranging from their theoretical description to their observational consequences. At the interface lies the numerical simulations of the regular rotating Hayward model mentioned above. These simulations produce an image on the observer's sky, i.e. a set of pixels to which is associated the specific intensity of a given photon. These images are computed by integrating backward in time the null geodesics, using the ray-tracing code GYOTO for which we developed an extension implementing the regular rotating Hayward model. Their comparison to typical Kerr black holes images will allow a better understanding of the forthcoming results of the Event Horizon Telescope currently observing the supermassive black hole candidate Sgr A* at the center of the galaxy.

This dissertation is organized as follows. The first chapter (Chap. 1) deals with fundamentals of General Relativity, and aims at providing the reader with the essential ideas of General

Relativity as well as its main tools. Special attention shall be paid to the definition of singularities, and to the proof of Penrose's 1965 theorem: the rest of the dissertation will be concerned with non-singular black holes, and the way they manage to circumvent Penrose's theorem is to be highlighted for each of them. Chapter 2 is the last introductive chapter, whose purpose is to present famous (singular) black hole solutions in General Relativity. Doing so we will come across several different notions of horizons, all summarized in App. A, the retained one to describe astrophysically relevant black holes being the trapping horizon. Our first encounter with non-singular black holes will occur in Chapter 3, where we will present Bardeen and Hayward static black holes and then follow the first approach mentioned above, the one of modified gravity, to recover their metrics. Chapters 4 & 5 will be devoted to rotating non-singular black holes: we will present our regular rotating Hayward model, providing in its regime with horizons the first fully regular rotating black hole, and then compute with GYOTO the images we would observe if it were surrounded by an accretion structure similar to the one of Sgr A*. Finally, Chapter 6 will deal with an attempt to model dynamical non-singular black holes describing the formation and evaporation of a non-singular trapped region.

FUNDAMENTALS OF GENERAL RELATIVITY



$q \sim n = j \quad r \quad \mathbb{Z} h . t \quad r h \sim n = j \quad w \mathbb{Z} . t$

“Si je suis entré dans l’horizon, c’est que je connais le chemin !”

(*Textes des Sarcophages* VII, 2w-2x, L2Li [30, 43].)

The purpose of this first chapter¹ is twofold. To begin with, we aim at giving an intuitive approach to Einstein’s general theory of relativity (Section 1) . Furthermore, we develop the various relativistic tools that will be needed in the rest of this dissertation, which range from basic notions of differential geometry (Section 2) to Einstein’s equations (Section 3). This will lead us to define the notion of singularity in Section 4 and to give a formal proof of Penrose’s 1965 singularity theorem, hence setting the scene for the study of non-singular black holes in the next chapters. Finally, we will come across several notions of horizons, which are summarized in App. A.

Contents

1	Space, time and gravitation: from Galileo to Einstein	6
2	Spacetime in General Relativity	12
3	Einstein’s equations	27
4	Singularity theorems	31

¹The following sources have been used extensively to write this introductive chapter: [96], [63], [57], [67], and [122].

1 Space, time and gravitation: from Galileo to Einstein

There is something unique about gravitation. It is the only force we know that couples identically to every massive object². In other words, a feather and a billiard ball launched from the same height on the Moon will reach its surface simultaneously (since no other force than gravitation, like the friction of the atmosphere, applies there). This universality of free fall, already identified by Galileo in the 16th century, will lead us to consider gravitation not merely as a force but as an intrinsic property of spacetime. This spacetime is a paradigm in favour of which we will argue in Section 1.1, before following Einstein and showing in Section 1.2 that gravitation is an expression of its curvature.

1.1 The fruitful union of space and time

1.1.1 Emergence of the notion of spacetime

At the 80th Assembly of German Natural Scientists and Physicians in 1908, Hermann Minkowski spoke about space and time in these terms:

“The views of space and time which I wish to lay before you have sprung from the soil of experimental physics, and therein lies their strength. They are radical. Henceforth, space by itself, and time by itself, are doomed to fade away into mere shadows, and only a kind of union of the two will preserve an independent reality.”

Evoking “the soil of experimental physics”, Minkowski was actually referring to the experiments of Albert Michelson and Edward Morley in the 1880’s. These experiments aimed at measuring the speed of light from Earth in two opposite directions on a circular orbit around the Sun. At that time, light was thought to propagate in a medium called ether, which had a relative velocity with respect to Earth. Hence, the speed of light measured from Earth at two different points of its orbit, where it thus has two different relative velocities with respect to the ether, should vary.

This fact simply stems from the *Galilean transformations* between two inertial frames of reference R and R' with relative velocity v (see Fig. 1.1):

$$\left\{ \begin{array}{l} t' = t \\ x' = x - vt \\ y' = y \\ z' = z \end{array} \right. \quad (1.1)$$

Michelson and Morley did not detect any difference between the two experiments performed at two opposite points of the Earth’s orbit, hence calling into question the theory of ether. This

²This is not true for quantum objects though, due to the Schrödinger equation.

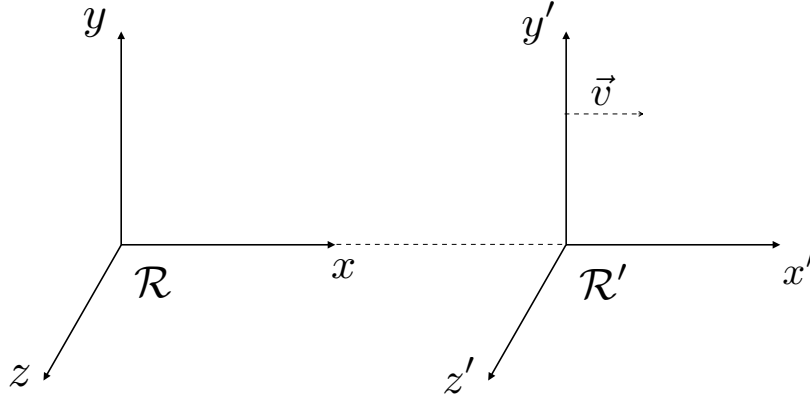


Figure 1.1: Illustration of two inertial frames, \mathcal{M} and \mathcal{M}' , with a velocity \vec{v} in the x direction relative to each other.

led Einstein to postulate in 1905 that the speed of light³ c is the same in all inertial frames.

This postulate has dramatic consequences, as we shall see now. Let us consider a light ray bouncing back and forth on two mirrors, as illustrated in Fig. 1.2. In the frame where the mirrors are at rest, after one bounce one has:

$$\begin{cases} \Delta t = \frac{2L}{c}, \\ \Delta x = 2L, \\ \Delta y = 0, \\ \Delta z = 0 \end{cases} \quad (1.2)$$

The same situation seen in a frame where the mirrors are moving towards the right at a constant velocity v gives a quite different result. As illustrated in Fig. 1.2, the distance travelled by the light ray from the point of view of an observer in R' is:

$$d = 2\sqrt{L^2 + \left(\frac{\Delta x'}{2}\right)^2} \quad (1.3)$$

Following Einstein's postulate, we now get

$$\begin{cases} \Delta t' = \frac{2}{c}\sqrt{L^2 + \left(\frac{\Delta x'}{2}\right)^2}, \\ \Delta x' = v\Delta t', \\ \Delta y' = 0, \\ \Delta z' = 0 \end{cases} \quad (1.4)$$

Combining the equations for $\Delta t'$ and $\Delta x'$, we obtain

$$\frac{\Delta t'}{\Delta t} = \frac{1}{\sqrt{1 - \frac{v^2}{c^2}}} \equiv \gamma \quad (1.5)$$

³We do not use $c = 1$ for now.

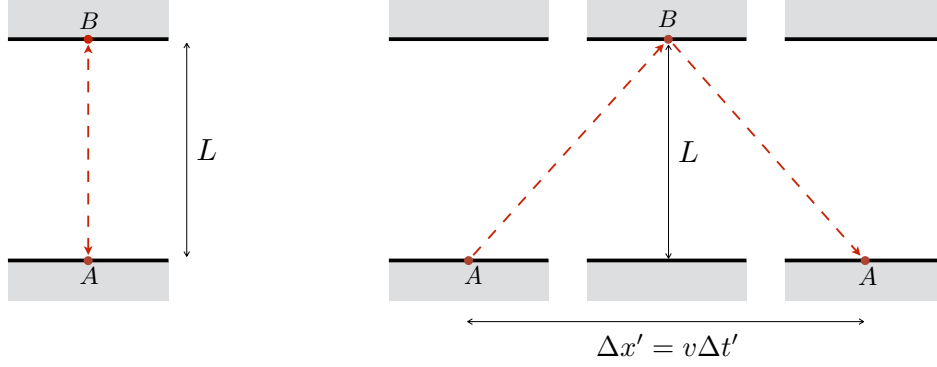


Figure 1.2: Thought experiment illustrating the relativity of time. On the left panel, in a reference frame \mathcal{R} , a light ray is bouncing back and forth vertically on two mirrors separated by a distance L . On the right, in a reference frame \mathcal{R}' , the two mirrors are moving with a velocity \vec{v} in the x direction with respect to the frame of the left panel. Hence, a light ray travels a bigger distance $A \rightarrow B \rightarrow A$ when the mirrors are moving (right). Since the speed of light is constant in all inertial frames, it means that the observer in \mathcal{R}' will measure a bigger time interval $\Delta t'$ than the one in \mathcal{R} . Consequently, “time goes more slowly” in \mathcal{R}' .

Hence, the time interval measured in R' is bigger than the one measured in R ! We are forced to abandon the absolute vision of time stemming from Galileo’s transformations. The new transformations, known as *Lorentz’s transformations*, are:

$$\begin{cases} ct' = \gamma \left(ct - \frac{vx}{c} \right) \\ x' = \gamma (x - vt) \\ y' = y \\ z' = z \end{cases} \quad (1.6)$$

They can be obtained by requiring that the interval

$$\Delta s^2 = -c^2 \Delta t^2 + \Delta x^2 + \Delta y^2 + \Delta z^2 \quad (1.7)$$

remains invariant under such a transformation: $\Delta s^2 = \Delta s'^2$. This simply enforces the fact that a light ray propagates at the same velocity c in all inertial frames.

The spatial and temporal components in Lorentz’s transformations (1.6) thus clearly get mixed up when going from an inertial frame to another, and two observers in these frames measure different times (if v is not too small compared to c , i.e. for relativistic motions). This mixing of space and time leads us to think the motion of observers in terms of a new paradigm, *spacetime*, that we will develop in the following section.

1.1.2 The spacetime of special relativity

If light propagates at the same velocity in all inertial frames, it must then be the highest possible one, i.e. all particles must travel at speed at most equal to c . This is easy to infer from the

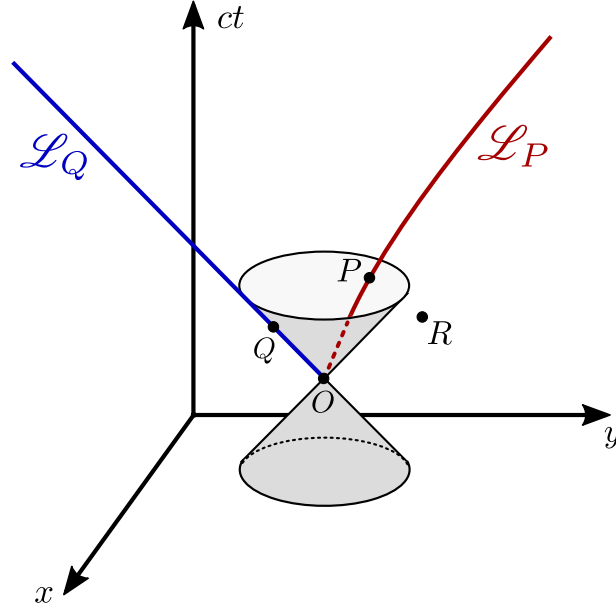


Figure 1.3: Lightcone in Minkowski's spacetime (with one less dimension of space). The event Q is on the future lightcone of O , while P is inside the lightcone. Finally, R is separated from O by a spacelike interval. \mathcal{L}_P is a timelike curve, and \mathcal{L}_Q is a null one.

invariance of the speed of light: for an observer moving at $0.99c$, a photon passing by will still travel at velocity c ; the latter is thus an unsurpassable velocity.

The spacetime of special relativity, called Minkowski's spacetime, is a 4-dimensional structure which enforces the invariance of the speed of light as well as its unsurpassable nature. It consists of a set of points, called *events*, characterized by four coordinates (t, x, y, z) . Any two points are separated by the interval

$$\Delta s^2 = -\Delta t^2 + \Delta x^2 + \Delta y^2 + \Delta z^2, \quad (1.8)$$

where, from now on, we set $c = 1$. When the points are infinitesimally close, this allows defining the line element

$$ds^2 = -dt^2 + dx^2 + dy^2 + dz^2, \quad (1.9)$$

which, as we shall see in Sec. 2.1.3, is associated with a metric which defines a notion of distance on the spacetime.

Hence, the separation of any two points $\Delta s'$ falls into one the three following categories :

- $\Delta s^2 < 0$: the interval is *timelike*
- $\Delta s^2 = 0$: the interval is *null*
- $\Delta s^2 > 0$: the interval is *spacelike*

A curve is then said to be timelike (resp. null, spacelike) if every two points are separated by a timelike (resp. null, spacelike) interval.

Considering a point O in Fig. 1.3, one can draw the light rays emerging from it, which satisfy $\Delta s^2 = 0$: this produces the *lightcone* at O , and in particular the null curve \mathcal{L}_O . O is therefore separated from the event Q by a interval, which means that the two can be linked only by a light ray. P is inside the future lightcone of O , the two points are separated by a timelike interval ($\Delta s^2 < 0$). It means that observers with velocities $v < c$ can relate them. Finally, R is outside the future lightcone of O since they are separated by a spacelike interval ($\Delta s^2 > 0$): no observer can go from O to R , for he would have to travel faster than light.

In the end, the spacetime structure gives a global coherent picture which enforces causality. The future lightcone of O consists of all the events of spacetime that O can have an influence on, and it is preserved under Lorentz transformations. Put another way, all inertial observers, regardless the velocity they may have, will agree on the causal relation between two events separated by a timelike or null interval. This is not the case when the events are separated by a spacelike interval. For instance, two different observers could measure $t_R < t_O$ and $t_R > t_O$.

1.2 Gravitation enters the game

Before getting into the formal description of General Relativity (Sec. 2), let us introduce the main ideas of the theory.

1.2.1 Equivalence principles

We mentioned previously the universality of free fall highlighted by Galileo. It actually comes from the equality between the gravitational mass m_g , associated with the weight $P = m_g g$ in a gravitational field g , and the inertial mass m_i stemming from Newton's second law $F = m_i a$ giving the force applied to an object to give it an acceleration a . When the only force applied to an object is gravity, assuming $m_i = m_g$ one gets

$$a = g, \quad \text{i.e.} \quad \frac{d^2 x}{dt^2} = g \quad (1.10)$$

Hence, the way a body falls in a gravitational field does not depend on its internal composition. Moreover, we can erase locally the effects of a static and uniform gravitational field by going to an accelerated frame:

$$\begin{cases} t' = t \\ x' = x - \frac{1}{2} g t^2 \end{cases} \Rightarrow \frac{d^2 x'}{dt'^2} = 0. \quad (1.11)$$

This result is expressed in the *weak equivalence principle*, stated as follows.

Definition 1.1 (Weak equivalence principle). *At each point of spacetime, in an arbitrary gravitational field, one can define a locally inertial frame in a small enough region. In this frame, the motion of a free particle (i.e., only subject to gravity) is linear and uniform.*

A classical illustration of the weak equivalence principle is the elevator in free fall. For an observer in such an elevator, all objects around him will fall at the same (increasing) speed. His frame of reference is thus a locally inertial frame, in which the motion of the objects surrounding him is linear and uniform.

Einstein extended this principle in the following way.

Definition 1.2 (Einstein's equivalence principle). *In the locally inertial frame of the weak equivalence principle, all (non-gravitational) laws of nature are those of special relativity.*

The notion of *locally* inertial frame is primordial here. Indeed, in the presence of a gravitational field one cannot construct a global reference frame, otherwise the spacetime would be Minkowski's. It thus remains to define how to connect two different regions of spacetime with coordinates (x^μ) and (x'^μ) , where two (independent) locally inertial frames can be constructed.

To do so, we will need an additional assumption: the laws of Physics do not depend on the specific choices of coordinates. In particular we require that the lightcone structure be preserved under a general transformation of coordinates $x^\alpha \rightarrow x'^\alpha$, i.e. $ds^2 = ds'^2$ with:

$$ds^2 = g_{\mu\nu} dx^\mu dx^\nu = ds'^2 = g'_{\alpha\beta} dx'^\alpha dx'^\beta \quad (1.12)$$

Since the differentials dx'^α are by definition $dx'^\alpha = \frac{\partial x'^\alpha}{\partial x^\mu} dx^\mu$, we get:

$$ds'^2 = g'_{\alpha\beta} \frac{\partial x'^\alpha}{\partial x^\mu} dx^\mu \frac{\partial x'^\beta}{\partial x^\nu} dx^\nu \quad (1.13)$$

Hence, we have

$$g'_{\alpha\beta} = \frac{\partial x^\mu}{\partial x'^\alpha} \frac{\partial x^\nu}{\partial x'^\beta} g_{\mu\nu} . \quad (1.14)$$

The invariance of the line element ds^2 thus imposes a very specific constraint on the transformation law of the metric. As will be shown in Sec. 2.1.3, the metric is actually a covariant object, a tensor of type $(0, 2)$, and thus transforms naturally as prescribed by eq. (1.14).

1.2.2 Gravity as a curvature of spacetime

The universal coupling of gravity, summarized in the weak equivalence principle, suggests that gravity is not merely a force but a property of spacetime itself. In this Section, we will give two ways of seeing that gravity is actually related to the curvature of spacetime.

A first hint at the presence of curvature can be directly inferred from Einstein's equivalence principle. Indeed, let us make a coordinate transformation from a locally inertial frame with coordinates (X^μ) to a general frame with coordinates (x^μ) . The line element reads:

$$ds^2 = \eta_{\mu\nu} dX^\mu dX^\nu . \quad (1.15)$$

Generalizing eq. (1.11), the coordinate transformations to get to (x^μ) are $dX^\mu = \frac{\partial X^\mu}{\partial x^\alpha} dx^\alpha$. Hence, the line element can be rewritten:

$$ds^2 = \frac{\partial X^\mu}{\partial x^\alpha} \frac{\partial X^\nu}{\partial x^\beta} \eta_{\mu\nu} dx^\alpha dx^\beta . \quad (1.16)$$

The coordinate transformation from (X^μ) to (x^μ) can always be made, but the reverse cannot. Einstein's equivalence principle implies that in the presence of gravity, any observer can go only *locally* from coordinates (x^μ) to (X^μ) , in which the line element takes the simple form (1.15). Such a transformation is thus not possible *globally* when gravity comes into play.

The line element thus takes a more complicated form in the presence of a gravitational field. But it encodes geometry, and can be seen in Minkowski's spacetime as a generalization of the Pythagorean theorem. Hence, the presence of a gravitational field will lead to a modification of geometry, and to the presence of a nonvanishing curvature (which will be defined precisely in Section 2.2).

Another, more explicit way of seeing this is through a thought experiment. Let us consider an accelerating rocket, in which a light ray is sent from the left wall to the right one. The light ray propagates in straight line, and during the time it needs to cross the rocket, the latter has accelerated. Hence, the light ray will reach the right wall at a smaller height than the one it was sent from: for an observer in the rocket, the acceleration has curved the light ray ! Via the Einstein equivalence principle, this acceleration is locally equivalent to a gravitational field. Hence, we can expect light rays to be curved in a gravitational field.

In the end, the gravitational field appears not to be an additional field of spacetime. It rather represents the deviation of the spacetime geometry from the Minkowskian flat geometry, and is materialized by the curvature of spacetime.

2 Spacetime in General Relativity

We have now written down the physical principles underlying the theory of General Relativity, but they remain to be implemented in a mathematical and practical framework. This is the aim of this section, where we will introduce the mathematical tools of the theory. They will prove necessary to understand the corner stone of GR, Einstein's equations, as well as the singularity theorems, that we will develop in Secs. 3 & 4.

2.1 Manifolds and tensors

2.1.1 Manifolds

An essential notion in order to describe the spacetime of General Relativity is the one of a manifold. Intuitively, a manifold is a set of points linked in a continuous way and which locally looks like \mathbb{R}^n , but perhaps not globally [6]. A natural example is the surface of the Earth which looks flat locally, but clearly not globally !

More precisely, we will be interested in manifolds on which we can make differential calculus, called *differentiable manifolds*. The easiest type of differentiable manifolds to work with is the smooth manifold, defined as follows.

Definition 1.3. A smooth n -dimensional⁴ manifold \mathcal{M} is a topological space equipped with charts $\varphi_\alpha : \mathcal{U}_\alpha \rightarrow \mathbb{R}^n$ such that:

- (i) \mathcal{U}_α are a finite number of open sets covering \mathcal{M} , called an atlas,
- (ii) the transition map $\varphi_\alpha \circ \varphi_\beta^{-1} : \mathbb{R}^n \rightarrow \mathbb{R}^n$ is smooth (i.e. C^∞) when $\mathcal{U}_\alpha \cap \mathcal{U}_\beta \neq \emptyset$.

Property (i) is at the heart of our intuitive definition of a manifold: locally, one can label the points $p \in \mathcal{U}_\alpha \subset \mathcal{M}$ by n coordinates (x^i) by using the chart φ_α . But globally, one may need more than one open set \mathcal{U}_α to cover the whole manifold.

Property (ii) allows defining unambiguously smooth functions $f : \mathcal{M} \rightarrow \mathbb{R}$. f is smooth if for all α , $f \circ \varphi_\alpha^{-1} : \mathbb{R}^n \rightarrow \mathbb{R}$ is smooth (see Fig. 1.4). One can show that f is smooth on $V = \mathcal{U}_\alpha \cap \mathcal{U}_\beta$ using the chart \mathcal{U}_α : it suffices to show that $f \circ \varphi_\alpha^{-1}$ is smooth on $\varphi_\alpha(V) \subset \mathbb{R}^n$. Thanks to property (ii), we arrive at the same conclusion by using the patch \mathcal{U}_β : if $f \circ \varphi_\alpha^{-1}$ is smooth on $\varphi_\alpha(V)$, then $f \circ \varphi_\beta^{-1}$ will be smooth on $\varphi_\beta(V)$ since $f \circ \varphi_\beta^{-1} = (f \circ \varphi_\alpha^{-1}) \circ (\varphi_\alpha \circ \varphi_\beta^{-1})$

2.1.2 Tensors on manifolds

Now that we are equipped with a notion of manifold, we need to define various objects on it that will allow us to do some Physics. For instance, the notion of metric tensor, giving the concept of distance on a manifold, will be of the uttermost importance to define the spacetime of General Relativity.

A few steps are nonetheless necessary to get to the notion of tensors. Let us first define what a curve on a manifold is.

⁴in the following, we will restrict ourselves to 4-dimensional spacetimes ($n = 4$)

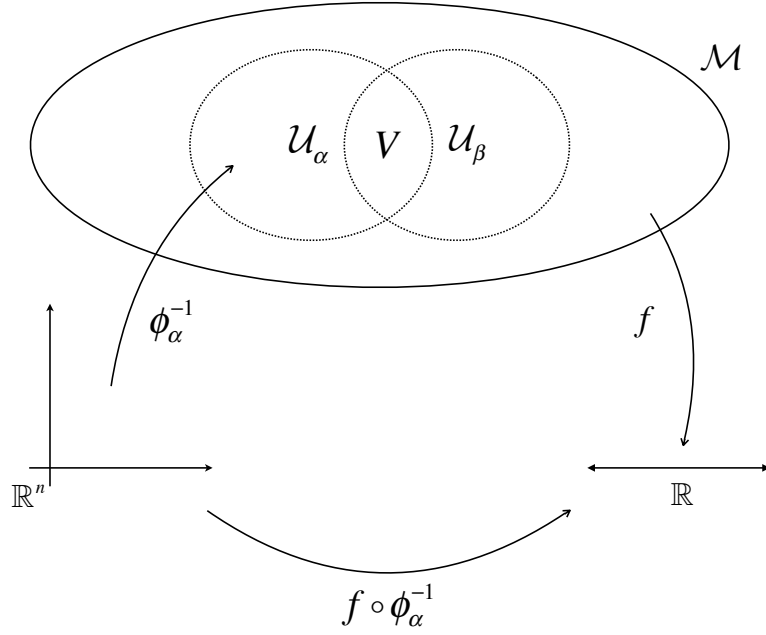


Figure 1.4: Smooth n -dimensional manifold \mathcal{M} along with two of its charts \mathcal{U}_α and \mathcal{U}_β . The open sets \mathcal{U}_α covering \mathcal{M} constitute an atlas. The function $f : \mathcal{M} \rightarrow \mathbb{R}$ is smooth iff $f \circ \phi_\alpha^{-1}$ is smooth for every \mathcal{U}_α in the atlas.

Definition 1.4. A (smooth) curve is a subset $\mathcal{L} \subset \mathcal{M}$ that is the image of a smooth map $I \subset \mathbb{R} \rightarrow \mathcal{M}$:

$$\begin{aligned} P : I &\rightarrow \mathcal{M} \\ \lambda &\mapsto p = P(\lambda) \in \mathcal{L}. \end{aligned}$$

P is called a *parametrization* of \mathcal{L} , while λ is a *parameter* along \mathcal{L} .

One can also define a *scalar field* on a manifold \mathcal{M} as a function $f : \mathcal{M} \rightarrow \mathbb{R}$. One can then define a vector tangent to \mathcal{L} by applying it to f as follows.

Definition 1.5. A vector \mathbf{v} tangent to \mathcal{L} at $p = P(\lambda)$ is an operator matching every scalar field f to the real number

$$\mathbf{v}(f) = \left. \frac{df}{d\lambda} \right|_{\mathcal{L}} \equiv \lim_{\epsilon \rightarrow 0} \frac{1}{\epsilon} [f(P(\lambda + \epsilon)) - f(P(\lambda))] \quad (1.17)$$

One can define coordinates (x^α) around $p \in \mathcal{M}$, and thus n different curves \mathcal{L}_α going through p and parametrized by $\lambda = x^\alpha$. This allows defining ∂_α , the vector tangent to \mathcal{L}_α , when a scalar field f is applied to it:

$$\partial_\alpha(f) = \left. \frac{df}{dx^\alpha} \right|_{\mathcal{L}_\alpha} = \frac{\partial f}{\partial x^\alpha} \quad (1.18)$$

One can then rewrite any vector \mathbf{v} applied to f as follows⁵

$$\mathbf{v}(f) = \frac{\partial f}{\partial x^\alpha} \frac{dX^\alpha}{d\lambda} = \boldsymbol{\partial}_\alpha(f) \frac{dX^\alpha}{d\lambda} \quad (1.19)$$

Since this is valid for all scalar fields f , we can decompose any vector as

$$\mathbf{v} = v^\alpha \boldsymbol{\partial}_\alpha, \text{ with } v^\alpha = \frac{dX^\alpha}{d\lambda} \quad (1.20)$$

Definition 1.6. *The set of all tangent vectors to a curve at p constitutes the tangent vector space $T_p\mathcal{M}$ to \mathcal{M} at p . The vectors $\boldsymbol{\partial}_\alpha$ form a basis of $T_p\mathcal{M}$, and the coefficients v^α are the components of \mathbf{v} with respect to the coordinates (x^α) .*

One can define linear forms on $T_p\mathcal{M}$ as follows.

Definition 1.7. *A linear form is a mapping $\omega : \mathbf{v} \in T_p\mathcal{M} \mapsto \langle \omega, \mathbf{v} \rangle \in \mathbb{R}$ that is linear: $\langle \omega, \mathbf{v} + \mathbf{u} \rangle = \lambda \langle \omega, \mathbf{v} \rangle + \langle \omega, \mathbf{u} \rangle$ for all $\mathbf{u}, \mathbf{v} \in T_p\mathcal{M}$ and $\lambda \in \mathbb{R}$.*

Definition 1.8. *The dual space of $T_p\mathcal{M}$, denoted by $T_p^*\mathcal{M}$, consists of all the linear forms at p . Given the natural basis $(\boldsymbol{\partial}_\alpha)$ of $T_p\mathcal{M}$, there exists a unique basis $(\mathbf{d}x^\alpha)$ of $T_p^*\mathcal{M}$ such that $\langle \mathbf{d}x^\alpha, \boldsymbol{\partial}_\beta \rangle = \delta^\alpha_\beta$.*

We now have all necessary tools to define tensors on a manifold.

Definition 1.9. *A tensor of type (k, l) at $p \in \mathcal{M}$ is a mapping*

$$\begin{aligned} \mathbf{T} : \underbrace{T_p^*\mathcal{M} \times \cdots \times T_p^*\mathcal{M}}_{k \text{ times}} \times \underbrace{T_p\mathcal{M} \times \cdots \times T_p\mathcal{M}}_{l \text{ times}} &\rightarrow \mathbb{R} \\ (\omega_1, \cdots, \omega_k, \mathbf{v}_1, \cdots, \mathbf{v}_l) &\mapsto \mathbf{T}(\omega_1, \cdots, \omega_k, \mathbf{v}_1, \cdots, \mathbf{v}_l). \end{aligned}$$

that is linear with respect to each of its arguments.

According to this definition, vectors are simply tensors of type $(1, 0)$ while linear forms are tensors of type $(0, 1)$. Given a basis (\mathbf{e}_α) of $T_p\mathcal{M}$ and a dual basis (\mathbf{e}^α) in $T_p^*\mathcal{M}$, a tensor of type (k, l) reads

$$\mathbf{T} = T^{\alpha_1 \cdots \alpha_k}_{\beta_1 \cdots \beta_l} \mathbf{e}_{\alpha_1} \otimes \cdots \otimes \mathbf{e}_{\alpha_k} \otimes \mathbf{e}^{\beta_1} \otimes \cdots \otimes \mathbf{e}^{\beta_l}. \quad (1.21)$$

2.1.3 The metric tensor

Let us now define precisely the metric tensor which generalizes the notion of distance on a manifold, and which will be essential to define curvature as well as the trajectories of observers in spacetime.

Definition 1.10. *A pseudo-Riemannian metric tensor \mathbf{g} on \mathcal{M} is a tensor field obeying the following properties:*

⁵We are now using Einstein's summation convention

- (i) \mathbf{g} is a bilinear form acting at each point $p \in \mathcal{M}$ on vectors in the tangent space: $\mathbf{g}(p) : (\mathbf{u}, \mathbf{v}) \in T_p \mathcal{M} \times T_p \mathcal{M} \rightarrow \mathbf{g}(\mathbf{u}, \mathbf{v}) \in \mathbb{R}$,
- (ii) \mathbf{g} is symmetric: $\mathbf{g}(\mathbf{u}, \mathbf{v}) = \mathbf{g}(\mathbf{v}, \mathbf{u})$,
- (iii) \mathbf{g} is non-degenerate: at any point $p \in \mathcal{M}$, a vector \mathbf{u} such that $\forall \mathbf{v} \in T_p \mathcal{M}, \mathbf{g}(\mathbf{u}, \mathbf{v}) = 0$ is necessarily the null vector.

How does this formal definition of tensors, and in particular of the metric tensor, relate to the one often used by physicists, characterizing them by the way they transform under coordinate changes? As we have seen in Section 1.2.1, imposing that the light cone be invariant under general transformations of coordinates implies a condition on the metric:

$$g'_{\alpha\beta} = \frac{\partial x^\mu}{\partial x'^\alpha} \frac{\partial x^\nu}{\partial x'^\beta} g_{\mu\nu} \quad (1.22)$$

Let us check that this property stems from our definition 1.9 of tensors. As we shall see, it actually directly results from their multilinearity. Let us consider \mathbf{g} as a $(0, 2)$ tensor, i.e. a bilinear form (the precise definition of the metric tensor will be given in Section 2.1.3, but is not needed for this argument), to which we apply the infinitesimal vector $d\mathbf{x} = dx^\alpha \partial_\alpha = dx'^\alpha \partial'_\alpha$ expressed in two different bases.

We have first:

$$\begin{aligned} \mathbf{g}(d\mathbf{x}, d\mathbf{x}) &= \mathbf{g}(dx^\mu \partial_\mu, dx^\nu \partial_\nu) \\ &= \mathbf{g}(\partial_\mu, \partial_\nu) dx^\mu dx^\nu \quad \text{by linearity of each argument} \\ &= g_{\mu\nu} dx^\mu dx^\nu \end{aligned} \quad (1.23)$$

And with the vectors expressed in the prime basis:

$$\begin{aligned} \mathbf{g}(d\mathbf{x}, d\mathbf{x}) &= \mathbf{g}(dx'^\alpha \partial'_\alpha, dx'^\beta \partial'_\beta) \\ &= \mathbf{g}(\partial'_\alpha, \partial'_\beta) dx'^\alpha dx'^\beta \\ &= g'_{\alpha\beta} dx'^\alpha dx'^\beta \end{aligned} \quad (1.24)$$

But the differentials dx'^α are by definitions related to dx^μ by $dx'^\alpha = \frac{\partial x'^\alpha}{\partial x^\mu} dx^\mu$. Hence, equating (1.23) and (1.24) leads to:

$$g_{\mu\nu} dx^\mu dx^\nu = g'_{\alpha\beta} \frac{\partial x'^\alpha}{\partial x^\mu} dx^\mu \frac{\partial x'^\beta}{\partial x^\nu} dx^\nu, \quad (1.25)$$

and finally, as expected:

$$g'_{\alpha\beta} = \frac{\partial x^\mu}{\partial x'^\alpha} \frac{\partial x^\nu}{\partial x'^\beta} g_{\mu\nu}. \quad (1.26)$$

In the bases where the metric is diagonal, it can be shown that it always has the same number s of negative (and thus $(n - s)$ positive) components among $(g_{\alpha\beta})$: this is the *signature* of the metric. When $s = 0$, \mathbf{g} is called a *Riemannian* metric and is positive-definite. When $s = 1$, \mathbf{g} is a

Lorentzian metric.

We are now able to define the category of manifolds we will be dealing with in the subsequent chapters.

Postulate 1.1. *The spacetime of General Relativity consists of a Lorentzian manifold, which is a pair $(\mathcal{M}, \mathbf{g})$ where \mathcal{M} is a smooth manifold and \mathbf{g} is a Lorentzian metric tensor on \mathcal{M} .*

How is it that Lorentzian manifolds are best suited for describing the spacetime of General Relativity? We can provide two answers to this question.

First, the metric is not positive-definitive: this allows implementing the finiteness of the speed of light and hence causality at each point of the manifold through the use of a light cone, which will not be changed under general transformations of coordinates. The trajectories of physical observers, necessary satisfying causality, are then timelike curves inside the light cone.

Furthermore, a Lorentzian manifold allows one to encode the equivalence principle. Indeed, let us consider a spacetime very different from Minkowski's, for instance with some curvature (which will be defined properly in Section 2.2). At a given point p , it will always be possible to define some inertial coordinates X^μ such that the spacetime resembles Minkowski's: $g_{\mu\nu}(p) = \eta_{\mu\nu}$ and $(\partial_\sigma g_{\mu\nu})_p = 0$. This means, in total agreement with the equivalence principle, that one can locally cancel the effects of gravity and place oneself in the frame of a freely-falling observer. Of course this is valid only locally, as emphasized by the expression of the metric in the neighbourhood of p :

$$g_{\mu\nu} = \eta_{\mu\nu} + \frac{1}{2}(\partial_\sigma \partial_\rho g_{\mu\nu})_p X^\sigma X^\rho + \dots \quad (1.27)$$

The fact that one cannot impose that the second derivatives of the metric be null is precisely the manifestation of curvature.

2.2 Curvature

In this section, we will define the notion of curvature of a manifold \mathcal{M} in an intrinsic way, i.e. without requiring that there exist a higher-dimensional space in which \mathcal{M} may be embedded. A way of doing so consists in defining the parallel transport of tensors (Section 2.2.1). The curvature can thus be characterized by parallel transporting them along a closed curve, via the Riemann tensor (Section 2.2.2).

2.2.1 Levi-Civita connection on a manifold

What do we mean by parallel transport along a curve? This notion is best illustrated for vectors, where parallel transport boils down to transporting a vector while it keeps pointing in the same direction. In the usual Euclidean plane, the parallel transport along a closed curve is trivial as

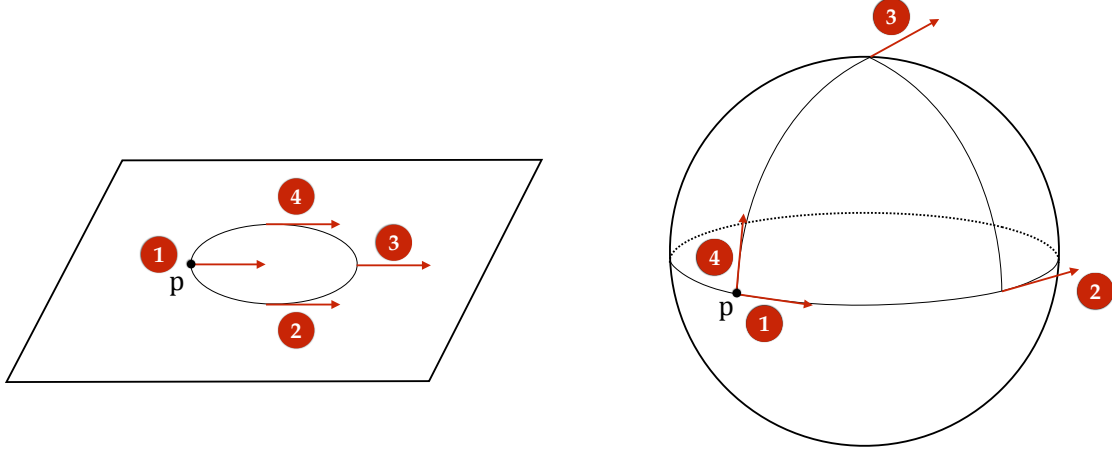


Figure 1.5: Parallel transport of a vector along a closed curve in a (flat) Euclidean plane (left) and on a (curved) sphere (right), following the path $1 \rightarrow 2 \rightarrow 3 \rightarrow 4$. Keeping the same direction all the way along, the vector on the sphere follows its curvature and has rotated after travelling along the loop, contrarily to the vector on the plane.

illustrated in Fig. 1.5 (left). Transporting the same vector along a closed curve on a 2-sphere (Fig. 1.5 (right)) is not as easy: at each point $p \in S^2$, the vector belongs to a different tangent space $T_p S^2$.

Hence we will need an additional structure on the manifold in order to compare vectors (and then tensors) belonging to different tangent spaces. The structure which allows defining the variation of a vector field $\mathbf{v} \in \mathcal{H}(\mathcal{M})$, hence providing a way of connecting various tangent spaces, is called an *affine connection*.

Definition 1.11. An affine connection on \mathcal{M} is a mapping

$$\begin{aligned} \nabla : \mathcal{H}(\mathcal{M}) \times \mathcal{H}(\mathcal{M}) &\rightarrow \mathcal{H}(\mathcal{M}) \\ (\mathbf{u}, \mathbf{v}) &\mapsto \nabla_{\mathbf{u}} \mathbf{v} \end{aligned}$$

which satisfies the following properties:

- (i) ∇ is bilinear
- (ii) For any scalar field f ,

$$\nabla_{f\mathbf{u}} \mathbf{v} = f \nabla_{\mathbf{u}} \mathbf{v}$$

- (iii) For any scalar field f , the Leibniz rule holds:

$$\nabla_{\mathbf{u}}(f\mathbf{v}) = \langle \nabla f, \mathbf{u} \rangle \mathbf{v} + f \nabla_{\mathbf{u}} \mathbf{v} \quad \text{where} \quad \nabla f = \frac{\partial f}{\partial x^\alpha} \mathbf{d}x^\alpha$$

The vector $\nabla_{\mathbf{u}} \mathbf{v}$ is called the *covariant derivative* of \mathbf{v} along \mathbf{u} . The affine connection can be generalized to tensors: the covariant derivative of a tensor \mathbf{T} along a vector \mathbf{u} is a tensor of the

same type as \mathbf{T} .

An affine connection is entirely defined by its components $C_{\alpha\beta}^\mu$. Its action on a basis (\mathbf{e}_α) at a given point reads:

$$\nabla_{\mathbf{e}_\beta} \mathbf{e}_\alpha \equiv C_{\alpha\beta}^\mu \mathbf{e}_\mu \quad (1.28)$$

We will use in the rest of this thesis a specific type of affine connection, the Levi-Civita connection, whose existence stems from the fundamental theorem of Riemannian geometry.

Theorem 1.1 (Fundamental theorem of Riemannian geometry). *Let (M, \mathbf{g}) be a pseudo-Riemannian manifold. Then there exists a unique connection ∇ , called the Levi-Civita connection, which satisfies*

- (i) ∇ is torsion-free: for any scalar field f , $\nabla_a \nabla_b f = \nabla_b \nabla_a f$
- (ii) ∇ preserves the metric: $\nabla \mathbf{g} = 0$

The condition of preservation of the metric simply means that we require the connection to preserve the notion of distance, and in particular the structure of the lightcone. It implies the following form for the connection coefficients, which are the *Christoffel symbols*:

$$C_{\beta\gamma}^\alpha = \Gamma_{\beta\gamma}^\alpha \equiv \frac{1}{2} g^{\alpha\lambda} (\partial_\beta g_{\gamma\lambda} + \partial_\gamma g_{\beta\lambda} - \partial_\lambda g_{\beta\gamma}) \quad (1.29)$$

The absence of torsion means that the Christoffel symbols are symmetric with respect to their downstairs indices:

$$\Gamma_{\beta\gamma}^\alpha = \Gamma_{\gamma\beta}^\alpha \quad (1.30)$$

Given a tensor field \mathbf{T} of type (k, l) , one can define the covariant derivative of $\nabla \mathbf{T}$ with respect to the affine connection ∇ . It is a tensor field of type $(k, l + 1)$ whose components are:

$$\begin{aligned} \nabla_\mu T^{\alpha_1 \dots \alpha_k}_{\beta_1 \dots \beta_l} &\equiv (\nabla \mathbf{T})^{\alpha_1 \dots \alpha_k}_{\beta_1 \dots \beta_l \mu} \\ &= \partial_\mu T^{\alpha_1 \dots \alpha_k}_{\beta_1 \dots \beta_l} + \sum_{i=1}^k \Gamma_{\sigma\mu}^{\alpha_i} T^{\alpha_1 \dots \sigma \dots \alpha_k}_{\beta_1 \dots \beta_l} - \sum_{i=1}^l \Gamma_{\beta_i \mu}^\sigma T^{\alpha_1 \dots \alpha_k}_{\beta_1 \dots \sigma \dots \beta_l} \end{aligned} \quad (1.31)$$

\downarrow i^{th} position
 \uparrow i^{th} position

2.2.2 Riemann and Ricci tensors

Let us come back to Fig. 1.5. Once the vector is parallelly transported around a closed curve on the sphere, it comes back rotated at the origin because of the curvature of the 2-sphere.

This notion of curvature can actually be encoded in the noncommutation of covariant derivatives applied to a vector:

$$\nabla_\gamma \nabla_\beta v_\alpha - \nabla_\beta \nabla_\gamma v_\alpha = R^\delta_{\alpha\beta\gamma} v_\delta \quad (1.32)$$

where the $R^\delta_{\alpha\beta\gamma}$ are the components of the *Riemann tensor*. Computing explicitly the left-hand side of eq. (1.32) using eqs. (1.31) and (1.29) leads to the expression of the Riemann tensor:

$$R^d_{abc} \equiv \partial_b \Gamma^d_{ac} - \partial_c \Gamma^d_{ab} + \Gamma^e_{ac} \Gamma^d_{db} - \Gamma^e_{ab} \Gamma^d_{ec} \quad (1.33)$$

One can then define the *Ricci tensor* \mathbf{R} (which is a contraction of the Riemann tensor) through its components:

$$R_{ab} \equiv R^c_{acb} \quad (1.34)$$

And finally the *Ricci scalar*, also called *scalar curvature*, reads

$$R = R_{ab} g^{ab} \quad (1.35)$$

Curvature scalars, i.e. scalars formed from the contraction of the Riemann tensor (or other tensors such as Weyl's tensor), will be of the utmost importance in the following. Along with the Ricci scalar, the Kretschmann scalar K will often be computed in the following:

$$K = R_{\alpha\beta\gamma\delta} R^{\alpha\beta\gamma\delta}. \quad (1.36)$$

Indeed, contrarily to tensors whose components depend on the choice of a specific basis, scalars are coordinate-independent. The divergence of the curvature scalars thus provides a way of characterizing singularities in spacetime, as will be explained in more details in Section 4.

2.3 Geodesics

2.3.1 Geodesics' equation

As previously mentioned, the particles which are subject solely to gravity play a peculiar role in General Relativity. They are associated with locally inertial frames, in which gravity is erased and the laws of special relativity are valid. Gravitation being described as a deformation of spacetime with respect to the flat geometry, it is natural to define the worldlines of these particles in free fall, called *geodesics*, as lines that "curve as little as possible" [122]. They will reduce to a straight line in a flat geometry, since inertial observers in Minkowski's spacetime are at rest or in linear and uniform motion. The following definition encapsulates these properties.

Definition 1.12. A smooth curve \mathcal{L} of a pseudo-Riemannian manifold $(\mathcal{M}, \mathbf{g})$ is called a *geodesic* iff it admits a parametrization P whose associated tangent vector field \mathbf{v} is transported parallelly to itself along \mathcal{L} :

$$\nabla_{\mathbf{v}} \mathbf{v} = 0 \quad (1.37)$$

Such a parametrization is called an *affine parametrization* of parameter λ . Recall that a smooth curve is the image of a smooth map $\mathcal{I} \rightarrow \mathcal{M}$ (see Def. 1.4). The parametrization is then

defined by n functions $X^\alpha : \mathcal{I} \rightarrow \mathbb{R}$ such that $x^\alpha(P(\lambda)) = X^\alpha(\lambda)$. In terms of components, the tangent vector is thus $v^\alpha = \frac{dX^\alpha}{d\lambda}$, where the (X^α) are the coordinates in the neighbourhood of a point $p \in \mathcal{L}$. Hence, eq. (1.37) reads:

$$\begin{aligned} 0 &= v^\alpha \nabla_\alpha v^\beta \\ &= v^\beta \frac{\partial v^\alpha}{\partial x^\beta} + \Gamma_{\beta\gamma}^\alpha v^\beta v^\gamma \\ &= \mathbf{v}(v^\alpha) + \Gamma_{\beta\gamma}^\alpha v^\beta v^\gamma \quad \text{by eq. (1.20)} \\ &= \frac{dv^\alpha}{d\lambda} + \Gamma_{\beta\gamma}^\alpha v^\beta v^\gamma \quad \text{by eq. (1.17)} \end{aligned} \tag{1.38}$$

The geodesic equation thus reads:

$$\frac{d^2 X^\alpha}{d^2 \lambda} + \Gamma_{\beta\gamma}^\alpha \frac{dX^\beta}{d\lambda} \frac{dX^\gamma}{d\lambda} = 0 \tag{1.39}$$

The interpretation of the geodesic equation is insightful and deeply rooted in the equivalence principle. Actually, $\nabla_{\mathbf{v}} \mathbf{v}$ is the acceleration of a particle along the geodesic with velocity \mathbf{v} . Hence, the acceleration of a particle following a geodesic vanishes: no force is exerted on this particle, which is in free-fall. The inertial observers of General Relativity are those subject only to gravity. The curved structure of spacetime thus really takes into account the gravitational attraction, and does not treat it as a force.

2.3.2 Congruences of geodesics

A *congruence of geodesics* is a family of geodesics such that through each point of spacetime, there passes one and only one geodesic from this family. The geodesics among a given congruence are thus non-intersecting.

The expansion of a congruence of geodesics can be defined as the fractional change of area of a surface following the geodesics. Let us consider a codimension 2 surface \mathcal{S} and a vector field \mathbf{l} associated with a congruence of light rays, also called *null congruence* (Fig. 1.6). Let us take an infinitesimal parameter $\epsilon > 0$ and displace each point on \mathcal{S} by the infinitesimal vector $\epsilon \mathbf{l}$. This forms the new surface \mathcal{S}_ϵ , and the resulting expansion of \mathcal{S} along \mathbf{l} is

$$\theta_{(\mathbf{l})} \equiv \lim_{\epsilon \rightarrow 0} \frac{\delta A_\epsilon - \delta A}{\delta A} \tag{1.40}$$

It can actually be shown that the expansion scalar θ is independent of the choice of \mathcal{S} , and is a property of the geodesic congruence itself. In the rest of this dissertation, we will use the following definition of the expansion scalar:

$$\theta_{(\mathbf{l})} = h^{\mu\nu} \nabla_\mu l_\nu, \tag{1.41}$$

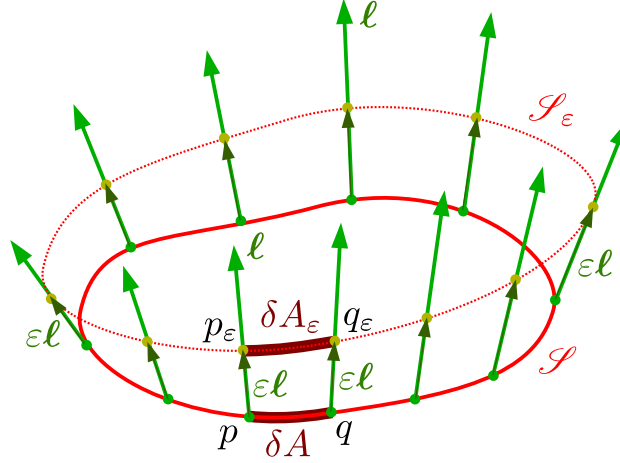


Figure 1.6: Codimension 2 surface \mathcal{S} and its image by a translation along the infinitesimal vector $\epsilon \mathbf{l}$. Figure taken from [63].

which is equivalent to (1.40). $h^{\mu\nu}$ are the components of the induced metric \mathbf{h} , defined via the two independent null vector fields \mathbf{l} and \mathbf{k} (such that $\mathbf{l} \cdot \mathbf{k} = -1$):

$$\mathbf{h} = \mathbf{g} + \mathbf{l} \otimes \mathbf{k} + \mathbf{k} \otimes \mathbf{l} . \quad (1.42)$$

Raychaudhuri's equation describes the evolution of the expansion scalar. In the case of a congruence of null geodesics, the equation reads

$$\frac{d\theta_{(l)}}{d\lambda} = -\frac{1}{2}\theta_{(l)}^2 - \sigma^2 + \omega^2 - R_{\mu\nu}l^\mu l^\nu \quad (1.43)$$

where σ is the shear scalar and ω the rotation parameter. This equation will prove essential in establishing Penrose's singularity theorem in Sec. 4.

2.4 Causal structure

This Section aims at giving a first approach to black holes and a way of representing them, namely Carter-Penrose diagrams.

2.4.1 Basic definitions

The metric tensor defined in Sec. 2.1.3 allows classifying vectors in terms of their causal nature.

Definition 1.13. A vector \mathbf{v} belonging to the tangent space of a manifold equipped with a metric \mathbf{g} of signature $(-+++)$ is

- *timelike* if $\mathbf{g}(\mathbf{v}, \mathbf{v}) < 0$,
- *null or lightlike* if $\mathbf{g}(\mathbf{v}, \mathbf{v}) = 0$,

- spacelike if $g(\mathbf{v}, \mathbf{v}) > 0$.

Adding the notion of tangent vector (Def. 1.5), this allows defining the causal nature of curves on a manifold.

Definition 1.14. A differential curve $\lambda(t)$ is said to be *timelike* (resp. *null*, *spacelike*) if at each $p \in \mathcal{L}$, the vector tangent \mathbf{v} to the curve is *timelike* (resp. *null*, *spacelike*).

It is said to be *causal* if \mathbf{v} is either *timelike* or *null*.

Particles always follow causal curves: the massive ones follow timelikes curves, and the massless ones null curves.

Let us now define the notion of future and past of a point, which will be of the uttermost importance in the following.

Definition 1.15. The *chronological future* $I^+(p)$ (resp. *chronological past* $I^-(p)$) of $p \in \mathcal{M}$ is the set of events that can be reached by a future (resp. past) directed timelike curve starting from p . For any subset $\mathcal{S} \supset \mathcal{M}$, we define $I^\pm(\mathcal{S}) = \bigcup_{p \in \mathcal{S}} I^\pm(p)$.

The definition of the causal future is analogous, except that it includes null curves.

Definition 1.16. The *causal future* $J^+(p)$ (resp. *chronological past* $J^-(p)$) of $p \in \mathcal{M}$ is the set of events that can be reached by a future (resp. past) directed causal curve starting from p . For any subset $\mathcal{S} \supset \mathcal{M}$, we define $J^\pm(\mathcal{S}) = \bigcup_{p \in \mathcal{S}} J^\pm(p)$.

$I^\pm(p)$ can be shown to be an open set, so is $I^\pm(\mathcal{S})$ as a union of open sets. One can show that $J^\pm(p)$ is a closed set when the spacetime is globally hyperbolic (see [57]).

The particularly simple example of Minkowski's space illustrates very well these notions, as seen in Fig. 1.3. The interior of the future null cone is $I^+(p)$, while $J^+(p)$ consists of all points in and on the future null cone. This future null cone is simply the boundary of $I^+(p)$: $\partial I^+(p) = J^+(p) \setminus I^+(p)$.

As will be explained in Sec. 4, a way of looking for singularities on a manifold consists in studying geodesics which should not stop abruptly at a finite affine parameter if no singularity is present. Let us first define *intextendible geodesics*.

Definition 1.17. A geodesic $\gamma: \mathcal{I}_v \rightarrow \mathcal{M}$ is said to be *maximal* or *geodesically inextendible* if the domain \mathcal{I}_v of γ is the largest possible.

This allows defining *geodesic completeness*, a notion that will play a key role in the demonstration of Penrose's singularity theorem (1.3).

Definition 1.18. A manifold \mathcal{M} is said to be geodesically complete if every inextendible geodesic is defined on the entire real line.

Another important notion in Penrose's theorem will be the one of Cauchy surface. We first need to define achronal sets and boundaries as follows.

Definition 1.19. A set \mathcal{S} is said to be achronal if there are no two points with timelike separation, i.e. $I^+(\mathcal{S}) \cap \mathcal{S} = \emptyset$.

Definition 1.20. An achronal boundary is a set of the form $\partial I^\pm(\mathcal{S})$, for some $\mathcal{S} \subset \mathcal{M}$.

We now have all the tools to introduce Cauchy developments, and consequently Cauchy surfaces.

Definition 1.21. The future (resp. past) Cauchy development $D^+(\mathcal{S})$ of an achronal set \mathcal{S} embedded in a manifold \mathcal{M} , or domain of dependence, is the set of all points $p \in \mathcal{M}$ such that every past (resp. future) inextendible causal curve through p intersects \mathcal{S} .

Definition 1.22. A Cauchy surface is an achronal subset \mathcal{S} of \mathcal{M} which is met by every inextendible causal curve. Equivalently, \mathcal{S} is such that $D^-(\mathcal{S}) \cup D^+(\mathcal{S}) = \mathcal{M}$.

In the following, we will make a synonymous use of the presence of a Cauchy surface and of the property of *global hyperbolicity*. This stems from the following theorem.

Theorem 1.2. \mathcal{M} is globally hyperbolic if and only if \mathcal{M} admits a Cauchy surface.

When a spacetime is not globally hyperbolic, it admits no Cauchy surface and hence possesses a *Cauchy horizon* (for concrete examples, see App. A.4).

Definition 1.23. Let Σ be a partial Cauchy surface, i.e. a Cauchy surface for only some part of spacetime. The future (resp. past) Cauchy horizon is the boundary of $D^+(\Sigma)$ (resp. $D^-(\Sigma)$).

2.4.2 Black holes: a first approach

The aim of this section consists in giving a first definition of a black hole, before studying in detail various black hole spacetimes in Chapter 2. A black hole can be seen as region of spacetime from which nothing can escape, neither matter nor light. To make this definition more precise, we will need to introduce the concept of future infinity, which is best represented on a *Carter-Penrose diagram*.

These diagrams, also called *conformal diagrams*, are a very convenient way of representing a whole spacetime on a sheet of paper. Their key properties are the following:

1. light rays propagate at $\pm 45^\circ$
2. the infinities are brought back to a finite distance.

	Definition	(t, r)	(τ, χ)
\mathcal{I}^+	future null infinity	$(+\infty, +\infty)$ $(t - r)$ finite	$(\pi - \chi, 0 < \chi < \pi)$
\mathcal{I}^-	past null infinity	$(-\infty, +\infty)$ $(t + r)$ finite	$(\chi - \pi, 0 < \chi < \pi)$
i^+	future timelike infinity	$(+\infty, \text{finite})$	$(\pi, 0)$
i^-	past timelike infinity	$(-\infty, \text{finite})$	$(-\pi, 0)$
i^0	spacelike infinity	$(\text{finite}, +\infty)$	$(0, \pi)$

Table 1.1: Definitions of timelike, null and spacelike infinities in Minkowski's spacetime, in terms of the initial coordinates (t, r) as well as of the conformal ones (τ, χ) .

Let us define more precisely the latter property, by considering the simple example of Minkowski's spacetime. The metric reads, as seen previously:

$$ds^2 = -dt^2 + dr^2 + r^2 d\theta^2 + r^2 \sin^2 \theta^2 d\varphi^2 \quad (1.44)$$

By making the (non-trivial) coordinate change

$$\begin{cases} \tau = \arctan(t+r) + \arctan(t-r), \\ \chi = \arctan(t+r) - \arctan(t-r), \end{cases} \quad (1.45)$$

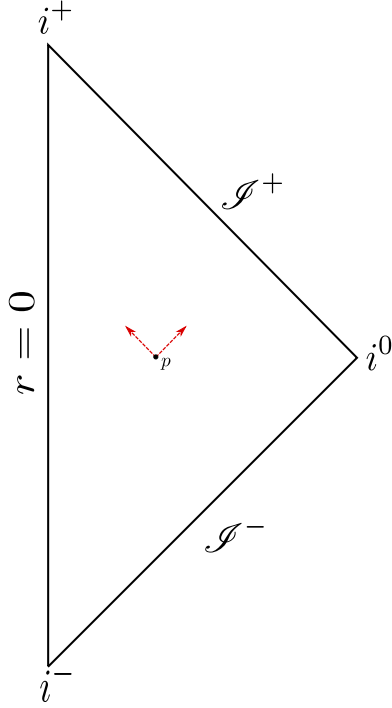
one can rewrite eq. (1.44) as

$$ds^2 = \left(\frac{1}{\cos \tau + \cos \chi} \right)^2 [-d\tau^2 + d\chi^2 + \sin^2 \chi^2 (d\theta^2 + \sin^2 \theta^2 d\varphi^2)] \quad (1.46)$$

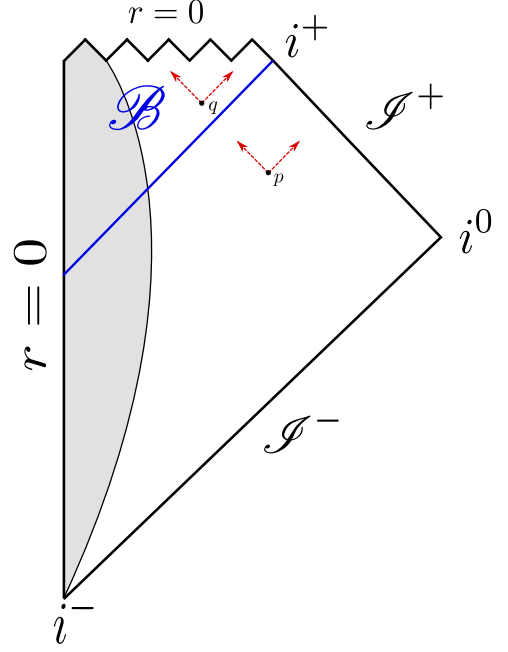
Thanks to the arctangent function, the new coordinates (τ, χ) remain finite when the previous coordinates (t, r) diverge. This is illustrated on Table 1.1, where we define future and past infinities.

The line elements in brackets, in the r.h.s. of eq. (1.46), defines a metric conformally related to g :

$$\tilde{g}_{\mu\nu} d\tilde{x}^\mu d\tilde{x}^\nu = -d\tau^2 + d\chi^2 + \sin^2 \chi^2 (d\theta^2 + \sin^2 \theta^2 d\varphi^2). \quad (1.47)$$



(a) Minkowski's spacetime.



(b) Oppenheimer-Snyder's collapse of a star.

Figure 1.7: Carter-Penrose diagrams of the Minkowski spacetime and the Oppenheimer-Snyder collapse. On the latter, the collapsing star is depicted in grey. Each point on the diagram is a 2-sphere, and light rays propagate at $\pm 45^\circ$. They can always reach \mathcal{I}^+ on Minkowski's diagram, while those in the black hole region \mathcal{B} of the Oppenheimer-Snyder diagram are forced to fall into the singularity ($r = 0$).

$\mathcal{I} = \mathcal{I}^+ \cup \mathcal{I}^-$ is said to be the conformal boundary of (\mathcal{M}, g) within the conformal completion $(\tilde{\mathcal{M}} = \mathcal{M} \cup \mathcal{I}, \tilde{g})$. The complete Minkowski spacetime is represented by the Penrose diagram in Fig. 1.7(a).

On this diagram, radial light rays propagate at $\pm 45^\circ$. This is simply because

$$g_{\mu\nu} dx^\mu dx^\nu = 0 \iff \tilde{g}_{\mu\nu} d\tilde{x}^\mu d\tilde{x}^\nu = 0 \iff d\tau^2 = d\chi^2. \quad (1.48)$$

In such a spacetime, all null geodesics terminate on \mathcal{I}^+ and the timelike geodesics end on i^+ (after potentially crossing $r = 0$). In a word, no geodesic is trapped in a compact region forever. This is expected in Minkowski's spacetime, where no black hole is present.

But this may guide us to give a *global definition of a black hole*. This rather formal definition consists in considering a black hole as the set of points of \mathcal{M} that are not in the causal past of future null infinity, i.e.

$$\mathcal{B} = \mathcal{M} \setminus (J^-(\mathcal{I}^+) \cap \mathcal{M}). \quad (1.49)$$

The event horizon, a null codimension 1 hypersurface causally separating the black hole region

from the rest of spacetime, is then

$$\mathcal{H} = \partial\mathcal{B} . \quad (1.50)$$

One should note that these definitions of the black hole and the event horizon are teleological, and thus prevent any human being from ever claiming the observation of a black hole... Indeed, they involve future null infinity and thus require the knowledge of the entirety of spacetime: an observer would hence need to wait for the end of time before announcing his discovery.

The concept of black hole encoded in eq. (1.49) is best grasped when considering an actual example, such as the Oppenheimer-Snyder collapse of a star. It is actually in order to avoid repeating the locution “completely collapsed object” that John Wheeler contributed to popularise the term “black hole” in 1967 ⁶. The associated Penrose diagram is shown in Fig. 1.7(b), where the shells of collapsing matter are pictured in grey. This spacetime can be divided into two zones, on one side or the other of the event horizon (blue line). Outside, the situation seems rather similar to Minkowski’s spacetime: radial outgoing null rays can reach \mathcal{I}^+ , and timelike observers i^+ . However, inside the \mathcal{B} zone the situation is dramatically different: every causal curve is doomed to fall towards $r = 0$, which leaves it no choice but ending its trajectory on the curvature singularity (which is called so because some curvature scalars, as the Kretschmann scalar K , diverge at $r = 0$). Hence no observer nor light ray going crossing the event horizon will ever be able to escape.

3 Einstein’s equations

3.1 Formulation of the equations

3.1.1 Energy-momentum tensor

Before connecting the curvature of spacetime to its matter content via Einstein’s equations, one has to define this content. More precisely, one has to do this in a covariant way, i.e. so that that any two observers will agree on the matter content.

To this end, let us consider the simple example of dust, i.e. of a time-dependent distribution of electrically neutral non-interacting particles, each of rest mass m_0 . An observer at rest with respect to this distribution of matter will measure the proper energy density of the fluid, which is $\rho_0 = n_0 m_0$ (n_0 being the density of particles). Now, what density would measure an observer with constant velocity v ? Since, due to Lorentz transformations, lengths are contracted in the direction of motion, one gets

⁶the name was shouted at him during a conference, but it was actually first coined during the First Texas Symposium on Relativistic Astrophysics in Dallas, in 1963 [16]

$$\begin{aligned} m_0 &\rightarrow \gamma m_0 \\ n_0 &\rightarrow \gamma n_0, \end{aligned} \tag{1.51}$$

where γ is the Lorentz factor defined in eq. (1.5):

$$\gamma = \left(1 - \frac{v^2}{c^2}\right)^{-\frac{1}{2}}. \tag{1.52}$$

Hence, the energy density of the fluid seen from the observer with velocity v becomes:

$$\rho \rightarrow \gamma^2 \rho \tag{1.53}$$

Actually, it transforms as the 00-component of a rank-2 tensor. This quick argument encourages us to define the matter content of a spacetime via a rank-2 tensor named *energy-momentum tensor* as follows.

Definition 1.24. *The energy-momentum tensor, or stress-energy tensor \mathbf{T} of a fluid, is a symmetric tensor of type (0,2). \mathbf{T} is such that an observer at rest with respect to the fluid will measure:*

1. *an energy density T^{00} ,*
2. *an energy flux cT^{0i} in the i -direction,*
3. *a momentum density T^{i0}/c in the i -direction,*
4. *the rate of flow T^{ij} of the i -component of momentum per unit area in the j -direction.*

The energy-momentum of a fluid satisfies a conservation equation which enforces the conservation of both the energy and momentum associated with the fluid:

$$\nabla_a T^{ab} = 0 \tag{1.54}$$

Most of exact energy-momentum tensors are only known in very specific and often simplified situations (with a high degree of symmetry), such as the dust previously mentioned. Among all the possible expressions for the energy-momentum tensors, physicists have thus tried to define the “physically reasonable” ones. That is where the energy conditions come from; they play a central role in the singularity theorems (Section 4.2).

The weak energy condition, for instance, imposes that every timelike observer must measure non-negative energy densities. The expression of these conditions in terms of the components of the energy-momentum tensor (see [96]), as well as the implication links between them, are visible in Fig. 1.8.

One should regard these conditions with caution. Indeed, the strong energy condition is currently violated by the acceleration of the expansion of the universe [10], and the null energy condition is violated in quantum experiments involving Casimir’s effect [52]. In Chapter 6, our goal will precisely be to violate the weakest of energy conditions, the null energy condition, in order to make dynamical regular black holes evaporate.

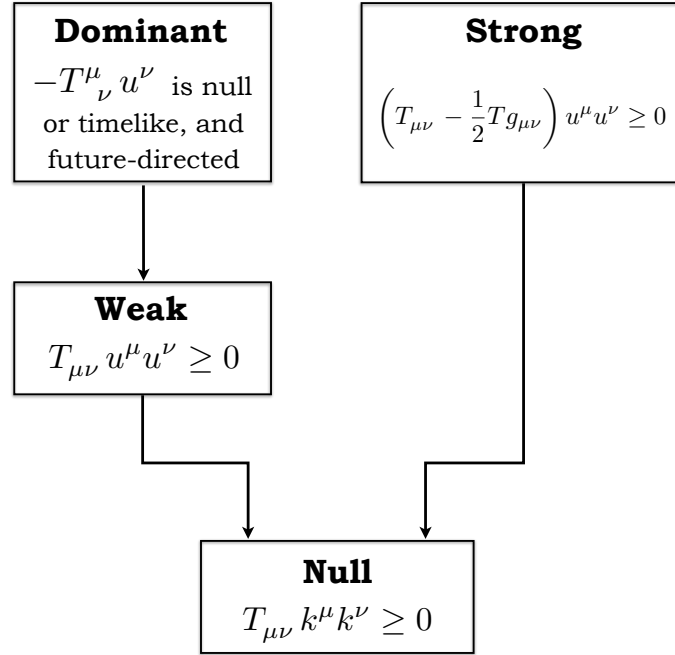


Figure 1.8: Main energy conditions, as well as their causal relations. The null energy condition is the weakest one, implied by all the others: when violated, so are all energy conditions.

3.1.2 The equations

We now have a way of describing the matter content of a spacetime, but it remains to relate it to the curvature of the latter. A simple way consists in building a rank-2 tensor out of the Riemann curvature tensor. Einstein first used the Ricci tensor \mathbf{R} , but realized it was not divergence free. By conservation of energy and momentum, he could thus not equate R_{ab} with T_{ab} . He then defined the now famous Einstein tensor \mathbf{G} , leading to Einstein's equations:

$$G_{ab} \equiv R_{ab} - \frac{1}{2} R g_{ab} = 8\pi T_{ab} , \quad \text{or} \quad \mathbf{G} = 8\pi \mathbf{T} , \quad (1.55)$$

where the 8π factor ensures that one recovers Poisson's equation in the weak-field limit. Eq. (1.55) contains 16 equations, but we can as of now remove 6 of them due to the symmetry of the tensors involved. An additional 4 equations (one for each coordinate) can be removed due to the general covariance of the theory under diffeomorphisms. This latter step actually directly stems from the identity

$$\nabla_a G^{ab} = 0 . \quad (1.56)$$

Finally, this leaves us with 6 independent equations to describe the spacetime formed by a given source of matter.

Einstein's equations can be written in an even more general form, adding a cosmological constant Λ to the l.h.s. of eq. (1.55) while preserving its divergence-free property:

$$\boxed{R_{ab} - \frac{1}{2}Rg_{ab} + \Lambda g_{ab} = 8\pi T_{ab}} . \quad (1.57)$$

3.2 Lagrangian formulation: Einstein-Hilbert's action

Einstein's equations can be reformulated using the variational formalism, which will prove useful in Chap. 3. Let us introduce the action

$$\begin{aligned} S[g_{\mu\nu}, \varphi] &= S_{\text{EH}}[g_{\mu\nu}] + S_{\text{mat}}[g_{\mu\nu}, \varphi] \\ &= \int d^4x \sqrt{-g} \left(\frac{1}{16\pi} \mathcal{L}_{\text{EH}} + \mathcal{L}_{\text{mat}} \right) , \end{aligned} \quad (1.58)$$

where S_{EH} is the Einstein-Hilbert action, of lagrangian density $\mathcal{L}_{\text{EH}} = R^{\mu\nu} g_{\mu\nu} = R$. \mathcal{L}_{mat} is the lagrangian density of matter fields, represented by the variable φ .

By the principle of least action, a variation of the action (1.58) according to a variation $g_{\mu\nu} \rightarrow g_{\mu\nu} + \delta g_{\mu\nu}$ of the metric must lead to

$$\frac{\delta}{\delta g^{\mu\nu}} (S_{\text{EH}} + S_{\text{mat}}) = 0 . \quad (1.59)$$

The variation of the Einstein-Hilbert action requires to compute the variation of the Ricci tensor, hence of the Riemann tensor and the Christoffel symbols. The computational details are not of interest here, and can be found in [76]. One gets

$$\frac{\delta S_{\text{EH}}}{\delta g^{\mu\nu}} = \frac{\sqrt{-g}}{16\pi} \left(R_{\mu\nu} - \frac{1}{2}Rg_{\mu\nu} \right) = \frac{\sqrt{-g}}{16\pi} G_{\mu\nu} . \quad (1.60)$$

Hence, in the absence of matter ($\mathcal{L}_{\text{mat}} = 0$), eq. (1.59) reduces to Einstein's equations in vacuum:

$$R_{\mu\nu} - \frac{1}{2}Rg_{\mu\nu} = 0 . \quad (1.61)$$

To obtain the full Einstein's equations in presence of matter, one has to define the energy-momentum tensor of matter as follows:

$$T_{\mu\nu} \equiv -\frac{2}{\sqrt{-g}} \frac{\delta S_{\text{mat}}}{\delta g^{\mu\nu}} . \quad (1.62)$$

Even if this definition may seem *ad hoc*, it can actually be shown (see [76]) that the r.h.s of eq. (1.62) is a divergence free symmetric tensor, hence enforcing the conservation of energy and momentum.

Finally, we have only considered the variation of the action (1.58) with respect to the variation of the metric. But one can also consider variations with respect to the variable φ , encoding

the matter fields. The Einstein-Hilbert part of the action will not be affected by this variation, hence the resulting equations will be the equations of motion of the matter fields in the curved spacetime.

4 Singularity theorems

What is so special about singularities in General Relativity? How can one explain the profusion of singularity theorems, while singularities are also known features of Newton's and Maxwell's theory? Well, this is simply because in the framework of General Relativity, singularities can occur regardless of the degree of symmetry of a physical system.

Let us consider the collapse of a perfectly spherical nonrotating shell of dust. In Newton's theory, this leads to a singularity at the centre because all the matter reaches $r = 0$ simultaneously. Had we started with a slightly distorted configuration of matter, no singularity would have occurred.

In General Relativity, a nonspherical gravitational collapse leads to a singularity because the keypoint is that there exists a trapped surface, i.e. a surface from which particles following timelike or null curves can only go to decreasing values of the radial coordinate. These trapped surfaces are associated with a very strong gravitational field, dragging back even the outgoing light rays emanating from the surface.

In this section we will define precisely what a singularity is, before exhibiting the first theorem which proves the existence of such a singularity regardless of the symmetry of a specific physical configuration: Penrose's 1965 singularity theorem [94]. We will then go through the proof in details in order to understand the role of its assumptions, and to be able to circumvent it when we will work with non-singular black holes. Finally, we will merely quote another singularity theorem formulated by Hawking and Penrose in 1970 [68].

4.1 What is a singularity?

Sketching the notion of singularity is a risky business, that we shall now undertake with caution following [67, 122]. We could be tempted to identify singularities as the locus in spacetime where curvature blows up, as was the case with the gravitational collapse 2.4.2. But we should not forget that a spacetime consists of a manifold \mathcal{M} together with a metric \mathbf{g} defined everywhere on \mathcal{M} . Therefore, singularities such as $r = 0$ in Schwarzschild's solution are not part of spacetime.

Hence, a criterion for defining singularities could take advantage of the "holes" left by their removal from spacetime. A physically relevant way of exploring the presence of these "holes" is to follow observers along timelike *inextendible* geodesics, i.e. geodesics whose domain of definition is

the largest possible (Def. 1.17). If the affine parameter of this geodesic does not cover the entire real line, the geodesic is said to be *incomplete* (Def. 1.18). It means that the trajectory of our observer ends after or before a finite interval of proper time, which is a good enough reason to call such a spacetime singular.

This timelike (and null) *geodesic completeness* is precisely what is established by the singularity theorems under certain assumptions, as we shall see in the next section (4.2). But these theorems are not exactly forthcoming with details regarding the nature of singularities. They establish that there exists at least one timelike or null incomplete geodesic, but not whether it is a curvature singularity (like in Schwarzschild's spacetime) or a non-curvature singularity (like in Taub-NUT spacetime, see [87]). Conversely, it should be noted that a curvature singularity, which stems from the divergence of some second derivatives of the metric, does not imply the incompleteness of any geodesic [37].

Despite the difficulties generated by the quest for a definition of singularities, we need a practical definition for the singularity-free black holes we will be considering in this thesis.

Definition 1.25. *We will consider that a spacetime is non-singular, or regular, if it is timelike and null geodesically complete and does not contain any curvature singularity.*

In practice, we will check that:

- (i) the assumptions of Penrose's singularity theorem are not simultaneously satisfied, i.e. that we have a large enough leeway to circumvent the theorem,
- (ii) the curvature scalars do not diverge.

This being said, one should keep in mind that the above definition is not ideal, as the two following points illustrate very well:

- there exists spacetimes with a non-zero Riemann tensor but whose curvature scalars all vanish [105],
- there exist geodesically complete spacetimes which contain an inextendible timelike curve of bounded acceleration and finite length, which should then also be considered singular [60].

4.2 Penrose's singularity theorem (1965)

4.2.1 Notion of trapped surface

The cornerstone of Penrose's theorem is the presence of a trapped surface, which describes regions of spacetime subject to very strong gravitational fields.

Definition 1.26. A trapped surface Σ in \mathcal{M} is a closed (i.e. compact without boundary)⁷ co-dimension two spacelike submanifold of \mathcal{M} such that the two families of ingoing (−) and outgoing (+) null geodesics orthogonal to Σ are converging on Σ : $\theta_- < 0$ and $\theta_+ < 0$ on Σ .

By comparison, a *normal surface* is such that $\theta_- < 0$ and $\theta_+ > 0$. The fact that $\theta_+ < 0$ on trapped surfaces expresses the very strong gravitational field which characterizes them: even outgoing light rays are directed towards decreasing values of the radial coordinate r .

In the following chapters we will also make use of *anti-trapped surfaces*. They are defined similarly to trapped surfaces, except that this time the ingoing vectors are directed towards increasing values of r : $\theta_- > 0$ and $\theta_+ > 0$.

The boundary between a normal surface and a trapped (or anti-trapped) surface is a *trapping horizon*. These trapping horizons fall into four different categories, which are detailed in App. A.

4.2.2 Formulation and proof

Theorem 1.3 (Penrose, 1965 [94]). Let \mathcal{M} be a spacetime satisfying the following conditions:

- (i) \mathcal{M} is globally hyperbolic
- (ii) \mathcal{M} possesses a noncompact Cauchy surface S
- (iii) $R_{\mu\nu}k^\mu k^\nu \geq 0$ for all null vector k (null convergence condition).

If \mathcal{M} contains a trapped surface Σ , then \mathcal{M} is future null geodesically incomplete.

Numerous examples of non-singular black holes will be displayed through this dissertation, it is thus of the uttermost importance to understand how these models manage to circumvent Penrose’s singularity theorem. For that purpose, we will study in detail a proof of this theorem which can be found in [57].

A schematic view of the proof is given in Fig. 1.9. The general idea is to construct a specific future inextendible null geodesic γ in the boundary of the future of Σ , $\partial I^+(\Sigma)$, and then to show that it must be future incomplete. It should be noted, as emphasized in [94], that no assumption of symmetry is made.

In order for this geodesic not to escape from $\partial I^+(\Sigma)$ and to be inextendible, $\partial I^+(\Sigma)$ must not be compact. This is proven in step 1 of Fig. 1.9: if $\partial I^+(\Sigma)$ were compact one can show that it would be a compact Cauchy surface, which is incompatible with the assumption of existence of a noncompact Cauchy surface S given that all Cauchy surfaces are homeomorphic. As a boundary, $\partial I^+(\Sigma)$ is closed; this allows constructing a sequence of points q_k in $\partial I^+(\Sigma)$. This sequence can diverge to infinity due to the noncompactness of $\partial I^+(\Sigma)$ (step 2). It is then shown in step 4 that

⁷In this dissertation, when referring to a trapped surface, we will by definition consider that it is a closed surface (contrarily, for instance, to Hawking & Ellis [67]).

all points q_k can be reached by a null geodesic γ_k starting from Σ . By compactness of Σ (step 5), the sequence of geodesics γ_k converges towards γ , an inextendible null geodesic in $\partial I^+(\Sigma)$ (step 6). Step 9 is the crucial point of the proof: the Raychaudhuri equation, to which is applied the null convergence condition (step 7), gives the evolution of the null expansion in the outgoing direction of the hypersurface H which contains γ . Since Σ is trapped, the inverse of the expansion θ_0^{-1} must be negative there, and then reach 0 from below in a finite affine time. Hence θ_H diverges in a finite affine time, which shows that γ is future incomplete.

Let us now give the formal proof, following the steps of Fig. 1.9 and giving the details of each of them.

Step 1

We will show that the existence of a noncompact Cauchy surface S in \mathcal{M} implies that the boundary of the future of a trapped surface Σ is noncompact. To do so we will need the following two propositions, which are standard results of differential geometry whose proof is given in [92].

Proposition 1.1. *Let $S \subset \mathcal{M}$. An achronal boundary $\partial I^+(S)$, if nonempty, is a closed achronal C^0 hypersurface in \mathcal{M} .*

Proposition 1.2. *If S is a compact C^0 achronal hypersurface in a globally hyperbolic spacetime \mathcal{M} , then S must be a compact Cauchy surface for \mathcal{M} .*

Let us start with the future of the boundary of a trapped surface Σ , $\partial I^+(\Sigma)$, which is by definition an achronal boundary (see Def. (1.20)). By Proposition (1.1), $\partial I^+(\Sigma)$ is an achronal C^0 hypersurface.

Let us now assume $\partial I^+(\Sigma)$ to be compact. By Proposition (1.2), $\partial I^+(\Sigma)$ must then be a compact Cauchy surface. However, by assumption of the theorem, there exists a noncompact Cauchy surface S for \mathcal{M} . Since all Cauchy surfaces are homeomorphic, this leads to a contradiction and to the conclusion that $\partial I^+(\Sigma)$ must be noncompact.

Step 2

$\partial I^+(\Sigma)$ is a boundary, hence it is closed. Then one can build a sequence of points q_k in $\partial I^+(\Sigma)$, and since $\partial I^+(\Sigma)$ is noncompact this sequence can diverge to infinity.

Step 3

In order to prove step 3, the following proposition is needed.

Proposition 1.3. *In a spacetime \mathcal{M} , if q is in the causal future of p but not in its timelike future, then any future directed causal curve from p to q must be a null geodesic (when suitably parameterized).*

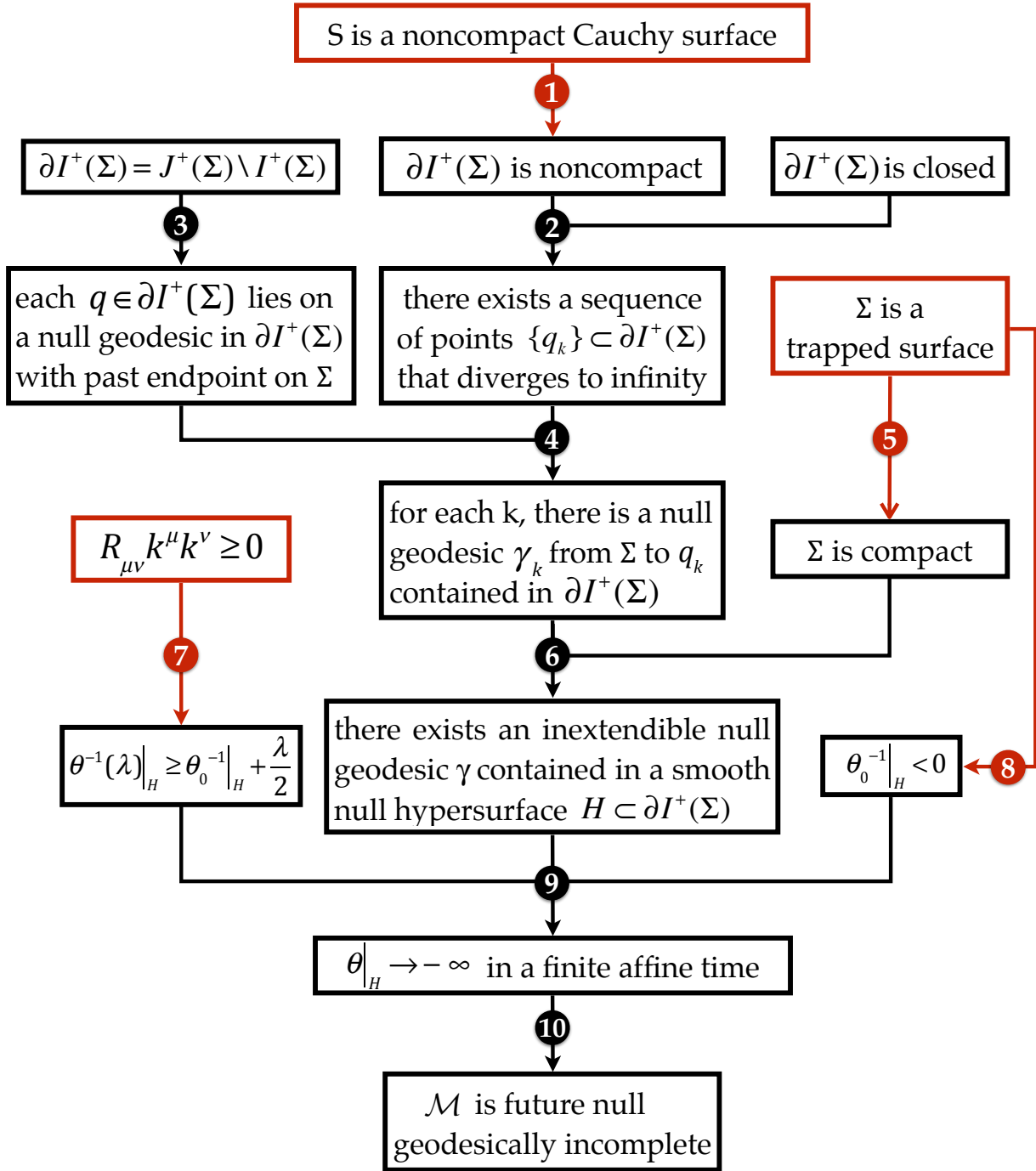


Figure 1.9: Schematic view of a proof of Penrose's singularity theorem (1965). The assumptions of the theorem are depicted by red boxes. The arrows represent logical links between the various steps of the proof, and the numbers indicate the order of reading.

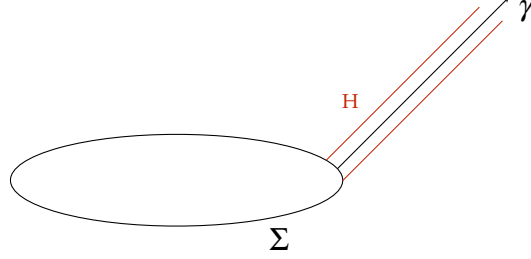


Figure 1.10: Inextendible geodesic in $\partial I^+(\Sigma)$ contained in a null hypersurface H and emanating from a trapped surface Σ . It is the geodesic constructed explicitly at step 6 of the proof (Fig. 1.9), which will prove to be incomplete.

$\partial I^+(\Sigma)$ is by definition the closure of $I^+(\Sigma)$ deprived of its interior, i.e. $\partial I^+(\Sigma) = J^+(\Sigma) \setminus I^+(\Sigma)$. Hence each $q \in \partial I^+(\Sigma)$ is in the causal future of a point on Σ but not in its timelike future. By Proposition (1.3), q must thus lie on a null geodesic in $\partial I^+(\Sigma)$ with past endpoint on Σ .

Step 4

The result of step 3 can be applied to the sequence of points q_k . Hence, for each k there is a null geodesic γ_k from Σ to q_k , which is contained in $\partial I^+(\Sigma)$.

Step 5

By assumption of the theorem, Σ is a trapped surface, and in particular by definition a closed codimension two spacelike submanifold of \mathcal{M} . Hence, Σ is compact.

Step 6

Since Σ is compact, there must exist a subsequence γ_k which converges to a future inextendible null geodesic γ contained in $\partial I^+(\Sigma)$. As seen in Fig. 1.10, this geodesic can be chosen outward pointing and is contained in a smooth null hypersurface $H \subset \partial I^+(\Sigma)$. It remains now to show that γ is future null incomplete. To do so we will need to compute the null expansion scalar of H along γ .

Step 7

The null expansion scalar $\theta = \theta(\lambda)$ of H along γ is given by the Raychaudhuri equation:

$$\frac{d\theta}{d\lambda} = -\frac{1}{2}\theta^2 - \sigma^2 + \omega^2 - R_{\mu\nu}k^\mu k^\nu, \quad (1.63)$$

where k^μ is tangent to γ . Assuming the null convergence condition, and since the geodesic congruence generated by k is irrotational ($\omega = 0$), the Raychaudhuri equation becomes:

$$\left. \frac{d\theta}{d\lambda} \right|_H \leq -\frac{1}{2}\theta^2, \quad (1.64)$$

hence:

$$\left. \frac{d}{d\lambda} \theta^{-1} \right|_H \geq \frac{1}{2}. \quad (1.65)$$

Finally:

$$\left. \theta^{-1} \right|_H \geq \left. \theta_0^{-1} \right|_H + \frac{\lambda}{2}, \quad (1.66)$$

where $\left. \theta_0 \right|_H$ is the expansion scalar of H on Σ .

Step 8

Σ being a trapped surface, the expansion scalar in both ingoing and outgoing null directions must be negative. Hence, $\left. \theta_0^{-1} \right|_H < 0$.

Step 9

Considering the elements of steps 6,7,8 altogether, we are now able to show that $\theta(\lambda)|_H$ diverges in a finite affine time. Indeed, since $\left. \theta_0^{-1} \right|_H < 0$, $\left. \theta^{-1} \right|_H$ must reach zero as λ increases. Thus $\theta|_H \rightarrow -\infty$ in a finite affine time $\lambda = -2 \left. \theta_0^{-1} \right|_H$.

Step 10

The geodesic γ is thus not defined for $\lambda \geq -2 \left. \theta_0^{-1} \right|_H$. Hence γ is not defined on the entire real line, and by Def. (1.18) \mathcal{M} is future null geodesically incomplete.

4.2.3 Circumventing the theorem

For the purpose of studying non-singular black holes, let us now discuss the assumptions of Penrose's theorem that we could violate. Actually the only one that we will not call into question is the existence of a trapped surface, since the models of black holes to be studied in this dissertation all possess at least a trapping horizon. But this leaves us several options to circumvent the theorem:

- violate *global hyperbolicity*,
- consider a spacetime \mathcal{M} with a *compact Cauchy surface*,
- violate the null convergence condition $R_{\mu\nu}k^\mu k^\nu \geq 0$, i.e. *violate the null energy condition* assuming Einstein's equations hold.

A violation of global hyperbolicity is equivalent to the absence of a Cauchy surface in the spacetime. This situation will be illustrated with Bardeen's black hole [11], which dates back to 1968. As pointed out by Hawking and Ellis [67], this spacetime satisfies all the conditions of Penrose's theorem but the existence of a Cauchy surface, it contains trapped surfaces but no singularity. Another example of such a spacetime is Hayward's static black hole [71], that will be presented in detail in Sec. 1.2.

Is there any interest in building non-singular black hole spacetimes with a compact Cauchy surface S ? Actually, there is not. Indeed, the assumption of noncompactness of the Cauchy surface was used at only one place in the proof, in the first step. The key point was that if $\partial I^+(\Sigma)$ were not only a C^0 achronal hypersurface but also a compact one, it should be a compact Cauchy surface (Proposition 1.2). S being a noncompact Cauchy surface, this led to a contradiction since Cauchy surfaces are homeomorphic, and thus to the noncompactness of $\partial I^+(\Sigma)$.

But as pointed out by Hawking & Ellis in [67], one can replace the noncompactness of S by the assumption of existence of a future inextendible curve from S which does not intersect $\partial I^+(\Sigma)$. This amounts to assuming that an observer can avoid falling into the collapsing star, which is well motivated physically. In this case the hypersurface $\partial I^+(\Sigma)$ is not a Cauchy surface since it is not crossed by the observer. At least one of the assumptions of Proposition (1.2) must thus be violated, it happens to be the compactness of $\partial I^+(\Sigma)$ since by assumption \mathcal{M} is globally hyperbolic.

The last possibility consists in violating the null convergence condition, which is tantamount to the null energy condition if Einstein's equations are satisfied. A violation of the energy conditions is often related to the presence of quantum effects, for instance the weak energy condition is violated in the Casimir effect [52]. In Chap. 6, we will introduce regular dynamical black hole models possessing a Cauchy surface but violating the null energy condition, which prevents them from the conclusions of Penrose's theorem.

4.3 Hawking & Penrose's singularity theorem (1970)

Assuming the existence of a Cauchy hypersurface and the presence of a trapped surface, the Penrose theorem leads to a breakdown of our ability to predict the future [67]. Indeed, either a singularity forms, or a Cauchy horizon is required so that it does not form. But it may appear more physically motivated to drop the global hyperbolicity condition than to accept the presence of a singularity. That is why Hawking and Penrose formulated a theorem which does not require the global hyperbolicity of the spacetime, nonetheless predicting the existence of a singularity.

Theorem 1.4 (Hawking & Penrose, 1970 [68]). *The spacetime (\mathcal{M}, g) is not timelike and null geodesically complete if:*

1. *the null convergence condition is satisfied: $R_{\mu\nu}k^\mu k^\nu \geq 0$ for all non-spacelike vector k^μ*

2. *the generic condition is satisfied*
3. *the chronology condition holds on \mathcal{M} (i.e. there are no closed timelike curves)*
4. *There exists at least one of the following*
 - (i) *a compact achronal set without edge*
 - (ii) *a trapped surface*
 - (iii) *a point p such that on every past (or every future) null geodesic from p the expansion θ of the null geodesics from p becomes negative*

It should be noted that the null convergence condition is tantamount, if Einstein's equations are fulfilled, to

$$\left(T_{\mu\nu} - \frac{1}{2}T_{\alpha}^{\alpha}g_{\mu\nu}\right)k^{\mu}k^{\nu} \geq 0, \quad (1.67)$$

which is nothing but the strong energy condition (see Fig. 1.8).

Finally, we notice that Theorem 1.4 does not make any mention of *future* incompleteness. It can indeed be applied to a past trapped surface in a cosmological setup to show that the associated spacetime is past geodesically incomplete, i.e. that the Universe emerged from the Big-Bang singularity.

BLACK HOLE SOLUTIONS IN GENERAL RELATIVITY



$rd \sim n = t(w) \quad n = j \quad 'nh \quad wsr \quad m \quad \mathfrak{z}h.t !$

“C’est dans l’horizon que m’ont été données vie et puissance !”

(*Textes des Sarcophages* IV, 109a, S1C [42, 64].)

Solutions to Einstein’s equations are reputedly hard to find, due to the nonlinearity of the latter. But various solutions do exist, in the astrophysical or cosmological regime. We will focus in this Chapter¹ on the former, which incidentally gave birth to the very first solution to Einstein equations, namely the Schwarzschild solution. This static metric, describing the empty spacetime around a spherically symmetric object, was obtained by Schwarzschild in 1915 [104] and will be discussed in Section 1. A generalization of this spacetime to the case of a charged, still static body, was found by Reissner and Nordström. It will be detailed in Section 2, and the metric will be of interest when we obtain black hole solutions from modified theories of gravity in Chapter 3. We will then move on to a stationary solution in Section 3, namely Kerr’s metric, describing the spacetime associated with a rotating black hole. This metric will be the basis for the non-singular model of a rotating black hole at the center of the Galaxy that we propose and study in Chapters 4 & 5. Finally, we will present a simple model of collapse, given by Vaidya’s metric (Section 4), which we will use in Chapter 6 to propose models of collapse leading to non-singular black holes.

Contents

1	Schwarzschild’s solution	42
2	Reissner-Nordström solution	50
3	Kerr’s solution	57
4	Vaidya’s solution and gravitational collapse	66

¹The main sources used to write this chapter are the following: [96], [63], [76], [31] and [67].

1 Schwarzschild's solution

1.1 Solving Einstein's equations in vacuum

Let us start with a spherically symmetric metric cast in its most general form:

$$ds^2 = -e^{2\psi(t,r)} F(t,r) dt^2 + F^{-1}(t,r) dr^2 + r^2 d\theta^2 + r^2 \sin^2 \theta d\varphi^2 \quad (2.1)$$

The geometrical part of Einstein's equations, namely the Einstein tensor, is computed in details in App. B.1. The result is

$$G^t_t = \frac{rF' + F - 1}{r^2} \quad (2.2)$$

$$G^r_r = -\frac{\dot{F}}{r} \quad (2.3)$$

$$G^t_r = \frac{\dot{F} e^{-2\psi}}{r F^2} \quad (2.4)$$

$$G^r_r = \frac{2rF\psi' + rF' + F - 1}{r^2} \quad (2.5)$$

$$G^\theta_\theta = G^\varphi_\varphi = \frac{e^{-2\psi}}{2rF^3} [2rF^4 e^{2\psi} (\psi'^2 + \psi'') + F^3 e^{2\psi} (rF'' + 2F') - rF\dot{F}\psi - 2r\dot{F}^2 + rF\ddot{F} + (3rF' + 2F)e^{2\psi} F^3 \psi'] \quad (2.6)$$

We can parametrize F using a function $M(t, r)$:

$$F(t, r) \equiv 1 - \frac{2M(t, r)}{r} \quad (2.7)$$

Assuming Einstein's equations $G_{\mu\nu} = 8\pi T_{\mu\nu}$, we get:

$$\frac{\partial M}{\partial r} = -4\pi r^2 T^t_t \quad (2.8)$$

$$\frac{\partial M}{\partial t} = 4\pi r^2 T^r_t \quad (2.9)$$

$$\frac{\partial \psi}{\partial r} = 4\pi r F^{-1} (-T^t_t + T^r_r) \quad (2.10)$$

We want to solve Einstein's equations in vacuum, i.e. with a vanishing energy-momentum tensor. Solving eqs. (2.8) and (2.9), we get $M \equiv M_0 = \text{cst.}$ Moreover, eq. (2.10) yields $\psi' = 0$. Along with $M' = \dot{M} = 0$, this condition is sufficient to satisfy the last Einstein's equations: $G^t_r = G^\theta_\theta = G^\varphi_\varphi = 0$. We are thus free to choose $\psi = 0$ (which amounts to reparametrizing time) hence leading to the line element:

$$ds^2 = -\left(1 - \frac{2M_0}{r}\right) dt^2 + \left(1 - \frac{2M_0}{r}\right)^{-1} dr^2 + r^2 d\theta^2 + r^2 \sin^2 \theta d\varphi^2 \quad (2.11)$$

Starting from a spherically symmetric metric and solving Einstein's equation in vacuum, we actually ended up with a *static* solution: no component of the metric with line element (2.11) depends on the time t . We have thus proved Birkhoff's theorem.

Theorem 2.1 (Birkhoff). *The spacetime geometry outside a general spherically symmetric matter distribution is the Schwarzschild static geometry*

Actually, the line element (2.11) represents the *Schwarzschild solution*², and the coordinates (t, r, θ, φ) are the *Schwarzschild-Droste coordinates*. This metric describes the gravitational field around a spherical body of mass M_0 .

Two singularities appear in this metric, since it diverges for $r = 0$ and $r = 2M_0$. But these two singularities are quite different in nature. To see this, let us compute the Ricci and Kretschmann scalars:

$$R \equiv R_{\mu\nu}g^{\mu\nu} = 0 \quad (2.12)$$

$$K \equiv R_{\mu\nu\rho\sigma}R^{\mu\nu\rho\sigma} = \frac{48M_0^2}{r^6} \quad (2.13)$$

The Kretschmann scalar diverges at $r = 0$, which is thus the locus of a curvature singularity. However, as we shall see in the next section, $r = 2M_0$ is merely a coordinate singularity which can be dealt with by an appropriate choice of coordinates.

1.2 Crossing the horizon

Let us look at the radial null geodesics of Schwarzschild's spacetime. The radial null curves are defined by $ds^2 = 0$ with $d\theta = d\varphi = 0$. We thus get

$$\frac{dt}{dr} = \pm \left(1 - \frac{2M_0}{r}\right)^{-1}. \quad (2.14)$$

This quantity gives the outgoing (+) and ingoing (−) slopes of a lightcone in a (t, r) diagram. Hence, as $r \rightarrow 2M_0$, $dt/dr \rightarrow \pm\infty$ and the lightcone seems to close up (Fig. 2.1). The coordinates (t, r) are thus suited only to describe the regions with $0 < r < 2M_0$ and $r > 2M_0$, and the hypersurface $r = 2M_0$ is a coordinate singularity. In terms of the ranges of the Schwarzschild-Droste coordinates (t, r, θ, φ) , these regions are:

$$\begin{cases} \mathcal{M}_I \equiv \mathbb{R} \times (2M_0, +\infty) \times \mathbb{S}^2, \\ \mathcal{M}_{II} \equiv \mathbb{R} \times (0, 2M_0) \times \mathbb{S}^2 \end{cases}. \quad (2.15)$$

The full region is called the *Schwarzschild-Droste domain*:

$$\mathcal{M}_{SD} \equiv \mathcal{M}_I \cup \mathcal{M}_{II}. \quad (2.16)$$

Let us now obtain a new coordinate system defined both on \mathcal{M}_I , \mathcal{M}_{II} , and on the hypersurface $r = 2M_0$. Eq. (2.14) can be integrated, yielding:

$$t = \pm r_* + \text{cst}, \quad \text{with } r_* = r + 2M_0 \ln \left| \frac{r}{2M_0} - 1 \right| \quad (2.17)$$

²obtained by Karl Schwarzschild in 1915, who was then a German soldier on the Russian front.

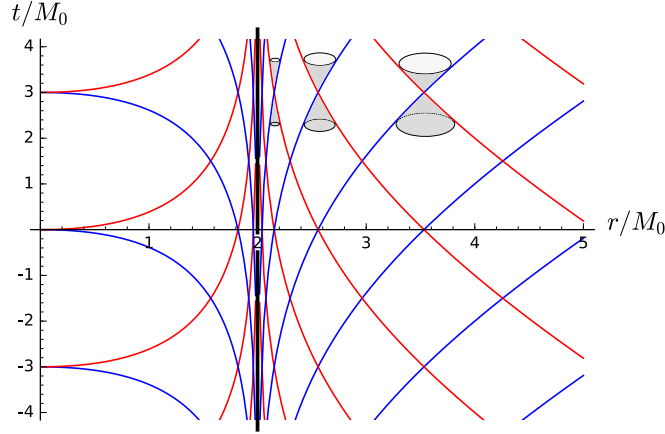


Figure 2.1: Ingoing (red) and outgoing (blue) null geodesics on the Schwarzschild-Droste domain with $\theta = \pi/2$, $\varphi = \pi$. The lightcone, defined by the intersections of these geodesics, closes up as one approaches the Schwarzschild horizon at $r = 2M_0$ (in black).

From the two solutions of eq. (2.17), we can define the advanced and retarded times v and u such that:

$$t = -r_* + v \quad (2.18)$$

$$t = r_* + u \quad (2.19)$$

When t increases, r must increase for a fixed u and decrease for a fixed v . Hence, the parameters u and v label respectively radial null outgoing and ingoing curves. These curves actually are null geodesics with parameter $\lambda = r$, as can be shown using eq. (1.39).

We can now use for instance v as a spacetime coordinate. The line element (2.11) can then be cast in terms of the *null ingoing Eddington-Finkelstein coordinates*

$$ds^2 = -\left(1 - \frac{2M_0}{r}\right)dv^2 + 2dvdr + r^2d\Omega^2, \quad (2.20)$$

where $d\Omega^2 \equiv r^2d\theta^2 + r^2\sin^2\theta d\varphi^2$. The metric \mathbf{g} associated with this line element erases the coordinate singularity at $r = 2M_0$, since both the metric and the inverse metric are regular there (except for $\theta = 0$ and $\theta = \pi$, which are merely singularities of the spherical coordinates):

$$[g_{\mu\nu}] = \begin{pmatrix} \frac{2M_0}{r} - 1 & 1 & 0 & 0 \\ 1 & 0 & 0 & 0 \\ 0 & 0 & r^2 & 0 \\ 0 & 0 & 0 & r^2\sin^2\theta \end{pmatrix}, \quad [g^{\mu\nu}] = \begin{pmatrix} 0 & 1 & 0 & 0 \\ 1 & 1 - \frac{2M_0}{r} & 0 & 0 \\ 0 & 0 & 1/r^2 & 0 \\ 0 & 0 & 0 & 1/r^2\sin^2\theta \end{pmatrix} \quad (2.21)$$

Put another way, observers can now start from \mathcal{M}_I , reach the hypersurface $r = 2M_0$ in a finite coordinate time and even cross it to reach the region \mathcal{M}_{II} . This can be seen from the slopes of the

lightcone in a (v, r) diagram:

$$\frac{dv}{dr} = \begin{cases} 0 & \text{(ingoing)} \\ 2\left(1 - \frac{2M_0}{r}\right)^{-1} & \text{(outgoing)} \end{cases} \quad (2.22)$$

The curves satisfying eq. (2.22) are plotted in Fig. 2.2(a). They form a lightcone at each point, which becomes more and more tilted as r approaches $r = 2M_0$ from the region \mathcal{M}_{I} . After crossing $r = 2M_0$, the lightcones are so tilted that future timelike curves can only have decreasing values of r : the region \mathcal{M}_{II} is gravitationally trapped. This can be proved by computing the expansion of null radial outgoing geodesics θ_+ . From the results of App. A.3,

$$\theta_+ = \frac{1}{r} \left(1 - \frac{2M_0}{r}\right) \quad (2.23)$$

Hence,

$$\begin{cases} \theta_+ > 0 & \text{on } \mathcal{M}_{\text{I}}, \\ \theta_+ = 0 & \text{at } r = 2M_0, \\ \theta_+ < 0 & \text{on } \mathcal{M}_{\text{II}}. \end{cases} \quad (2.24)$$

We conclude that the hypersurface \mathcal{H} , in the future of \mathcal{M}_{I} and such that $r = 2M_0$, called the Schwarzschild horizon, is a future outer trapping horizon (FOTH). Due to the staticity of the metric, it is also an event horizon, a no-return causal boundary. Observers crossing this horizon and reaching \mathcal{M}_{II} must then travel solely towards decreasing values of r before finally reaching the singularity.

The advanced time v has allowed us to extend the motion of particles across the horizon in the future of \mathcal{M}_{I} : ingoing light rays with constant $v = t + r^*$ and decreasing r must have an increasing t . We can now use the retarded time $u = t - r^*$ to define a similar extension in the past of \mathcal{M}_{I} . The line element (2.11) in terms of the *null outgoing Eddington-Finkelstein coordinates* reads:

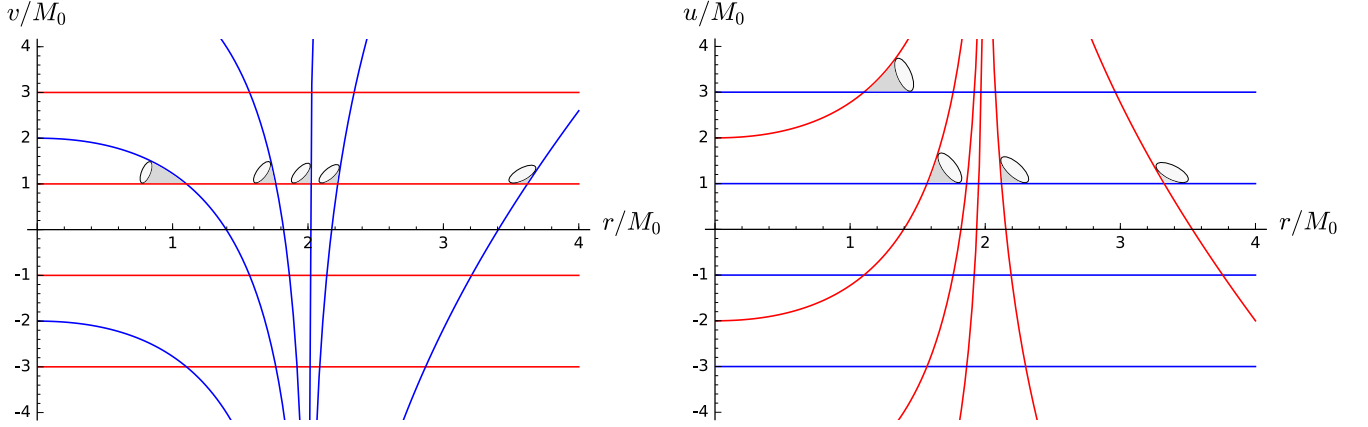
$$ds^2 = -\left(1 - \frac{2M_0}{r}\right) du^2 - 2du dr + r^2 d\Omega^2. \quad (2.25)$$

It should be emphasized that this metric now describes \mathcal{M}_{I} but also a new region \mathcal{M}_{III} in the past of \mathcal{M}_{I} with $r < 2M_0$. The light rays are now defined by

$$\frac{du}{dr} = \begin{cases} 0 & \text{(outgoing)} \\ -2\left(1 - \frac{2M_0}{r}\right)^{-1} & \text{(ingoing)} \end{cases} \quad (2.26)$$

The lightcones in a (u, r) diagram are plotted in Fig. 2.2(b). They are particularly tilted in region \mathcal{M}_{III} : particles can only travel towards increasing values of r there. This result can be backed up by the computation of the expansion of a congruence of null radial ingoing geodesics, using the results of Sec. 3 in Chapter 1:

$$\theta_- = -\frac{1}{r} \left(1 - \frac{2M_0}{r}\right) \quad (2.27)$$



(a) Ingoing Eddington-Finkelstein patch. $r = 2M_0$ is a future outer trapping horizon (FOTH), characteristic of a black hole.

(b) Outgoing Eddington-Finkelstein patch. $r = 2M_0$ is a past outer trapping horizon (POTH), characteristic of a white hole.

Figure 2.2: Ingoing and outgoing Eddington-Finkelstein patches of the Schwarzschild spacetime, obtained for $\theta = \pi/2$ and $\varphi = \pi$. The ingoing (red) and outgoing (blue) null curves form a lightcone at each crossing point, whose future part is drawn solely. The region \mathcal{M}_{II} is trapped, while \mathcal{M}_{III} is anti-trapped.

Therefore,

$$\begin{cases} \theta_- < 0 & \text{on } \mathcal{M}_I, \\ \theta_- = 0 & \text{at } r = 2M_0, \\ \theta_- > 0 & \text{on } \mathcal{M}_{III}. \end{cases} \quad (2.28)$$

Hence, even ingoing lightrays have to go to higher values of r in \mathcal{M}_{III} ; the hypersurface such that $r = 2M_0$ between \mathcal{M}_I and \mathcal{M}_{III} is then a past outer trapping horizon (POTH). This is why this region is called a *white hole*.

1.3 Maximal extension of the Schwarzschild spacetime

The Schwarzschild metric (2.11) can also be cast in a double null form, using both u and v :

$$ds^2 = -\left(1 - \frac{2M_0}{r}\right) du dv + r^2 d\Omega^2 \quad (2.29)$$

But this form of the metric is singular at $r = 2M_0$, since the metric is non-invertible. The metric (2.29) actually does not cover either the outgoing nor the ingoing Eddington-Finkelstein patch because $v - u = 2r + 4M_0 \left| \frac{r}{2M_0} - 1 \right|$ diverges at $r = 2M_0$. This issue can be cured by introducing the *null Kruskal-Szekeres coordinates* on \mathcal{M}_I :

$$\begin{cases} U \equiv -e^{-u/4M_0} \\ V \equiv e^{v/4M_0} \end{cases} \quad (2.30)$$

One then has

$$du dv = 16M_0^2 e^{(u-v)/4M_0} dU dV \quad (2.31)$$

But from eqs. (2.18) and (2.19), and while $r > 2M_0$ one gets

$$e^{(u-v)/4M_0} = e^{-r/2M_0} \left(\frac{r}{2M_0} - 1 \right)^{-1}, \quad (2.32)$$

which yields

$$du \, dv = 16M_0^2 e^{-r/2M_0} \left(\frac{r}{2M_0} - 1 \right)^{-1} dU \, dV = \frac{32M_0^3}{r} e^{-r/2M_0} \left(1 - \frac{2M_0}{r} \right)^{-1} dU \, dV.$$

Finally, the line element can be rewritten

$$ds^2 = -\frac{32M_0^3}{r} e^{-r/2M_0} dU \, dV + r^2 d\Omega^2, \quad (2.33)$$

where r is defined implicitly via the relation

$$e^{r/2M_0} \left(\frac{r}{2M_0} - 1 \right) = -UV, \quad (2.34)$$

which directly stems from eq. (2.32). For now, this metric describes the region \mathcal{M}_I of the manifold, which is such that $V > 0$, $U < 0$. There exists a very convenient way of representing even noncompact spacetimes on a sheet of paper, via a compactification which brings back infinities to a finite distance. We can take for instance:

$$\begin{cases} \tilde{U} \equiv \arctan U, \\ \tilde{V} \equiv \arctan V. \end{cases} \quad (2.35)$$

And the metric can finally be written

$$ds^2 = -\frac{32M_0^3}{r} e^{-r/2M_0} \frac{d\tilde{U}}{\cos^2 \tilde{U}} \frac{d\tilde{V}}{\cos^2 \tilde{V}} + r^2 d\Omega^2, \quad (2.36)$$

where eq. (2.32) gives the following implicit definition of r in terms of \tilde{U} and \tilde{V} :

$$e^{r/2M_0} \left(\frac{r}{2M_0} - 1 \right) = -\tan \tilde{U} \tan \tilde{V}. \quad (2.37)$$

As seen in Fig. 2.3(a), we can then represent the region \mathcal{M}_I , defined by $U < 0$, $V > 0$ or equivalently $\tilde{U} \in (-\frac{\pi}{2}, 0)$ and $\tilde{V} \in (0, \frac{\pi}{2})$, on a (\tilde{U}, \tilde{V}) diagram. Each point of such a diagram is a 2-sphere spanned by the coordinates (θ, φ) . Ingoing light rays propagate at constant \tilde{V} while the outgoing ones are at constant \tilde{U} . The location of $r = 2M_0$ can be found directly from eq. (2.37): $\tilde{U} = 0$ or $\tilde{V} = 0$. The region \mathcal{M}_I is then represented in Fig. 2.3(a) by a square delimited by $\tilde{U} = 0$ and $\tilde{V} = 0$ ($r = 2M_0$), as well as $\tilde{V} = \frac{\pi}{2}$ ($v = +\infty$) and $\tilde{U} = -\frac{\pi}{2}$ ($u = -\infty$).

The coordinates U and V (and thus \tilde{U} and \tilde{V}) are perfectly regular at the horizon, which leads us to extend them in the future and the past as was done with Eddington-Finkelstein's. Let us start by describing \mathcal{M}_{II} and the future extension, like in the case of the ingoing patch of

Fig. 2.2(a). By definition, $U = -e^{-u/4M_0}$ is negative on \mathcal{M}_I and null for $r = 2M_0$; a new definition is thus needed to account for positive values of U on \mathcal{M}_{II} :

$$\begin{cases} U \equiv +e^{-u/4M_0} & \text{on } \mathcal{M}_{II} \\ \tilde{U} = \arctan U \end{cases} \quad (2.38)$$

This allows us to recover the ingoing Eddington-Finkelstein patch, as shown in Fig. 2.3(a). It should be noted that on \mathcal{M}_{II} the relation (2.37) implicitly defining r still holds. Indeed, $r < 2M_0$ and thus

$$\frac{1}{2}(v - u) = r + r2M_0 \ln \left(1 - \frac{r}{2M_0} \right), \quad (2.39)$$

hence:

$$e^{r/2M_0} \left(1 - \frac{r}{2M_0} \right) = e^{(v-u)/4M_0} = UV. \quad (2.40)$$

The location of the singularity in the (\tilde{U}, \tilde{V}) diagram can be easily deduced. The condition $r = 0$ indeed yields

$$\tan \tilde{U} \tan \tilde{V} = 1, \quad (2.41)$$

and then

$$0 = \sin \tilde{U} \sin \tilde{V} - \cos \tilde{U} \cos \tilde{V} = \cos(\tilde{U} + \tilde{V}). \quad (2.42)$$

The singularity is thus located at $\tilde{U} + \tilde{V} = \pm \frac{\pi}{2}$.

A similar extension can be done in the past, taking $\tilde{V} \rightarrow -\tilde{V}$, hence covering the region \mathcal{M}_{III} as did the outgoing Eddington-Finkelstein patch. The associated (\tilde{U}, \tilde{V}) diagram is depicted in Fig. 2.3(b).

Finally, a last region appears when one considers both the transformations $\tilde{U} \rightarrow -\tilde{U}$ and $\tilde{V} \rightarrow -\tilde{V}$. This region \mathcal{M}_{III} is a copy of the original normal (i.e., untrapped) region \mathcal{M}_I , and is depicted on the full Carter-Penrose diagram of Fig. 2.4. It is shown easily that the relation

$$e^{r/2M_0} \left(\frac{r}{2M_0} - 1 \right) = -\tan \tilde{U} \tan \tilde{V} \quad (2.43)$$

holds on each of the four regions. The coordinates (\tilde{U}, \tilde{V}) thus allow the covering of the maximally extended Schwarzschild spacetime \mathcal{M} :

$$\mathcal{M}: \quad (\tilde{U}, \tilde{V}) \in \left(-\frac{\pi}{2}, \frac{\pi}{2} \right)^2, \quad \tan \tilde{U} \tan \tilde{V} < 1. \quad (2.44)$$

This maximal extension reveals the two different natures of the horizon $r = 2M_0$, which are detailed on Table 2.1.

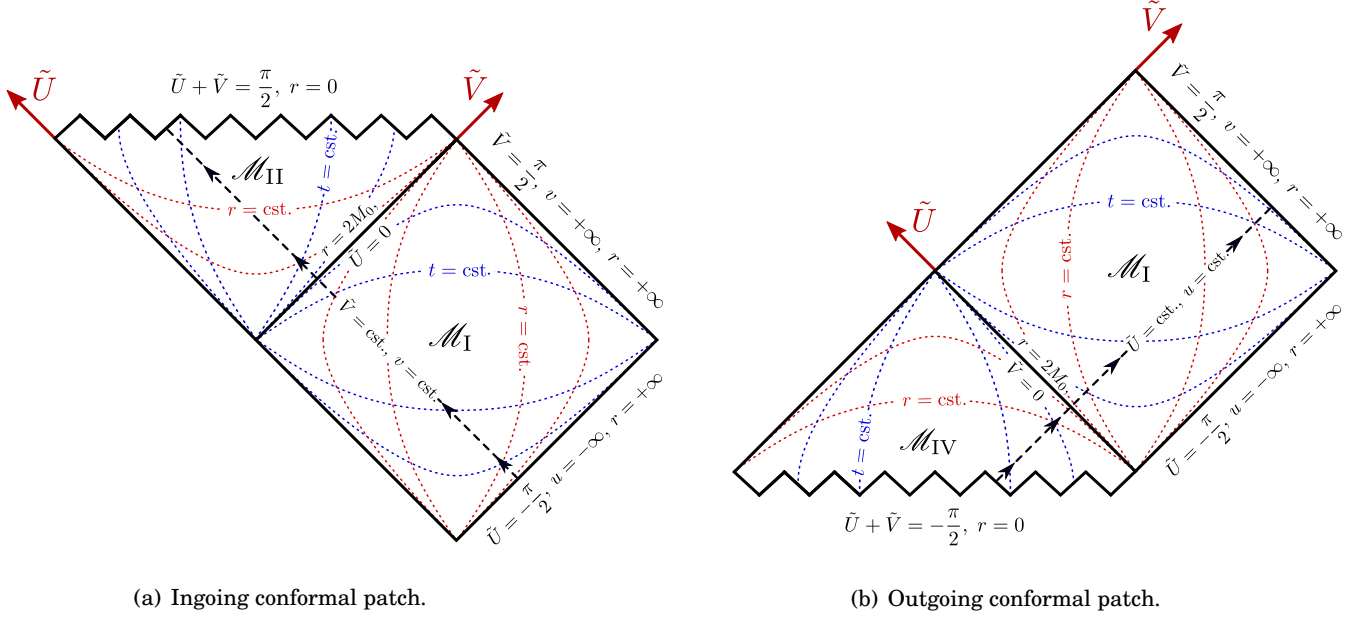


Figure 2.3: Ingoing and outgoing Eddington-Finkelstein conformal patches of the Schwarzschild spacetime, drawn in terms of the compactified Kruskal coordinates $(\tilde{U}_+, \tilde{V}_+)$. Each point of the diagram is a 2-sphere spanned by the coordinates (θ, φ) . Hypersurfaces of constant t and constant r are respectively drawn in dotted blue and red lines. They change of causal nature (from spacelike to timelike, or vice versa) at the horizon, as t and r exchange roles in the metric (2.11). Light rays propagate at $\pm 45^\circ$. Each patch is geodesically incomplete, as illustrate null past ingoing geodesics in \mathcal{M}_{II} , and null future ingoing geodesics in \mathcal{M}_{IV} .

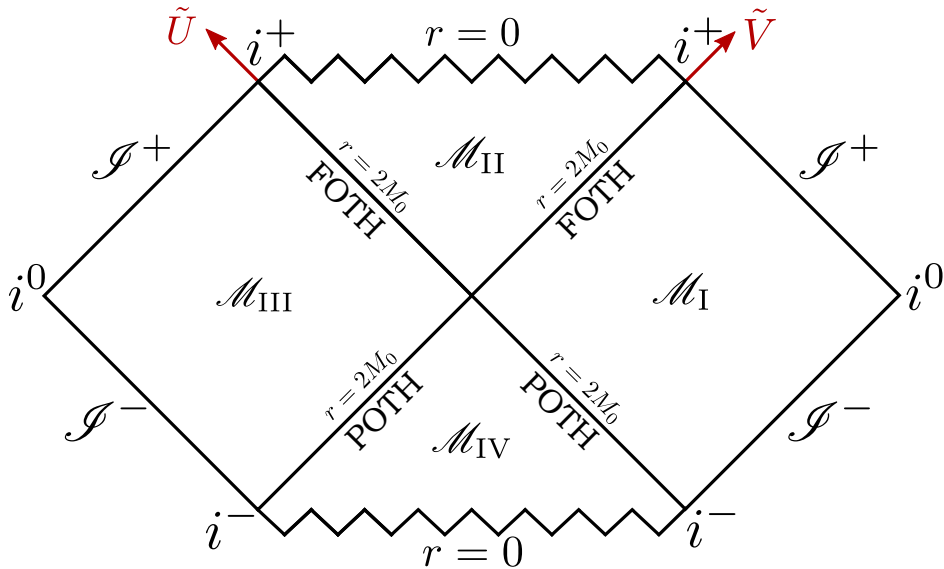


Figure 2.4: Maximal extension of Schwarzschild's spacetime, drawn in the compactified Kruskal coordinates $(\tilde{U}_+, \tilde{V}_+)$. It is obtained by gluing the ingoing and outgoing patches of Fig. 2.3 and adding a copy \mathcal{M}_{III} of region \mathcal{M}_{I} so that every geodesic be complete (or reach the curvature singularity $r=0$). The future null and timelike infinities (\mathcal{I}^+ , i^+), as well as their past counterparts (\mathcal{I}^- , i^-) and timelike infinity (i^0) are those defined on Table 1.1.

Trapping horizon	Definition	Location
Future outer (FOTH)	$\theta_+ = 0$	$\tilde{V}_+ = 0, \quad \tilde{U}_+ \in \left(0, \frac{\pi}{2}\right)$
	$\mathcal{L}_- \theta_+ < 0$	$\tilde{U}_+ = 0, \quad \tilde{V}_+ \in \left(0, \frac{\pi}{2}\right)$
Past outer (POTH)	$\theta_- = 0$	$\tilde{V}_+ = 0, \quad \tilde{U}_+ \in \left(-\frac{\pi}{2}, 0\right)$
	$\mathcal{L}_+ \theta_- < 0$	$\tilde{U}_+ = 0, \quad \tilde{V}_+ \in \left(-\frac{\pi}{2}, 0\right)$

Table 2.1: Types of horizon present in the maximal extension of Schwarzschild's spacetime, as well as their location in terms of the coordinates $(\tilde{U}_+, \tilde{V}_+)$. $r = 2M_0$ actually includes both the future and past outer trapping horizons. More details can be found in App. A.3

2 Reissner-Nordström solution

2.1 Properties

The metric of Reissner-Nordström solution, which describes a static charged black hole, is given by the line element

$$ds^2 = -\left(1 - \frac{2M_0}{r} + \frac{Q^2}{r^2}\right) dt^2 + \left(1 - \frac{2M_0}{r} + \frac{Q^2}{r^2}\right)^{-1} dr^2 + r^2 d\Omega^2 \quad (2.45)$$

It is obtained by solving Maxwell's equations, which yield an electromagnetic-field tensor with one nonvanishing component $F^{tr} = \frac{Q}{r^2}$, and then Einstein's equations. Q is the electric charge of the black hole of mass M_0 .

A fundamental property of Reissner-Nordström solution is that it possesses two horizons: an inner and an outer one. In order to prove this, let us compute the expansion of null radial outgoing geodesics θ_+ . As was done with Schwarzschild's solution, we can define the advanced and retarded times

$$\begin{cases} v = t + r^* \\ u = t - r^* \end{cases}, \quad (2.46)$$

with

$$r^* = \int \frac{dr}{F_{\text{RN}}(r)} = M_0 \ln |(r - r_+)(r - r_-)| + \frac{2M_0^2 - Q^2}{2\sqrt{M_0^2 - Q^2}} \ln \left| \frac{r - r_+}{r - r_-} \right|. \quad (2.47)$$

Then, the metric (2.45) can be cast in terms of the advanced time:

$$ds^2 = -F_{\text{RN}}(r)dv^2 + 2dvdr + r^2d\Omega^2, \quad (2.48)$$

with $F_{\text{RN}}(r) = 1 - \frac{2M_0}{r} + \frac{Q^2}{r^2}$.

The results of Sec. 3 in Chapter 1 apply, and the outgoing expansion thus reads

$$\theta_+ = \frac{F_{\text{RN}}(r)}{r}. \quad (2.49)$$

Hence, the spacetime admits trapping horizons if and only if

$$\theta_+ = 0 \iff 1 - \frac{2M_0}{r} + \frac{Q^2}{r^2} = 0 \quad (2.50)$$

Actually, there are two horizons:

$$r_{\pm} = M_0 \pm \sqrt{M_0^2 - Q^2} \quad (2.51)$$

In Schwarzschild's case, the horizon $r = 2M_0$ actually integrated a past and a future outer horizon. In Reissner-Nordström case, a similar situation occurs: the outer horizon $r = r_+$ will integrate the FOTH and POTH, while the inner horizon $r = r_-$ will integrate the FITH and PITH. The FOTH and FITH are defined via θ_+ , but the other two require computing θ_- with the ingoing Eddington-Finkelstein metric (see App. A.3):

$$ds^2 = -F_{\text{RN}}(r)du^2 - 2dudr + r^2d\Omega^2, \quad (2.52)$$

In the end, the expansion

$$\theta_- = -\frac{F_{\text{RN}}(r)}{r} \quad (2.53)$$

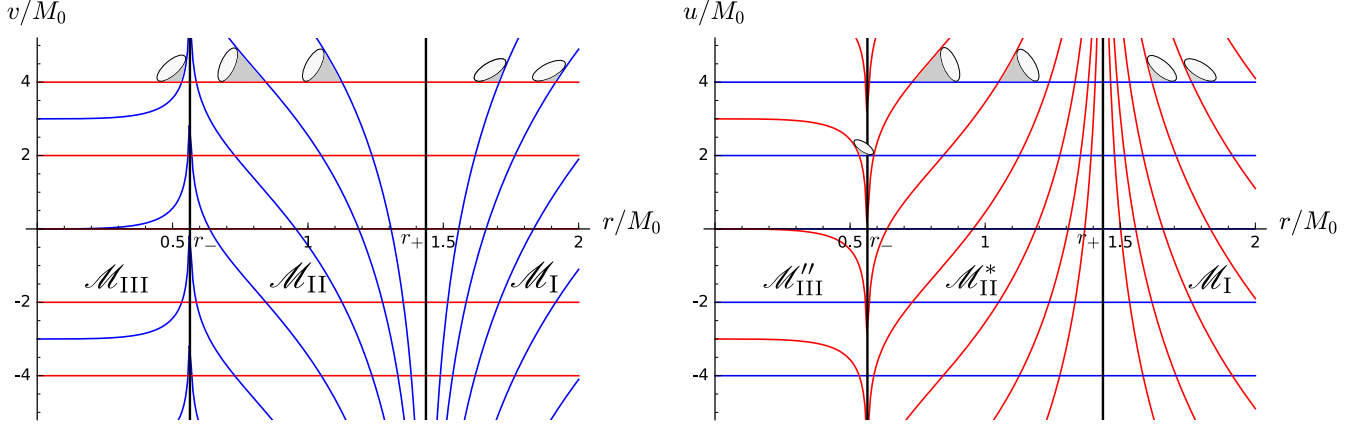
vanishes as expected when $r = r_{\pm}$.

A spacetime diagram in terms of the coordinates (v, r) and (u, r) helps in understanding the structure of the black hole (see Fig. 2.5).

On the left panel, the region \mathcal{M}_{II} between the two horizons is trapped (both θ_- and θ_+ are negative there), while \mathcal{M}_{I} and \mathcal{M}_{III} are normal (untrapped) regions. A singularity is located at $r = 0$ in \mathcal{M}_{III} , it is thus a timelike surface. It is easy to verify that $r = 0$ is a curvature singularity, for instance by computing the Kretschmann scalar:

$$K = \frac{8(6M_0^2r^2 - 12QM_0r + 7Q^2)}{r^8} \quad (2.54)$$

Since the singularity is a timelike hypersurface, it is not reached by all geodesics entering the trapped region. This is visible in Fig. 2.5(a): in region \mathcal{M}_{III} the lightcone is not as tilted as in



(a) Ingoing Eddington-Finkelstein patch. $r = r_+$ is a future outer trapping horizon (FOTH), while $r = r_-$ is a future inner trapping horizon (FITH)

(b) Outgoing Eddington-Finkelstein patch. $r = r_+$ is a past outer trapping horizon (POTH), while $r = r_-$ is a past inner trapping horizon (PITH)

Figure 2.5: Ingoing and outgoing Eddington-Finkelstein patches of the Reissner-Nordström spacetime, obtained for $\theta = \pi/2$ and $\varphi = \pi$. The ingoing (dotted red lines) and outgoing (dotted blue lines) null curves form a lightcone at each crossing point, whose future part is drawn solely. The region \mathcal{M}_{II} is trapped, while $\mathcal{M}_{\text{II}}^*$ is anti-trapped.

region \mathcal{M}_{II} , and for instance an observer can stay at a constant $r < r_-$.

In Fig. 2.5(b), an anti-trapped region $\mathcal{M}_{\text{II}}^*$ is visible. It is a white hole region relating a new asymptotically-flat region $\mathcal{M}_{\text{III}}''$ to \mathcal{M}_{I} , as will become clearer after examining the maximal extension of Reissner-Nordström spacetime.

2.2 Maximal extension of Reissner-Nordström spacetime

The metric can be cast in double null form:

$$ds^2 = -F_{\text{RN}}(r)du dv + r^2 d\theta^2 + r^2 d\Omega^2. \quad (2.55)$$

It is singular at $r = 0$, $r = r_+$ and $r = r_-$, but the last two are merely coordinate singularities. In particular,

$$\frac{v-u}{2} = r^* \rightarrow \mp\infty \quad \text{when} \quad r \rightarrow r_{\pm}. \quad (2.56)$$

Let us first examine the singularity at $r = r_+$ by introducing the coordinates

$$\begin{cases} U_+ = \mp e^{-\kappa_+ u}, \\ V_+ = e^{\kappa_+ v}, \end{cases} \quad (2.57)$$

where $\kappa_+ \equiv \frac{1}{2}F'_{\text{RN}}(r_+)$. One then has

$$dU_+ dV_+ = -\kappa_+^2 U_+ V_+ du dv \quad (2.58)$$

Hence, the metric reads:

$$ds^2 = \frac{F_{\text{RN}}(r)}{\kappa_+^2 U_+ V_+} dU_+ dV_+ + r^2 d\theta^2 + r^2 d\Omega^2 . \quad (2.59)$$

These new coordinates allow us to define a regular metric at $r = r_+$. First, the coordinates are regular there:

$$U_+ V_+ = \mp e^{\kappa_+(v-u)} = \mp e^{2\kappa_+ r^*} \rightarrow 0 \quad \text{when} \quad r \rightarrow r_+ . \quad (2.60)$$

To show that the metric itself is indeed regular at $r = r_+$, we can approximate F_{RN} at first order near $r \simeq r_+$:

$$F_{\text{RN}}(r) \simeq 2\kappa_+(r - r_+) . \quad (2.61)$$

Hence

$$r^* = \int \frac{dr}{F_{\text{RN}}(r)} \simeq \frac{1}{2\kappa_+} \ln |\kappa_+(r - r_+)| \quad (2.62)$$

Then

$$U_+ V_+ = \mp e^{2\kappa_+ r^*} \simeq \mp \kappa_+(r - r_+) \simeq \mp \frac{F_{\text{RN}}(r)}{2} . \quad (2.63)$$

The metric thus reads, near $r \simeq r_+$,

$$ds^2 \equiv \mp \frac{2}{\kappa_+^2} dU_+ dV_+ + r^2 d\Omega^2 , \quad (2.64)$$

and is regular at the horizon $r = r_+$. This choice of coordinates has allowed us to go from \mathcal{M}_{I} to \mathcal{M}_{II} in Fig. 2.5(a), or from $\mathcal{M}_{\text{II}}^*$ to \mathcal{M}_{I} in Fig. 2.5(b).

However, the coordinates (U_+, V_+) do not allow us to cross the horizon $r = r_-$. Indeed, $r^* \rightarrow +\infty$ there and hence

$$U_+ V_+ = \mp e^{2\kappa_+ r^*} \rightarrow \mp \infty . \quad (2.65)$$

It is then necessary to define new coordinates:

$$\begin{cases} U_- = e^{\kappa_- u} , \\ V_- = \mp e^{-\kappa_- v} , \end{cases} \quad (2.66)$$

These coordinates allow us to go from \mathcal{M}_{II} to \mathcal{M}_{III} in Fig. 2.5(a) or from $\mathcal{M}_{\text{III}}''$ to $\mathcal{M}_{\text{II}}^*$ in Fig. 2.5(b), following the procedure used for the coordinates (U_+, V_+) .

The ingoing and outgoing Eddington-Finkelstein patches of Fig. 2.5 can now be drawn using a compactified version of the Kruskal coordinates:

$$\begin{cases} \tilde{U}_\pm \equiv \arctan U_\pm \\ \tilde{V}_\pm \equiv \arctan V_\pm \end{cases} . \quad (2.67)$$

They are visible in Fig. 2.6 below. Each patch contains both r_- and r_+ , and thus necessitates the use of both the coordinate sets $(\tilde{U}_-, \tilde{V}_-)$ and $(\tilde{U}_+, \tilde{V}_+)$.

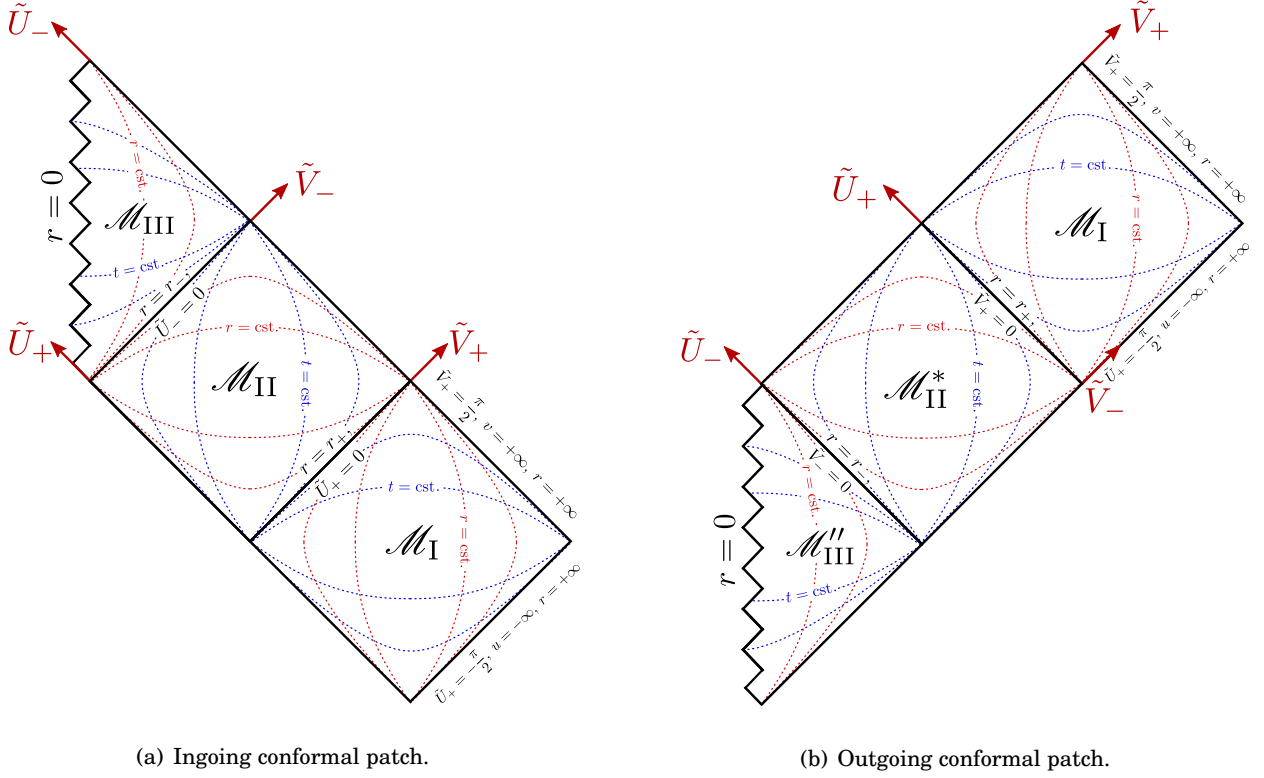


Figure 2.6: Ingoing and outgoing Eddington-Finkelstein conformal patches of the Reissner-Nordström spacetime, drawn in terms of the compactified Kruskal coordinates $(\tilde{U}_+, \tilde{V}_+)$ and $(\tilde{U}_-, \tilde{V}_-)$. Each point of the diagram is a 2-sphere spanned by the coordinates (θ, φ) . Hypersurfaces of constant t and constant r are respectively drawn in dotted blue and red lines. Light rays propagate at $\pm 45^\circ$. Each patch is geodesically incomplete, as illustrate null future outgoing geodesics in \mathcal{M}_{III} , and null past outgoing geodesics in $\mathcal{M}_{\text{III}}''$.

Finally, the maximal extension is obtained by letting $(\tilde{U}_\pm, \tilde{V}_\pm)$ take both positive and negative values (see Fig. 2.7). For instance, there exists another copy of region \mathcal{M}_I , \mathcal{M}_I' , accessible when one considers $V_+ \rightarrow -V_+$ (or equivalently $\tilde{V}_+ \rightarrow -\tilde{V}_+$). And another copy of the region \mathcal{M}_{III} , $\mathcal{M}_{\text{III}}'$, is revealed when taking $U_- \rightarrow -U_-$ (or equivalently $\tilde{U}_- \rightarrow -\tilde{U}_-$).

Let us follow the timelike trajectory of a massive particle starting from \mathcal{M}_I , depicted by a blue arrow in Fig. 2.7. The particle first crosses r_+ and reaches the trapped region \mathcal{M}_{II} , it is then forced to go decreasing values of r before eventually reaching r_- . It then arrives in the normal region \mathcal{M}_{III} containing a timelike singularity. Once the particle reaches $\mathcal{M}_{\text{II}}^*$, it is in an anti-trapped region and has to move towards increasing values of r . It then crosses r_+ and reaches a new asymptotically-flat universe \mathcal{M}_I'' . At this point, the extension can be pursued by introducing a new coordinate patch $(\tilde{U}_+, \tilde{V}_+)$ specific to the outer horizon r_+ , then a patch $(\tilde{U}_-, \tilde{V}_-)$ specific to the inner horizon r_- , and so on. The maximal extension of Reissner-Nordström solution consists in an infinite lattice of such coordinate patches, linking asymptotically-flat universes via black holes tunnels.

Table 2.2 summarizes the features of the four different trapping horizons, which are presented more formally in App. A.3. It should also be mentioned that the inner horizon $r = r_-$ is a Cauchy horizon (see App. A.1 for details). As was shown by Poisson and Israel [97, 98], when a perturbation is applied to Reissner-Nordström spacetime, near this inner horizon the gravitational-mass parameter of the black hole increases exponentially: it is the *mass inflation* phenomenon. The inner horizon of this spacetime is thus unstable. This property is not specific to Reissner-Nordström solution and is actually shared by the next black-hole spacetime that we will present, namely Kerr's solution.

	Trapping horizon	Definition	Location
Outer horizon	Future outer (FOTH)	$\theta_+ = 0$	$\tilde{V}_+ = 0, \tilde{U}_+ \in \left(0, \frac{\pi}{2}\right)$
		$\mathcal{L}_- \theta_+ < 0$	$\tilde{U}_+ = 0, \tilde{V}_+ \in \left(0, \frac{\pi}{2}\right)$
	Past outer (POTH)	$\theta_- = 0$	$\tilde{V}_+ = 0, \tilde{U}_+ \in \left(-\frac{\pi}{2}, 0\right)$
		$\mathcal{L}_+ \theta_- < 0$	$\tilde{U}_+ = 0, \tilde{V}_+ \in \left(-\frac{\pi}{2}, 0\right)$
Inner horizon	Future inner (FITH)	$\theta_+ = 0$	$\tilde{V}_- = 0, \tilde{U}_- \in \left(-\frac{\pi}{2}, 0\right)$
		$\mathcal{L}_- \theta_+ > 0$	$\tilde{U}_- = 0, \tilde{V}_- \in \left(-\frac{\pi}{2}, 0\right)$
	Past inner (PITH)	$\theta_- = 0$	$\tilde{V}_- = 0, \tilde{U}_- \in \left(0, \frac{\pi}{2}\right)$
		$\mathcal{L}_+ \theta_- > 0$	$\tilde{U}_- = 0, \tilde{V}_- \in \left(0, \frac{\pi}{2}\right)$

Table 2.2: Types of horizon present in the maximal extension of Reissner-Nordström spacetime, as well as their location in terms of the coordinates $(\tilde{U}_+, \tilde{V}_+)$ and $(\tilde{U}_-, \tilde{V}_-)$. The outer (event) horizon $r = r_+$ actually includes both the future outer and past outer trapping horizons, while the inner horizon $r = r_-$ includes both the future inner and past inner trapping horizons.

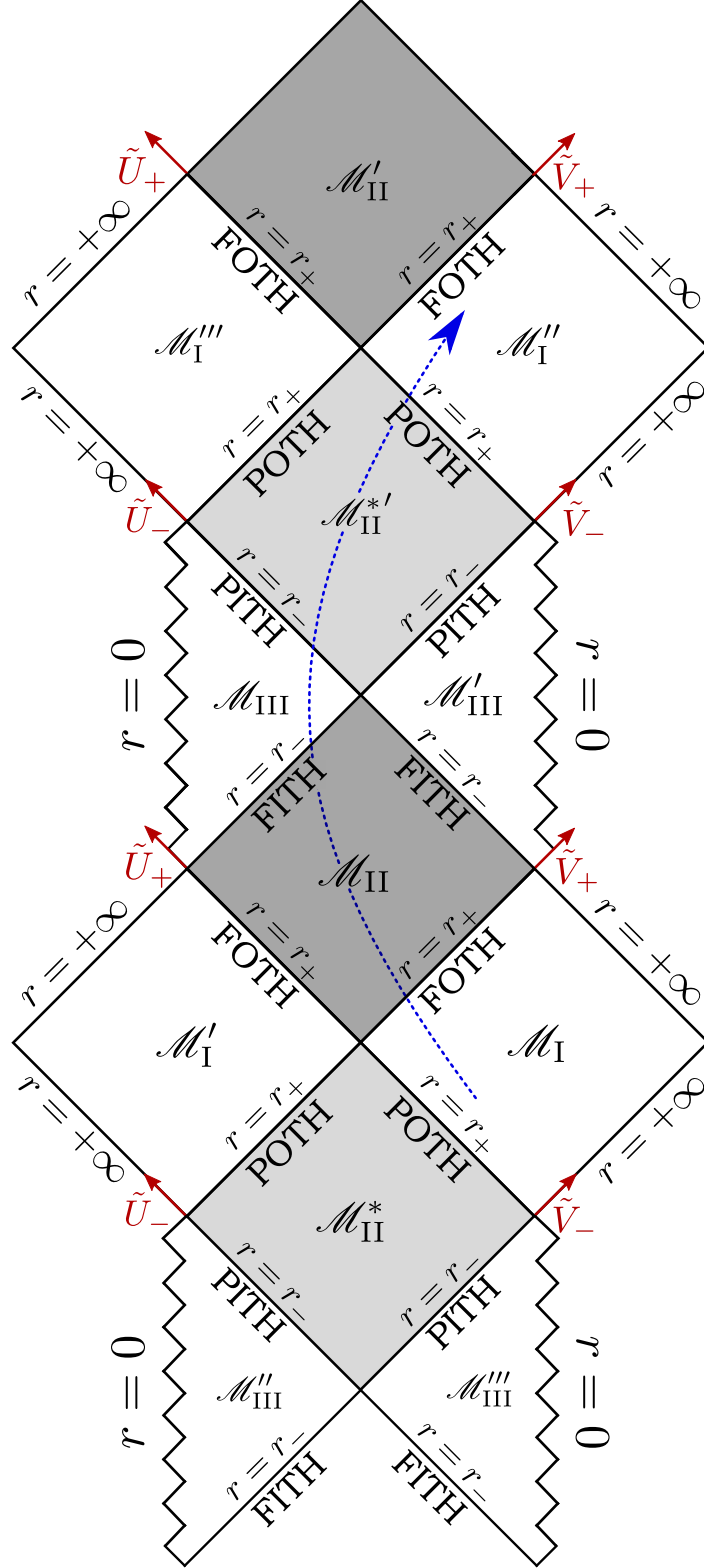


Figure 2.7: Section of the maximal extension of Reissner-Nordström spacetime, drawn in the compactified Kruskal coordinates $(\tilde{U}_+, \tilde{V}_+)$ and $(\tilde{U}_-, \tilde{V}_-)$. It is obtained by gluing the ingoing and outgoing patches of Fig. 2.6 and adding copies of normal regions so that every geodesic not reaching $r = 0$ be complete. The full extension consists in an infinite repetition of the drawn block.

3 Kerr's solution

3.1 Properties of the Kerr spacetime

3.1.1 Metric of a rotating black hole

An exact solution to Einstein's equations describing rotating black holes was found by Roy Kerr in 1963 [78]. The Kerr metric reads

$$ds^2 = -\left(1 - \frac{2rM_0}{\Sigma}\right)dt^2 - \frac{4arM_0 \sin^2 \theta}{\Sigma} dt d\varphi + \frac{\Sigma}{\Delta} dr^2 + \Sigma d\theta^2 + \sin^2 \theta \left(r^2 + a^2 + \frac{2a^2 r M_0 \sin^2 \theta}{\Sigma}\right) d\varphi^2 \quad (2.68)$$

where

$$\Sigma \equiv r^2 + a^2 \cos^2 \theta, \quad \Delta \equiv r^2 - 2M_0 r + a^2, \quad (2.69)$$

and the Boyer-Lindquist coordinates (t, r, θ, φ) cover $\mathbb{R}^2 \times \mathbb{S}^2$. M_0 is the mass of the black hole, a is its angular momentum (or *spin*) in units of M_0 .

We can clearly see that the metric is not static anymore but stationary, since the symmetry $t \rightarrow -t$ of Schwarzschild's metric has disappeared. So has the symmetry $\varphi \rightarrow -\varphi$: the spacetime is not spherically symmetric anymore, but remains axisymmetric (the metric is invariant under $\theta \rightarrow \pi - \theta$ and its coefficients do not depend on φ).

A manifestation of the rotation associated with this spacetime is the dragging of inertial frames. Let us consider an observer with zero angular momentum and 4-velocity \mathbf{u} . Then,

$$\mathbf{u} \cdot \partial_\varphi = 0 \quad \Longleftrightarrow \quad g_{t\varphi} \dot{t} + g_{\varphi\varphi} \dot{\varphi} = 0 \quad (2.70)$$

Hence, the observer has an angular velocity

$$\omega = \frac{d\varphi}{dt} = -\frac{g_{t\varphi}}{g_{\varphi\varphi}} = \frac{2Mar}{\Sigma}. \quad (2.71)$$

This velocity grows as the observer reaches smaller and smaller values of r , i.e. approaches the black hole.

3.1.2 Ergosphere

A very intriguing property of this spacetime is that observers will even be forced to rotate below a certain radius (depending on θ), which defines the *ergosphere*. Let us consider a static observer, with 4-velocity

$$u^\mu = \gamma \xi^\mu \equiv \gamma \frac{dx^\mu}{dt}, \quad (2.72)$$

where γ is a normalization factor:

$$\gamma \equiv (-g_{\mu\nu} \xi^\mu \xi^\nu)^{-1/2} = \frac{1}{\sqrt{-g_{tt}}}. \quad (2.73)$$

$\xi = \partial_t$ becomes null when $g_{tt} = 0$, and the observers can not remain static. They have crossed the ergosphere, which is defined by

$$g_{tt} = 0 \iff r = M_0 + \sqrt{M_0^2 - a^2 \cos^2(\theta)} . \quad (2.74)$$

As in the case of Schwarzschild's static solution, ξ is a Killing vector since the components of the metric do not depend on t . However, contrarily to Schwarzschild's case, $\xi \cdot \xi = 0$ defines neither a Killing nor an event horizon since the ergosphere is not a null hypersurface (see App. A for definitions). When ∂_t is non-timelike, an observer cannot remain at constant values of the spatial coordinates: this happens below the trapping horizon in Schwarzschild's spacetime, inside the trapped region in which no particle can stay at a constant radial coordinate, while it occurs in Kerr's spacetime as soon as the ergosphere is crossed, i.e. inside the *ergoregion* in which particles have to move in the φ direction. The trapping horizons, defining spacelike $r = \text{cst.}$ regions in Kerr's spacetime, will be the object of study of the next section.

3.1.3 Trapping horizons

Let us thus investigate the causal structure of the Kerr spacetime, and in particular the presence of horizons. First, we notice that some components of the Kerr metric (2.68) appear to diverge when $\Sigma = 0$ or $\Delta = 0$. The former condition is actually associated with a curvature singularity (see 3.1.4), but the latter merely reveals coordinate singularities associated with horizons. To see this, let us define the *Kerr coordinates* in order to remove the divergence of g_{rr} when $\Delta = 0$:

$$\begin{cases} v = t + r^* , \\ \psi = \varphi + r^\dagger , \end{cases} \quad (2.75)$$

where

$$r^* = \int \frac{r^2 + a^2}{\Delta} dr , \quad r^\dagger = \int \frac{a}{r} dr . \quad (2.76)$$

The metric then reads

$$\begin{aligned} ds^2 = & - \left(1 - \frac{2rM(r)}{\Sigma} \right) dv^2 + 2 dv dr - \frac{4arM(r)\sin^2\theta}{\Sigma} dv d\psi - 2a \sin^2(\theta) dr d\psi + \Sigma d\theta^2 \\ & + \sin^2\theta \left(r^2 + a^2 + \frac{2a^2rM(r)\sin^2\theta}{\Sigma} \right) d\psi^2 . \end{aligned} \quad (2.77)$$

Using the results of App. A.3.2, the expansion of null outgoing geodesics, which is vanishing at future trapping horizons, reads

$$\theta_+ = \frac{r \Delta}{(a^2 + r^2) \Sigma} . \quad (2.78)$$

Hence (for $r \neq 0$),

$$\theta_+ = 0 \iff \Delta = 0 \quad (2.79)$$

Since

$$\Delta = r^2 - 2M_0 r + a^2 = (r - r_+)(r - r_-) \quad (2.80)$$

with

$$r_{\pm} = M_0 \pm \sqrt{M_0^2 - a^2}, \quad (2.81)$$

we have:

- $\theta_+ > 0$ on $\mathcal{M}_I \equiv \mathbb{R} \times (r_+, +\infty) \times \mathbb{S}^2$
- $\theta_+ = 0$ on $\mathcal{H}_{\text{out}} \equiv \{p \in \mathbb{R}^2 \times \mathbb{S}^2, \quad r(p) = r_+\}$
- $\theta_+ < 0$ on $\mathcal{M}_{II} \equiv \mathbb{R} \times (r_-, r_+) \times \mathbb{S}^2$
- $\theta_+ = 0$ on $\mathcal{H}_{\text{in}} \equiv \{p \in \mathbb{R}^2 \times \mathbb{S}^2, \quad r(p) = r_-\}$
- $\theta_+ > 0$ on $\mathcal{M}_{III} \equiv \mathbb{R} \times (-\infty, r_-) \times \mathbb{S}^2 \setminus \mathcal{R}$

Let us now investigate the causal nature of the future trapping horizons at $r = r_-$ and $r = r_+$. A way of proceeding consists in studying the hypersurfaces $r = \text{cst.}$ via their normal vector, which is the gradient vector field ∇r of components

$$\partial^\mu r = g^{\mu\nu} \partial_\nu r = g^{\mu r}. \quad (2.82)$$

The null hypersurfaces with $r = \text{cst.}$ will possess a null normal vector ∇r obeying

$$g(\nabla r, \nabla r) = 0, \quad (2.83)$$

and thus

$$0 = g^{\mu\nu} \partial_\mu r \partial_\nu r = g^{rr} = \frac{\Delta}{\Sigma}. \quad (2.84)$$

From eqs. (2.78) and (2.84), we deduce that the hypersurfaces $r = \text{cst.}$ are

- timelike on \mathcal{M}_I and \mathcal{M}_{III} ,
- null for $r = r_+$ and $r = r_-$, which correspond respectively to \mathcal{H}_{out} and \mathcal{H}_{in} ,
- spacelike on \mathcal{M}_{II} .

In the end, we have that \mathcal{M}_{II} is actually a gravitationally trapped region ($\theta_+ < 0$), while \mathcal{H}_{in} and \mathcal{H}_{out} are null future inner and outer trapping horizons. \mathcal{H}_{out} is the *event horizon* of Kerr's black hole while \mathcal{H}_{in} is called the *inner horizon*; they also both are Killing horizons. As in the case of Reissner-Nordström solution, it was shown by Barrabès et al. [15] that the inner horizon is unstable against perturbations.

Finally, eq. (2.81) shows that the Kerr black hole is defined for $a^2 \leq M^2$ only. In the limiting case $a^2 = M^2$, the metric (2.68) describes an *extremal* Kerr black hole with only one horizon ($r_- = r_+$). For $a^2 > M^2$, there exists no horizon and the metric (2.68) describes a naked singularity.

3.1.4 The ring singularity

We have mentioned that the radial coordinate r spans the whole real line \mathbb{R} , to the contrary of Schwarzschild's and Reissner-Nordström solutions. For the latter, $r = 0$ is a singular point, the locus of a curvature singularity. In the case of Kerr's solution, $r = 0$ actually is a 3-dimensional cylinder $\mathcal{T}_0 = \mathbb{R} \times \mathbb{S}^2$ called the throat, with induced metric

$$d\sigma^2 = -dt^2 + a^2 \cos^2 \theta d\theta^2 + a^2 \sin^2 \theta d\varphi^2. \quad (2.85)$$

The throat can be split into three components,

$$\mathcal{T}_0 = \mathcal{T}_0^+ \cup \mathcal{R} \cup \mathcal{T}_0^- \quad (2.86)$$

with:

- $\mathcal{T}_0^+ = \mathbb{R} \times (0, \frac{\pi}{2}) \times (0, 2\pi)$
- $\mathcal{R} = \{p \in \mathbb{R}^2 \times \mathbb{S}^2, \quad r(p) = 0 \quad \text{and} \quad \theta = \frac{\pi}{2}\}$
- $\mathcal{T}_0^- = \mathbb{R} \times (\frac{\pi}{2}, \pi) \times (0, 2\pi)$

From eq. (2.85), \mathcal{T}_0^+ and \mathcal{T}_0^- are timelike hypersurfaces, and are thus 2-way traversable. \mathcal{R} , however, is the locus of a curvature singularity. This is visible, for instance, from the expression of the Kretschmann scalar:

$$K = \frac{48M_0^2(r^2 - a^2 \cos^2 \theta)(\Sigma^2 - 16a^2 r^2 \cos^2 \theta)}{\Sigma^6}, \quad (2.87)$$

which diverges when $\Sigma = r^2 + a^2 \cos^2 \theta = 0$. Due to its topology, $\mathcal{R} \simeq \mathbb{R} \times \mathbb{S}^1$ is called the *ring singularity* of Kerr's spacetime.

3.2 Maximal extension of the Kerr spacetime

The construction of the maximal extension of the Kerr spacetime is extremely similar to the Reissner-Nordström one, and will thus be only briefly sketched in this Section.

The first step has already been done: it consisted in extending the original metric 2.68 in the future by defining the *Kerr coordinates* (v, r, θ, ψ) , which allowed crossing the outer (r_+) horizon starting from region \mathcal{M}_I . Null *ingoing* geodesics are then characterized by $v = \text{cst.}$ and $\psi = \text{cst.}$ (as well as $\theta = \text{cst.}$)

Null *outgoing* geodesics are characterized by $u = \text{cst.}$ and $\psi' = \text{cst.}$, with

$$\begin{cases} u = t - r^*, \\ \psi' = \varphi - r^\dagger. \end{cases} \quad (2.88)$$

The coordinates (u, r, θ, ψ') define a past extension of the original metric (2.68). Following a past-directed outgoing geodesic, it will cross a past outer trapping horizon at $r = r_+$ and then a past inner trapping horizon at $r = r_-$. These horizons are defined by a vanishing expansion of null ingoing geodesics θ_- , whose expression is obtained in App. A.3.2:

$$\theta_- = -\frac{2\Delta}{\Sigma} \quad (2.89)$$

The region $\mathcal{M}_{\text{II}}^*$, comprised between $r = r_-$ and $r = r_+$, is thus anti-trapped: $\theta_- > 0$, and even ingoing geodesics must travel towards increasing values of r .

In order to obtain two-dimensional conformal diagrams, where lights rays propagate at 45° , of the ingoing and outgoing patches described above, one can use u and v simultaneously. Due to the dependence of the metric coefficients on θ , one can only draw two-dimensional conformal diagrams for specific values of θ . Choosing for simplicity $\theta = 0$, the metric in double null form reads

$$ds^2 = \frac{\Delta}{r^2 + a^2} du dv \equiv -F_K(r) du dv, \quad (2.90)$$

which is singular at the horizon.

As in Reissner-Nordström case, one can define Kruskal coordinates specific to the outer (+) and inner (−) horizons:

$$\begin{cases} U_+ = \mp e^{\kappa_- u}, & V_+ = e^{\kappa_+ v}, \\ U_- = \mp e^{-\kappa_+ u}, & V_- = -e^{-\kappa_- v}, \end{cases} \quad (2.91)$$

where $\kappa_\pm = \frac{1}{2}F'_K(r_\pm)$.

The final step consists in compactifying these Kruskal coordinates:

$$\begin{cases} \tilde{U}_\pm = \arctan U_\pm, \\ \tilde{V}_\pm = \arctan V_\pm. \end{cases} \quad (2.92)$$

These coordinates are used to build the ingoing (a) and outgoing (b) patches of Fig. 2.8. An ingoing photon starting from \mathcal{M}_{I} hence crosses the FOTH $r = r_+$, the trapped region \mathcal{M}_{II} , the PITH $r = r_-$ and then reaches the normal region \mathcal{M}_{III} . An outgoing photon starting from $\mathcal{M}_{\text{III}}''$ will cross the FITH $r = r_-$, the anti-trapped region $\mathcal{M}_{\text{II}}^*$, the POTH $r = r_+$ before reaching the normal region \mathcal{M}_{I} .

These patches have each extended the spacetime starting from \mathcal{M}_{I} , but this extension is not maximal. Indeed, outgoing photons of the ingoing patch in \mathcal{M}_{III} stop artificially at $\tilde{V}_- = 0$, just like the ingoing photons of the outgoing patch in \mathcal{M}_{III} stop at $\tilde{U}_+ = 0$. The maximal extension of Kerr's spacetime, shown in Fig. 2.9, actually consists of an infinite lattice of these ingoing and outgoing patches.

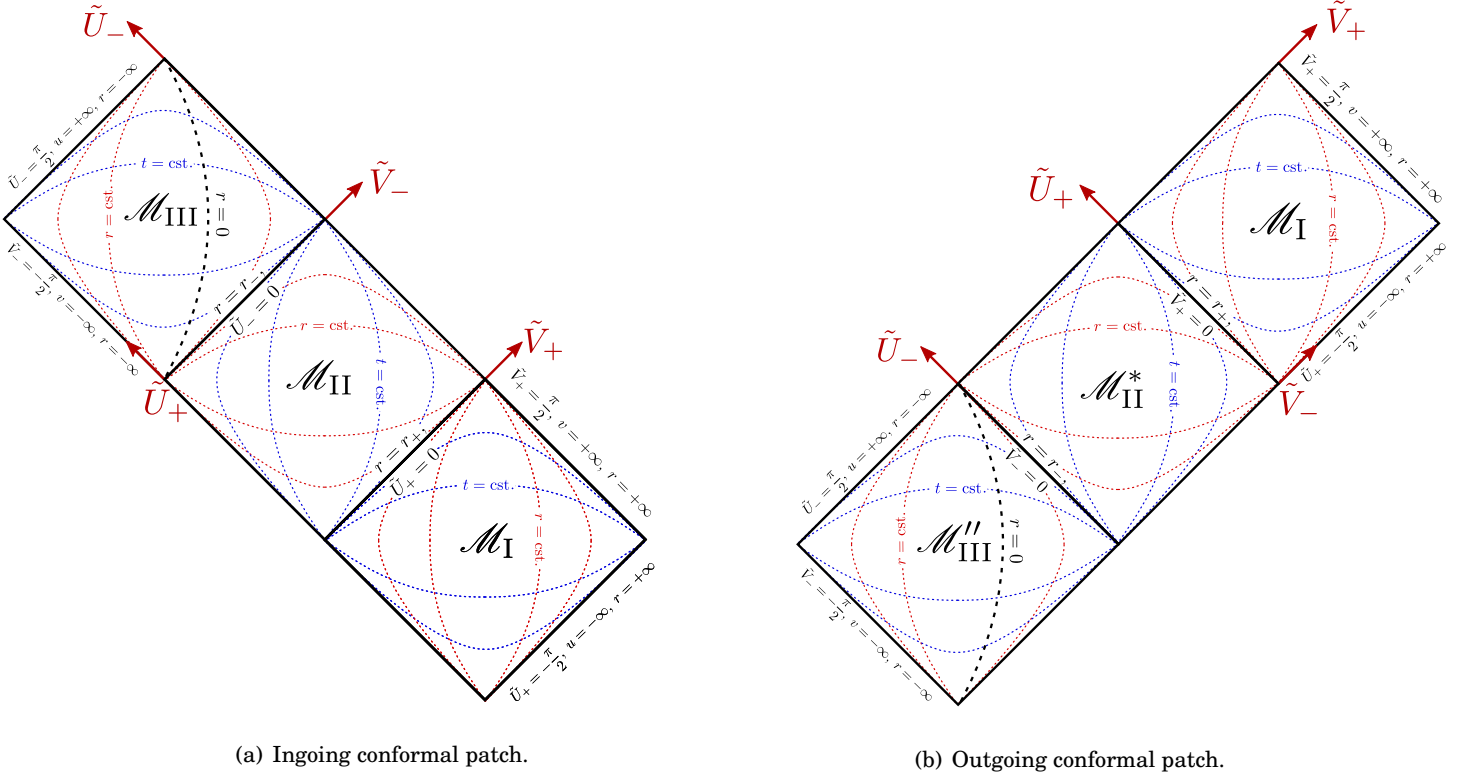


Figure 2.8: Ingoing and outgoing Eddington-Finkelstein conformal patches of the Kerr spacetime for $\theta = 0$, drawn in terms of the compactified Kruskal coordinates $(\tilde{U}_+, \tilde{V}_+)$ and $(\tilde{U}_-, \tilde{V}_-)$. Each point of the diagram is a circle spanned by the coordinate φ . Hypersurfaces of constant t and constant r are respectively drawn in dotted blue and red lines. Light rays propagate at $\pm 45^\circ$. Each patch is geodesically incomplete, as illustrate null future outgoing geodesics in \mathcal{M}_{III} , and null past outgoing geodesics in $\mathcal{M}_{\text{III}}''$. A major difference with Reissner-Nordström spacetime is the presence of a ring singularity at $r = 0$ for $\theta = \pi/2$.

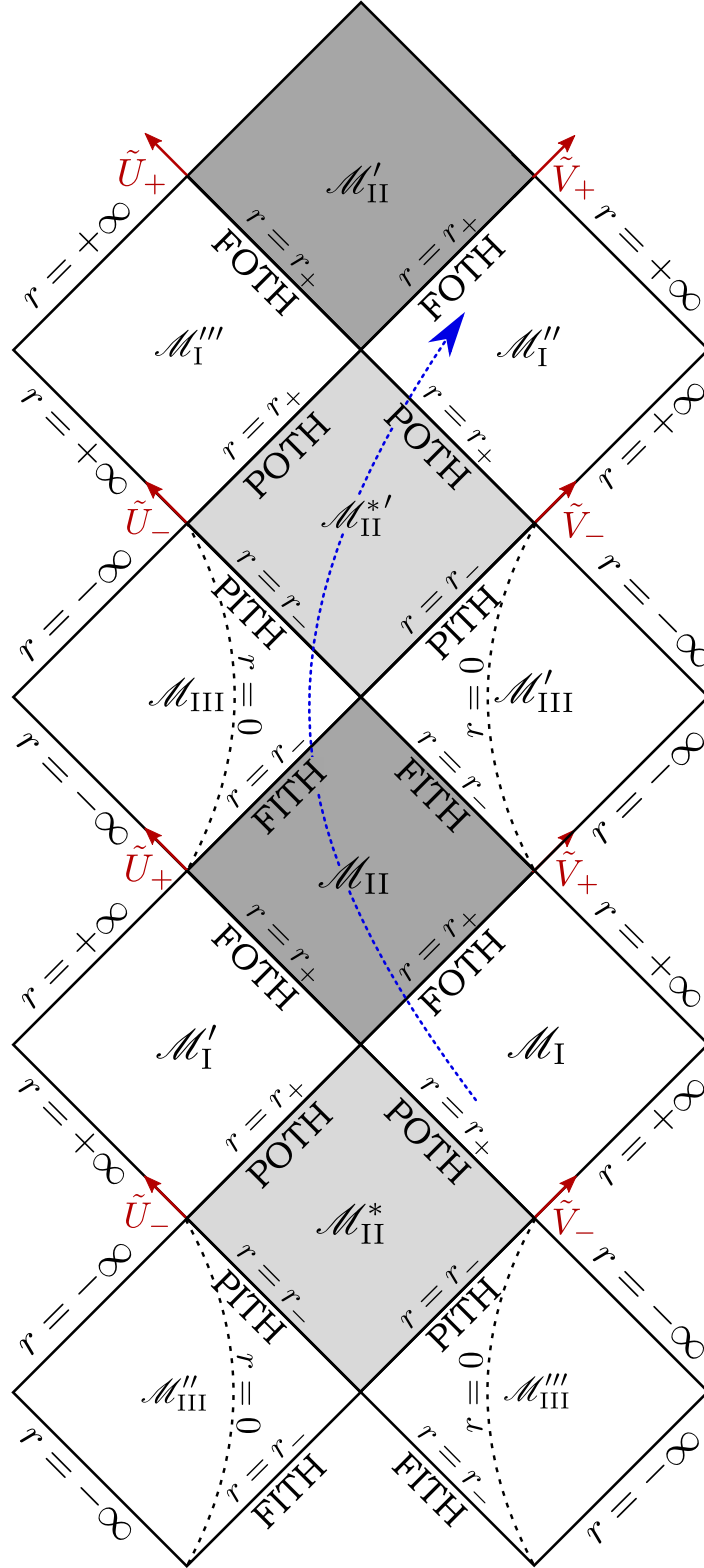


Figure 2.9: Section of the maximal extension of Kerr's spacetime for $\theta = 0$, drawn in the compactified Kruskal coordinates $(\tilde{U}_+, \tilde{V}_+)$ and $(\tilde{U}_-, \tilde{V}_-)$. It is obtained by gluing the ingoing and outgoing patches of Fig. 2.8 and adding copies of normal regions so that every geodesic be complete (as it should be since there is no singularity for $\theta = 0$). The full extension consists in an infinite repetition of the drawn block.

3.3 Deriving Kerr's solution from the Newman-Janis algorithm

An initially *ad hoc* procedure was presented in 1965 by E. Newman and A. Janis to construct Kerr's rotating solution from the static Schwarzschild one [90]. This *Newman-Janis algorithm* has later been applied more generally to known static spherically symmetric solutions of Einstein's equations in order to generate new rotating ones [47], as we will see in Chapter 4. In particular, Kerr-Newman's metric, describing a rotating charged black hole, was obtained by applying the Newman-Janis algorithm to Reissner-Nordström metric [89].

Let us now detail the algorithm and apply it to Schwarzschild's metric as a seed metric. We will follow the five steps introduced by Drake & Szekeres [47].

1. Write the static spherically symmetric seed metric in terms of null retarded coordinates (u, r, θ, φ) . Here,

$$ds^2 = -\left(1 - \frac{2M_0}{r}\right)du^2 - 2dudr + r^2d\Omega^2 \quad (2.93)$$

2. Find a null tetrad $Z_a^\mu = (l^\mu, n^\mu, m^\mu, \bar{m}^\mu)$ such that the inverse metric be written (in our $(-+++)$ convention):

$$g^{\mu\nu} = -l^\mu n^\nu - l^\nu n^\mu + m^\mu \bar{m}^\nu + m^\nu \bar{m}^\mu, \quad (2.94)$$

with $l_\mu l^\mu = m_\mu m^\mu = n_\mu n^\mu = 0$, $l_\mu n^\mu = -m_\mu \bar{m}^\mu = 1$, $l_\mu m^\mu = n_\mu m^\mu = 0$. Here, we have

$$l^\mu = \delta_r^\mu \quad (2.95)$$

$$n^\mu = \delta_t^\mu - \frac{1}{2}\left(1 - \frac{2M_0}{r}\right)\delta_r^\mu \quad (2.96)$$

$$m^\mu = \frac{1}{\sqrt{2}r}\left(\delta_\theta^\mu + \frac{i}{\sin\theta}\delta_\varphi^\mu\right) \quad (2.97)$$

$$\bar{m}^\mu = \frac{1}{\sqrt{2}r}\left(\delta_\theta^\mu - \frac{i}{\sin\theta}\delta_\varphi^\mu\right). \quad (2.98)$$

3. Extend the coordinates x^μ to complex coordinates \tilde{x}^μ , and then complexify the null tetrad:

$$Z_a^\mu(x^\rho) \rightarrow \tilde{Z}_a^\mu(\tilde{x}^\rho, \bar{\tilde{x}}^\rho), \quad (2.99)$$

This procedure defines a new metric \tilde{g} whose components are real functions of complex variables,

$$\tilde{g} : \tilde{\mathbf{x}} \times \tilde{\mathbf{x}} \mapsto \tilde{g}(\tilde{\mathbf{x}}, \tilde{\mathbf{x}}) \in \mathbb{R}. \quad (2.100)$$

Furthermore, we require that

$$\tilde{Z}_a^\mu(\tilde{x}^\rho, \bar{\tilde{x}}^\rho) \Big|_{\tilde{\mathbf{x}}=\bar{\tilde{\mathbf{x}}}} = Z_a^\mu(x^\rho) \quad (2.101)$$

It should be emphasized that there exists a lot of different choices for the transformation (2.99) satisfying (2.100) and (2.101). This is why the algorithm may appear as an *ad hoc*

procedure. However, Drake & Szekeres [47] managed to prove uniqueness theorems regarding the Newman-Janis algorithm without specifying the transformation (2.99). For instance, the only Petrov type D spacetime generated by the Newman-Janis algorithm with a vanishing Ricci scalar is the Kerr-Newman spacetime.

A choice that will work in order to recover Kerr's metric is the following:

$$\tilde{l}^\mu = \delta_r^\mu \quad (2.102)$$

$$\tilde{n}^\mu = \delta_t^\mu - \frac{1}{2} \left(1 - M_0 \left(\frac{1}{\tilde{r}} + \frac{1}{\bar{\tilde{r}}} \right) \right) \delta_r^\mu \quad (2.103)$$

$$\tilde{m}^\mu = \frac{1}{\sqrt{2}\tilde{r}} \left(\delta_\theta^\mu + \frac{i}{\sin\tilde{\theta}} \delta_\varphi^\mu \right) \quad (2.104)$$

$$\bar{\tilde{m}}^\mu = \frac{1}{\sqrt{2}\tilde{r}} \left(\delta_\theta^\mu - \frac{i}{\sin\tilde{\theta}} \delta_\varphi^\mu \right). \quad (2.105)$$

This allows the metric \tilde{g} to be real valued, provided $\tilde{\theta} = \bar{\tilde{\theta}} \in \mathbb{R}$.

4. Perform a coordinate transformation, writing the coordinates \tilde{x}^ρ as

$$\tilde{u} = u' - ia \cos \theta' \quad (2.106)$$

$$\tilde{r} = r' + ia \cos \theta' \quad (2.107)$$

$$\tilde{\theta} = \theta' \quad (2.108)$$

$$\tilde{\varphi} = \varphi', \quad (2.109)$$

where a is a constant. The new coordinates u' and r' are now defined on the whole real line: $(u', r') \in (-\infty, +\infty)^2$. Under this change of coordinates, the null tetrad transforms as follows

$$Z_a'^\mu = \frac{\partial x'^\mu}{\partial \tilde{x}^a} \tilde{Z}_a^\mu, \quad (2.110)$$

with

$$\left[\frac{\partial x'^\mu}{\partial \tilde{x}^a} \right] = \begin{pmatrix} 1 & 0 & ia \sin \theta' & 0 \\ 0 & 1 & -ia \sin \theta' & 0 \\ 0 & 0 & 1 & 0 \\ 0 & 0 & 0 & 1 \end{pmatrix} \quad (2.111)$$

The components of the tetrad are then

$$l'^\mu = \delta_1^\mu \quad (2.112)$$

$$n'^\mu = \delta_0^\mu - \frac{1}{2} \left(1 - M_0 \left(\frac{1}{\tilde{r}} + \frac{1}{\bar{\tilde{r}}} \right) \right) \delta_1^\mu \quad (2.113)$$

$$m'^\mu = \frac{1}{\sqrt{2}\tilde{r}} \left[ia \sin \tilde{\theta} (\delta_0^\mu - \delta_1^\mu) + \delta_2^\mu + \frac{i}{\sin \tilde{\theta}} \delta_3^\mu \right] \quad (2.114)$$

$$\bar{m}'^\mu = \frac{1}{\sqrt{2}\tilde{r}} \left[-ia \sin \tilde{\theta} (\delta_0^\mu - \delta_1^\mu) + \delta_2^\mu - \frac{i}{\sin \tilde{\theta}} \delta_3^\mu \right]. \quad (2.115)$$

They can be rewritten in terms of the prime coordinates $(u', r', \theta', \varphi')$, using:

$$\begin{cases} \tilde{r} = r' + ia \cos \theta' \\ \bar{\tilde{r}} = \bar{r}' - ia \cos \theta' \\ \tilde{\theta} = \theta' , \end{cases} \quad (2.116)$$

which gives

$$\left(\frac{1}{\tilde{r}} + \frac{1}{\bar{\tilde{r}}} \right) M_0 = \frac{2M_0 r'}{r'^2 + a^2 \cos^2 \theta'} \quad (2.117)$$

We can now omit the prime signs to simplify notations, and use the coordinates (u, r, θ, φ) which from now on span $\mathbb{R}^2 \times \mathbb{S}^2$. From eq. (2.112)-(2.115), we can use eq. (2.94) in reverse to get:

$$[g_{\mu\nu}] = \begin{pmatrix} -1 + \frac{2M_0 r}{\Sigma} & 1 & 0 & -a \sin^2 \theta \frac{2M_0 r}{\Sigma} \\ \cdot & 0 & 0 & a \sin^2 \theta \\ \cdot & \cdot & \Sigma & 0 \\ \cdot & \cdot & \cdot & \sin^2 \theta \left(r^2 + a^2 - a^2 \sin^2 \theta \frac{2M_0 r}{\Sigma} \right) \end{pmatrix} \quad (2.118)$$

where we have defined $\Sigma \equiv r^2 + a^2 \cos^2 \theta$.

5. Transform the metric to Boyer-Lindquist coordinates. Here, we recover easily the form (2.68) by the following change of coordinates:

$$dt = du - \frac{r^2 + a^2}{\Delta} dr , \quad d\varphi = d\varphi - \frac{a}{\Delta} dr . \quad (2.119)$$

where we have defined $\Delta \equiv r^2 + a^2 - 2M_0 r$.

4 Vaidya's solution and gravitational collapse

4.1 An exact dynamical solution to Einstein's equations

There is not a plethora of exact solutions to Einstein's equations, even less of dynamical ones. It is thus worth mentioning Vaidya's solution, published in 1951 to describe the gravitational field of a radiating star [116]. In its outgoing version, Vaidya's metric is the same as the outgoing Eddington-Finkelstein metric (2.26) except that the mass M_0 is allowed to depend on the retarded time u :

$$ds^2 = - \left(1 - \frac{2M(u)}{r} \right) du^2 - 2du dr + r^2 d\Omega^2 . \quad (2.120)$$

Computing the Einstein tensor associated with this metric, one gets only one nonvanishing component:

$$\mathbf{G} = - \frac{2 \frac{\partial M}{\partial u}}{r^2} \mathbf{du} \otimes \mathbf{du} . \quad (2.121)$$

This geometry corresponds, via Einstein's equation, to the following energy-momentum tensor:

$$\mathbf{T} = - \frac{\frac{\partial M}{\partial u}}{4\pi r^2} \mathbf{du} \otimes \mathbf{du} . \quad (2.122)$$

The radial null outgoing geodesics are such that $u = \text{cst.}$ Hence, a radial null outgoing vector $k^\mu = \frac{dx^\mu}{d\lambda}$ will have only one nonzero component k^r . Choosing $\lambda = r$ as an affine parameter, we get

$$[k^\mu] = (0, 1, 0, 0), \quad [k_\mu] = (-1, 0, 0, 0) \quad (2.123)$$

Hence the 1-form \mathbf{k} reads

$$\mathbf{k} = -\mathbf{d}u, \quad (2.124)$$

and we can write

$$\mathbf{T} = -\frac{\frac{\partial M}{\partial u}}{4\pi r^2} \mathbf{k} \otimes \mathbf{k}. \quad (2.125)$$

This energy-momentum tensor represents a fluid with energy density

$$\rho = -\frac{\frac{\partial M}{\partial u}}{4\pi r^2} \quad (2.126)$$

It has a null 4-velocity k^μ and is called *null dust* due to the form (2.125) of its energy-momentum tensor. The outgoing Vaidya metric satisfies the null energy condition $\mathbf{T}(\mathbf{k}, \mathbf{k}) \geq 0$ if and only if M is a decreasing function of u :

$$\frac{dM}{du} \leq 0 \quad (2.127)$$

There also exists an ingoing version of the Vaidya solution. The *ingoing Vaidya metric* reads:

$$ds^2 = -\left(1 - \frac{2M(v)}{r}\right) dv^2 + 2dvdr + r^2 d\Omega^2. \quad (2.128)$$

The radial null ingoing geodesics are such that $v = \text{cst.}$ Hence, a radial null ingoing vector $l^\mu = \frac{dx^\mu}{d\lambda}$ will have only one nonzero component l^r . Choosing $\lambda = -r$ as an affine parameter, we get

$$[l^\mu] = (0, -1, 0, 0), \quad [l_\mu] = (-1, 0, 0, 0) \quad (2.129)$$

Hence the 1-form \mathbf{l} reads

$$\mathbf{l} = -\mathbf{d}v. \quad (2.130)$$

Solving Einstein's equations as in the outgoing case, we get the following energy-momentum tensor:

$$\mathbf{T} = \frac{\frac{\partial M}{\partial v}}{4\pi r^2} \mathbf{l} \otimes \mathbf{l}. \quad (2.131)$$

It represents ingoing null dust with energy density

$$\rho = \frac{\frac{\partial M}{\partial v}}{4\pi r^2}. \quad (2.132)$$

The null energy condition is now satisfied provided

$$\frac{dM}{dv} \geq 0 \quad (2.133)$$

4.2 Gravitational collapse of ingoing null dust

The ingoing Vaidya metric can be used, for instance, to model the gravitational collapse of a thick shell of null dust. We will provide a schematic Penrose diagram for this process, which will allow us to give a concrete example of distinct apparent and event horizons in preparation for Chapter 6.

We consider the following mass function:

$$M(v) = \begin{cases} 0 & \text{for } v \leq v_1 \\ m(v) & \text{for } v_1 < v < v_2 \\ m(v_2) & \text{for } v \geq v_2, \end{cases} \quad (2.134)$$

where m is an increasing function of v .

Let us discuss first the existence of an apparent horizon, which is characterized by a change of sign of the null outgoing congruence θ_+ . To compute θ_+ , let us take an outgoing radial null vector k with components:

$$[k^\mu] = \left(1, \frac{1}{2} \left(1 - \frac{2M(v)}{r} \right), 0, 0 \right). \quad (2.135)$$

Then,

$$\theta_+ \equiv h^{\mu\nu} \nabla_\mu k_\nu = \frac{r - 2M(v)}{r^2}, \quad (2.136)$$

where h is the induced metric on the 2-sphere. Hence, an apparent horizon forms as soon as $M(v) > 0$.

The flux of ingoing null dust starts at $v = v_1$, as can be seen in Fig. 2.10. An apparent horizon then develops and reaches higher and higher values of r as M increases. We can show that the apparent horizon is spacelike in the interval $v_1 < v < v_2$, as ingoing null dust comes in. To see this, let us describe the apparent horizon via a function $\varphi \equiv r - 2M(v) = 0$. Then,

$$g^{\mu\nu} \partial_\mu \varphi \partial_\nu \varphi = -4 \frac{dM}{dv}. \quad (2.137)$$

In the interval $v_1 < v < v_2$, $M(v)$ is increasing and thus the trapping horizon is spacelike since its normal $\partial_\mu \varphi$ is timelike.

For $v \geq v_2$, $M = m(v_2)$ is constant and thus the apparent horizon becomes null and remains at a constant $r = 2m(v_2)$. The event horizon can then be drawn backwards from future infinity, as a null hypersurface. The Penrose-Carter diagram of a Vaidya collapse, shown in Fig. 2.10, allows emphasizing two features of the event horizon not shared by the apparent horizon. First it is a teleological notion, since one has to wait for the end of times (i.e., to reach future infinity) before drawing the event horizon. Second, the event horizon is not necessarily related to strong gravitational fields (in the sense $\theta_+ < 0$): in the Vaidya collapse, an event horizon is present in

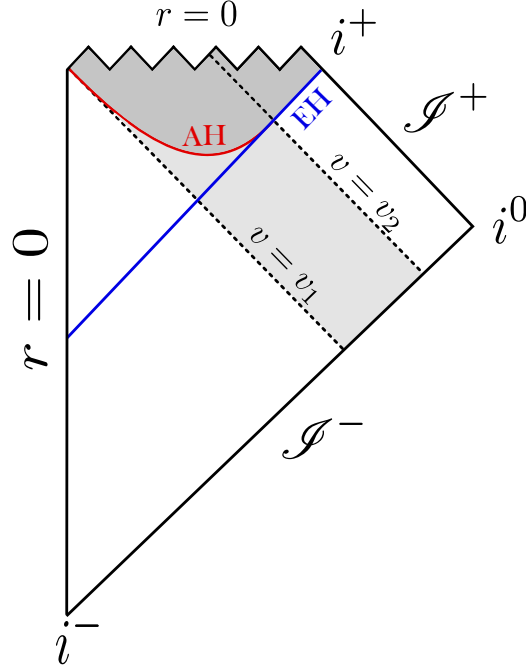
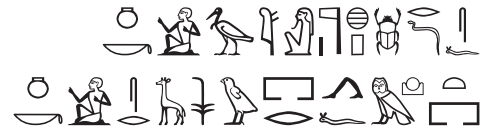


Figure 2.10: Carter-Penrose diagrams of a Vaidya collapse. The thick null shells are pictured in light grey, while the trapped region, in deep grey, is delineated by the apparent horizon (AH). The latter is spacelike and becomes null as $t \rightarrow +\infty$, where it tends towards the event horizon (EH).

the Minkowski part ($v < v_1$) of the spacetime. The apparent horizon, to the contrary, delineates a gravitationally trapped region in dark grey in Fig. 2.10.

STATIC NON-SINGULAR BLACK HOLES



jnk b3 šw ntr hpr(=w) ds=f

jnk sr(w) sw pr=f m 3h.t

“Je suis le ba de Chou, le dieu qui est venu à l’existence de lui-même. [...]”

C’est moi qui ai annoncé quand il est sorti de l’horizon !”

(*Textes des Sarcophages* I, 314b-320d-322a, S1C [30, 40].)

In this chapter, we encounter for the first time non-singular black holes and present some results related to static and spherically symmetric ones. These results consist in recovering known static non-singular black holes, such as Bardeen’s and Hayward’s, from modified theories of gravity. They were obtained with K. Noui, J. Ben Achour and H. Liu in [17] and [18]. We will start by introducing in detail the Bardeen and Hayward non-singular black holes (Sec. 1) and review how they can be seen as a solution to Einstein’s equations in the presence of non-linear electrodynamics. Sec. 2 will be devoted to the analysis of static spherically symmetric spacetimes in a tensor-scalar theory called mimetic gravity, which opens up the possibility to recover Hayward’s and Bardeen’s metrics. Finally, in Sec. 3 we will describe the Hamiltonian formulation of General Relativity and see how, in the spirit of loop quantum gravity, it can be modified to add quantum corrections once again allowing us to recover non-singular black hole solutions.

Contents

1	Examples of static non-singular black holes	72
2	Static non-singular black holes from mimetic gravity	80
3	Loop quantum deformation of Schwarzschild’s black hole	89

1 Examples of static non-singular black holes

Let us start with a review of Bardeen's and Hayward's non-singular black holes as well as their potential non-linear electrodynamical source, before investigating in Secs. 2 and 3 how they could be recovered in theories of modified gravity.

1.1 Bardeen's spacetime

1.1.1 Metric and horizons

The Bardeen model, which dates back to 1968 [11], is the first example of regular black hole ever mentioned in the literature. Its metric reads

$$ds^2 = -B(r)dt^2 + B(r)^{-1}dr^2 + r^2 d\Omega^2 \quad \text{with} \quad B(r) \equiv 1 - \frac{2M_B(r)}{r} \equiv 1 - \frac{2M_0 r^2}{(r^2 + g^2)^{\frac{3}{2}}} \quad (3.1)$$

where g is a constant. When $g \rightarrow 0$, one recovers Schwarzschild's spacetime with mass M_0 . It allows the components of the metric, and most importantly the curvature scalars, not to diverge as $r \rightarrow 0$. Indeed, the Ricci and Kretschmann scalars read

$$\begin{cases} R = \frac{6M_0 g^2 (4g^2 - r^2)}{(r^2 + g^2)^{\frac{7}{2}}} \\ K = \frac{12M_0^2 (8g^2 - 4g^6 r^2 + 47g^4 r^4 - 12g^2 r^6 + 4r^8)}{(r^2 + g^2)^7} \end{cases} \quad (3.2)$$

To see that the metric (3.1) describes a black hole, let us compute the expansion of null radial outgoing geodesics. The results of App. A.3.2 apply, hence

$$\theta_+ = \frac{B(r)}{r} \quad (3.3)$$

For $M_0 > M_* \equiv \frac{3\sqrt{3}}{4}g$, $B(r) = 0$ admits two distinct solutions (and only one in the limiting case $M_0 = M_*$, see Fig. 3.1). These are future outer and inner trapping horizons, which surround a gravitationally trapped region. It has been shown recently that the mass inflation phenomenon occurs not only in Reissner-Nordström and Kerr's spacetimes but also in all spherically symmetric models of regular black holes [29], including Bardeen's model as well as Hayward's. This is a serious limitation of these models.

1.1.2 Avoiding singularities

In light of Penrose's singularity theorem proved in Sec. 4.2 of Chap. 1, since Bardeen's spacetime is non-singular and possesses a trapped surface, it must violate (at least) one of the following properties:

- global hyperbolicity
- existence of a noncompact Cauchy surface

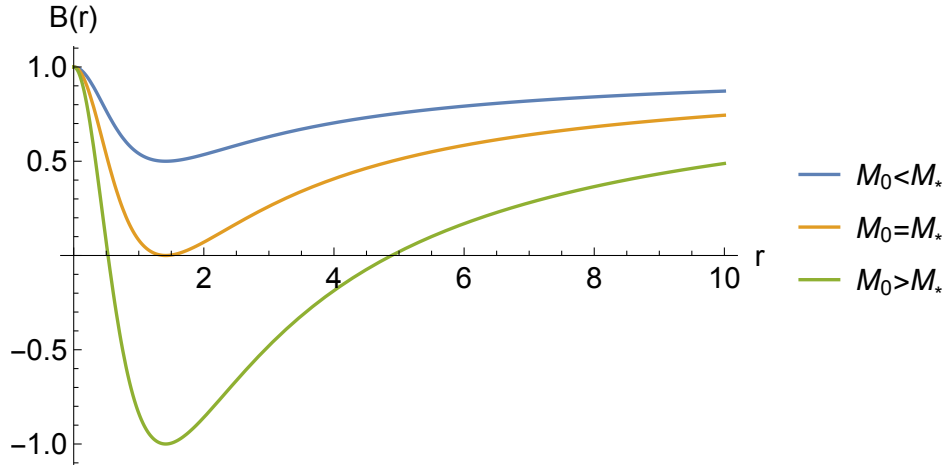


Figure 3.1: Plot of Bardeen's function $B(r)$ for different values of M_0 , keeping $b = 1$. The zeros of H represent future trapping horizons: there are two horizons when $M_0 > M_*$, only one when $M_0 = M_*$, and none when $M_0 < M_*$.

- satisfaction of the null energy condition

The spacetime satisfies the weak energy condition, and thus by continuity the null energy condition. But Bardeen's spacetime possesses a Cauchy horizon. Hence the first two properties are not satisfied, this is how Penrose's theorem happens to be circumvented. The Cauchy horizon is visible in red in Fig. 3.2, where the Carter-Penrose diagram of Bardeen's and Hayward's spacetimes has been drawn.

One might wonder then how Bardeen's spacetime copes with the singularity theorem 1.4 by Hawking and Penrose, not requiring the existence of a Cauchy surface anymore. Actually, this theorem relies on the fulfilment of the strong energy condition, which Bardeen's spacetime violates (as mentioned in [67]).

1.2 Hayward's spacetime

1.2.1 Metric and horizons

Hayward introduced in 2006 another regular black hole, in order to describe the formation and evaporation of non-singular black holes. We will use it extensively in Chap. 6, where dynamics will enter the game. Let us, as for now, present the static version of his model, which is defined by the metric

$$ds^2 = -H(r)dt^2 + H(r)^{-1}dr^2 + r^2 d\Omega^2 \quad \text{with} \quad H(r) \equiv 1 - \frac{2M_H(r)}{r} \equiv 1 - \frac{2M_0 r^2}{r^3 + 2M_0 b^2}, \quad (3.4)$$

where b is a constant. It might be interpreted, according to Hayward, as a Planckian cutoff.

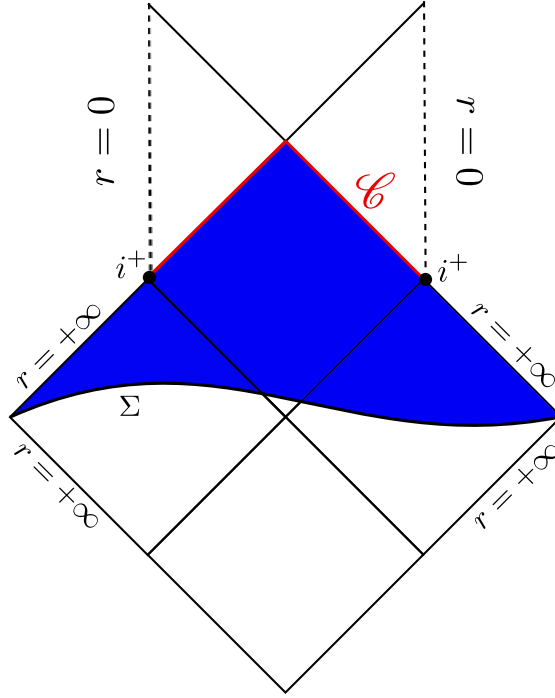


Figure 3.2: Carter-Penrose diagram of Bardeen's and Hayward's spacetimes. The future domain of dependence of the hypersurface Σ (in blue) is limited by a Cauchy horizon (in red) due to the presence of i^+ .

This metric behaves as a Schwarzschild metric in the limit $r \rightarrow +\infty$:

$$H(r) \underset{r \rightarrow +\infty}{\simeq} 1 - \frac{2M_0}{r}, \quad (3.5)$$

and as a de Sitter one near the center:

$$H(r) \underset{r \rightarrow 0}{\simeq} 1 - \frac{r^2}{b^2}. \quad (3.6)$$

This de Sitter core will actually protect the spacetime from the presence of a singularity at the center. Indeed, the Ricci and Kretschmann curvature invariants read

$$\begin{cases} R = \frac{24(4b^2m_0 - r^3)b^2m_0^2}{(2b^2m_0 + r^3)^3} \\ K = \frac{48(32b^8m_0^4 - 16b^6m_0^3r^3 + 72b^4m_0^2r^6 - 8b^2m_0r^9 + r^{12})m_0^2}{(2b^2m_0 + r^3)^6} \end{cases} \quad (3.7)$$

As in Bardeen's case, future trapping horizons are present if

$$\theta_+ = \frac{H(r)}{r} \quad (3.8)$$

For $M_0 > M_* \equiv \frac{3\sqrt{3}}{4}b$, $B(r) = 0$ admits two distinct solutions (and only one in the limiting case $M_0 = M_*$, see Fig. 3.3). These are future outer and inner trapping horizons, which surround a gravitationally trapped region.

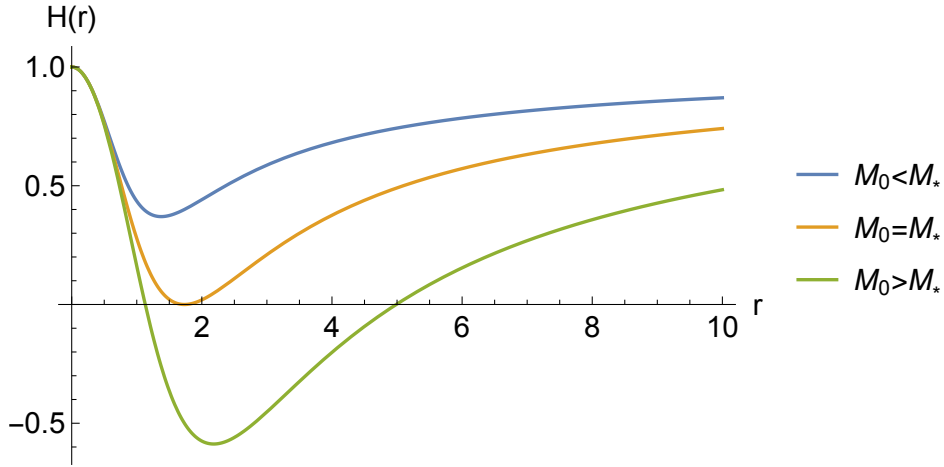


Figure 3.3: Plot of Hayward's function $H(r)$ for different values of M_0 , keeping $b = 1$. The zeros of B represent future trapping horizons: there are two horizons when $M_0 > M_*$, only one when $M_0 = M_*$, and none when $M_0 < M_*$.

1.2.2 Avoiding singularities

As Bardeen's spacetime, Hayward's one possesses a Cauchy horizon, and is therefore not globally hyperbolic. This allows avoiding the conclusions of Penrose's 1965 singularity theorem 1.3. It also violates the strong energy condition, hence circumventing Hawking & Penrose's singularity theorem 1.4.

1.3 Energy-momentum tensor from non-linear electrodynamics

1.3.1 General static case in spherical symmetry

The parameter g in eq. (3.1) did not have any physical interpretation before the work of Ayón-Beato & García [5]. They showed that g can actually be interpreted as the monopole charge of a self-gravitating magnetic field described by a nonlinear electrodynamics.

A substantial part of the reasoning in [5] is valid for a general function $M(r)$, and we will apply it later on in Bardeen's case (Sec. 1.3.2) as well as Hayward's case (Sec. 1.3.3). Let us then start with a spherically symmetric metric in the form

$$ds^2 = -F(r)dt^2 + \frac{1}{F(r)}dr^2 + r^2 d\Omega^2, \quad (3.9)$$

with $F(r) \equiv 1 - \frac{2M(r)}{r}$.

Let us take the following action of nonlinear electrodynamics in curved spacetime:

$$S = \frac{1}{16\pi} \int d^4x \sqrt{-g} (R + 16\pi \mathcal{L}(\mathcal{F})), \quad (3.10)$$

where $\mathcal{F} = F_{\mu\nu}F^{\mu\nu}$, and \mathcal{L} is a Lagrangian density depending only on \mathcal{F} . The electromagnetic tensor $F_{\mu\nu}$ is defined through the vector potential A_μ :

$$F_{\mu\nu} = \nabla_\mu A_\nu - \nabla_\nu A_\mu . \quad (3.11)$$

The Einstein equations deduced from the action (3.10) read

$$G_{\mu\nu} = 8\pi T_{\mu\nu} , \quad (3.12)$$

with

$$\begin{aligned} T_{\mu\nu} &\equiv -\frac{2}{\sqrt{-g}} \frac{\delta S_{\text{mat}}}{\delta g^{\mu\nu}} \\ &= -\frac{2}{\sqrt{-g}} \frac{\delta}{\delta g^{\mu\nu}} \int d^4x \sqrt{-g} \mathcal{L}(\mathcal{F}) \\ &= \mathcal{L} g_{\mu\nu} - 4 \mathcal{L}_{\mathcal{F}} F_\mu{}^\alpha F_{\nu\alpha} , \end{aligned} \quad (3.13)$$

while the nonlinear Maxwell equations are

$$\nabla_\mu (\mathcal{L}_{\mathcal{F}} F^{\mu\nu}) = 0 \quad (3.14)$$

Eq. (3.14) reduces to the standard Maxwell equations when $\mathcal{L}(\mathcal{F}) = \mathcal{F}$.

Ayón-Beato & García chose the following ansatz for the Maxwell tensor:

$$\mathbf{F} = B(r, \theta) \mathbf{d}\theta \wedge \mathbf{d}\varphi , \quad (3.15)$$

where $B(r, \theta)$ is a general function of r and θ , and \wedge denotes the exterior product (or antisymmetrized tensor product). They call it a “magnetic ansatz” since the only nonvanishing components of the Maxwell tensor are $F_{\theta\varphi}$ and $F_{\varphi\theta}$.

Let us now solve the nonlinear Maxwell equations (3.14), which can be written in the form

$$\mathbf{dH} = 0 , \quad (3.16)$$

where \mathbf{H} is the Hodge dual of $\mathcal{L}_{\mathcal{F}} \mathbf{F}$:

$$\mathbf{H} = \star(\mathcal{L}_{\mathcal{F}} \mathbf{F}) . \quad (3.17)$$

The Lagrangian density \mathcal{L} is a function of \mathcal{F} only, and since the spacetime considered is spherically symmetric one has $\mathcal{L}_{\mathcal{F}} = \mathcal{L}_{\mathcal{F}}(r)$. Hence,

$$\mathbf{H} = \frac{B(r, \theta) \mathcal{L}_{\mathcal{F}}(r)}{r^2 \sin(\theta)} \mathbf{d}t \wedge \mathbf{d}r . \quad (3.18)$$

In order to have $\mathbf{dH} = 0$, one must thus set

$$B(r, \theta) = f(r) \sin(\theta) , \quad (3.19)$$

where f is a function of r . Since \mathbf{F} is an exact form, it is closed:

$$0 = \mathbf{dF} = f'(r) \sin(\theta) \mathbf{dr} \wedge \mathbf{d\theta} \wedge \mathbf{d\varphi} . \quad (3.20)$$

Hence $f(r)$ is a constant, and we choose $f(r) = Q_m$ where Q_m is a magnetic monopole charge. The nonlinear Maxwell equations are thus satisfied, for any $\mathcal{L}(\mathcal{F})$, if we take¹

$$\mathbf{A} = -Q_m \cos \theta \mathbf{d\varphi} . \quad (3.21)$$

Let us now solve Einstein's equations. The nonzero components of the Einstein tensor are

$$\begin{cases} G_t^t = G_r^r = \frac{rF' + F - 1}{r^2} = -\frac{2M'(r)}{r^2} \\ G_\theta^\theta = G_\varphi^\varphi = \frac{rF'' + 2F'}{2r} = -\frac{M''(r)}{r} \end{cases} . \quad (3.22)$$

Meanwhile, the nonzero components of the energy-momentum tensor are

$$\begin{cases} T_t^t = T_r^r = \mathcal{L} \\ T_\theta^\theta = T_\varphi^\varphi = \mathcal{L} - \frac{4g^2}{r^4} \mathcal{L}_{\mathcal{F}} \end{cases} . \quad (3.23)$$

The tt and rr parts of Einstein's equations then yield

$$\mathcal{L} = -\frac{1}{4\pi} \frac{M'(r)}{r^2} . \quad (3.24)$$

This condition is actually sufficient to satisfy the $\theta\theta$ and $\varphi\varphi$ parts of Einstein's equations. To see this, let us compute $M''(r)$ assuming eq. (3.24) holds:

$$\begin{aligned} M''(r) &= (-4\pi r^2 \mathcal{L}) \\ &= -8\pi r \mathcal{L} - 4\pi r^2 \mathcal{L}_{\mathcal{F}} \partial_r \mathcal{F} \\ &= -8\pi r \mathcal{L} + \frac{32\pi g^2 \mathcal{L}_{\mathcal{F}}}{r^3} , \end{aligned} \quad (3.25)$$

since \mathcal{L} depends only on $\mathcal{F} = \frac{2g^2}{r^4}$. Hence,

$$G_\theta^\theta = G_\varphi^\varphi = -\frac{M''(r)}{r} = 8\pi \mathcal{L} - \frac{32\pi g^2}{r^4} \mathcal{L}_{\mathcal{F}} = 8\pi T_\theta^\theta = 8\pi T_\varphi^\varphi \quad (3.26)$$

Einstein's equations will then be satisfied provided eq. (3.24) holds. Therefore, given a specific mass function $M(r)$, one has to find a Lagrangian \mathcal{L} depending only on $\mathcal{F} = \frac{2g^2}{r^4}$ such that $\mathcal{L} = -\frac{1}{4\pi} \frac{M'(r)}{r^2}$.

¹Note that this vector potential is singular at $r = 0$ (since $\mathbf{d\varphi}$ contains terms in $1/r$), just as in the case of an electric monopole.

1.3.2 Recovering Bardeen's mass function

Fan and Wang considered in [51] a generalization of Bardeen's metric:

$$M(r) = \frac{\alpha^{-1} q^3 r^\mu}{(r^2 + q^2)^{\frac{\mu}{2}}}, \quad (3.27)$$

where α and q are two constants satisfying $\alpha = \frac{q^4}{2Q_m^2}$, and $\mu > 0$ is a dimensionless constant. We will for instance recover Bardeen's metric for $\mu = 3$ and $\alpha^{-1} q^3 = M_0$.

Then, they used the following Lagrangian to satisfy Einstein's equations:

$$\mathcal{L}(\mathcal{F}) = -\frac{\mu}{4\pi\alpha} \frac{(\alpha \mathcal{F})^{\frac{5}{4}}}{(1 + \sqrt{\alpha \mathcal{F}})^{1 + \frac{\mu}{2}}} \quad (3.28)$$

Let us show that this yields indeed

$$\mathcal{L}(\mathcal{F}) = -\frac{1}{4\pi} \frac{M'(r)}{r^2} \quad (3.29)$$

First,

$$\begin{aligned} M'(r) &= \alpha^{-1} q^3 \mu \frac{r^{\mu-1}(r^2 + q^2)^{\frac{\mu}{2}} - r^{\mu+1}(r^2 + q^2)^{\frac{\mu}{2}-1}}{(r^2 + q^2)^\mu} \\ &= \frac{2\mu Q_m^2 r^{\mu-1}}{q} \frac{1 - r^2(r^2 + q^2)^{-1}}{(r^2 + q^2)^{\frac{\mu}{2}}} \\ &= \frac{2q\mu Q_m^2 r^{\mu-1}}{(r^2 + q^2)^{\frac{\mu}{2}+1}} \end{aligned} \quad (3.30)$$

As concerns the Lagrangian,

$$\alpha \mathcal{F} = \frac{q^4}{2Q_m^2} \cdot \frac{2Q_m^2}{r^4} = \frac{q^4}{r^4}, \quad (3.31)$$

and thus

$$\begin{aligned} \mathcal{L}(\mathcal{F}) &= -\frac{\mu}{4\pi\alpha} \frac{(\alpha \mathcal{F})^{\frac{5}{4}}}{(1 + \sqrt{\alpha \mathcal{F}})^{1 + \frac{\mu}{2}}} \\ &= -\frac{\mu Q_m^2}{2\pi q^4} \frac{q^5 (r^2)^{1 + \frac{\mu}{2}}}{(r^2 + q^2)^{1 + \frac{\mu}{2}}} \\ &= -\frac{q\mu Q_m^2 r^{\mu-3}}{2\pi (r^2 + q^2)^{1 + \frac{\mu}{2}}}, \end{aligned} \quad (3.32)$$

which proves that eq. (3.29) holds.

Coming back to Bardeen's metric, we have in the end shown that the metric (3.9) with

$$M(r) = \frac{M_0 r^3}{\left(r^2 + \left(\frac{2Q_m^2}{M_0}\right)^2\right)^{\frac{3}{2}}} \quad (3.33)$$

is supported by nonlinear electrodynamics with a Maxwell field

$$\mathbf{F} = Q_m \sin\theta \mathbf{d}\theta \wedge \mathbf{d}\varphi, \quad \mathcal{F} = F_{\mu\nu} F^{\mu\nu} = \frac{2Q_m^2}{r^4}, \quad (3.34)$$

and a Lagrangian

$$\mathcal{L}(\mathcal{F}) = -\frac{3M_0^4}{32\pi Q_m^6} \frac{\left(\frac{8Q_m^6}{M_0^4} \mathcal{F}\right)^{\frac{5}{4}}}{\left(1 + \sqrt{\frac{8Q_m^6}{M_0^4} \mathcal{F}}\right)^{1+\frac{5}{2}}}. \quad (3.35)$$

In the weak field limit (for small \mathcal{F}), $\mathcal{L}(\mathcal{F}) \propto \mathcal{F}^{5/4}$ and one unfortunately does not recover standard Maxwell electrodynamics.

1.3.3 Recovering Hayward's mass function

Another category of Lagrangians is found by Fan & Wang, corresponding to generalized Hayward metrics of the form

$$M(r) = \frac{\alpha^{-1} q^3 r^\mu}{r^\mu + q^\mu}, \quad (3.36)$$

where, again, α and q are two constants satisfying $\alpha = \frac{q^4}{2Q_m^2}$, and $\mu > 0$ is a dimensionless constant. As before, it is straightforward to show that the Lagrangian

$$\mathcal{L}(\mathcal{F}) = -\frac{\mu}{4\pi\alpha} \frac{(\alpha \mathcal{F})^{\frac{\mu+3}{4}}}{\left(1 + (\alpha \mathcal{F})^{\frac{\mu}{4}}\right)^2} \quad (3.37)$$

satisfies

$$\mathcal{L}(\mathcal{F}) = -\frac{1}{4\pi} \frac{M'(r)}{r^2}. \quad (3.38)$$

Hayward's case is recovered for $\mu = 3$, $\alpha^{-1} q^3 = M_0$.

Finally, the metric (3.9) with

$$M(r) = \frac{M_0 r^3}{r^3 + \left(\frac{2Q_m^2}{M_0}\right)^3} \quad (3.39)$$

is supported by nonlinear electrodynamics with a Maxwell field

$$\mathbf{F} = Q_m \sin\theta \mathbf{d}\theta \wedge \mathbf{d}\varphi, \quad \mathcal{F} = F_{\mu\nu} F^{\mu\nu} = \frac{2Q_m^2}{r^4}, \quad (3.40)$$

and a Lagrangian

$$\mathcal{L}(\mathcal{F}) = -\frac{3M_0^4}{32\pi Q_m^6} \frac{\left(\frac{8Q_m^6}{M_0^4} \mathcal{F}\right)^{\frac{3}{2}}}{\left(1 + \left(\frac{8Q_m^6}{M_0^4} \mathcal{F}\right)^{\frac{3}{4}}\right)^2}. \quad (3.41)$$

In the weak field limit, $\mathcal{L}(\mathcal{F}) \propto \mathcal{F}^{3/2}$ and standard Maxwell electrodynamics is not recovered either.

2 Static non-singular black holes from mimetic gravity

This section aims at presenting the work I contributed to within the scope of a paper we published with K. Noui , J. Ben Achour, and H. Liu [17]. The main aspect I was interested in was the recovery of static non-singular black holes with a modified theory of gravitation called *mimetic gravity*. This work, even if it could not be concluded, will be presented in Sec. 2.3.2. Before that we will introduce mimetic gravity in Sec. 2.1 as well as its generalization and, following [35], show in Sec. 2.3.1 how it can describe a non-singular black hole with limiting curvature (more precisely with a bounded Ricci scalar).

2.1 Mimetric gravity

2.1.1 Original theory

Mimetic gravity was first introduced by Chamseddine & Mukhanov [34] as a gravity theory with an extra degree of freedom able to mimic cold dark matter. It is a tensor-scalar theory, where the physical metric $g_{\mu\nu}$ is written in terms of a scalar field ϕ and an auxiliary metric $\tilde{g}_{\mu\nu}$:

$$g_{\mu\nu} \equiv \mp \tilde{X} \tilde{g}_{\mu\nu} \quad \text{where} \quad \tilde{X} \equiv \tilde{g}^{\mu\nu} \phi_\mu \phi_\nu , \quad (3.42)$$

and where we use the notation $\phi_\mu \equiv \partial_\mu \phi$. We do not fix for now the sign (± 1) .

The action reads

$$\tilde{S}[\tilde{g}_{\mu\nu}, \phi] = \frac{1}{16\pi} \int d^4x \sqrt{-g(\tilde{g}_{\mu\nu}, \phi)} R(g_{\mu\nu}(\tilde{g}_{\mu\nu}, \phi)) , \quad (3.43)$$

where g and R , computed out of the physical metric $g_{\mu\nu}$, are written in terms of the scalar field and the auxiliary metric. Note that this action, as well as the physical metric $g_{\mu\nu}$, are conformally invariant: they remain the same under a transformation $\tilde{g}_{\mu\nu} \rightarrow \Omega(x) \tilde{g}_{\mu\nu}$, where $\Omega(x)$ is an arbitrary function of the spacetime. The conformal mode of the metric hence becomes dynamical, and the theory propagates an additional scalar degree of freedom with respect to gravity (see [33] for details)

From eq. (3.42), the inverse metrics satisfy

$$g^{\mu\nu} = \mp \frac{1}{\tilde{X}} \tilde{g}^{\mu\nu} . \quad (3.44)$$

Hence, we see that $g_{\mu\nu}$ satisfies the so-called *mimetic condition*:

$$X \equiv g^{\mu\nu} \phi_\mu \phi_\nu = \mp 1 . \quad (3.45)$$

This allows rewriting the action of the theory in a simpler way with a new dynamical variable λ as follows:

$$S[g_{\mu\nu}, \phi, \lambda] \equiv \int d^4x \sqrt{-g} \left[\frac{1}{16\pi} R + \lambda (g^{\mu\nu} \phi_\mu \phi_\nu \pm 1) \right] . \quad (3.46)$$

The variation of this action with respect to λ yields the mimetic condition²

$$X \pm 1 = 0 \quad (3.47)$$

The variation with respect to ϕ yields

$$\nabla_\mu (\lambda \phi^\mu) = 0, \quad (3.48)$$

and finally with respect to $g_{\mu\nu}$:

$$G_{\mu\nu} = 8\pi T_{\mu\nu} \quad \text{with} \quad T_{\mu\nu} = -2\lambda\phi_\mu\phi_\nu + \lambda(X \pm 1)g_{\mu\nu} \quad (3.49)$$

Taking the trace of (3.49), we get

$$\lambda = \pm \frac{1}{16\pi} R. \quad (3.50)$$

Then, eqs. (3.48) and (3.49) read

$$\nabla_\mu (R \phi^\mu) = 0, \quad G_{\mu\nu} \pm R \phi_\mu \phi_\nu = 0. \quad (3.51)$$

Let us show that, contrarily to what usually happens, the equation for the scalar field is actually not independant from Einstein's equations. First, by conservation of the Einstein tensor we have

$$\begin{aligned} 0 &= \nabla^\mu G_{\mu\nu} \\ &= \nabla^\mu (R \phi_\mu \phi_\nu) \\ &= \nabla^\mu (R \phi_\mu) \phi_\nu + R \phi^\mu \phi_{\mu\nu}. \end{aligned} \quad (3.52)$$

Then, the mimetic condition $\phi_\mu \phi^\mu = \pm 1$ implies

$$\begin{aligned} 0 &= \nabla_\nu (\phi_\mu \phi^\mu) \\ &= 2\phi^\mu \phi_{\mu\nu}. \end{aligned} \quad (3.53)$$

Combining eqs. (3.52) and (3.53) finally yields

$$\nabla^\mu (R \phi_\mu) = 0. \quad (3.54)$$

Hence, the equations of motion associated with the action (3.46) can be summarized as follows:

$$G_{\mu\nu} \pm R \phi_\mu \phi_\nu = 0, \quad X \pm 1 = 0, \quad \lambda = \pm \frac{1}{16\pi} R. \quad (3.55)$$

²which allows recovering eq. (3.45) for the (+) choice in the action (3.46).

2.1.2 Extended mimetic gravity

In [81], mimetic gravity was extended thanks to the presence of a gauge symmetry generalizing the original conformal symmetry. The mimetic action (3.46) can then be generalized to the form

$$S[g_{\mu\nu}, \phi, \lambda] \equiv \int d^4x \sqrt{-g} \left[\frac{f(\phi)}{32\pi} R + L_\phi(\phi, \chi_1, \dots, \chi_p) + \lambda(X \pm 1) \right], \quad (3.56)$$

where f is an arbitrary function of ϕ , L_ϕ depends on ϕ and χ_n which are variables constructed with second derivatives of the scalar field according to

$$\chi_n \equiv \text{Tr}([\phi]^n) \equiv \sum_{\mu_1, \dots, \mu_n} \phi_{\mu_1}^{\mu_2} \phi_{\mu_2}^{\mu_3} \cdots \phi_{\mu_{n-1}}^{\mu_n} \phi_{\mu_n}^{\mu_1}. \quad (3.57)$$

Here, we have used the notation $[\phi]$ for the matrix whose coefficients are $[\phi]_{\mu\nu} \equiv \phi_{\mu\nu}$. Indices are lowered and raised by the metric and its inverse. One can show that this extended action defines the most general mimetic gravity like theory [81, 106] which propagates at most three degrees of freedom (one scalar conformal mode in addition to the usual two tensorial modes). Due to the mimetic condition $X \pm 1 = 0$, any X dependency in f or L_ϕ can be removed. More precisely, as it was shown in [81], if one starts with an action (3.56) where f and L_ϕ depend also on X (and eventually its derivatives $\partial_\mu X$), the associated equations of motion are equivalent to the equations of motion obtained from the same action where f and L_ϕ are evaluated to $X = \mp 1$ (and eventually $\partial_\mu X = 0$).

The Euler-Lagrange equations for (3.56) can be easily obtained in full generality. But, for simplicity, we assume that f is a constant (and thus independent of ϕ) which can be fixed to $f = 1$. Deriving the action with respect to ϕ and $g_{\mu\nu}$ respectively leads to the equations

$$\frac{\partial L_\phi}{\partial \phi} - 2\nabla^\mu (\lambda \phi_\mu) + \sum_{n=1}^p n \nabla^{\mu\nu} \left([\phi]_{\mu\nu}^{n-1} \frac{\partial L_\phi}{\partial \chi_n} \right) = 0 \quad \text{and} \quad G_{\mu\nu} = 8\pi T_{\mu\nu}, \quad (3.58)$$

where $[\phi]^n$ is the power n of the matrix $[\phi]$ with the convention $[\phi]_{\mu\nu}^0 \equiv g_{\mu\nu}$, and now the energy-momentum tensor reads

$$T_{\mu\nu} = -2\lambda \phi_\mu \phi_\nu + \lambda(X \pm 1)g_{\mu\nu} + T_{\mu\nu}^{(\phi)}, \quad (3.59)$$

with

$$T_{\mu\nu}^{(\phi)} \equiv L_\phi g_{\mu\nu} + \sum_{n=1}^p n \left\{ -2 \frac{\partial L_\phi}{\partial \chi_n} [\phi]_{\mu\nu}^n + \nabla^\alpha \left[\frac{\partial L_\phi}{\partial \chi_n} \left([\phi]_{\alpha\mu}^{n-1} \phi_\nu + [\phi]_{\alpha\nu}^{n-1} \phi_\mu - [\phi]_{\mu\nu}^{n-1} \phi_\alpha \right) \right] \right\}. \quad (3.60)$$

To get rid of λ in the Einstein equations, we proceed as in the previous case. First, we take the trace of the second equation in (3.58) to express λ in terms of ϕ and $g_{\mu\nu}$

$$\lambda = \mp \frac{1}{2} \left(\frac{R}{8\pi} + T^{(\phi)} \right), \quad T^{(\phi)} = 4L_\phi - \sum_{n=1}^p n \left\{ 2 \frac{\partial L_\phi}{\partial \chi_n} \chi_n + \nabla^\alpha \left[\phi_\alpha \frac{\partial L_\phi}{\partial \chi_n} \chi_{n-1} \right] \right\}. \quad (3.61)$$

Then we substitute this expression in eqs. (3.58). Furthermore, the equation for the scalar field can be obtained from the conservation of the energy-momentum tensor, and thus is not independent from Einstein equations.

Hence, as the trace of Einstein equations is trivially satisfied (the trace has been used to determine λ), the equations of motion are equivalent to the mimetic condition and (the traceless part of) Einstein equations only:

$$X \pm 1 = 0, \quad G_{\mu\nu} = \pm \left(R + 8\pi T^{(\phi)} \right) \phi_\mu \phi_\nu + 8\pi T_{\mu\nu}^{(\phi)}. \quad (3.62)$$

Solutions to these equations have been studied in the context of cosmology [36] and black holes [35] with a particular choice for L_ϕ which makes the solutions non-singular. Here, we focus on black hole solutions and we are going to see how one can choose L_ϕ to resolve the black hole singularity.

2.2 General construction of static spherically symmetric spacetimes in mimetic gravity

We will now develop a general procedure to construct static spherically symmetric spacetimes in mimetic gravity, in the hope of being able to describe later on non-singular black holes with this formalism. Let us then consider a spherically symmetric spacetime whose metric in Schwarzschild coordinates is given by

$$ds^2 = -F_1(r) dt^2 + F_2(r) dr^2 + r^2(d\theta^2 + \sin^2\theta d\varphi^2), \quad (3.63)$$

in terms of the two functions F_1 and F_2 which depend on the radial coordinate r only.

Now, we ask the question whether one can find a theory of extended mimetic gravity of the form (3.56) which admits (3.63) as a solution. This is possible if there exists a function $f(\phi)$ and a scalar-field Lagrangian $L_\phi(\phi, \chi_1, \dots, \chi_p)$ such that the equations (3.62) are satisfied.

2.2.1 Solving the mimetic condition

The mimetic condition $X \pm 1 = 0$ fixed ϕ in terms of the geometry (3.63). If we consider solutions where the scalar field is also static, i.e. $\phi(r)$ is a function of r only, then

$$\left(\frac{d\phi}{dr} \right)^2 = \mp F_2(r). \quad (3.64)$$

It then appears that static scalar field solutions are only possible in regions of spacetime where $\pm F_2(r) \leq 0$. When the metric (3.63) describes a geometry with an event horizon, then $F_2(r)$ changes sign. This is obviously the case for the Schwarzschild spacetime where $F_2(r) > 0$ outside the black hole and $F_2(r) < 0$ inside the black hole (or equivalently behind the horizon from the point of view of an observer at infinity for instance). In that case, one would work with the + sign Lagrangian to be able to describe the region inside the black hole with a static scalar field. In general, as we are interested in resolving singularities inside black holes, we will consider only + sign Lagrangians from now on. Hence, we focus on regions where $F_2(r) \leq 0$ and $F_1(r) \leq 0$ as well, and then we will use the notations $F_1 = -A^2$ and $F_2 = -B^2$. Without loss of generality, we choose the positive solution for ϕ_r :

$$\phi_r(r) = \sqrt{|F_2(r)|} \equiv B(r). \quad (3.65)$$

2.2.2 Solving the modified Einstein equations

Concerning the traceless Einstein equations (3.62), they are viewed as equations where the unknown is the Lagrangian (more precisely the functions f and L_ϕ). For static spherically symmetric spacetime with a static scalar field, Einstein's equations have three independent components G_t^t , G_r^r and $G_\theta^\theta = G_\phi^\phi$. But in our case the trace of Einstein's equations is already automatically satisfied, which leaves us only two non-trivial independent equations,

$$G_{rr} - B^2 R = 8\pi B^2 T_{rr}^{(\phi)} + 8\pi T_{tt}^{(\phi)}, \quad G_{tt} = 8\pi T_{tt}^{(\phi)}, \quad (3.66)$$

where the l.h.s. of each equation is fixed by the choice of the geometry. Thus, this defines a system of partial differential equations for $f(\phi)$ and $L(\phi, \chi_1, \dots, \chi_p)$ whose derivatives appear in the components of the energy-momentum tensor only, in the r.h.s. of each equations. In fact, one can find solutions when $f(\phi) = 1$ and L_ϕ does not depend on ϕ , what we are going to assume from now on. As there are only two equations (3.66) to satisfy, it is a priori sufficient to look for Lagrangians L_ϕ which depend only on two arguments. Thus, for simplicity, we assume that L_ϕ depends on the first two arguments χ_1 and χ_2 only. In that case, the expression of the energy-momentum tensor (3.60) simplifies and is given by

$$\begin{aligned} T_{\mu\nu}^\phi &= \left[L_\phi - \square\phi \frac{\partial L_\phi}{\partial \chi_1} - \phi^\alpha \nabla_\alpha \left(\frac{\partial L_\phi}{\partial \chi_1} \right) \right] g_{\mu\nu} + \phi_\mu \nabla_\nu \left(\frac{\partial L_\phi}{\partial \chi_1} \right) + \phi_\nu \nabla_\mu \left(\frac{\partial L_\phi}{\partial \chi_1} \right) \\ &+ 2 \left[\phi_\mu \square\phi_\nu + \phi_\nu \square\phi_\mu - \phi^\alpha \nabla_\alpha \phi_{\mu\nu} - \phi_{\mu\nu} \square\phi \right] \frac{\partial L_\phi}{\partial \chi_2} + 2 \left[\phi_\mu \phi_{\alpha\nu} + \phi_\nu \phi_{\alpha\mu} - \phi_\alpha \phi_{\mu\nu} \right] \nabla^\alpha \left(\frac{\partial L_\phi}{\partial \chi_2} \right). \end{aligned} \quad (3.67)$$

To compute the non-vanishing components T_{rr}^ϕ and T_{tt}^ϕ of the tensor, we need to compute first the components of $\phi_{\mu\nu}$. It is easy to show that the only non-vanishing components of $\phi_{\mu\nu}$ are

$$\phi_{tt} = -\frac{\phi_r}{2F_2} \frac{dF_1}{dr} = -\frac{AA'}{B}, \quad \phi_{\theta\theta} = \frac{\phi_{\phi\phi}}{\sin^2\theta} = \frac{r\phi_r}{F_2} = -\frac{r}{B}, \quad (3.68)$$

where prime denotes derivative with respect to r . Notice that one can interpret the fact that $\phi_{rr} = 0$ from the mimetic condition $X + 1 = 0$ which implies that $\phi^\mu \phi_{\mu\nu} = 0$, thus $\phi^r \phi_{rr} = 0$ and finally $\phi_{rr} = 0$ as $\phi_r \neq 0$. We also need to compute third derivatives of the scalar field $\nabla_\alpha \phi_{\mu\nu}$ which appear in the expression of the energy-momentum tensor, namely $\square\phi_r$, $\nabla_\alpha \phi_{tt}$ and $\nabla_\alpha \phi_{rr}$. One shows that $\nabla_\alpha \phi_{rr} = 0$ for any α . Furthermore, $\square\phi_r$ and the non-trivial component of $\nabla_\alpha \phi_{tt}$ are

$$\square\phi_r = \nabla^\alpha \phi_{\alpha r} = \frac{1}{B} \left[\left(\frac{A'}{A} \right)^2 + \frac{2}{r^2} \right], \quad \nabla_r \phi_{tt} = \frac{(A')^2}{B} - \frac{AA''}{B} + \frac{AA'B'}{B^2}. \quad (3.69)$$

Now, we have all the ingredients to compute the components of the energy-momentum tensor, and an immediate calculation leads to

$$\begin{aligned} T_{rr}^\phi &= -B^2 L_\phi - B \left(\frac{2}{r} + \frac{A'}{A} \right) \frac{\partial L_\phi}{\partial \chi_1} + 4 \left[\frac{2}{r^2} + \left(\frac{A'}{A} \right)^2 \right] \frac{\partial L_\phi}{\partial \chi_2} + B \frac{d}{dr} \left(\frac{\partial L_\phi}{\partial \chi_1} \right) \\ T_{tt}^\phi &= A^2 L_\phi + \frac{A}{B} \left(A' + \frac{2A}{r} \right) \frac{\partial L_\phi}{\partial \chi_1} + \frac{2A}{B^2} \left(\frac{A'B'}{B} - \frac{2A'}{r} - A'' \right) \frac{\partial L_\phi}{\partial \chi_2} + \frac{A^2}{B} \frac{d}{dr} \left(\frac{\partial L_\phi}{\partial \chi_1} \right) - \frac{2AA'}{B^2} \frac{d}{dr} \left(\frac{\partial L_\phi}{\partial \chi_2} \right). \end{aligned} \quad (3.70)$$

From these expressions, it is straightforward to deduce its trace which is given by

$$T^\phi = 4L_\phi + \frac{4}{B} \left(\frac{2}{r} + \frac{A'}{A} \right) \frac{\partial L_\phi}{\partial \chi_1} + \frac{2}{B} \frac{d}{dr} \left(\frac{\partial L_\phi}{\partial \chi_1} \right) - \frac{2}{B^2} \left(\frac{2}{r} + \frac{A'}{A} \right) \frac{d}{dr} \left(\frac{\partial L_\phi}{\partial \chi_2} \right) + \frac{2}{B^2} \left(\frac{2B'}{rB} + \frac{A'B'}{AB} - \frac{6}{r^2} - \frac{2(A')^2}{A^2} - \frac{A''}{A} - \frac{4A'}{rA} \right) \frac{\partial L_\phi}{\partial \chi_2}. \quad (3.71)$$

2.3 Application to non-singular black holes

Let us now focus, at last, on non-singular black holes. We will first review the limiting curvature mechanism introduced by Chamseddine and Mukhanov, which produces a non-singular black hole from an ansatz on the energy-momentum tensor. We will then follow a complementary approach, in order to find the energy-momentum tensor associated with a given non-singular black hole geometry.

2.3.1 A non-singular black hole from limiting curvature mechanism

The non-singular black hole introduced by Chamseddine and Mukhanov in [35] is a “static” spherically symmetric solution of the general mimetic action (3.56) where L_ϕ is a function of χ_1 only defined by

$$L_\phi(\chi_1) = \frac{2}{3} \rho_m f(x), \quad x = \frac{\chi_1}{\sqrt{\rho_m}}, \quad f(x) \equiv 1 + \frac{1}{2} x^2 - \sqrt{1 - x^2} - x \arcsin x, \quad (3.72)$$

where ρ_m defines a new energy scale in the theory. This expression of L_ϕ seems to be an ad hoc choice a priori, but it leads to very appealing non-singular cosmological and black-hole solutions. Notice that, in the cosmological sector, the equation of motion of the scale factor reproduces exactly the effective dynamics of LQC as it was pointed out in [20, 83].

Let us now consider a spherically symmetric spacetime only, and let us explain physically why (3.72) produces non-singular black hole solutions. For that purpose, we start writing the metric in Schwarzschild coordinates

$$ds^2 = -F(r)dt^2 + \frac{1}{F(r)}dr^2 + r^2(d\theta^2 + \sin^2\theta d\varphi^2), \quad (3.73)$$

where F is a function of r only. In usual general relativity (with no modifications), Einstein equations lead to the Schwarzschild solution where $F(r) = 1 - 2M_0/r$, M_0 being the mass of the black hole. Computing the expansion of outgoing null geodesics in the advanced Eddington-Finkelstein coordinates, non-singular when $F(r) = 0$, one obtains $\theta_+ = F(r)/r$ (see App. A.3.2). There exists thus a future trapping horizon at $r = 2M_0$, which is an event horizon due to the staticity of the metric. One can therefore distinguish between the outside ($F > 0$ or $r > 2M_0$, thus $\theta_+ > 0$) and the inside of the black hole which is gravitationally trapped ($F < 0$ or $r < 2M_0$, thus $\theta_+ < 0$). The singularity occurs inside the black hole where the curvature becomes arbitrary large (in the limit $r \rightarrow 0$).

It was shown in the original paper [35] that the action (3.56) with the field Lagrangian (3.72) reproduces correctly the Schwarzschild metric far from the high curvature regions (compared with the scale ρ_m). In particular, spherically symmetric solution (3.73) possesses an event horizon, very similar to the Schwarzschild horizon. Thus one can still define a region inside (or behind) the horizon ($F < 0$) and a region outside the horizon ($F > 0$).

Concerning the scalar field, let us start assuming that it depends on r and T for purposes of generality. We will shortly reduce ourselves to the case of a static scalar field $\phi(r)$. The scalar field satisfies the mimetic condition which reads

$$-\frac{1}{F(r)}\left(\frac{\partial\phi}{\partial t}\right)^2 + F(r)\left(\frac{\partial\phi}{\partial r}\right)^2 \pm 1 = 0. \quad (3.74)$$

This equation allows to resolve the scalar field ϕ in terms of the geometry $F(r)$. A simple class of solutions of this partial differential equation can be obtained from the ansatz

$$\phi(r, t) = qt + \psi(r), \quad (3.75)$$

where q is a constant and ψ satisfies

$$\left(\frac{d\psi}{dr}\right)^2 = \frac{q^2 \mp F}{F^2}. \quad (3.76)$$

It is clear that the equation (3.76) admits a solution only if the condition $q^2 \mp F \geq 0$ is fulfilled. As a result, in the static case (where $q = 0$), one cannot find any global spherically symmetric solution for the spacetime. Indeed, the condition $\pm F \leq 0$ implies that only the action with a + (resp. -) sign could lead to a description of the region inside (resp. outside) the black hole. Only a non-static solution for the scalar field ($q \neq 0$) could enable us to describe a fully static spherically symmetric spacetime. However, we will proceed as in [35]: we will restrict ourselves to the region inside the black hole (we expect the limiting curvature hypothesis to affect mainly the regions inside the black hole), we choose a mimetic action with a + sign, and we will argue how this is enough to resolve indeed the singularity. From a phenomenological point of view, we could interpret the action (3.56) with (3.72) as an effective description of general relativity in a region (inside the black hole) where the curvature becomes high (with respect to the scale ρ_m). Such a modification could result from quantum gravity effects for instance [83].

When the scalar field is static, the mimetic condition reduces to a simple differential equation

$$\left(\frac{d\phi}{dr}\right)^2 = -\frac{1}{F}, \quad (3.77)$$

in the region (behind the horizon) where $F \leq 0$ (with appropriate boundary conditions). The form of L_ϕ (the presence of $\arcsin(r)$ or $\sqrt{1-x^2}$ with $x = \chi_1/\sqrt{\rho_m}$ for instance) imposes that the scalar field ϕ must satisfy the condition

$$|\chi_1| \leq \sqrt{\rho_m} \implies \left|\frac{d}{dr}\left(r^2\sqrt{-F}\right)\right| \leq \sqrt{\rho_m} r^2. \quad (3.78)$$

If one naively substitutes the Schwarzschild solution in this inequality, one gets the condition that

$$\rho \equiv \frac{M_0}{r^3} \leq \frac{2}{9} \rho_m, \quad (3.79)$$

which can be interpreted as the fact that the density inside the black hole is bounded from above. Hence, one would expect the singularity to be resolved. This has been shown to be indeed the case in [35] from a resolution of the equations of motion.

2.3.2 Recovering known static non-singular black holes

We can now proceed in reverse, and try to find the energy-momentum tensor from mimetic gravity associated with a metric of the form:

$$ds^2 = -F(r)dt^2 + \frac{1}{F(r)}dr^2 + r^2(d\theta^2 + \sin^2\theta d\varphi^2), \quad (3.80)$$

This form of the metric encompasses both the Hayward and Bardeen metrics, which are recovered for

$$F(r) = H(r) \equiv 1 - \frac{2M_0 r^2}{r^3 + 2b^2 M_0} \quad (3.81)$$

or

$$F(r) = B(r) \equiv 1 - \frac{2M_0 r^2}{(r^2 + g^2)^{\frac{3}{2}}}, \quad (3.82)$$

where m_0 , b and g are three positive constants (see Sec. 1).

Following the results of Sec. 2.2.1, we solve the mimetic condition inside the black hole by choosing

$$\phi_r(r) = \sqrt{-F(r)} \quad (3.83)$$

The components of the energy-momentum tensor we are interested in, as well as the trace, can then be computed using the results of Sec. 2.2.2:

$$\begin{aligned} T_{rr}^\phi &= \frac{1}{2r^2 F^2} \left[2 \frac{\partial L_\phi}{\partial \chi_2} r^2 \left(\frac{\partial F}{\partial r} \right)^2 + 2 L_\phi r^2 F + 16 \frac{\partial L_\phi}{\partial \chi_2} F^2 \right. \\ &\quad \left. + \left(\frac{\partial L_\phi}{\partial \chi_1} r^2 \frac{\partial F}{\partial r} - 2 \left(\frac{d}{dr} \frac{\partial L_\phi}{\partial \chi_1} r^2 - 2 \frac{\partial L_\phi}{\partial \chi_1} r \right) F \right) \sqrt{-F} \right] \\ T_{tt}^\phi &= -\frac{1}{2r} \left[2 \frac{\partial L_\phi}{\partial \chi_2} r F \frac{\partial^2 F}{\partial r^2} + 2 L_\phi r F + 2 \left(\frac{d}{dr} \frac{\partial L_\phi}{\partial \chi_2} r + 2 \frac{\partial L_\phi}{\partial \chi_2} \right) F \frac{\partial F}{\partial r} \right. \\ &\quad \left. + \left(\frac{\partial L_\phi}{\partial \chi_1} r \frac{\partial F}{\partial r} + 2 \left(\frac{d}{dr} \frac{\partial L_\phi}{\partial \chi_1} r + 2 \frac{\partial L_\phi}{\partial \chi_1} \right) F \right) \sqrt{-F} \right] \\ T^\phi &= \frac{1}{r^2 F} \left[\frac{\partial L_\phi}{\partial \chi_2} r^2 \left(\frac{\partial F}{\partial r} \right)^2 + \frac{\partial L_\phi}{\partial \chi_2} r^2 F \frac{\partial^2 F}{\partial r^2} + 4 L_\phi r^2 F + 4 \left(\frac{d}{dr} \frac{\partial L_\phi}{\partial \chi_2} r + 3 \frac{\partial L_\phi}{\partial \chi_2} \right) F^2 \right. \\ &\quad \left. + \left(\frac{d}{dr} \frac{\partial L_\phi}{\partial \chi_2} r^2 + 6 \frac{\partial L_\phi}{\partial \chi_2} r \right) F \frac{\partial F}{\partial r} + 2 \left(\frac{\partial L_\phi}{\partial \chi_1} r^2 \frac{\partial F}{\partial r} + \left(\frac{d}{dr} \frac{\partial L_\phi}{\partial \chi_1} r^2 + 4 \frac{\partial L_\phi}{\partial \chi_1} r \right) F \right) \sqrt{-F} \right] \end{aligned}$$

The Einstein tensor and Ricci scalar read:

$$G_{tt} = -\frac{rF\frac{\partial F}{\partial r} + F^2 - F}{r^2}, \quad (3.84)$$

$$G_{rr} = \frac{r\frac{\partial F}{\partial r} + F - 1}{r^2 F}, \quad (3.85)$$

$$R = -\frac{r^2\frac{\partial^2 F}{\partial r^2} + 4r\frac{\partial F}{\partial r} + 2F - 2}{r^2}. \quad (3.86)$$

The traceless Einstein's equations then become:

$$\begin{aligned} rF\frac{\partial F}{\partial r} + F^2 - F = 4\pi r \left[2\frac{\partial L_\phi}{\partial \chi_2} rF\frac{\partial^2 F}{\partial r^2} + 2L_\phi rF + 2\left(\frac{d}{dr}\frac{\partial L_\phi}{\partial \chi_2} r + 2\frac{\partial L_\phi}{\partial \chi_2}\right)F\frac{\partial F}{\partial r} \right. \\ \left. + \left(\frac{\partial L_\phi}{\partial \chi_1} r\frac{\partial F}{\partial r} + 2\left(\frac{d}{dr}\frac{\partial L_\phi}{\partial \chi_1} r + 2\frac{\partial L_\phi}{\partial \chi_1}\right)F\right)\sqrt{-F} \right], \end{aligned} \quad (3.87)$$

and

$$\begin{aligned} r^2\frac{\partial^2 F}{\partial r^2} + 3r\frac{\partial F}{\partial r} + F - 1 = \frac{4\pi}{F} \left[2\frac{\partial L_\phi}{\partial \chi_2} r^2 F\frac{\partial^2 F}{\partial r^2} + 6L_\phi r^2 F + 8\left(\frac{d}{dr}\frac{\partial L_\phi}{\partial \chi_2} r + \frac{\partial L_\phi}{\partial \chi_2}\right)F^2 \right. \\ \left. + 2\left(\frac{d}{dr}\frac{\partial L_\phi}{\partial \chi_2} r^2 + 6\frac{\partial L_\phi}{\partial \chi_2} r\right)F\frac{\partial F}{\partial r} \right. \\ \left. + 3\left(\frac{\partial L_\phi}{\partial \chi_1} r^2\frac{\partial F}{\partial r} + 2\left(\frac{d}{dr}\frac{\partial L_\phi}{\partial \chi_1} r^2 + 2\frac{\partial L_\phi}{\partial \chi_1} r\right)F\right)\sqrt{-F} \right] \end{aligned} \quad (3.88)$$

Unfortunately, we did not manage to find an explicit solution L_ϕ of the eqs. (3.87)-(3.88). However, the existence of two variables for L_ϕ , χ_1 and χ_2 , ensures that a solution must exist in principle and can be found numerically.

3 Loop quantum deformation of Schwarzschild's black hole

Let us now introduce another way of modifying gravity in order to recover known static non-singular black holes, following the paper [18] that I contributed to with K. Noui, J. Ben Achour and H. Liu. We considered before a gravity theory coupled to a scalar field, we will now describe General Relativity as a Hamiltonian theory with constraints and directly implement quantum corrections on these constraints. The natural way of dealing with these constraints is to use Ashtekar variables, hence following the spirit of loop quantum gravity.

3.1 Introduction to canonical gravity

A proper introduction to canonical gravity in terms of Ashtekar's variables would require a full chapter of this dissertation. Such a treatment lies way beyond the scope of this Section, which aims at sketching the main ideas of the canonical formulation of General Relativity in which Einstein's equations are written in terms of constraints satisfying a closed algebra. This formulation, in terms of Ashtekar's variables reduced to spherically symmetric spacetimes, will be particularly well suited to implement quantum corrections on the constraint algebra. More details can be found in [58, 82, 101, 108].

3.1.1 3 + 1 decomposition of Einstein-Hilbert action

So far, we have been dealing with a covariant approach to General Relativity, in which time and space are described on an equal footing. This will not be the case anymore in the Hamiltonian formulation of General Relativity. For the latter, configuration variables $\varphi(x)$ as well as their canonical conjugate momenta $\pi_\varphi(x)$ will be defined on a spacelike surface Σ_t at a given time t . Hamilton's equations will describe the evolution of these fields as time evolves, the topology of the considered manifold will thus be restricted to $\mathbb{R} \times \Sigma$.

Let us consider a manifold equipped with metric \mathbf{g} , whose induced metric γ on Σ is such that

$$\gamma_{ij} = g_{ij} + n_i n_j , \quad (3.89)$$

where \mathbf{n} is a unit normal vector to Σ and the latin indices are spatial indices ranging from 1 to 3.

The first step of the 3 + 1 decomposition consists in writing the time vector ∂_t , along which the spacelike hypersurface Σ evolves, as a sum of components normal and tangential to Σ :

$$\partial_t = N \mathbf{n} + \mathbf{N} , \quad (3.90)$$

where we have introduced the lapse function N and the shift vector \mathbf{N} . The components of the

metric \mathbf{g} can be expressed in terms of N , \mathbf{N} and the components of the induced metric $\boldsymbol{\gamma}$ on Σ :

$$g_{00} = \mathbf{g}(\partial_t, \partial_t) = \partial_t \cdot \partial_t = -N^2 + \mathbf{N} \cdot \mathbf{N} + 2N\mathbf{n} \cdot \mathbf{N} = -N^2 + N_i N^i \quad (3.91)$$

$$g_{0i} = \mathbf{g}(\partial_t, \partial_i) = \partial_t \cdot \partial_i = (N\mathbf{n} + \mathbf{N}) \cdot \partial_i = \partial_i \cdot \mathbf{N} = N_i \quad (3.92)$$

$$g_{ij} = \gamma_{ij} \quad (3.93)$$

Hence, one can write

$$\begin{aligned} ds^2 &= g_{\mu\nu} dx^\mu dx^\nu \\ &= \left(-N^2 + N_i N^i \right) dt^2 + 2N_i dt dx^i + \gamma_{ij} dx^i dx^j \\ &= -N^2 dt^2 + \gamma_{ij} \left(dx^i + N^i dt \right) \left(dx^j + N^j dt \right) \end{aligned} \quad (3.94)$$

We now wish to write the Einstein-Hilbert action (1.58) of Chap. 1 in terms of this 3 + 1 decomposition. Recall that the action reads

$$S_{EH} = \frac{1}{16\pi} \int d^4x \sqrt{-g} R. \quad (3.95)$$

One can first write $\sqrt{-g} d^4x$ as follows:

$$\sqrt{-g} d^4x = \sqrt{\gamma} N d^3x dt. \quad (3.96)$$

And the four-dimensional Ricci scalar R evaluated on Σ can be written, thanks to Gauss-Codazzi equations (see [62, 96] for details),

$$R = {}^3R + K^{ij} K_{ij} - K^2 - 2\nabla_\alpha \left(n^\beta \nabla_\beta n^\alpha - n^\alpha \nabla_\beta n^\beta \right). \quad (3.97)$$

3R is the three-dimensional Ricci scalar computed with the induced metric $\boldsymbol{\gamma}$, while \mathbf{K} is the (three-dimensional) extrinsic curvature tensor, characterizing the curvature of Σ embedded in \mathcal{M} :

$$K_{ab} = \frac{1}{2} \mathcal{L}_{\mathbf{n}} \gamma_{ab}. \quad (3.98)$$

In particular, one has

$$K^2 = \gamma_{ij} \gamma_{kl} K^{ij} K^{kl}. \quad (3.99)$$

It can then be shown (see [62] for details) that the Einstein-Hilbert can eventually be written

$$S_{EH} = \int_{t_1}^{t_2} dt \int_{\Sigma_t} dx^3 N \sqrt{\gamma} \left({}^3R + K^{ij} K_{ij} - K^2 \right) \quad (3.100)$$

3.1.2 Hamiltonian formulation of General Relativity

We now have all the ingredients to introduce the Hamiltonian formulation of General Relativity, also called ADM formulation due to the pioneering work of R. Arnowitt, S. Deser and C. Misner in the 50's [4]. Notice that S_{EH} now depends not explicitly on the metric \mathbf{g} and its first and second derivatives but on the new configuration variables of the ADM phase space $q = (\gamma_{ij}, N, N^i)$ and

their time derivatives \dot{q} .

The Lagrangian density of the gravitational field reads, from eq. (3.100):

$$\mathcal{L}(q, \dot{q}) = N \sqrt{\gamma} \left({}^3R + K^{ij} K_{ij} - K^2 \right) = N \sqrt{\gamma} \left({}^3R + \left(\gamma^{ik} \gamma^{jl} - \gamma^{ij} \gamma^{kl} \right) K_{ij} K_{kl} \right). \quad (3.101)$$

Since K_{ij} can be written as

$$K_{ij} = \frac{1}{2N} \left(\gamma_{ik} \nabla_j N^k + \gamma_{jk} \nabla_i N^k - \dot{\gamma}_{ij} \right) \quad (3.102)$$

it appears that $\mathcal{L}(q, \dot{q})$ depends neither on the time derivative of N nor on the one of \mathbf{N} . Hence, the lapse function and the shift vector are not dynamical variables but Lagrange multipliers, which will enforce constraints in the Hamiltonian formulation. The only dynamical variable is thus the metric γ_{ij} . Its canonically conjugate momentum is

$$\pi^{ij} \equiv \frac{\partial \mathcal{L}}{\partial \dot{\gamma}_{ij}} = \sqrt{\gamma} \left(K \gamma^{ij} - K^{ij} \right) \quad (3.103)$$

The Hamiltonian density then reads

$$\mathcal{H} = \pi^{ij} \dot{\gamma}_{ij} - \mathcal{L} \quad (3.104)$$

Using eqs. (3.101), (3.102) and (3.103), the Hamiltonian can then be written

$$H = \int_{\Sigma_t} d^3x \sqrt{\gamma} \left(N C + N^i C_i \right), \quad (3.105)$$

where

$$C = -{}^3R - K^2 + K_{ij} K^{ij} \quad (3.106)$$

$$C_i = 2 \left(\nabla_j K^j_i - \nabla_i K \right) \quad (3.107)$$

The Hamilton equations with respect to the configuration variables N and N^i are

$$C = 0 \quad (3.108)$$

$$C_i = 0 \quad (3.109)$$

Eq. (3.108) is called the Hamiltonian constraint, while eq. (3.109) is the vectorial (or spatial diffeomorphism) constraint. These four equations impose four constraints on the curvature of Σ , which are analogous to the freedom of choosing the four coordinates x^μ in the explicitly covariant version of General Relativity. Eqs. (3.108) and (3.109) imply that the Hamiltonian must vanish on shell.

The other Hamiltonian equations are the ones concerned with the dynamical variables of the theory:

$$\frac{\delta H}{\delta \pi^{ij}} = \dot{\gamma}_{ij} \quad (3.110)$$

$$\frac{\delta H}{\delta \gamma_{ij}} = -\dot{\pi}^{ij} \quad (3.111)$$

These two equations are associated with six degrees of freedom (the six independent components of the symmetric tensor γ). Taking into account the Hamiltonian and vectorial constraints, this leads to $6 - 4 = 2$ degrees of freedom for the theory, which was expected.

Another way to recover the Hamilton equations consists in using the Poisson brackets, which give the temporal evolution of a quantity F as follows:

$$\dot{F} = \{F, H\} = \{F, C(N) + C(\mathbf{N})\} , \quad (3.112)$$

where $C[N]$ and $C[\mathbf{N}]$ are the *smeared* (i.e., integrated) Hamiltonian and vectorial constraints:

$$C(N) = \int_{\Sigma_t} d^3x \sqrt{\gamma} N C \quad (3.113)$$

$$C(\mathbf{N}) = \int_{\Sigma_t} d^3x \sqrt{\gamma} N^i C_i . \quad (3.114)$$

The Poisson brackets are defined by

$$\{\pi^{ij}(x), \gamma_{kl}(x')\} = \delta_{(k}^i \delta_{l)}^j \delta(x - x') . \quad (3.115)$$

The smeared constraints appear to satisfy a fundamental property, namely a closed algebra, also called Dirac algebra:

$$\{C(\mathbf{N}), C(\mathbf{N}')\} = C([\mathbf{N}, \mathbf{N}']) \quad (3.116)$$

$$\{C(\mathbf{N}), C(N')\} = C\left(\frac{\partial N'}{\partial \mathbf{N}}\right) \quad (3.117)$$

$$\{C(N), C(N')\} = C\left(\frac{1}{\gamma} \left(N \partial^i N' - N' \partial^i N\right)\right) \quad (3.118)$$

This algebra is said to be closed because every Poisson bracket between two smeared constraints produces another smeared constraint. Since the Hamiltonian is nothing but a sum of the Hamiltonian and vectorial constraints, it means that its Poisson bracket with another constraint will produce nothing more than one of the original constraints. In other words, the time evolution of a constraint

$$\dot{C}(N) = \{C(N), H\} \quad (3.119)$$

will not produce any new constraints. The Hamiltonian and vectorial constraints (3.108) and (3.109) are thus called *first class*.

3.1.3 Ashtekar variables in spherical symmetry

Now that we have an explicit Hamiltonian for General Relativity, it is quite tempting to apply a quantization procedure in the hope of obtaining canonical quantum gravity. This procedure consists first in promoting the phase space variables to the rank of operators ($\hat{\gamma}_{ij}$, $\hat{\pi}^{ij}$) on a Hilbert space, and the Poisson brackets to commutators. The constraint H can then be promoted to an operator \hat{H} , and the physical Hilbert space will be the one in which each state ψ satisfies the Wheeler-DeWitt equation

$$\hat{H} \psi = 0 . \quad (3.120)$$

Despite the apparent simplicity of this procedure, it has never been accomplished successfully. The main issue lies in the very complex form of the Hamiltonian constraint and the resulting ambiguities in defining a corresponding operator. Canonical quantum gravity based on the ADM phase space has thus up to now never been constructed.

Ashtekar introduced in 1984 new variables, related to the variables (γ_{ij} , π^{ij}) of the ADM phase space via a canonical transformation, and thus allowing the recovery of Einstein's classical theory. We won't dive into the details of these variables, but simply mention their main advantage. It is merely that, with these new variables, the Hamiltonian constraint simplifies a lot and actually becomes polynomial, which gives hope as regards the possibility of applying the quantization procedure. The introduction of these variables thus paved the way towards a renewal of the canonical approach to quantum gravity, and in particular launched the programme of loop quantum gravity (LQG).

The Ashtekar variables stem from the formulation of General Relativity as a gauge theory. The configuration variables behave like an $SU(2)$ Yang-Mills connection, from which one can reconstruct the extrinsic curvature. Their canonically conjugate momenta are called densitized triads, and are used to reconstruct the spatial metric γ .

Instead of introducing them in full generality, we will concentrate on their formulation for spherically symmetric spacetimes. The work we have been doing to obtain a Hamiltonian formulation of General Relativity will be of great use: we will still be studying General Relativity in Hamiltonian form, but merely with new canonical variables. In the spherically symmetric case, notice first of all that the metric becomes:

$$ds^2 = -N^2 dt^2 + \gamma_{rr} (dr + N^r dt)^2 + \gamma_{\theta\theta} d\Omega^2 . \quad (3.121)$$

In this case, the metric components can be expressed in terms of the Ashtekar variables $E^\varphi(r)$ and $E^r(r)$ (see [22] for details):

$$\gamma_{rr} \equiv \frac{(E^\varphi)^2}{E^r} , \quad \gamma_{\theta\theta} \equiv E^r . \quad (3.122)$$

The other half of Ashtekar variables, canonically conjugate to (E^φ, E^r) , is (K_φ, K_r) . In analogy with eq. (3.115), the variables satisfy

$$\{K_\varphi(x), E^\varphi(y)\} = \delta(x - y), \quad \{K_r(x), E^r(y)\} = 2\delta(x - y), \quad (3.123)$$

where the Poisson bracket is defined as follows:

$$\begin{aligned} \{F(r), g(y)\} = 2 \int dr_1 & \left(\frac{\delta F(r)}{\delta K_r(r_1)} \frac{\delta g(y)}{\delta E^r(r_1)} + \frac{1}{2} \frac{\delta F(r)}{\delta K_\varphi(r_1)} \frac{\delta g(y)}{\delta E^\varphi(r_1)} \right. \\ & \left. - \frac{\delta F(r)}{\delta E^r(r_1)} \frac{\delta g(y)}{\delta K_r(r_1)} - \frac{1}{2} \frac{\delta F(r)}{\delta E^\varphi(r_1)} \frac{\delta g(y)}{\delta K_\varphi(r_1)} \right). \end{aligned} \quad (3.124)$$

As before, the lapse function N and the shift vector \mathbf{N} are Lagrange multipliers which enforce the Hamiltonian and vectorial constraints. These constraints now read

$$H = \frac{E^\varphi}{2\sqrt{E^r}}(1 + K_\varphi^2 - \Gamma_\varphi^2) + \sqrt{E^r}(K_\varphi K_r + \partial_r \Gamma_\varphi), \quad (3.125)$$

$$V = 2E^\varphi \partial_r K_\varphi - K_r \partial_r E^r, \quad (3.126)$$

where $\Gamma_\varphi \equiv -\frac{\partial_r E^r}{2E^\varphi}$. Following the results of the Hamiltonian formulation developed above, we define the smeared constraints $H[N]$ and $V[N^r]$:

$$H[N] = \int dx N \left(\frac{E^\varphi(r)}{2\sqrt{E^r(r)}} (1 + K_\varphi^2(r) - \Gamma_\varphi^2(r)) + \sqrt{E^r(r)} (K_\varphi(r) K_r(r) + \partial_r \Gamma_\varphi(r)) \right), \quad (3.127)$$

$$V[N^r] = \int dx N^r (2E^\varphi(r) \partial_r K_\varphi(r) - K_r(r) \partial_r E^r(r)), \quad (3.128)$$

Pursuing the analogy with the Hamiltonian formulation with variables (γ_{ij}, π^{ij}) , and in particular eq. (3.116), it can be shown that the smeared constraints satisfy a closed Poisson algebra:

$$\{H[N], V[N_1^r]\} = -H[N_1^r N^r], \quad (3.129)$$

$$\{V[N_1^r], V[N_2^r]\} = V[N_1^r (N_2^r)' - N_2^r (N_1^r)'], \quad (3.130)$$

$$\{H[N_1], H[N_2]\} = V[\gamma^{rr} (N_1 N_2' - N_2 N_1')], \quad (3.131)$$

The Einstein equations are obtained as before from the Hamilton equations, describing the time evolution of a function F :

$$\dot{F} = \{F, H[N] + V[N^r]\} \quad (3.132)$$

To summarize, we now have a set of equations, eqs. (3.129)-(3.132), strictly equivalent to General Relativity. However, this formulation will allow us to apply rather straightforwardly quantum corrections to General Relativity, as will be shown in the next section.

3.2 Deforming the constraint algebra

3.2.1 Effective Einstein's equations for a general deformation

Instead of performing the proper quantization of eqs. (3.129)-(3.132) and defining the constraints as operators, we will follow a much simpler approach to investigate non-singular black hole

solutions. This approach consists in applying by hand a deformation of the constraint algebra, which implements quantum corrections to the theory at the classical level. We will then be left with effective Einstein's equations, which should be an approximation of the properly quantized theory up to some energy scale.

The choice of this deformation of the constraint algebra is not entirely up to us, since it must be *anomaly-free*. Put another way, it must be such that the Poisson algebra (3.129)-(3.131) remains closed. A brief argument by Thiemann [108] allows an understanding of this. Imagine that some first-class constraints C_1 , C_2 and C_3 , promoted to operators in quantum canonical gravity, are such that

$$[\hat{C}_1, \hat{C}_2] = i\hbar \hat{C}_3 + \hbar^2 \hat{A}, \quad (3.133)$$

where \hat{A} is not a linear combination of \hat{C}_1 , \hat{C}_2 and \hat{C}_3 , while the classical counterpart of this commutator is

$$\{C_1, C_2\} = C_3. \quad (3.134)$$

Suppose that a simultaneous solution ψ to the three constraints has been found: $\hat{C}_i \psi = 0$ for $i = 1, 2, 3$. Then by eq. (3.133) one must also have $\hat{A} \psi = 0$, which is a new constraint since \hat{A} is not a linear combination of the first-class constraints. Therefore, ψ must obey a quantum condition without any classical counterpart, and the quantum theory thus has less states than the classical one has observables: it can thus not have the correct classical limit. The operator \hat{A} is called an anomaly, and should thus be avoided by all means.

To summarize: the Poisson algebra (3.129)-(3.131) of the classical theory is closed, hence so must be the algebra of commutators in the quantized theory in order to avoid anomalies. Consequently, the deformed constraint algebra we will consider later, supposed to represent an approximation of the quantized theory, also must be closed, and thus anomaly-free.

Let us parametrize the deformation of the Hamiltonian constraint as follows:

$$H = \frac{E^\varphi}{2\sqrt{E^r}} \left[1 + f(K_\varphi) - \Gamma_\varphi^2 \right] + \sqrt{E^r} \left[g(K_\varphi) K_r + \partial_r \Gamma_\varphi \right]. \quad (3.135)$$

As initially derived in [21, 25, 110], one needs to take $g(x) = f'(x)/2$ so that the Poisson algebra remains closed. Indeed, this leads to the following deformed Poisson bracket between the Hamiltonian constraints:

$$\{H[N_1], H[N_2]\} = V \left[\frac{f''(K_\varphi)}{2} \gamma^{rr} (N_1 N_2' - N_2 N_1') \right]. \quad (3.136)$$

Such a deformation is *anomaly-free* since the Poisson algebra remains closed, and *point-wise* due to its local character.

Let us show that we can solve explicitly Einstein's equations for any $F(r)$, before analyzing the associated geometry in the next sections. We will solve Hamilton's evolution equations (3.132) for the phase space variables E^r , E^φ and K_φ , and finally determine K_r via the Hamiltonian constraint (3.135). Let us start with E^r :

$$\begin{aligned}\dot{E}^r &= \{E^r, H[N] + V[N^r]\} \\ &= \{E^r, H[N]\} + \{E^r, V[N^r]\}\end{aligned}\tag{3.137}$$

The first Poisson bracket reads

$$\begin{aligned}\{E^r(r), H[N]\} &= \left\{E^r(r), \int dr_1 N(r_1) \left(\frac{E^\varphi(r_1)}{2\sqrt{E^r(r_1)}} (1 + f(K_\varphi(r_1)) - \Gamma_\varphi^2(r_1)) \right. \right. \\ &\quad \left. \left. + \sqrt{E^r(r_1)} \left(\frac{f'(K_\varphi(r_1))}{2} K_r(r_1) + \partial_{r_1} \Gamma_\varphi(r_1) \right) \right) \right\} \\ &= \left\{E^r(r), \int dr_1 N(r_1) \sqrt{E^r(r_1)} \frac{f'(K_\varphi(r_1))}{2} K_r(r_1) \right\} \\ &= -2 \int dr_2 \frac{\delta E^r(r)}{\delta E^r(r_2)} \frac{\delta}{\delta K_r(r_2)} \left(\int dr_1 N(r_1) \sqrt{E^r(r_1)} \frac{f'(K_\varphi(r_1))}{2} K_r(r_1) \right) \\ &= - \int dr_2 N(r_2) \delta(r - r_2) \sqrt{E^r(r_2)} f'(K_\varphi(r_2)) \\ &= -N(r) \sqrt{E^r(r)} f'(K_\varphi(r))\end{aligned}$$

The other reads

$$\begin{aligned}\{E^r(r), V[N^r]\} &= \left\{E^r(r), \int dr_1 N^r(r_1) (2E^\varphi(r_1) \partial_{r_1} K_\varphi(r_1) - K_r(r_1) \partial_{r_1} E^r(r_1)) \right\} \\ &= - \left\{E^r(r), \int dr_1 N^r(r_1) K_r(r_1) \partial_{r_1} E^r(r_1) \right\} \\ &= 2 \int dr_2 \frac{\delta E^r(r)}{\delta E^r(r_2)} \frac{\delta}{\delta K_r(r_2)} \left(\int dr_1 N^r(r_1) K_r(r_1) \partial_{r_1} E^r(r_1) \right) \\ &= 2 \int dr_2 N^r(r_2) \delta(r - r_2) \partial_{r_2} E^r(r_2) \\ &= 2N^r(r) \partial_r E^r(r)\end{aligned}$$

And finally:

$$\dot{E}^r = -N \sqrt{E^r} f'(K_\varphi) + 2N^r \partial_r E^r\tag{3.138}$$

The equation for E^φ is

$$\begin{aligned}\dot{E}^\varphi &= \{E^\varphi, H[N] + V[N^r]\} \\ &= \{E^\varphi, H[N]\} + \{E^\varphi, V[N^r]\},\end{aligned}\tag{3.139}$$

with

$$\begin{aligned}
 \{E^\varphi(r), H[N]\} &= \left\{ E^\varphi(r), \int dr_1 N(r_1) \left(\frac{E^\varphi(r_1)}{2\sqrt{E^r(r_1)}} (1 + f(K_\varphi(r_1)) - \Gamma_\varphi^2(r_1)) \right. \right. \\
 &\quad \left. \left. + \sqrt{E^r(r_1)} \left(\frac{f'(K_\varphi(r_1))}{2} K_r(r_1) + \partial_{r_1} \Gamma_\varphi(r_1) \right) \right) \right\} \\
 &= \left\{ E^\varphi(r), \int dr_1 \frac{N(r_1)}{2} \left(\frac{E^\varphi(r_1)}{\sqrt{E^r(r_1)}} f(K_\varphi(r_1)) + \sqrt{E^r(r_1)} f'(K_\varphi(r_1)) K_r(r_1) \right) \right\} \\
 &= - \int dr_2 \frac{\delta E^\varphi(r)}{\delta E^\varphi(r_2)} \frac{\delta}{\delta K_\varphi(r_2)} \left(\int dr_1 \frac{N(r_1)}{2} \left(\frac{E^\varphi(r_1)}{\sqrt{E^r(r_1)}} f(K_\varphi(r_1)) + \sqrt{E^r(r_1)} f'(K_\varphi(r_1)) K_r(r_1) \right) \right) \\
 &= - \int dr_2 \delta(x - r_2) \frac{N(r_2)}{2} \left(\frac{E^\varphi(r_2)}{\sqrt{E^r(r_2)}} f'(K_\varphi(r_2)) + \sqrt{E^r(r_2)} f''(K_\varphi(r_2)) K_r(r_2) \right) \\
 &= - \frac{N(r)}{2} \left(\frac{E^\varphi(r)}{\sqrt{E^r(r)}} f'(K_\varphi(r)) + \sqrt{E^r(r)} f''(K_\varphi(r)) K_r(r) \right),
 \end{aligned}$$

and

$$\begin{aligned}
 \{E^\varphi(r), V[N^r]\} &= \left\{ E^\varphi(r), \int dr_1 N^r(r_1) (2E^\varphi(r_1) \partial_{r_1} K_\varphi(r_1) - K_r(r_1) \partial_{r_1} E^r(r_1)) \right\} \\
 &= 2 \left\{ E^\varphi(r), \int dr_1 N^r(r_1) E^\varphi(r_1) \partial_{r_1} K_\varphi(r_1) \right\} \\
 &= -2 \int dr_2 \frac{\delta E^r(r)}{\delta E^r(r_2)} \frac{\delta}{\delta K_r(r_2)} \left(\int dr_1 N^r(r_1) E^\varphi(r_1) \partial_{r_1} K_\varphi(r_1) \right) \\
 &= -2 \int dr_2 \delta(x - r_2) \frac{\delta}{\delta K_r(r_2)} \left(N^r(r_1) E^\varphi(r_1) K_\varphi(r_1) - \int dr_1 \partial_{r_1} (N^r(r_1) E^\varphi(r_1)) K_\varphi(r_1) \right) \\
 &= -2 \int dr_2 \delta(x - r_2) (N^r(r_1) E^\varphi(r_1) \delta(r_2 - r_1) - \partial_{r_2} (N^r(r_2) E^\varphi(r_2))) \\
 &= 2 \partial_r (N^r E^\varphi(r)),
 \end{aligned}$$

where the boundary term proportional to $\delta(r_1 - r_2)$ vanishes after integration over r_2 .

Hence,

$$\dot{E}^\varphi = - \frac{N}{2} \left(\frac{E^\varphi}{\sqrt{E^r}} f'(K_\varphi) + \sqrt{E^r} f''(K_\varphi) K_r \right) + 2 \partial_r (N^r E^\varphi) \quad (3.140)$$

Finally, let us compute

$$\begin{aligned}
 \dot{K}_\varphi &= \{K_\varphi, H[N] + V[N^r]\} \\
 &= \{K_\varphi, H[N]\} + \{K_\varphi, V[N^r]\}.
 \end{aligned} \quad (3.141)$$

First,

$$\begin{aligned}
 \{K_\varphi(r), H[N]\} &= \left\{ K_\varphi(r), \int dr_1 N(r_1) \left(\frac{E^\varphi(r_1)}{2\sqrt{E^r(r_1)}} \left(1 + f(K_\varphi(r_1)) - \Gamma_\varphi^2(r_1) \right) \right. \right. \\
 &\quad \left. \left. + \sqrt{E^r(r_1)} \left(\frac{f'(K_\varphi(r_1))}{2} K_r(r_1) + \partial_{r_1} \Gamma_\varphi(r_1) \right) \right) \right\} \\
 &= \left\{ K_\varphi(r), \int dr_1 N(r_1) \left(\frac{E^\varphi(r_1)}{2\sqrt{E^r(r_1)}} \left(1 + f(K_\varphi(r_1)) - \left(-\frac{\partial_r E^r}{2E^\varphi} \right)^2 \right) + \sqrt{E^r(r_1)} \partial_{r_1} \left(-\frac{\partial_{r_1} E^r}{2E^\varphi} \right) \right) \right\} \\
 &= \int dr_2 \frac{\delta K_\varphi(r)}{\delta K_\varphi(r_2)} \frac{\delta}{\delta E^\varphi(r_2)} \int dr_1 N(r_1) \left[\frac{E^\varphi(r_1)}{2\sqrt{E^r(r_1)}} (1 + f(K_\varphi(r_1))) - \frac{(\partial_{r_1} E^r(r_1))^2}{8\sqrt{E^r(r_1)} E^\varphi(r_1)} \right. \\
 &\quad \left. - \frac{\sqrt{E^r(r_1)}}{2} \left(\frac{\partial_{r_1}^2 E^r(r_1)}{E^\varphi(r_1)} + \partial_{r_1} E^r \partial_{r_1} \left(\frac{1}{E^\varphi(r_1)} \right) \right) \right] \\
 &= \int dr_2 \delta(r - r_2) \frac{\delta}{\delta E^\varphi(r_2)} \left\{ \int dr_1 \left[\frac{N E^\varphi(r_1)}{2\sqrt{E^r(r_1)}} (1 + f(K_\varphi(r_1))) - \frac{N(r_1) (\partial_{r_1} E^r(r_1))^2}{8\sqrt{E^r(r_1)} E^\varphi(r_1)} \right. \right. \\
 &\quad \left. \left. - \frac{N(r_1) \sqrt{E^r(r_1)} \partial_{r_1}^2 E^r(r_1)}{2E^\varphi(r_1)} + \frac{\partial_{r_1} (N(r_1) \sqrt{E^r(r_1)} \partial_{r_1} E^r(r_1))}{2E^\varphi(r_1)} \right] - N(r_1) \frac{\sqrt{E^r(r_1)} \partial_{r_1} E^r(r_1)}{2E^\varphi(r_1)} \right\} \\
 &= \int dr_2 \delta(r - r_2) \left[\frac{N(r_2) (1 + f(K_\varphi(r_2)))}{2\sqrt{E^r(r_2)}} + \frac{N(r_2) (\partial_{r_2} E^r(r_2))^2}{8\sqrt{E^r(r_2)} (E^\varphi(r_2))^2} + \frac{\sqrt{E^r(r_2)}}{2(E^\varphi(r_2))^2} N(r_2) \partial_{r_2}^2 E^r(r_2) \right. \\
 &\quad \left. - \frac{\partial_{r_2} (\sqrt{E^r(r_2)} N(r_2) \partial_{r_2} E^r(r_2))}{2(E^\varphi(r_2))^2} + N(r_2) \frac{\sqrt{E^r(r_2)} \partial_{r_2} E^r(r_2)}{(2E^\varphi(r_2))^2} \delta(r_2 - r_1) \right] \\
 &= \frac{N(r) (1 + f(K_\varphi(r)))}{2\sqrt{E^r(r)}} + \frac{N(r) (\partial_r E^r)^2}{8\sqrt{E^r(r)} (E^\varphi(r))^2} + \frac{\sqrt{E^r(r)}}{2(E^\varphi(r))^2} N(r) \partial_r^2 E^r(r) - \frac{\partial_r (\sqrt{E^r(r)} N(r) \partial_r E^r(r))}{2(E^\varphi(r))^2}.
 \end{aligned}$$

Then,

$$\begin{aligned}
 \{K_\varphi(r), V[N^r]\} &= \left\{ K_\varphi(r), \int dr_1 N^r(r_1) (2E^\varphi(r_1) \partial_{r_1} K_\varphi(r_1) - K_r(r_1) \partial_{r_1} E^r(r_1)) \right\} \\
 &= 2 \left\{ K_\varphi(r), \int dr_1 N^r(r_1) E^\varphi(r_1) \partial_{r_1} K_\varphi(r_1) \right\} \\
 &= 2 \int dr_2 \frac{\delta K_\varphi(r)}{\delta K_\varphi(r_2)} \frac{\delta}{\delta E^\varphi(r_2)} \int dr_1 N^r(r_1) E^\varphi(r_1) \partial_{r_1} K_\varphi(r_1) \\
 &= 2 \int dr_2 \delta(r - r_2) N^r(r_2) \partial_{r_2} K_\varphi(r_2) \\
 &= 2 N^r(r) \partial_r K_\varphi(r).
 \end{aligned}$$

In the end,

$$\dot{K}_\varphi = \frac{N (1 + f(K_\varphi))}{2\sqrt{E^r}} + \frac{N (\partial_r E^r)^2}{2\sqrt{E^r} (E^\varphi)^2} + \frac{\sqrt{E^r}}{2(E^\varphi)^2} N \partial_r^2 E^r - \frac{\partial_r (\sqrt{E^r} N \partial_r E^r)}{2(E^\varphi)^2} + 2 N^r \partial_r K_\varphi \quad (3.142)$$

3.2.2 Solving effective Einstein's equations in the static case

We now aim at describing the interior of a non-singular static black hole. Because r and t exchange roles inside the black hole, we will be considering time-dependent fields only. Einstein's equations (3.138), (3.140) and (3.142) then dramatically simplify:

$$\dot{E}^r = -N\sqrt{E^r} f'(K_\varphi), \quad (3.143)$$

$$\dot{E}^\varphi = -\frac{N}{2} \left[\sqrt{E^r} K_r f''(K_\varphi) + \frac{E^\varphi}{\sqrt{E^r}} f'(K_\varphi) \right], \quad (3.144)$$

$$\dot{K}_\varphi = \frac{N}{2\sqrt{E^r}} [1 + f(K_\varphi)]. \quad (3.145)$$

The Hamiltonian constraint, from which we will deduce K_r , now reads

$$f'(K_\varphi) E^r K_r + [1 + f(K_\varphi)] E^\varphi = 0. \quad (3.146)$$

Let us now solve eqs (3.143)-(3.146) for any function f . A simplification occurs for the gauge fixing choice

$$N(t) f'(K_\varphi) = -2, \quad (3.147)$$

which is nothing but a reparametrization of time. Eq. (3.143) then reads

$$\frac{\dot{E}^r(t)}{\sqrt{E^r(t)}} = 2, \quad (3.148)$$

which yields

$$E^r(t) = (t + a)^2, \quad (3.149)$$

where a is a constant that we fix to $a = 0$, in order to recover Schwarzschild's solution in the classical limit.

Eq. (3.145) then simplifies:

$$\frac{f'(K_\varphi)}{1 + f(K_\varphi)} \dot{K}_\varphi = -\frac{1}{t}, \quad (3.150)$$

or equivalently

$$\partial_t \ln(1 + f(K_\varphi)) = -\frac{1}{t} \quad (3.151)$$

This equation can be immediately integrated:

$$f(K_\varphi) = \frac{r_s}{t} - 1, \quad (3.152)$$

where r_s is an integration constant with the dimension of a length. Combining the Hamiltonian constraint (3.146) and eq. (3.144) finally leads to

$$\frac{\dot{E}^\varphi}{E^\varphi} = \frac{1}{t} \left(1 - \frac{[1 + f(K_\varphi)] f''(K_\varphi)}{[f'(K_\varphi)]^2} \right). \quad (3.153)$$

Using eq. (3.152), this equation yields

$$\partial_t (\ln(E^\varphi)) = \partial_t \left(\ln \frac{r_s f'(K_\varphi)}{1 + f(K_\varphi)} \right) \quad (3.154)$$

This is immediately integrated:

$$E^\varphi = b \frac{f'(K_\varphi)}{1 + f(K_\varphi)}, \quad (3.155)$$

where b is a constant to be fixed later. The remaining variable K_r is given immediately from the Hamiltonian constraint (3.146) together with eqs. (3.149) and (3.155). Hence, we have integrated explicitly and completely the modified Einstein's equations. The metric (3.94) now reads

$$\begin{aligned} ds^2 &= -N^2 dt^2 + \gamma_{rr} (dr + N^r dt)^2 + \gamma_{\theta\theta} d\Omega^2 \\ &= -\frac{4}{f'(K_\varphi)^2} dt^2 + \frac{(E^\varphi)^2}{E^r} dr^2 + E^r d\Omega^2 \\ &= -\frac{4}{f'(K_\varphi)^2} dt^2 + \frac{1}{t^2} \left(\frac{b f'(K_\varphi)}{1 + f(K_\varphi)} \right)^2 dr^2 + t^2 d\Omega^2 \\ &= -\frac{1}{F(t)} dt^2 + \left(\frac{2b}{r_s} \right)^2 F(t) dr^2 + t^2 d\Omega^2, \end{aligned} \quad (3.156)$$

with

$$\begin{aligned} F(t) &= \frac{1}{4} f'(K_\varphi(t))^2 \\ &= \frac{1}{4} \left[f' \circ f^{-1} \left(\frac{r_s}{t} - 1 \right) \right]^2 \\ &= \left[2 \frac{df^{-1}}{dx} \left(\frac{r_s}{t} - 1 \right) \right]^{-2}. \end{aligned} \quad (3.157)$$

We recall that the aim of this metric is to describe the interior of a non-singular black hole. Hence, we should expect the constraint algebra (3.129)-(3.130) to be deformed near $t = 0$, but almost not near the horizon ($t \simeq r_s$) in order to recover Schwarzschild's solution. Hence, we expect metric (3.156) to reproduce Schwarzschild's solution for $f(x) \approx x^2$, which is the condition to reduce the deformed Hamiltonian constraint (3.135) to the undeformed one (3.125). In this case $f^{-1}(x) \approx \sqrt{x}$, and then $F(t) \approx |r_s/t - 1|$. Finally, setting $b = \frac{r_s}{2}$, we recover a metric for the inside of a Schwarzschild black hole of radius r_s .

3.2.3 The standard LQG deformation

We have now a way of exploring the geometry associated with the standard f taken in loop quantum gravity:

$$f(x) = \frac{\sin^2(\rho x)}{\rho^2}, \quad (3.158)$$

where ρ is a deformation real parameter that tends to zero at the classical limit. The reciprocal function then reads

$$f^{-1}(x) = \frac{\arcsin(\rho \sqrt{x})}{\rho}. \quad (3.159)$$

As a consequence, the effective metric for a black hole in loop quantum gravity is of the form (3.156) with

$$F(t) = \left(\frac{r_s}{t} - 1 \right) \left(1 + \rho^2 - \rho^2 \frac{r_s}{t} \right). \quad (3.160)$$

This metric is defined *a priori* for $t < r_s$ since Einstein's equations were solved inside the black hole, but it can be extended outside the trapped region by using a generalized advanced time coordinate v such that $dv = dr + dt/F(t)$:

$$ds^2 = F(t)dv^2 - 2dvdt + t^2 d\Omega^2. \quad (3.161)$$

The metric and inverse metric are then regular, and as shown in App. A.3.2, the vanishing of an outgoing congruence of null geodesics is tantamount to

$$F(t) = 0 \quad (3.162)$$

Hence, in addition to the future outer trapping horizon at $t = r_s$, a future inner trapping horizon is present for

$$1 + \rho^2 - \rho^2 \frac{r_s}{t} = 0 \iff t = \frac{\rho^2 r_s}{1 + \rho^2}. \quad (3.163)$$

The Ricci scalar reads

$$R = -\frac{2\rho^2}{t^2}, \quad (3.164)$$

and diverges for $t = 0$, which is the locus of a timelike curvature singularity as in Reissner-Nordström spacetime. Our metric is actually very similar to this solution, and leads to the same Penrose diagram.

However, a main difference is that an outer horizon ($t = r_s$) is always present in our geometry, while naked singularities appear for super-extreme RN black holes. In the end, this naive extension of the metric is not satisfactory since it does not allow the recovery of Schwarzschild's solution in the classical region ($r \gg r_s$), except if the parameter ρ becomes r -dependent and tends to zero, which would drastically modify the equations of motion [109].

3.3 Recovering known static spherically symmetric non-singular black holes

We have studied above the spacetime associated with a given deformation of the constraint algebra, using the standard function f considered in loop quantum gravity. The inverse problem can also be considered, namely finding a deformation of the constraint algebra for a given metric. From eq. (3.157), we can indeed obtain the inverse of the deformation function $f(x)$ in terms of the metric defined by $F(t)$:

$$f^{-1}(x) = \frac{1}{2} \int_0^x du \left| F\left(\frac{r_s}{1+u} \right) \right|^{-1/2}. \quad (3.165)$$

The metrics of interest to us are the ones of known static and spherically symmetric non-singular black holes, such as Hayward's and Bardeen's. We shall then try to find whether they can be

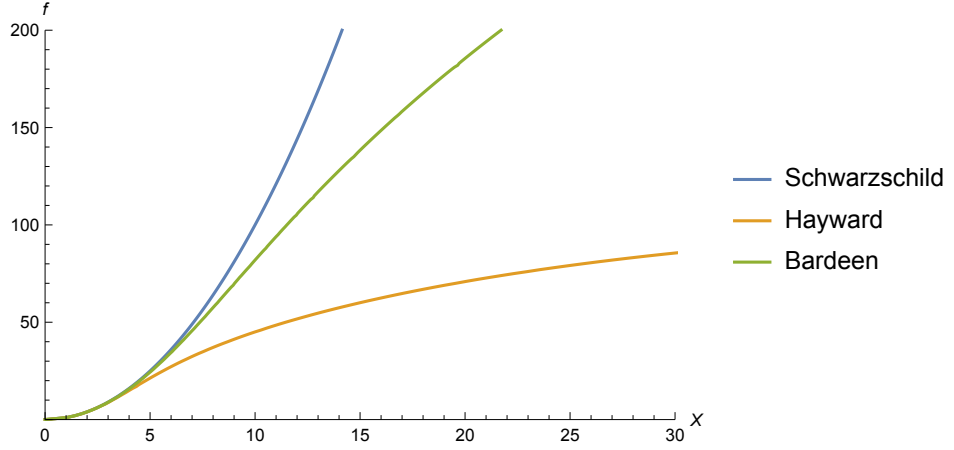
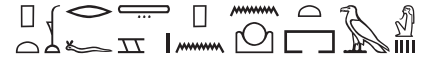


Figure 3.4: Plot of f as a function of x obtained by the numerical integration of eq. (3.165) for Schwarzschild's, Hayward's and Bardeen's black holes, with $m = 1$ and $b = g = 10^{-2}$.

obtained via a deformation of the constraint algebra parametrized according to eq. (3.146).

Unfortunately, the integral (3.165) with F replaced by Hayward's or Bardeen's functions (3.4) and (3.1) is not computable analytically. But the integration can be performed numerically, as is shown in Fig. 3.4 for $m = 1$ and $b = g = 10^{-2}$. As expected, Hayward and Bardeen's solutions tend to Schwarzschild's near the horizon: their functions f behave as x^2 at small x . Further work would be needed to investigate the features of f needed to avoid the presence of a singularity.

ROTATING NON-SINGULAR BLACK HOLES



pty/ptr r=f t3 pn n(y) 3hty.w

“Quel est donc ce pays des habitants de l’horizon?”

(*Textes des Sarcophages* IV, 223c, M8C [30, 42].)

This chapter is based on results I published with E. Gourgoulhon, T. Paumard and F. Vincent in [80]. It is devoted to the analytical study of rotating non-singular black holes, while their numerical aspects will be the topic of Chap. 5. This work originates from a paper by Bambi and Modesto [9], who applied in 2013 the Newman-Janis algorithm to the well known static Hayward black hole and claimed they had obtained a regular rotating black hole. We will review their construction in Sec. 1.1, before showing in Sec. 1.2 that the obtained spacetime is actually singular in the region of negative values of r . In Sec. 2, we will propose an improved rotating Hayward metric reducing to a Hayward static black hole in the nonrotating regime ($a = 0$). This metric will be shown to describe either a *regular rotating black hole* or a *naked rotating wormhole*. We will then study the associated energy-momentum tensor in Sec. 3, and show that the source derived from nonlinear electrodynamics in Toshmatov et al. [113] does not satisfy either Einstein’s nor nonlinear Maxwell’s equations. We actually show that the ansatz used by Toshmatov et al. for the electromagnetic field solely allows recovering the singular Kerr-Newman metric. We finally study analytically the geodesics of the spacetime (Sec. 4) in the hope of making connections with the observations.

Contents

1	Rotating Hawyard’s black hole: a first attempt by Bambi and Modesto	104
2	A non-singular model of rotating black hole	108
3	Energy-momentum tensor of the non-singular model	116
4	Analytical study of geodesics	122

1 Rotating Hayward's black hole: a first attempt by Bambi and Modesto

1.1 Applying the Newman-Janis algorithm to Hayward's spacetime

Let us first give the main steps of Bambi and Modesto's work [9], following the steps of the Newman-Janis algorithm presented in Section 3.3 of Chap. 2. They start from a spherically symmetric metric of the form¹

$$ds^2 = -f(r)dt^2 + f(r)^{-1}dr^2 + h(r)(d\theta^2 + \sin^2\theta d\varphi^2) \quad (4.1)$$

1. Defining the null retarded coordinate u such that $du = dt - \frac{dr}{f(r)}$, we obtain

$$ds^2 = -f(r)du^2 - 2dudr + h(r)(d\theta^2 + \sin^2\theta d\varphi^2) \quad (4.2)$$

2. The components of the null tetrad $Z_a^\mu = (l^\mu, n^\mu, m^\mu, \bar{m}^\mu)$ such that

$$g^{\mu\nu} = -l^\mu n^\nu - l^\nu n^\mu + m^\mu \bar{m}^\nu + m^\nu \bar{m}^\mu \quad (4.3)$$

read:

$$l^\mu = \delta_1^\mu \quad (4.4)$$

$$n^\mu = \delta_0^\mu - \frac{f(r)}{2}\delta_1^\mu \quad (4.5)$$

$$m^\mu = \frac{1}{\sqrt{2h(r)}} \left(\delta_2^\mu + \frac{i}{\sin\theta} \delta_3^\mu \right) \quad (4.6)$$

$$\bar{m}^\mu = \frac{1}{\sqrt{2\bar{h}(r)}} \left(\delta_2^\mu - \frac{i}{\sin\theta} \delta_3^\mu \right). \quad (4.7)$$

3. This step consists in transforming the coordinates (u, r, θ, φ) into the tilde coordinates $(\tilde{u}, \tilde{r}, \tilde{\theta}, \tilde{\varphi})$, allowed to take complex values. The null tetrad gets complexified via the two functions $f(r)$ and $h(r)$:

$$\begin{cases} f(r) \rightarrow \tilde{f}(\tilde{r}, \bar{\tilde{r}}) \\ h(r) \rightarrow \tilde{h}(\tilde{r}, \bar{\tilde{r}}), \end{cases} \quad (4.8)$$

keeping in mind the condition

$$\tilde{Z}_a^\mu(\tilde{x}^\rho, \bar{\tilde{x}}^\rho) \Big|_{\tilde{\mathbf{x}}=\bar{\tilde{\mathbf{x}}}} = Z_a^\mu(x^\rho) \quad (4.9)$$

¹We revisit their computation in our own notation conventions. In particular, we use a $(-+++)$ signature for the metric.

4. We now introduce the real coordinates $(u', r', \theta', \varphi')$ such that

$$\tilde{u} = u' - ia \cos \theta' \quad (4.10)$$

$$\tilde{r} = r' + ia \cos \theta' \quad (4.11)$$

$$\tilde{\theta} = \theta' \quad (4.12)$$

$$\tilde{\varphi} = \varphi' . \quad (4.13)$$

Hence we get the following tetrad components via $Z_a'^{\mu} = \frac{\partial x'^{\mu}}{\partial \tilde{x}^{\nu}} \tilde{Z}_a^{\nu}$:

$$l'^{\mu} = \delta_1^{\mu} \quad (4.14)$$

$$n'^{\mu} = \delta_0^{\mu} - \frac{\tilde{f}(\tilde{r}, \tilde{r})}{2} \delta_1^{\mu} \quad (4.15)$$

$$m'^{\mu} = \frac{1}{\sqrt{2\tilde{h}(\tilde{r}, \tilde{r})}} \left[ia \sin \tilde{\theta} (\delta_0^{\mu} - \delta_1^{\mu}) + \delta_2^{\mu} + \frac{i}{\sin \tilde{\theta}} \delta_3^{\mu} \right] \quad (4.16)$$

$$\bar{m}'^{\mu} = \frac{1}{\sqrt{2\tilde{h}(\tilde{r}, \tilde{r})}} \left[-ia \sin \tilde{\theta} (\delta_0^{\mu} - \delta_1^{\mu}) + \delta_2^{\mu} - \frac{i}{\sin \tilde{\theta}} \delta_3^{\mu} \right] . \quad (4.17)$$

Using eq. (4.10)-(4.13), we can rewrite these components in terms of the new coordinates $(u', r', \theta', \varphi')$. If we define formally two functions f' and h' such that

$$\begin{cases} f'(r', \theta') = \tilde{f}(\tilde{r}, \tilde{r}) \\ h'(r', \theta') = \tilde{h}(\tilde{r}, \tilde{r}) , \end{cases} \quad (4.18)$$

and use eq. (4.3) in reverse, we get the following metric:

$$[g'_{\mu\nu}] = \begin{pmatrix} -f'(r', \theta') & -1 & 0 & a \sin^2 \theta' (f'(r', \theta') - 1) \\ \cdot & 0 & 0 & -a \sin^2 \theta' \\ \cdot & \cdot & h'(r', \theta') & 0 \\ \cdot & \cdot & \cdot & \sin^2 \theta' [h'(r', \theta') + a^2 \sin^2 \theta' (2 - f'(r', \theta'))] \end{pmatrix} \quad (4.19)$$

5. We can perform a last coordinate change to go to the Boyer-Lindquist form of the metric using coordinates (t, r, θ, φ) , which contains only $g_{t\varphi}$ as non-diagonal term. This transformation reads

$$\begin{cases} u' \rightarrow t \quad \text{such that} \quad du' = dt + F(r') dr' \\ r' \rightarrow r = r' \\ \theta' \rightarrow \theta = \theta' \\ \varphi' \rightarrow \varphi \quad \text{such that} \quad d\varphi' = d\varphi + G(r') dr' , \end{cases} \quad (4.20)$$

with

$$\begin{cases} F(r') = \frac{h'(r', \theta') + a^2 \sin^2 \theta'}{f'(r', \theta') h'(r', \theta') + a^2 \sin^2 \theta'} , \\ G(r') = \frac{a}{f'(r', \theta') h'(r', \theta') + a^2 \sin^2 \theta'} . \end{cases} \quad (4.21)$$

This transformation is of course not always possible, since the r.h.s. of F and G must depend solely on the radial coordinate.

Let us from now on focus on the Hayward case, starting from metric (4.1) with

$$\begin{cases} f(r) = 1 - \frac{2M(r)}{r} & \text{with} \quad M(r) \equiv \frac{M_0 r^3}{r^3 + 2M_0 b^2} \\ h(r) = r^2. \end{cases} \quad (4.22)$$

The crucial step in the algorithm is the complexification of these two functions (step 3). Inspired by the Kerr case, we can write:

$$\begin{cases} f(r) \rightarrow \tilde{f}(\tilde{r}, \bar{\tilde{r}}) = 1 - \tilde{M}(\tilde{r}, \bar{\tilde{r}}) \left(\frac{1}{\tilde{r}} + \frac{1}{\bar{\tilde{r}}} \right) \\ h(r) \rightarrow \tilde{h}(\tilde{r}, \bar{\tilde{r}}) = \tilde{r} \bar{\tilde{r}}. \end{cases} \quad (4.23)$$

The only requirement on the complexification of M is that one should recover Kerr's metric in the limit $b \rightarrow 0$. Bambi and Modesto chose not to alter the form of M . With our notations, this gives

$$\tilde{M}(\tilde{r}, \bar{\tilde{r}}) = M\left(\frac{\tilde{r} + \bar{\tilde{r}}}{2}\right) \Rightarrow M'(r', \theta') = M(r'). \quad (4.24)$$

And finally, after going to the coordinates $(u', r', \theta', \varphi')$ defined via eqs. (4.10)-(4.13),

$$\begin{cases} \tilde{f}(\tilde{r}, \bar{\tilde{r}}) = f'(r', \theta') = 1 - \frac{2M(r')r'}{r'^2 + a^2 \cos^2 \theta'} \\ \tilde{h}(\tilde{r}, \bar{\tilde{r}}) = h'(r', \theta') = r'^2 + a^2 \cos^2 \theta' \end{cases} \quad (4.25)$$

In the end, going to the Boyer-Lindquist coordinates (t, r, θ, φ) satisfying eq. (4.20) with

$$\begin{cases} F(r') = \frac{r'^2 + a^2}{r'^2 - 2M_0 r' + a^2}, \\ G(r') = \frac{a}{r'^2 - 2M_0 r' + a^2}. \end{cases} \quad (4.26)$$

and then omitting the prime signs, we obtain the metric

$$[g_{\mu\nu}] = \begin{pmatrix} -1 + \frac{2M(r)r}{\Sigma} & 0 & 0 & -\frac{4aM(r)r \sin^2 \theta}{\Sigma} \\ \cdot & \frac{\Sigma}{\Delta} & 0 & 0 \\ \cdot & \cdot & \Sigma & 0 \\ \cdot & \cdot & \cdot & \sin^2 \left(r^2 + a^2 + \frac{2aM(r)r \sin^2 \theta}{\Sigma} \right) \end{pmatrix}. \quad (4.27)$$

It should be emphasized that in this procedure, we started with $r \geq 0$ but end up with $r \in (-\infty, +\infty)$, as claimed in [26]. This aspect is not mentioned in Bambi & Modesto's work, but it dramatically changes the nature of the spacetime. As we will see in next section, this model possesses a singularity in the $r < 0$ region.

1.2 Presence of a singularity in Bambi-Modesto's spacetime

By means of the Newman-Janis algorithm [90], Bambi and Modesto [9] (see also [112]) have obtained some rotating generalization of Hayward's metric as

$$ds^2 = - \left(1 - \frac{2rM(r)}{\Sigma} \right) dt^2 - \frac{4arM(r) \sin^2 \theta}{\Sigma} dt d\varphi + \frac{\Sigma}{\Delta} dr^2 + \Sigma d\theta^2 + \sin^2 \theta \left(r^2 + a^2 + \frac{2a^2 r M(r) \sin^2 \theta}{\Sigma} \right) d\varphi^2, \quad (4.28)$$

where

$$\begin{aligned}\Sigma &\equiv r^2 + a^2 \cos^2 \theta, \quad \Delta \equiv r^2 - 2M(r)r + a^2, \\ M(r) &\equiv m \frac{r^3}{r^3 + 2mb^2}.\end{aligned}\tag{4.29}$$

In addition to the total mass m and the characteristic length b , the new parameter with respect to Hayward's metric (3.4) is the spin parameter a , such that the total angular momentum is $J = am$. Note that the function $M(r)$ is identical to that defined by eq. (3.4) and that, except for the dependency of M with respect to r , the line element (4.28) is identical to that of the Kerr metric expressed in Boyer-Lindquist coordinates.

As claimed in Ref. [9], there is no singularity at $r = 0$ as long as $b \neq 0$ (see [112] for a rigorous proof). However, Bambi and Modesto say nothing about what happens for $r < 0$, and do not explicitly give the interval on which r is defined. As we have shown in Sec. 1.1, after applying the Newman-Janis algorithm, r should *a priori* be defined on the whole real line \mathbb{R} .

Nonetheless, even if the metric (4.28) were limited to $r \geq 0$, it would yield a spacetime that is not geodesically complete: some timelike and null geodesics would stop at $r = 0$ for a finite value of their affine parameter, while (i) there is no curvature singularity there and (ii) $r = 0$ is not a coordinate singularity as in Minkowski's spacetime. The last point can be seen by considering the value of the metric (4.28)-(4.29) at $r = 0$:

$$ds^2|_{r=0} = -dt^2 + \cos^2 \theta dr^2 + a^2 \cos^2 \theta d\theta^2 + a^2 \sin^2 \theta d\varphi^2.\tag{4.30}$$

If $a \neq 0$, this defines a regular (i.e. nondegenerate) metric, except for $\theta = \pi/2$, the vanishing of $\sin^2 \theta$ at $\theta = 0$ or π reflecting only the standard coordinate singularity of spherical coordinates on the rotation axis.

The Newman-Janis algorithm applied in Sec 1.1 already suggested to let r take any value in \mathbb{R} , but the regularity of the metric at $r = 0$ and the unphysical ending of geodesics definitely impose to extend the spacetime to negative values of r . In other words, we consider

$$\mathcal{M} = \mathbb{R}^2 \times \mathbb{S}^2\tag{4.31}$$

as the spacetime manifold, with (t, r) spanning \mathbb{R}^2 and (θ, φ) spanning the 2-sphere \mathbb{S}^2 .

Now, \mathcal{M} endowed with the metric (4.28)-(4.29) suffers from some curvature singularity, albeit not at $r = 0$. Indeed, the Ricci scalar is (see App. C.1.1 for the computation)

$$R = -\frac{24b^2r^2(r^3 - 4b^2)}{(a^2 \cos^2 \theta + r^2)(r^3 + 2b^2)^3},\tag{4.32}$$

where a, b, r are expressed in units of m , and R in units of m^2 .

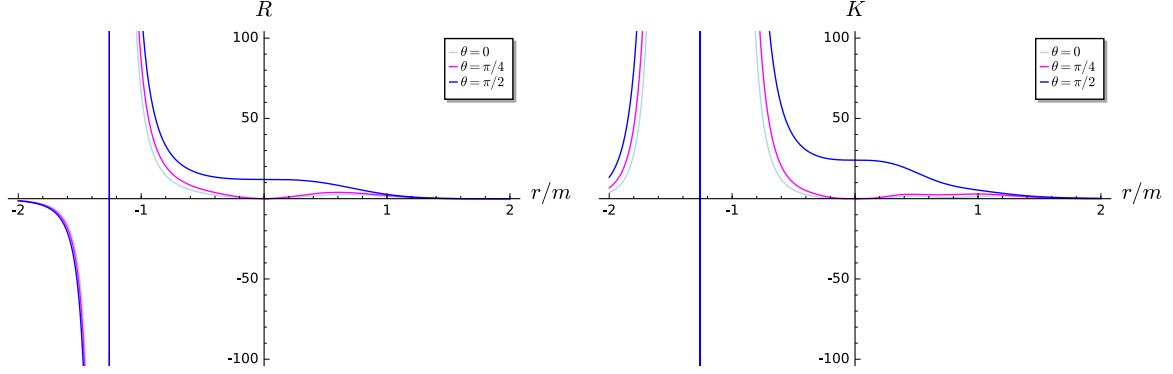


Figure 4.1: Ricci scalar (left) (in units of m^{-2}) and Kretschmann scalar (right) (in units of m^{-4}) as functions of r for the extension to $r < 0$ of Bambi and Modesto [9]’s rotating version of Hayward’s metric with $a/m = 0.9$ and $b/m = 1$. Note that both scalars are diverging at $r/m = -2^{1/3} \approx -1.26$.

The Kretschmann scalar (in units of m^4) reads

$$\begin{aligned}
 K = & \frac{48r^4}{(a^2 \cos^2 \theta + r^2)^6 (r^3 + 2b^2)^6} [(a^6 r^{14} \cos(\theta)^6 - 12a^8 b^4 r^6 \cos(\theta)^8 + 8a^6 b^2 r^{11} \cos(\theta)^6 \\
 & + 96a^8 b^6 r^3 \cos(\theta)^8 - 15a^4 r^{16} \cos^4 \theta + 36a^6 b^4 r^8 \cos(\theta)^6 - 192a^8 b^8 \cos(\theta)^8 - 200a^4 b^2 r^{13} \cos^4 \theta \\
 & + 944a^6 b^6 r^5 \cos(\theta)^6 + 15a^2 r^{18} \cos^2 \theta - 924a^4 b^4 r^{10} \cos^4 \theta + 64a^6 b^8 r^2 \cos(\theta)^6 + 56a^2 b^2 r^{15} \cos^2 \theta \\
 & - 48a^4 b^6 r^7 \cos^4 \theta - r^{20} - 276a^2 b^4 r^{12} \cos^2 \theta - 352a^4 b^8 r^4 \cos^4 \theta + 8b^2 r^{17} + 144a^2 b^6 r^9 \cos^2 \theta \\
 & - 72b^4 r^{14} - 128a^2 b^8 r^6 \cos^2 \theta + 16b^6 r^{11} - 32b^8 r^8)]
 \end{aligned} \tag{4.33}$$

They are both singular in the entire hypersurface defined by $r = -(2mb^2)^{1/3}$, as is visible in Fig. 4.1). The situation is in some way even worse than with Kerr’s spacetime, where the singularity at $r = 0$ could be avoided by observers with $\theta \neq \frac{\pi}{2}$.

We conclude that the rotating generalization (4.28)-(4.29) of Hayward’s metric proposed by Bambi & Modesto does not describe a regular black hole.

2 A non-singular model of rotating black hole

2.1 Regular extension to $r < 0$

2.1.1 Metric

Following a prescription applied by Torres [111] to rotating regular black holes arising from quantum gravity consideration, we define the metric tensor in all $\mathcal{M} = \mathbb{R}^2 \times \mathbb{S}^2$ by

$$ds^2 = - \left(1 - \frac{2rM(r)}{\Sigma} \right) dt^2 - \frac{4arM(r)\sin^2 \theta}{\Sigma} dt d\varphi + \frac{\Sigma}{\Delta} dr^2 + \Sigma d\theta^2 + \sin^2 \theta \left(r^2 + a^2 + \frac{2a^2 rM(r)\sin^2 \theta}{\Sigma} \right) d\varphi^2, \tag{4.34}$$

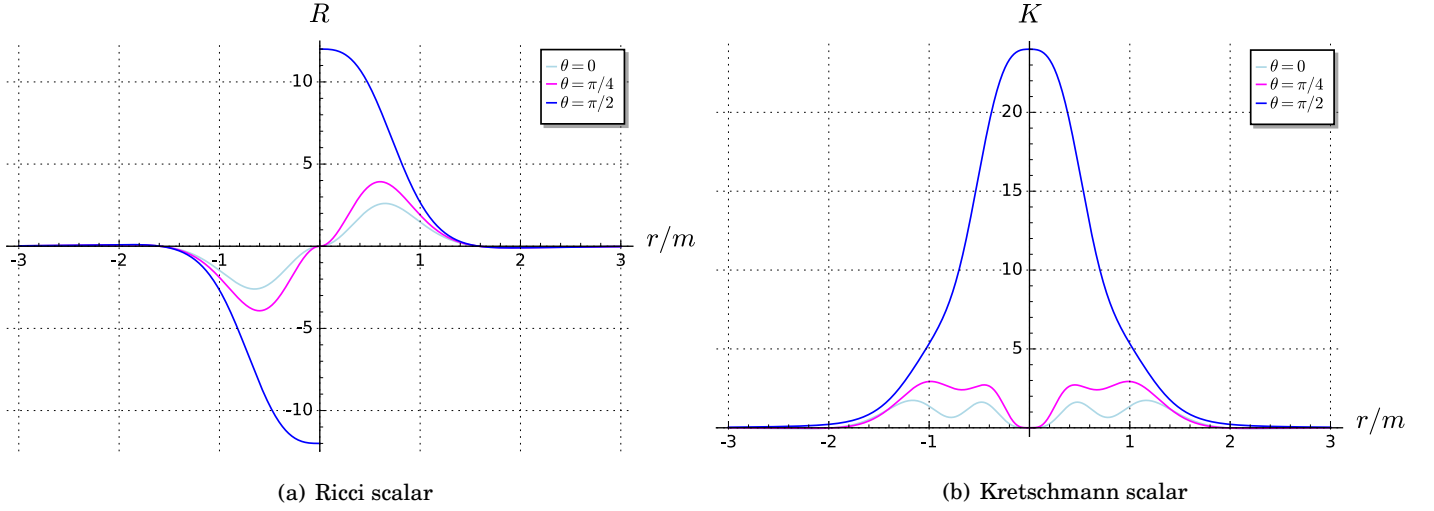


Figure 4.2: Ricci scalar (a) (in units of m^{-2}) and Kretschmann scalar (b) (in units of m^{-4}) of the improved rotating Hayward metric (4.34)-(4.35) with $a/m = 0.9$ and $b/m = 1$ as a function of r for $\theta = 0, \pi/4$ and $\pi/2$.

with

$$\begin{aligned} \Sigma &\equiv r^2 + a^2 \cos^2 \theta, \quad \Delta \equiv r^2 - 2M(r)r + a^2, \\ M(r) &\equiv m \frac{|r|^3}{|r|^3 + 2mb^2}. \end{aligned} \quad (4.35)$$

The difference with Bambi-Modesto's metric (4.28)-(4.29) lies only in the replacement of r by $|r|$ in the function $M(r)$. This is motivated by the expression of $M(r)$ in Torres' work [111]:

$$M(r)_{\text{Torres}} = m \frac{|r|^3}{|r|^3 + \tilde{\omega}(|r| + \gamma m)}, \quad (4.36)$$

where $\tilde{\omega}$ and γ are two constants. Note also that this metric allows recovering Kerr's metric in the limit $b = 0$, and Hayward's static black hole in the nonrotating limit ($a = 0$).

2.1.2 Regularity

The metric (4.34)-(4.35) has no more divergences for $\Sigma = 0$, due to the behaviour of $M(r)$ at $r = 0$. Actually, the metric does not have any curvature singularity anymore. This can be seen on Figs. 4.2(a) and 4.2(b), where the Ricci scalar R and Kretschmann scalar K are plotted for $a/m = 0.9$, $b/m = 1$ and various values of θ (see App. C.1.1 for details). In addition, we plot the Chern-Pontryagin scalar CP and Euler scalar E on Figs. 4.3(a) and 4.3(b), which are defined as

$$\begin{cases} CP = {}^*R^{\alpha\beta\gamma\delta}R_{\alpha\beta\gamma\delta}, \\ E = -K + 4R_{\mu\nu}R^{\mu\nu} - R^2. \end{cases} \quad (4.37)$$

All curvature scalars remain finite, although the Ricci scalar is discontinuous at the equatorial ring $r = 0$ and $\theta = \pi/2$ (see Fig. 4.2(a)).

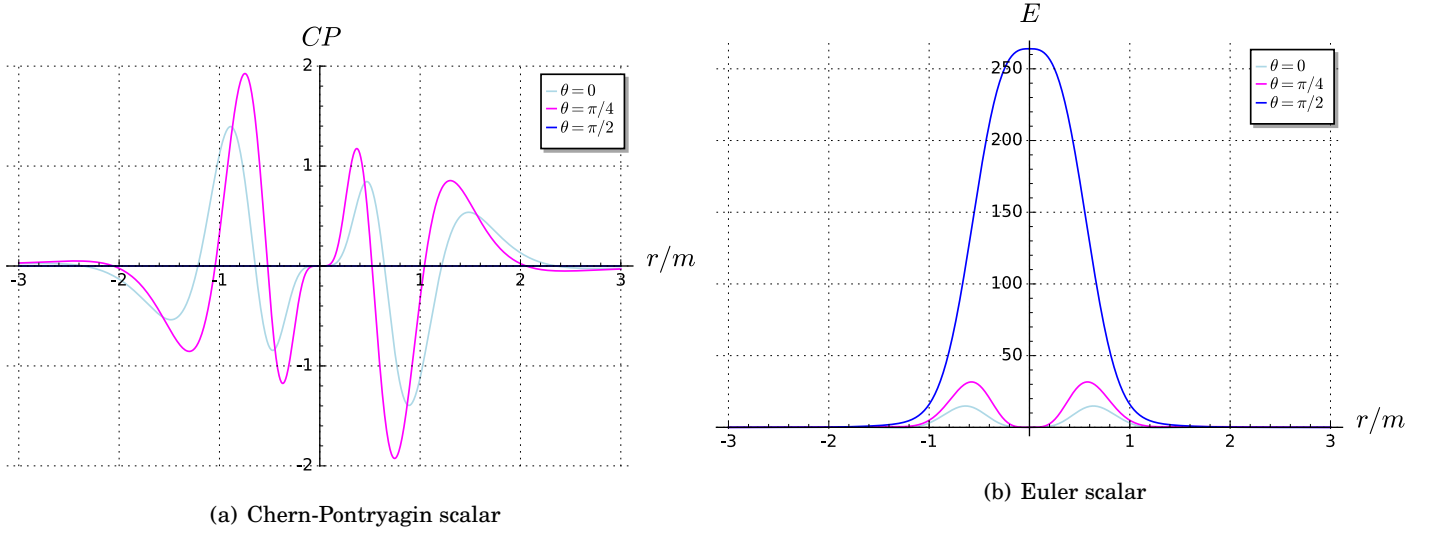


Figure 4.3: Chern-Pontryagin scalar (a) and Euler scalar (b) (in units of m^{-4}) of the improved rotating Hayward metric (4.34)-(4.35) with $a/m = 0.9$ and $b/m = 1$ as a function of r for $\theta = 0, \pi/4$ and $\pi/2$.

2.2 The two regimes of the model

2.2.1 Presence of horizons

As in Kerr's case, the metric component g_{rr} diverges for $\Delta = 0$. This coordinate singularity can be removed by a change of coordinates:

$$\begin{cases} v = t + \int \frac{r^2 + a^2}{\Delta} dr, \\ \psi = \varphi + \int \frac{a}{r} dr. \end{cases} \quad (4.38)$$

And the metric then reads

$$\begin{aligned} ds^2 = & - \left(1 - \frac{2rM(r)}{\Sigma} \right) dv^2 + 2dvdr - \frac{4arM(r)\sin^2\theta}{\Sigma} dv d\psi - 2a\sin^2(\theta)drd\psi + \Sigma d\theta^2 \\ & + \sin^2\theta \left(r^2 + a^2 + \frac{2a^2rM(r)\sin^2\theta}{\Sigma} \right) d\psi^2 \end{aligned} \quad (4.39)$$

One can then compute the expansion of null outgoing geodesics orthogonal to the 2-surfaces $r = \text{cst.}$ and $v = \text{cst.}$ (see App. A.3.3 for details):

$$\theta_+ = \frac{r\Delta}{a^2r^2 + r^4 + (a^4 + a^2r^2)\cos^2(\theta)} \quad (4.40)$$

The metric (4.34)-(4.35) then admits trapping horizons for

$$\Delta \equiv r^2 - 2M(r)r + a^2 = 0. \quad (4.41)$$

The way of characterizing the causal nature of the hypersurfaces $r = \text{cst.}$, and hence the horizons, is the same as in Sec. 3.1.3. The causal nature of a vector normal to these hypersurfaces is given by the sign of

$$g(\nabla r, \nabla r) = g^{\mu\nu} \partial_\mu r \partial_\nu r = g^{rr} = \frac{\Delta}{\Sigma}. \quad (4.42)$$

Hence, ∇r is a null vector when $\Delta = 0$. The horizons defined above by $\Delta = 0$ will then be null trapping horizons. They can be shown to be Killing and event horizons as well, the Killing horizon being associated with a linear combination of the following two Killing vectors:

- $\xi = \partial_t$, which is null at the ergosphere ($g_{tt} = 0$).
- $\eta = \partial_\varphi$, which is null for $g_{\varphi\varphi} = 0$. The region in which η is timelike contains closed timelike curves, as will be explained in Sec. 2.3.

2.2.2 Regular rotating Hayward black hole

Eq. (4.41) admits up to two real solutions depending on the values of the parameters a and b , and spacetime thus has zero, one or two trapping horizons (denoted r_- and r_+). In the latter case, the considered spacetime $\mathcal{M} = \mathbb{R}^2 \times \mathbb{S}^2$ can be written $\mathcal{M} = \mathcal{M}_I \cup \mathcal{H}_{\text{out}} \cup \mathcal{M}_{\text{II}} \cup \mathcal{H}_{\text{in}} \cup \mathcal{M}_{\text{III}}$, with:

$$\left\{ \begin{array}{l} \mathcal{M}_I \equiv \mathbb{R} \times (r_+, +\infty) \times \mathbb{S}^2, \\ \mathcal{H}_{\text{out}} \equiv \{p \in \mathbb{R}^2 \times \mathbb{S}^2, \quad r(p) = r_+\}, \\ \mathcal{M}_{\text{II}} \equiv \mathbb{R} \times (r_-, r_+) \times \mathbb{S}^2, \\ \mathcal{H}_{\text{in}} \equiv \{p \in \mathbb{R}^2 \times \mathbb{S}^2, \quad r(p) = r_-\}, \\ \mathcal{M}_{\text{III}} \equiv \mathbb{R} \times (-\infty, r_-) \times \mathbb{S}^2, \end{array} \right. . \quad (4.43)$$

In \mathcal{M}_{II} , i.e. between the two horizons, $\theta_+ < 0$: this region is gravitationally trapped, $r = r_+$ is a FOTH and $r = r_-$ a FITH. As for Kerr's spacetime, one could extend the spacetime in the past and describe an anti-trapped region, as well as past inner and outer trapping horizons. We will not deal with this extension in the following, since we are interested in describing astrophysical black holes.

The outermost null trapping horizon, which corresponds to the biggest value (r_+) of the radial coordinate among the solutions of eq. (4.41), is an *event horizon* that we will call *outer horizon*. The innermost null trapping horizon will be called *inner horizon*. The region of existence of the two horizons is depicted in blue in Fig. 4.4. The black line represents the extremal case, where $r_- = r_+$.

When $b = 0$ one recovers the Kerr case: two horizons exist for values of a ranging from $a = 0$ to $a = m$, the latter value corresponding to the extremal Kerr black hole, where the two horizons coincide. When $a = 0$ one recovers the Hayward case, with two horizons whose location depends on the value of the parameter b . The most interesting cases with horizons are the metrics well different from Kerr ($b = 0$) and Hayward ($a = 0$) ones, for instance the metric with $a = b = 0.5m$. The image of such configurations, computed using the ray-tracing code² GYOTO [120], will be

²Freely available at <http://gyoto.obspm.fr>

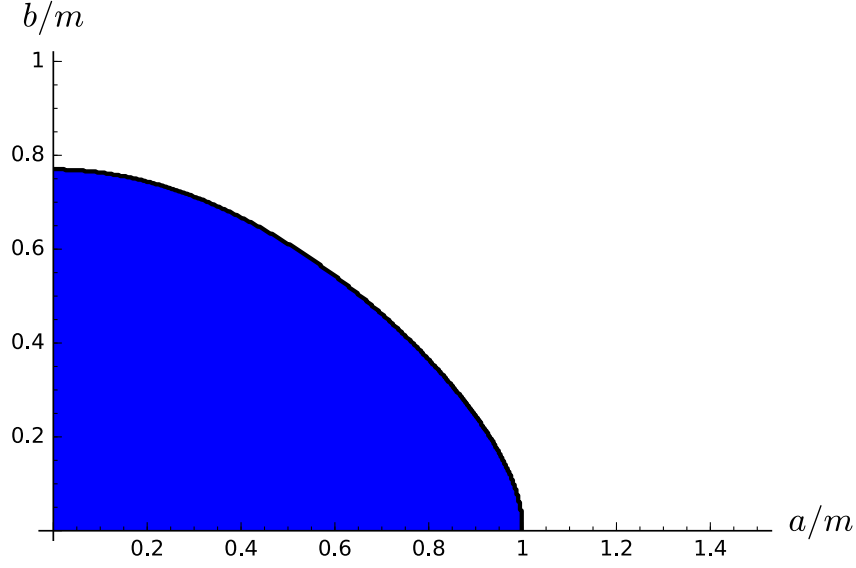


Figure 4.4: Region of existence of one (black line) or two (in blue) future trapping horizon(s), depending on the parameters a and b .

discussed in Sec. 3 of Chap. 5.

2.2.3 Naked rotating wormhole

In the absence of horizon (hence of trapped region), the spacetime can no longer be qualified of a regular rotating black hole. The hypersurface $r = 0$ is visible by any observer, and it is even traversable.

In $\mathcal{M} = \mathbb{R}^2 \times \mathbb{S}^2$, the hypersurface $r = 0$ is a 3-dimensional cylinder $\mathcal{T}_0 = \mathbb{R} \times \mathbb{S}^2$, spanned by the coordinates (t, θ, φ) , which we call the *throat*, as in the Kerr case [93]. The metric induced on \mathcal{T}_0 by the spacetime metric (4.34)-(4.35) is

$$d\sigma^2 = -dt^2 + a^2 \cos^2 \theta d\theta^2 + a^2 \sin^2 \theta d\varphi^2. \quad (4.44)$$

We may then split \mathcal{T}_0 into three components: $\mathcal{T}_0 = \mathcal{T}_0^+ \cup \mathcal{R} \cup \mathcal{T}_0^-$, where \mathcal{T}_0^+ is the Northern hemisphere $0 \leq \theta < \pi/2$ times (Cartesian product) \mathbb{R} , \mathcal{R} is the equatorial ring $\theta = \pi/2$ times \mathbb{R} and \mathcal{T}_0^- is the Southern hemisphere $\pi/2 < \theta \leq \pi$ times \mathbb{R} . Introducing in \mathcal{T}_0^+ or \mathcal{T}_0^- the coordinates

$$\begin{cases} X = a \sin \theta \cos \varphi, \\ Y = a \sin \theta \sin \varphi \end{cases} \quad X^2 + Y^2 \leq a^2, \quad (4.45)$$

the line element (4.44) reduces to

$$d\sigma^2 = -dt^2 + dX^2 + dY^2. \quad (4.46)$$

We recognize a 3-dimensional Minkowskian metric and conclude that, as long as $a \neq 0$, the throat \mathcal{T}_0 comprises two flat open disks of radius a times \mathbb{R} : \mathcal{T}_0^+ and \mathcal{T}_0^- . Moreover, from the signature of (4.44), it appears that the throat is timelike; it is therefore a 2-way membrane, i.e. it can be crossed by particles from the region $r > 0$ to the region $r < 0$, in the reverse way as well.

That is why we call each configuration of the metric (4.34)-(4.35) such that eq. (4.41) has no solution a *naked rotating wormhole*. Indeed, the wormhole whose throat is located at $r = 0$, which is also present in Kerr's case (with a singularity), is no longer hidden by any horizon. Photons can even go through the throat and come back to the observer, as will be shown in Sec. 3.2.3 of Chap. 5.

2.3 Causality

The Kerr spacetime possesses a well-known acausal region, the Carter time machine [32]. In this region, the Killing vector $\eta = \partial_\varphi$ is timelike, giving birth to closed timelike curves. However the whole spacetime does not become acausal thanks to the presence of an event horizon: the particles that are able to move backward in time are trapped inside the black hole.

Considering now the rotating Hayward metric extended to $r < 0$, one has to check whether η can become timelike even in the absence of horizons, in which case the whole spacetime would be acausal. Indeed, if ∂_φ becomes timelike, an observer can follow an integral curve of φ , with constant (t, r, θ) . After a rotation $\varphi \rightarrow \varphi + 2\pi$ around the axis $\theta = 0$, the observer comes back at the same point of space-time. Any observer could then come from infinity, use the closed timelike curve for a while, and reemerge from it: it would then have travelled in the future. In view of (4.34), one has

$$\eta \cdot \eta = g_{\varphi\varphi} = \left(r^2 + a^2 + \frac{2a^2 M(r) r \sin^2 \theta}{r^2 + a^2 \cos^2 \theta} \right) \sin^2 \theta, \quad (4.47)$$

so that

$$\eta \text{ timelike} \iff (r^2 + a^2)(r^2 + a^2 \cos^2 \theta) + 2a^2 M(r) r \sin^2 \theta < 0. \quad (4.48)$$

The only negative contribution in the left-hand side of (4.48) comes from the second term, when $r < 0$. It reaches a minimum for $\theta = \pi/2$. Fig. 4.5 shows that there exists a red region (region I) for which $g_{\varphi\varphi} < 0$ while no event horizon is present. The parameters a and b associated with such a region thus correspond to acausal spacetimes, which we will not deal with in this dissertation. It should be emphasized though that the cosmic censorship conjecture, which was used to discard spacetimes (without event horizon, hence with a visible singularity) that did not hide the acausal region, is no longer an argument here.

Region II also has causality issues, but these are hidden behind an event horizon. Regions III and IV are totally free of closed timelike curves, the latter is also devoid of any event horizon and represents a naked rotating wormhole.

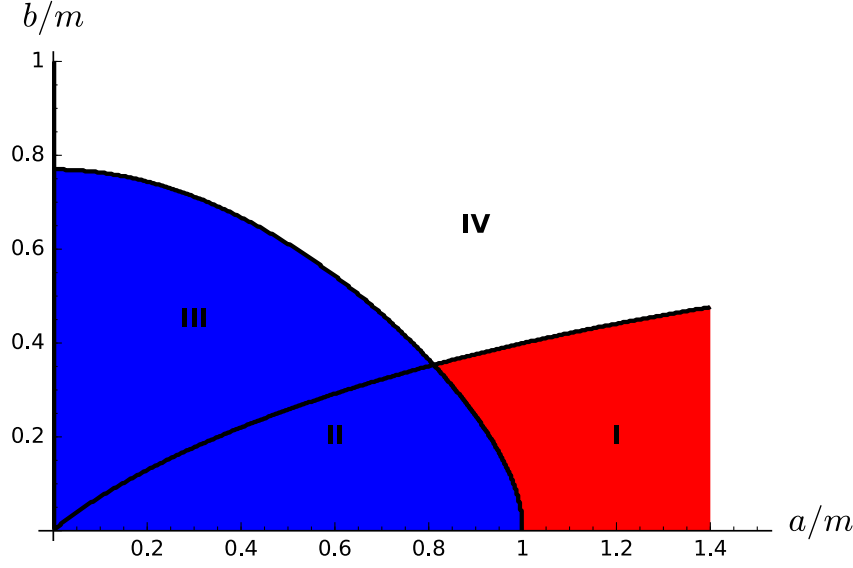


Figure 4.5: Regions of existence of an event horizon (in blue) and of negative $g_{\phi\phi}$ for $\theta = \pi/2$ in the absence of horizons (in red), depending on the parameters a and b .

2.4 Energy conditions

The existence of horizons, hence of trapped surfaces, along with the absence of singularity, questions the hypotheses of Penrose's singularity theorem. As mentioned in Secs. 1.3.2 & 1.3.3 of Chap. 3, both Bardeen and Hayward nonrotating metrics fulfill the null energy condition and circumvent the original theorem by Penrose (Thm. 1.3 of Chap. 1) by the lack of a Cauchy surface. In the improved version of the singularity theorem by Hawking and Penrose (Thm. 1.4 of Chap. 1), the hypothesis of existence of a Cauchy surface is relaxed, at the price of replacing the null energy condition by the strong one. This version is still compatible with Bardeen's and Hayward's regular black holes because both violate the strong energy condition.

In the rotating case, it has been shown by Torres [111] that any metric of the type (4.34) with $a \neq 0$ violates the weak energy condition in all the region $r < 0$ as soon as $M'(r) < 0$ there. This is the case for our choice (4.35) for $M(r)$.

Here, we investigate the violation of the weakest of all energy conditions, the null energy condition (NEC), defined in Sec. 3.1.1 of Chap. 1. It is the weakest condition in the sense that its violation also implies the violation of the weak, strong and dominant energy conditions (as shown in Fig. 1.8). For any null vector k^μ the NEC reads

$$T_{\mu\nu}k^\mu k^\nu \geq 0. \quad (4.49)$$

In order to compute this scalar we switch to the locally nonrotating frame which diagonalizes the

metric [14]. Its basis is such that $e_{\hat{\mu}} \cdot e_{\hat{\nu}} = \eta_{\hat{\mu}\hat{\nu}}$. The dual cobasis at each point (t, r, θ, φ) reads

$$\begin{aligned} e^{(t)} &= \sqrt{\frac{\Sigma\Delta}{A}} \mathbf{d}t, \\ e^{(r)} &= \sqrt{\frac{\Sigma}{\Delta}} \mathbf{d}r, \\ e^{(\theta)} &= \sqrt{\Sigma} \mathbf{d}\theta, \\ e^{(\varphi)} &= -\frac{2M(r)ar \sin\theta}{\sqrt{\Sigma A}} \mathbf{d}t + \sqrt{\frac{A}{\Sigma}} \sin\theta \mathbf{d}\varphi, \end{aligned} \tag{4.50}$$

with

$$A \equiv (r^2 + a^2)^2 - a^2 \Delta \sin^2 \theta. \tag{4.51}$$

Solving Einstein's equations "in reverse", we obtain $T_{\hat{\mu}\hat{\nu}} k^{\hat{\mu}} k^{\hat{\nu}} = G_{\hat{\mu}\hat{\nu}} k^{\hat{\mu}} k^{\hat{\nu}} / 8\pi$. This effective energy density is plotted in Fig. 4.6 in the case $a/m = 0.9$, $b/m = 1$ (see App. C.1.2 for details). One can see that the NEC is violated from near the centre up to $r \rightarrow -\infty$.

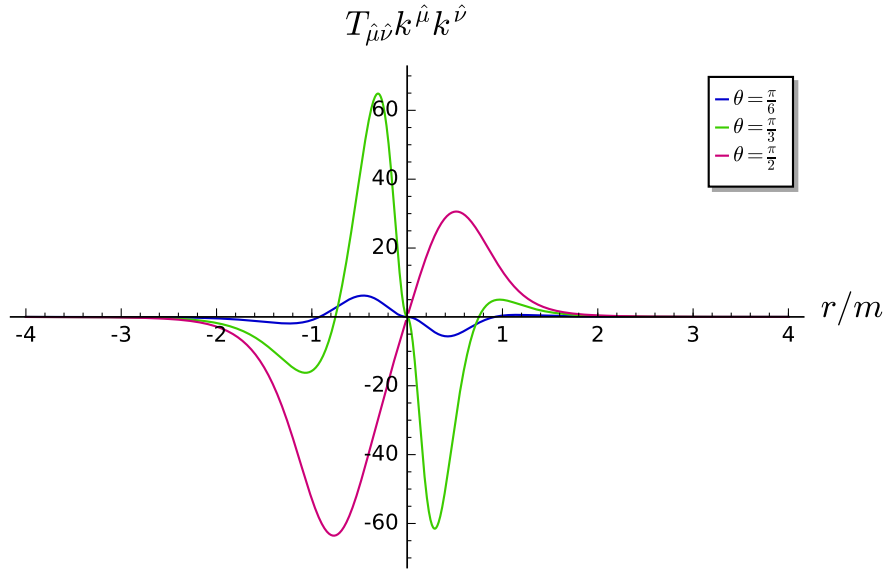


Figure 4.6: $T_{\hat{\mu}\hat{\nu}} k^{\hat{\mu}} k^{\hat{\nu}}$ as a function of r for $\theta = \pi/6, \pi/3, \pi/2$ and $a = 0.9, b = 1$. The NEC is violated when any of the curves goes below zero.

3 Energy-momentum tensor of the non-singular model

3.1 Results of Toshmatov et al.

3.1.1 A nonlinear electrodynamical source

In [113], Toshmatov et al. claimed they had found a nonlinear electrodynamical energy-momentum sourcing a metric of the following general form:

$$ds^2 = -\left(1 - \frac{2rM(r)}{\Sigma}\right)dt^2 - \frac{4arM(r)\sin^2\theta}{\Sigma}dt d\varphi + \frac{\Sigma}{\Delta}dr^2 + \Sigma d\theta^2 + \sin^2\theta \left(r^2 + a^2 + \frac{2a^2rM(r)\sin^2\theta}{\Sigma}\right)d\varphi^2. \quad (4.52)$$

They used the following action, coupling general relativity to nonlinear electrodynamics:

$$S = \frac{1}{16\pi} \int d^4x \sqrt{-g} (R - \mathcal{L}(\mathcal{F})), \quad (4.53)$$

where $\mathcal{F} = F_{\mu\nu}F^{\mu\nu}$. The electromagnetic tensor $F_{\mu\nu}$ is defined through the vector potential A_μ :

$$F_{\mu\nu} = \nabla_\mu A_\nu - \nabla_\nu A_\mu. \quad (4.54)$$

The Einstein equations deduced from the action (4.53) read

$$G_{\mu\nu} = 2 \left(\mathcal{L}_{\mathcal{F}} F_\mu{}^\alpha F_{\nu\alpha} - \frac{1}{4} \mathcal{L} g_{\mu\nu} \right), \quad (4.55)$$

while the nonlinear Maxwell equations are

$$\nabla_\mu (\mathcal{L}_{\mathcal{F}} F^{\mu\nu}) = 0 \quad (4.56)$$

Their ansatz for the vector potential is

$$\mathbf{A} = -\frac{Q_m a \cos\theta}{\Sigma} \mathbf{d}t + \frac{Q_m (r^2 + a^2) \cos\theta}{\Sigma} \mathbf{d}\varphi. \quad (4.57)$$

They then claim that

$$\mathcal{F} = \frac{Q_m^2 [a^3(3 - \cos(4\theta)) + 4(6a^2r^2 + 2r^4 + a^2(a^2 - 6r^2)\cos(2\theta))]}{4\Sigma^4}. \quad (4.58)$$

Finally they claim to solve Einstein's equations with respect to \mathcal{L} and $\mathcal{L}_{\mathcal{F}}$, yielding

$$\begin{cases} \mathcal{L} = \frac{r^2[(15a^4 - 8a^2r^2 + 8r^4 + 4a^2(5a^2 - 2r^2)\cos(2\theta) + 5a^4\cos(4\theta))M'(r) + 16a^2r\cos^2(\theta)\Sigma M''(r)]}{2\Sigma^4}, \\ \mathcal{L}_{\mathcal{F}} = \frac{2(r^2 - a^2\cos^2(\theta))M'(r) - r\Sigma M''(r)}{2Q_m^2}. \end{cases} \quad (4.59)$$

3.1.2 Issues in the derivation of the “solution”

As we mentioned to the authors, the way they solve Einstein's equations cannot ensure that \mathcal{L} is a function of \mathcal{F} only, i.e. that it be a proper lagrangian density. This was also noticed by

Rodrigues & Junior in [102]. Toshmatov et al. nonetheless claim in [114] that this introduces only a small inconsistency, and that the difference

$$\Delta \mathcal{L}_{\mathcal{F}} = \mathcal{L}_{\mathcal{F}} - \frac{\partial \mathcal{L}}{\partial \mathcal{F}} \equiv \mathcal{L}_{\mathcal{F}} - \frac{\partial \mathcal{L}}{\partial r} \frac{\partial r}{\partial \mathcal{F}} - \frac{\partial \mathcal{L}}{\partial \theta} \frac{\partial \theta}{\partial \mathcal{F}} \quad (4.60)$$

is on level 10^{-2} .

We disagree on two points. First, only the ratio $\Delta \mathcal{L}_{\mathcal{F}}/\mathcal{L}_{\mathcal{F}}$ could give a relevant dimensionless number to characterize the deviation from an exact lagrangian. Second, since $\mathcal{L}_{\mathcal{F}}$ must be a function of \mathcal{F} only, one must have

$$\frac{\partial \mathcal{L}}{\partial r} \frac{\partial r}{\partial \mathcal{F}} = \frac{\partial \mathcal{L}}{\partial \theta} \frac{\partial \theta}{\partial \mathcal{F}}, \quad (4.61)$$

and eq. (4.60) then actually reads

$$\Delta \mathcal{L}_{\mathcal{F}} = \mathcal{L}_{\mathcal{F}} - \frac{1}{2} \left(\frac{\partial \mathcal{L}}{\partial r} \frac{\partial r}{\partial \mathcal{F}} + \frac{\partial \mathcal{L}}{\partial \theta} \frac{\partial \theta}{\partial \mathcal{F}} \right). \quad (4.62)$$

In the end, the consistency checks that should be performed to quantify the deviation from an exact lagrangian are the following:

$$\begin{cases} X(r, \theta) \equiv 1 - \frac{1}{\mathcal{L}_{\mathcal{F}}} \frac{\partial \mathcal{L}}{\partial r} \frac{\partial r}{\partial \mathcal{F}} = 0, \\ Y(r, \theta) \equiv 1 - \frac{1}{\mathcal{L}_{\mathcal{F}}} \frac{\partial \mathcal{L}}{\partial \theta} \frac{\partial \theta}{\partial \mathcal{F}} = 0. \end{cases} \quad (4.63)$$

X and Y are plotted below in the case of the Hayward model, where

$$M(r) = 1 - \frac{2mr^3}{r^3 + 2mb^2} \quad (4.64)$$

It appears that both diverge for large values of r (Fig. 4.7, see App. C.1.4 for details). This is in contradiction with the results of Tomasthov et al., and shows that their lagrangian fails to be a function of \mathcal{F} only.

Another serious drawback in the derivation of Toshmatov et al. is that the authors do not check whether nonlinear Maxwell equations are satisfied. We will prove in Sec. 3.2.2 that with their choice of electromagnetic field (4.57), they can actually be satisfied only if $\mathcal{L}(\mathcal{F}) \propto \mathcal{F}$.

3.2 Exact solutions

3.2.1 Magnetic source

Bardeen's and Hayward's solutions are recovered with a magnetic Maxwell field $\mathbf{F} = g \sin(\theta) \mathbf{d}\theta \wedge \mathbf{d}\varphi$, stemming from the vector potential $\mathbf{A} = -g \cos \theta \mathbf{d}\varphi$. Let us now see whether Kerr's modified metric (4.34) can be sourced by a nonlinear magnetic field. In axially symmetric and stationary spacetimes, the Maxwell tensor will have only $F_{r\varphi}$ and $F_{\theta\varphi}$ as nonzero components. Let us write

$$\mathbf{A} = \alpha(r, \theta) \mathbf{d}\varphi, \quad (4.65)$$

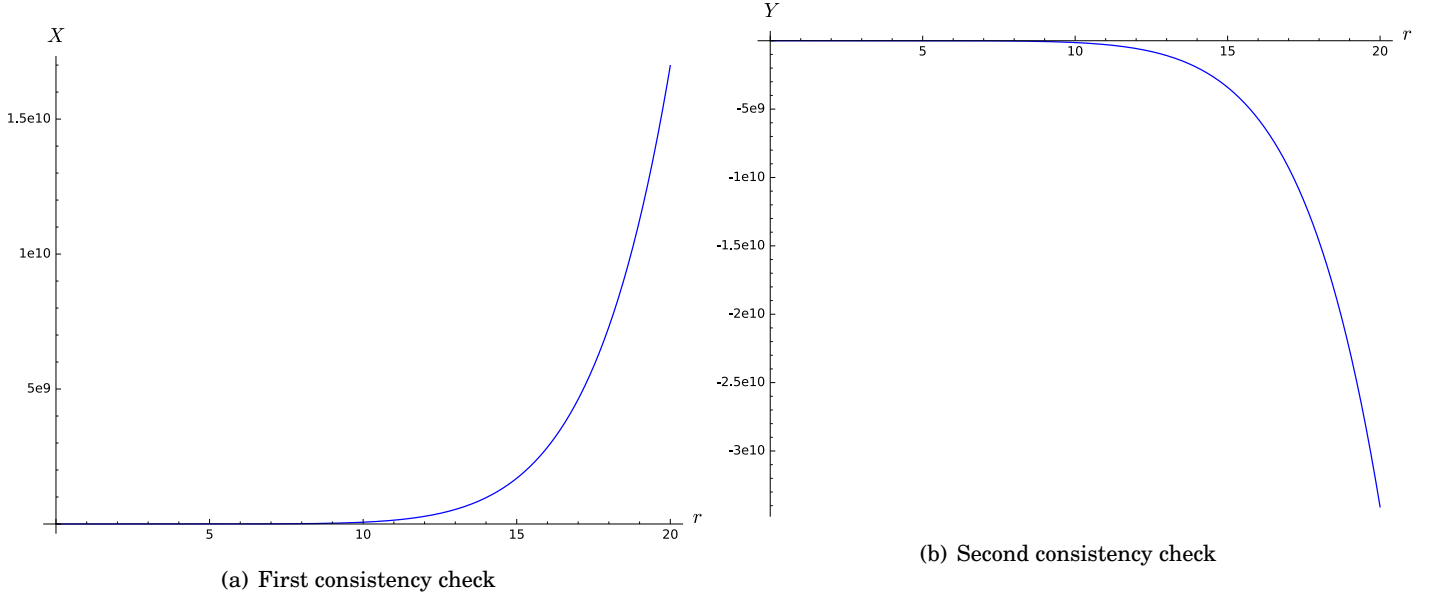


Figure 4.7: Plot of X and Y as a function of r , with $a = 0.5$, $b = 1/\sqrt{2}$, $Q_m = 1$, and $\theta = \pi/2$.

and then

$$\mathbf{F} = \partial_r \alpha \mathbf{d}r \wedge \mathbf{d}\varphi + \partial_\theta \alpha \mathbf{d}\theta \wedge \mathbf{d}\varphi. \quad (4.66)$$

Notice that with this construction, the first part of Maxwell's equations is automatically satisfied: $\mathbf{dF} = \mathbf{dA} = 0$. To check whether the second part is satisfied too, we can then compute the Hodge dual of $\mathcal{L}_{\mathcal{F}} \mathbf{F}$:

$$\begin{aligned} \star(\mathcal{L}_{\mathcal{F}} \mathbf{F}) &= \frac{(\Delta - a^2 \sin^2 \theta) \mathcal{L}_{\mathcal{F}} \dot{\alpha}}{\Sigma \Delta \sin \theta} \mathbf{d}t \wedge \mathbf{d}r - \frac{(\Delta - a^2 \sin^2 \theta) \mathcal{L}_{\mathcal{F}} \dot{\alpha}}{\Sigma \sin \theta} \mathbf{d}t \wedge \mathbf{d}\theta - \frac{2arM(r) \sin \theta \mathcal{L}_{\mathcal{F}} \alpha'}{\Sigma \Delta} \mathbf{d}r \wedge \mathbf{d}\varphi \\ &\quad + \frac{2arM(r) \sin \theta \mathcal{L}_{\mathcal{F}} \alpha'}{\Sigma} \mathbf{d}\theta \wedge \mathbf{d}\varphi \end{aligned} \quad (4.67)$$

where we denote $\partial_r \alpha = \alpha'$ and $\partial_\theta \alpha = \dot{\alpha}$. Defining

$$\begin{cases} f(r, \theta) = \frac{\Delta - a^2 \sin^2 \theta}{\Sigma \sin \theta}, \\ g(r, \theta) = \frac{2arM(r) \sin \theta}{\Sigma}, \end{cases} \quad (4.68)$$

we have

$$\star(\mathcal{L}_{\mathcal{F}} \mathbf{F}) = \frac{f \mathcal{L}_{\mathcal{F}} \dot{\alpha}}{\Delta} \mathbf{d}t \wedge \mathbf{d}r - f \mathcal{L}_{\mathcal{F}} \alpha' \mathbf{d}t \wedge \mathbf{d}\theta - \frac{g \mathcal{L}_{\mathcal{F}} \dot{\alpha}}{\Delta} \mathbf{d}r \wedge \mathbf{d}\varphi + g \mathcal{L}_{\mathcal{F}} \alpha' \mathbf{d}\theta \wedge \mathbf{d}\varphi. \quad (4.69)$$

Then,

$$\begin{aligned} \mathbf{d} \star(\mathcal{L}_{\mathcal{F}} \mathbf{F}) &= \frac{1}{\Delta} (\dot{f} \mathcal{L}_{\mathcal{F}} \dot{\alpha} + f \dot{\mathcal{L}}_{\mathcal{F}} \dot{\alpha} + f \mathcal{L}_{\mathcal{F}} \ddot{\alpha}) \mathbf{d}t \wedge \mathbf{d}r \wedge \mathbf{d}\theta + \frac{1}{\Delta} (\dot{g} \mathcal{L}_{\mathcal{F}} \dot{\alpha} + g \dot{\mathcal{L}}_{\mathcal{F}} \dot{\alpha} + g \mathcal{L}_{\mathcal{F}} \ddot{\alpha}) \mathbf{d}r \wedge \mathbf{d}\theta \wedge \mathbf{d}\varphi \\ &\quad + (f' \mathcal{L}_{\mathcal{F}} \alpha' + f \mathcal{L}'_{\mathcal{F}} \alpha' + f \mathcal{L}_{\mathcal{F}} \alpha'') \mathbf{d}t \wedge \mathbf{d}r \wedge \mathbf{d}\theta + (g' \mathcal{L}_{\mathcal{F}} \alpha' + g \mathcal{L}'_{\mathcal{F}} \alpha' + g \mathcal{L}_{\mathcal{F}} \alpha'') \mathbf{d}r \wedge \mathbf{d}\theta \wedge \mathbf{d}\varphi \end{aligned} \quad (4.70)$$

The nonlinear Maxwell equations then read

$$\mathbf{d} \star (\mathcal{L}_{\mathcal{F}} \mathbf{F}) = 0 \iff \begin{cases} \dot{f} \mathcal{L}_{\mathcal{F}} \dot{\alpha} + f \mathcal{L}_{\mathcal{F}} \ddot{\alpha} + f \mathcal{L}_{\mathcal{F}} \ddot{\alpha} = -\Delta [f' \mathcal{L}_{\mathcal{F}} \alpha' + f \mathcal{L}'_{\mathcal{F}} \alpha' + f \mathcal{L}_{\mathcal{F}} \alpha''] , \\ \dot{g} \mathcal{L}_{\mathcal{F}} \dot{\alpha} + g \mathcal{L}_{\mathcal{F}} \ddot{\alpha} + g \mathcal{L}_{\mathcal{F}} \ddot{\alpha} = -\Delta [g' \mathcal{L}_{\mathcal{F}} \alpha' + g \mathcal{L}'_{\mathcal{F}} \alpha' + g \mathcal{L}_{\mathcal{F}} \alpha''] , \end{cases} \quad (4.71)$$

Hence, for $f, g \neq 0$, a necessary condition for the equations to be satisfied is $f = g$. Therefore, there exists no solution for a generic $M(r)$.

Notice that we recover easily the static case. For $a = 0$, $g = 0$ and the equation for g is trivially satisfied. Moreover, the spacetime is spherically symmetric and $\mathcal{L}_{\mathcal{F}} = \mathcal{L}_{\mathcal{F}}(\mathcal{F})$ depends only on r , since $\mathcal{F} = \mathcal{F}(r)$. Then, the equation for f reduces to

$$\dot{f} \dot{\alpha} + f \ddot{\alpha} = 0 . \quad (4.72)$$

This equation is indeed satisfied for the Maxwell field used for Bardeen's and Hayward's solutions:

$$\alpha = -g \cos \theta . \quad (4.73)$$

3.2.2 Electromagnetic source

Let us now investigate the situation described by the vector potential of Toshmatov et al. (eq. (4.57)):

$$\mathbf{A} = -\frac{Q_m a \cos \theta}{\Sigma} \mathbf{d}t + \frac{Q_m (r^2 + a^2) \cos \theta}{\Sigma} \mathbf{d}\varphi . \quad (4.74)$$

We will not begin with Einstein's equations, but with the nonlinear Maxwell equations. As we shall see, they will give us a very strong constraint on the possible lagrangians \mathcal{L} , that we will then implement in Einstein's equations.

Due to the t -component of \mathbf{A} , the electromagnetic field will possess both electric and magnetic nonzero components:

$$\begin{aligned} \mathbf{F} = & -\frac{2Q_m a r \cos \theta}{\Sigma^2} \mathbf{d}t \wedge \mathbf{d}r + \frac{Q_m a \sin \theta (a^2 \cos^2 \theta - r^2)}{\Sigma^2} \mathbf{d}t \wedge \mathbf{d}\theta - \frac{2Q_m a^2 r \cos \theta \sin^2 \theta}{\Sigma^2} \mathbf{d}r \wedge \mathbf{d}\varphi \\ & - \frac{Q_m \sin \theta (r^4 + a^2 r^2 - (a^2 + r^2) a^2 \cos^2 \theta)}{\Sigma^2} \mathbf{d}\theta \wedge \mathbf{d}\varphi \end{aligned} \quad (4.75)$$

The electromagnetic field invariant $\mathcal{F} = F_{\mu\nu} F^{\mu\nu}$ then reads

$$\mathcal{F} = \frac{2(a^2 \cos^2 \theta + 2ar \cos(\theta) - r^2)(a^2 \cos^2 \theta - 2ar \cos(\theta) - r^2)Q_m^2}{\Sigma^4} , \quad (4.76)$$

and differs from the expression (4.58) of Toshmatov et al.

From eq. (4.75), we get

$$\mathbf{d} \star (\mathcal{L}_{\mathcal{F}} \mathbf{F}) = - \frac{2a^2 r \cos \theta \sin \theta \mathcal{L}'_{\mathcal{F}} + (r^2 - a^2 \cos^2 \theta) \dot{\mathcal{L}}_{\mathcal{F}}}{\Sigma^2} Q_m \mathbf{d}t \wedge \mathbf{d}r \wedge \mathbf{d}\theta$$

$$\frac{2a r (a^2 + r^2) \cos \theta \sin \theta \mathcal{L}'_{\mathcal{F}} + a \sin^2 \theta (r^2 - a^2 \cos^2 \theta) \dot{\mathcal{L}}_{\mathcal{F}}}{\Sigma^2} Q_m \mathbf{d}r \wedge \mathbf{d}\theta \wedge \mathbf{d}\varphi , \quad (4.77)$$

where $\mathcal{L}'_{\mathcal{F}} \equiv \frac{\partial \mathcal{L}_{\mathcal{F}}}{\partial r}$ and $\dot{\mathcal{L}}_{\mathcal{F}} \equiv \frac{\partial \mathcal{L}_{\mathcal{F}}}{\partial \theta}$. The nonlinear Maxwell equations thus reduce to

$$\mathbf{d} \star (\mathcal{L}_{\mathcal{F}} \mathbf{F}) = 0 \iff \begin{cases} 2a^2 r \cos \theta \sin \theta \mathcal{L}'_{\mathcal{F}} + (r^2 - a^2 \cos^2 \theta) \dot{\mathcal{L}}_{\mathcal{F}} = 0 , \\ 2a r (a^2 + r^2) \cos \theta \sin \theta \mathcal{L}'_{\mathcal{F}} + a \sin^2 \theta (r^2 - a^2 \cos^2 \theta) \dot{\mathcal{L}}_{\mathcal{F}} = 0 . \end{cases} \quad (4.78)$$

Hence,

$$\begin{cases} 2a r \cos \theta \sin \theta (r^2 + a^2 \cos^2 \theta) \mathcal{L}'_{\mathcal{F}} = 0 , \\ (r^2 - a^2 \cos^2 \theta) \left[a \cos^2 \theta + \frac{r^2}{a} \right] \dot{\mathcal{L}}_{\mathcal{F}} = 0 . \end{cases} \quad (4.79)$$

And finally:

$$\begin{cases} \mathcal{L}'_{\mathcal{F}} = 0 , \\ \dot{\mathcal{L}}_{\mathcal{F}} = 0 . \end{cases} \iff \mathcal{L}_{\mathcal{F}} = \text{cst.} \equiv \gamma \quad (4.80)$$

The choice of the constant does not affect the equations of motion (3.14), but it does change the energy-momentum tensor by a factor γ , and then Einstein's equations. We will then write

$$\mathcal{L} = \gamma \mathcal{F} . \quad (4.81)$$

Hence, the nonlinear Maxwell equations with the ansatz (4.57) must reduce to linear equations with a lagrangian proportional to the standard Maxwell lagrangian $\mathcal{L}_M = \mathcal{F}$.

Let us now solve Einstein's equations with an electromagnetic source described by the lagrangian $\mathcal{L} = \gamma \mathcal{F}$. As in Sec. 1.3.1 of Chap. 3, we use slightly different notations compared to the ones of Toshmatov et al. The action of nonlinear electrodynamics in curved spacetime reads:

$$S = \frac{1}{16\pi} \int d^4 x \sqrt{-g} (R + 16\pi \mathcal{L}(\mathcal{F})) . \quad (4.82)$$

Einstein's equations read

$$G_{\mu\nu} = 8\pi T_{\mu\nu} \quad (4.83)$$

with

$$\begin{aligned} T_{\mu\nu} &\equiv - \frac{2}{\sqrt{-g}} \frac{\delta S_{\text{mat}}}{\delta g^{\mu\nu}} \\ &= - \frac{2}{\sqrt{-g}} \frac{\delta}{\delta g^{\mu\nu}} \int d^4 x \sqrt{-g} \gamma \mathcal{F} \\ &= \mathcal{L} g_{\mu\nu} - 4 \mathcal{L}_{\mathcal{F}} F_{\mu}^{\alpha} F_{\nu\alpha} \end{aligned} \quad (4.84)$$

Note that these equations are rigorously equivalent to eq. (4.55) of Toshmatov et al., since our lagrangians are related by a factor $(-\frac{1}{16\pi})$.

With our expression (4.81) of the electromagnetic lagrangian, Einstein's equations read

$$G_{\mu\nu} = 8\pi\gamma \left(\mathcal{F} g_{\mu\nu} - 4F_\mu{}^\alpha F_{\nu\alpha} \right) \quad (4.85)$$

The independent components of the Einstein tensor are the following:

$$G^t_t = \frac{a^2 r^3 M'' - (a^4 r M'' + 2a^4 M') \cos^4 \theta + (2a^4 M' + (a^4 r - a^2 r^3) M'') \cos^2 \theta - 2(a^2 r^2 + r^4) M'}{\Sigma^3} \quad (4.86)$$

$$G^r_r = -\frac{2r^2 M'}{\Sigma^2} \quad (4.87)$$

$$G^\theta_\theta = -\frac{a^2 r \cos^2 \theta M'' + 2a^2 \cos^2 \theta M' + r^3 M''}{\Sigma^2} \quad (4.88)$$

$$G^\varphi_t = \frac{a r^3 M'' - 2a r^2 M' + (a^3 r M'' + 2a^3 M') \cos^2 \theta}{\Sigma^3} \quad (4.89)$$

$$G^\varphi_\varphi = \frac{(2(a^4 + 2a^2 r^2) M' + (a^4 r + a^2 r^3) M'') \sin^2 \theta - 2(a^4 + a^2 r^2) M' - (a^4 r + 2a^2 r^3 + r^5) M''}{\Sigma^3} \quad (4.90)$$

As concerns the components of the energy-momentum tensor, they read:

$$T^t_t = -\frac{2(a^2 \cos^2 \theta - 2a^2 - r^2) Q_m^2 \gamma}{\Sigma^3} \quad (4.91)$$

$$T^r_r = \frac{2Q_m^2 \gamma}{\Sigma^2} \quad (4.92)$$

$$T^\theta_\theta = -\frac{2Q_m^2 \gamma}{\Sigma^2} \quad (4.93)$$

$$T^\varphi_t = \frac{4Q_m^2 a \gamma}{\Sigma^3} \quad (4.94)$$

$$T^\varphi_\varphi = \frac{2(a^2 \cos^2 \theta - 2a^2 - r^2) Q_m^2 \gamma}{\Sigma^3} \quad (4.95)$$

Taking for instance the trace of Einstein's equations, one gets immediately $T^\mu_\mu = 0$ and thus

$$G^\mu_\mu = -\frac{2(rM'' + 2M')}{\Sigma} = 0, \quad (4.96)$$

hence

$$M'' = -\frac{2M'}{r} \quad (4.97)$$

Assuming eq. (4.97) holds, $G^\varphi_t = 8\pi T^\varphi_t$ yields

$$-\frac{4a r^2}{\Sigma^3} M' = \frac{32\pi \gamma a Q_m^2}{\Sigma^3}, \quad (4.98)$$

hence

$$M' = -\frac{8\gamma \pi Q_m^2}{r^2} \quad (4.99)$$

we will then write

$$M(r) = M_0 + \frac{8\gamma \pi Q_m^2}{r}, \quad (4.100)$$

where M_0 is a positive constant. This form of $M(r)$ is compatible with eq. 4.97, and is actually sufficient to solve all the remaining Einstein equations (see App. C.1.4 for details).

To conclude, there is thus no way of building a rotating regular black-hole metric from nonlinear electrodynamics with the electromagnetic field (4.75). This field however enables us, for $\gamma < 0$, to recover the Kerr-Newman metric [89] with electric charge $e = 4Q_m \sqrt{\pi|\gamma|}$:

$$\begin{aligned} ds^2 = & - \left(1 - \frac{2rM_0 - e^2}{\Sigma} \right) dt^2 - \frac{2a(2rM_0 - e^2)\sin^2\theta}{\Sigma} dt d\varphi + \frac{\Sigma}{\Delta} dr^2 + \Sigma d\theta^2 \\ & + \sin^2\theta \left(r^2 + a^2 + \frac{a^2(2rM_0 - e^2)\sin^2\theta}{\Sigma} \right) d\varphi^2, \end{aligned} \quad (4.101)$$

with

$$\Sigma \equiv r^2 + a^2 \cos^2\theta, \quad \Delta \equiv r^2 - 2M(r)r + a^2 + e^2. \quad (4.102)$$

4 Analytical study of geodesics

4.1 Circular orbits in the equatorial plane

4.1.1 Energy and angular momentum of a massive particle

Let us consider the geodesic motion of a test particle with momentum \mathbf{p} and mass $m_0 > 0$, following a circular orbit in the background of the metric (4.34). This motion occurs in the equatorial plane ($\theta = \pi/2$) due to the axisymmetry of the metric. Along with the property of stationarity, this also implies the existence of two Killing vectors $\xi = \partial_t$ and $\eta = \partial_\varphi$. The conserved energy and conserved angular momentum of the particle read:

$$\begin{aligned} E = -\xi \cdot \mathbf{p} &= -p^t (g_{tt} + g_{t\varphi} \Omega) \\ L = \eta \cdot \mathbf{p} &= p^t (g_{\varphi t} + g_{\varphi\varphi} \Omega), \end{aligned} \quad (4.103)$$

with $\Omega \equiv \frac{d\varphi}{dt}$.

The angular velocity Ω can be found by considering the Euler-Lagrange equation for a free particle whose Lagrangian is

$$\mathcal{L} = \frac{1}{2} g_{\mu\nu} \dot{x}^\mu \dot{x}^\nu, \quad (4.104)$$

with $\dot{x}^\mu \equiv \frac{dx^\mu}{d\lambda}$, where λ is an affine parameter. The Euler-Lagrange equation supplemented by the conditions for a circular orbit $\dot{r} = \ddot{r} = 0$ boils down to:

$$g_{tt,r} \dot{t}^2 + 2g_{t\varphi,r} \dot{t} \dot{\varphi} + g_{\varphi\varphi,r} \dot{\varphi}^2 = 0, \quad (4.105)$$

where the comma denotes a derivative with respect to the radial coordinate.

The angular velocity of a particle on a circular co- or contra-rotating orbit is then:

$$\Omega_{\pm} = \frac{-g_{t\varphi,r} \pm \sqrt{g_{t\varphi,r}^2 - g_{tt,r}g_{\varphi\varphi,r}}}{g_{\varphi\varphi,r}}. \quad (4.106)$$

The specific energy and angular momentum of a massive particle on a circular orbit in a stationary axisymmetric spacetime thus read:

$$\begin{aligned} \mathcal{E}_{\pm} &\equiv \frac{E_{\pm}}{m_0} = -\frac{g_{tt} + g_{t\varphi}\Omega_{\pm}}{\sqrt{-(g_{tt} + 2g_{t\varphi}\Omega_{\pm} + g_{\varphi\varphi}\Omega_{\pm}^2)}} \\ \mathcal{L}_{\pm} &\equiv \frac{L_{\pm}}{m_0} = \frac{g_{\varphi t} + g_{\varphi\varphi}\Omega_{\pm}}{\sqrt{-(g_{tt} + 2g_{t\varphi}\Omega_{\pm} + g_{\varphi\varphi}\Omega_{\pm}^2)}}. \end{aligned} \quad (4.107)$$

In the context of our metric (4.34), we obtain in the equatorial plane ($\theta = \pi/2$):

$$\begin{aligned} \mathcal{E}_{\pm} &= \frac{r^3 + a^2 r M'(r) - M(r)(a^2 + 2r^2 \mp 2ar\sqrt{A(r)})}{(r^3 - a^2 M(r) + a^2 r M'(r)) \sqrt{\frac{r^2 B_{\pm}(r)}{(r^3 - a^2 M(r) + a^2 r M'(r))^2}}} \\ \mathcal{L}_{\pm} &= \frac{-(a^3 + 3ar^2)M(r) + (a^3 r + ar^3)M'(r) \pm (a^2 r^2 + r^4 + 2a^2 r M(r))\sqrt{A(r)}}{(r^3 - a^2 M(r) + a^2 r M'(r)) \sqrt{\frac{r^2 B_{\pm}(r)}{(r^3 - a^2 M(r) + a^2 r M'(r))^2}}}, \end{aligned} \quad (4.108)$$

where

$$\begin{aligned} A(r) &= \frac{M(r)}{r} - M'(r) \\ B_{\pm}(r) &= -a^2 r^2 M'^2(r) + r^4 - 3a^2 M(r)^2 - 3(a^2 r + r^3)M(r) + (3a^2 r^2 + r^4 + 4a^2 r M(r))M'(r) \\ &\quad \pm 2[(a^3 + 3ar^2)M(r) - (a^3 r + ar^3)M'(r)]\sqrt{A(r)}. \end{aligned}$$

These expressions differ from Toshmatov et al. [113] (see App. C.1.3 for details and a comparison with the results of Bardeen et al. [14]).

Circular orbits can therefore exist only for $A(r) \geq 0$ and $B_{\pm}(r) > 0$. These three functions are plotted below, for $a/m = 0.9$ and $b/m = 1$. The regions of allowed co-rotating circular orbits are pictured in grey in Fig. 4.8. The region of positive r goes up to $r \rightarrow +\infty$, while the one of negative values of r exists only near the center. This is coherent, since from $r \rightarrow -\infty$ the metric (4.34) behaves as a Schwarzschild metric with negative mass: the repulsive gravity does not allow circular orbits for large enough negative radii.

4.1.2 Influence of the spin

Let us study how the regions of allowed circular orbits are modified when the spin varies. First of all, it should be noted that $A(r)$ does not depend on the value of the spin. Hence for a

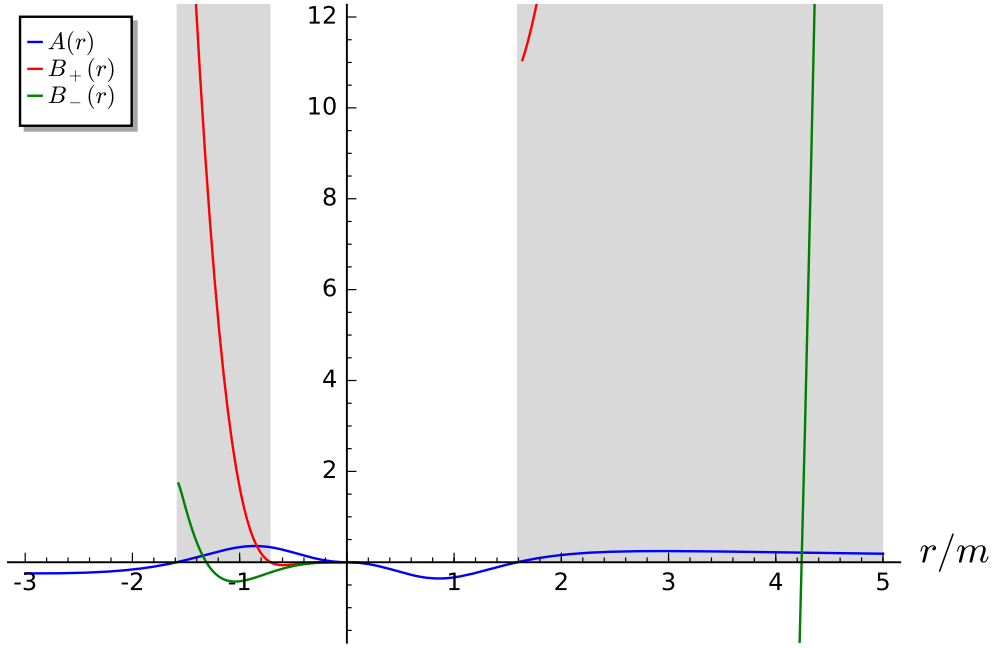


Figure 4.8: Plot of $A(r)$, $B_+(r)$ and $B_-(r)$ in the case $a/m = 0.9$, $b/m = 1$. The shaded regions represent the zones where circular orbits are allowed.

fixed b , e.g. $b/m = 1$ like in Fig. 4.8, the shaded regions will be modified only if $B_{\pm}(r)$ changes. As shown in Fig. 4.9, decreasing the value of a only widens the zone of circular orbits below $r = 0$. It thus does not have any impact on the allowed circular orbits with $r > 0$.

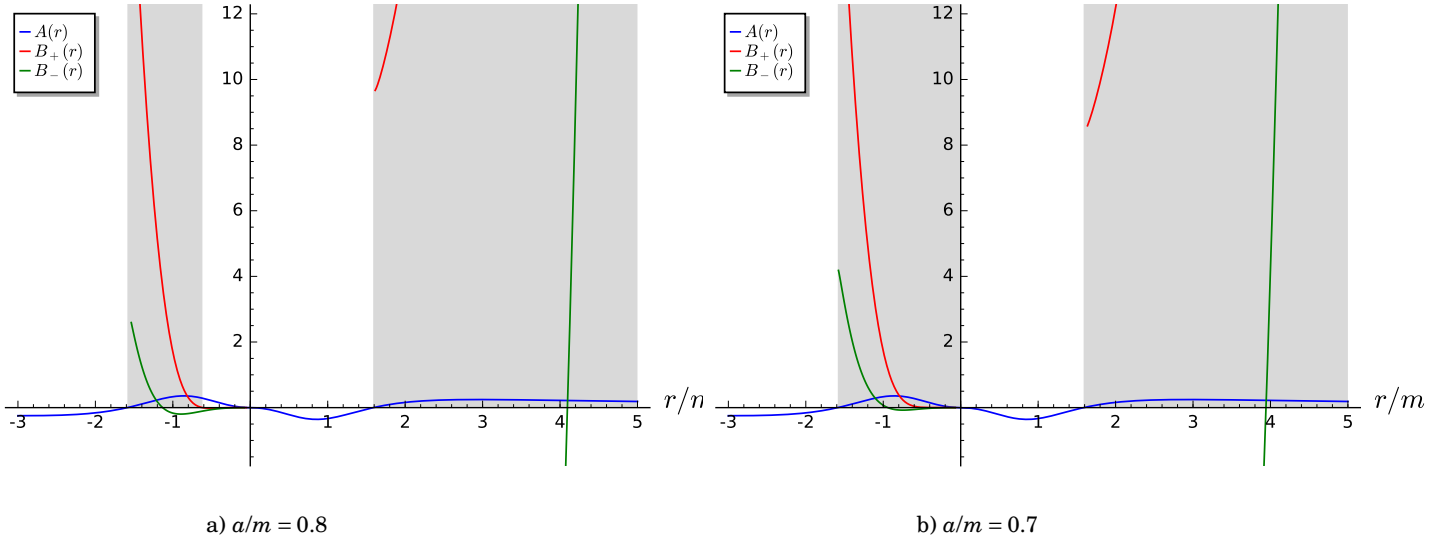


Figure 4.9: Plot of $A(r)$, $B_+(r)$ and $B_-(r)$ in the case $b/m = 1$, for two different values of the spin. The shaded region for the negative values of r gets wider as a decreases.

4.1.3 Influence of the parameter b

Contrarily to the spin, the parameter b has a direct influence on the region of allowed circular orbits of positive radius. Going from $b/m = 1$ (Fig. 4.8) to $b/m = 0.7$ and $b/m = 0.4$ (Fig. 4.10), at a constant $a/m = 0.9$, we observe that circular orbits can occur for smaller and smaller positive values of r .

Meanwhile, the region of allowed circular orbits with negative radius shrinks as b decreases. This region even disappears for $b/m = 0$, as one can see in Fig. 4.11(b) below. In this configuration, two horizons exist and circular orbits occur only for values of the radial coordinate above the radius of the outer horizon. For $b/m = 0.2$ (Fig. 4.11(a)), some circular orbits can also occur below the radius of the inner horizon.

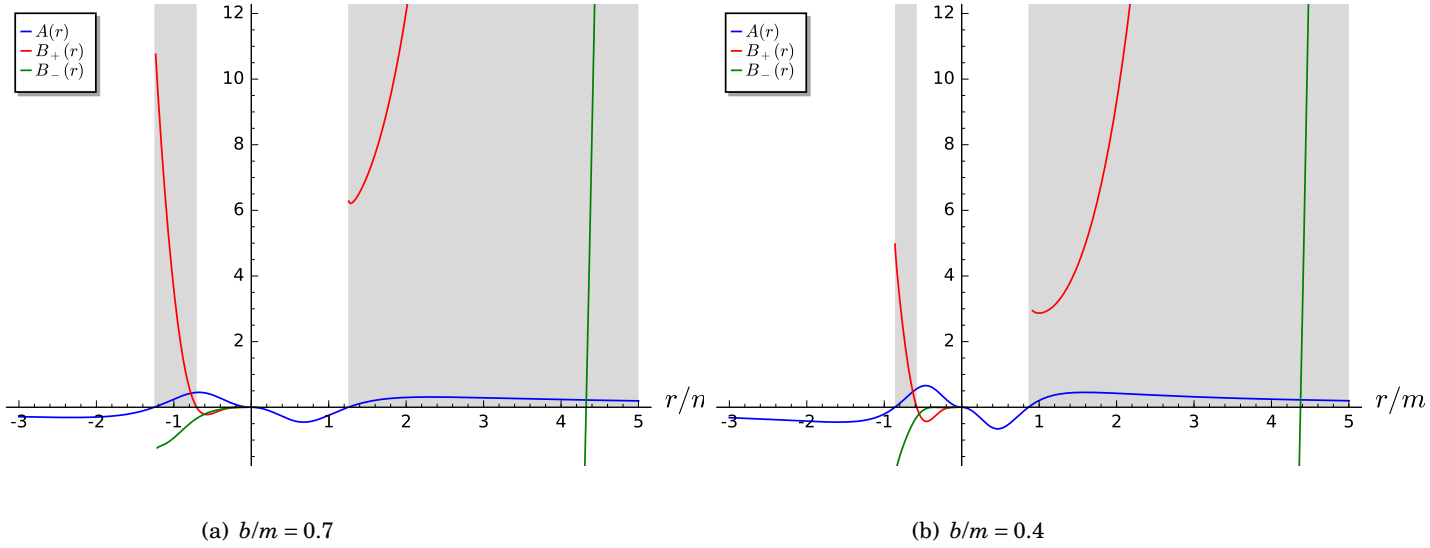


Figure 4.10: Plot of $A(r)$, $B_+(r)$ and $B_-(r)$ in the case $a/m = 0.9$ for two different values of b . The shaded region for the negative (resp. positive) values of r gets narrower (resp. wider) as b decreases.

4.1.4 Innermost stable circular orbit (ISCO)

The *innermost stable circular orbit (ISCO)*, which corresponds to the stable circular orbit of smallest r , is astrophysically relevant since it provides the highest orbital frequency possible around the central object. In particular, the ISCO frequency is involved in various models of quasi-periodic oscillations (QPO) [100].

In the Kerr case, it has been shown by Carter [32] that the radial geodesic motion is governed

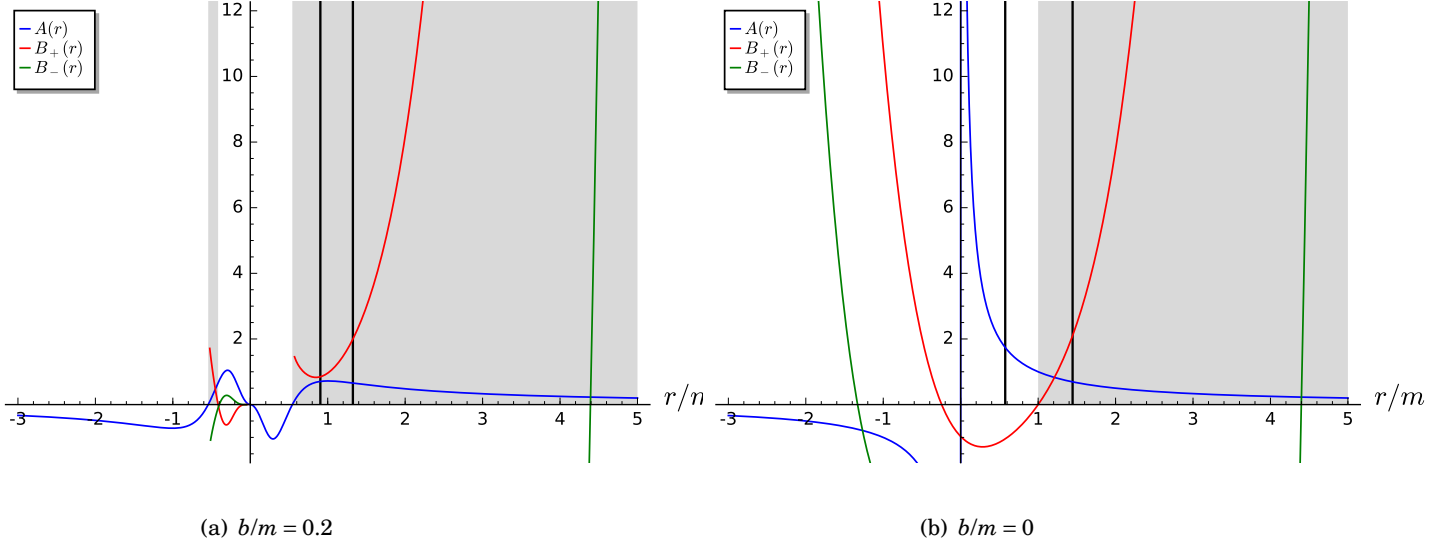


Figure 4.11: Plot of $A(r)$, $B_+(r)$ and $B_-(r)$ in the case $a/m = 0.9$, in the presence of two horizons (black vertical lines), for two different values of b .

by the following relation:

$$\Sigma \frac{dr}{d\lambda} = \sqrt{\mathcal{R}} \quad (4.109)$$

$$\mathcal{R} = [(r^2 + a^2)E - aL]^2 - \Delta [(aE - L)^2 + m_0^2 r^2 + \mathcal{Q}],$$

where λ is an affine parameter, m_0 the mass of the particle, and \mathcal{Q} , E , L are the three integrals of motion (respectively the Carter constant, the energy and the angular momentum of the test particle). The zeros of \mathcal{R} thus represent turning points of the motion of such a test particle in Kerr's spacetime.

Stable circular orbits are defined by the three conditions

$$\mathcal{R}(r) = 0, \quad \frac{d\mathcal{R}(r)}{dr} = 0, \quad \text{and} \quad \frac{d^2\mathcal{R}(r)}{dr^2} \leq 0. \quad (4.110)$$

The frequency (4.106) of a particle following a circular orbit reads:

$$\Omega_{\pm} = \frac{4ab^2m^2r - amr^4 \pm (4b^4m^2 + 4b^2mr^3 + r^6) \sqrt{-\frac{4b^2m^2r^2 - mr^5}{4b^4m^2 + 4b^2mr^3 + r^6}}}{r^7 - (a^2 - 4b^2)mr^4 + 4(a^2b^2 + b^4)m^2r} \quad (4.111)$$

The ISCO values of the radius and the orbital frequency (4.111), for co-rotating and contra-rotating orbits in the equatorial plane ($\mathcal{Q} = 0$), have been computed for different values of a and b (see App. C.1.3 for details). The result is shown in Table 4.1.

$b/m \backslash a/m$	0	0.5	1
0	<div>6m +3.20 mHz</div> <div>6m -3.20 mHz</div>	<div>5.84m +3.31 mHz</div> <div>5.84m -3.31 mHz</div>	<div>5.19m +3.86 mHz</div> <div>5.19m -3.86 mHz</div>
0.5	<div>4.23m +5.10 mHz</div> <div>7.55m -2.32 mHz</div>	<div>3.82m +5.80 mHz</div> <div>7.46m -2.36 mHz</div>	<div>1.59m +1.08 mHz</div> <div>7.14m -2.50 mHz</div>
0.9	<div>2.32m +10.6 mHz</div> <div>8.72m -1.89 mHz</div>	<div>1.04m +8.54 mHz</div> <div>8.65m -1.91 mHz</div>	<div>1.59m +1.07 mHz</div> <div>8.43m -1.98 mHz</div>

Table 4.1: Radial coordinate of the ISCO and orbital frequency of a test particle at the ISCO for various values of the parameters a/m and b/m , and $m = m_{\text{SgrA}^*}$. Four different results are associated with each combination of a/m and b/m : the radius of the ISCO (left) and the frequency Ω of the co-rotating (resp. contra-rotating) orbit (right) are located on the upper (resp. lower) pannel. The dark grey boxes correspond to the classical Kerr (and Schwarzschild for $a = 0$) black hole, the light grey boxes to the regime of rotating regular black hole (zones II and III of Fig. 4.5), while the others are associated with a naked rotating wormhole (zone IV of Fig. 4.5).

4.2 Null geodesics

Let us now focus on the propagation of light rays in order to understand the images that can be seen by an observer on Earth, such as the ones we will show in Chap. 5. Due to (4.109), in which we now take $m_0 = 0$, the condition for the existence of a photon of energy E with angular momentum L and Carter's constant \mathcal{Q} is

$$[(r^2 + a^2)E - aL]^2 - (r^2 + a^2 - 2rM(r))[(aE - L)^2 + \mathcal{Q}] \geq 0, \quad (4.112)$$

with $M(r)$ given by eq. (4.35).

In the case of a Kerr spacetime, $M(r) = m$ and eq. (4.112) is polynomial in r , of degree 4. It can then be shown that a photon trajectory has at most one radial turning point in the black hole exterior [56]. Here, due to the form (4.35) of $M(r)$, eq. (4.112) reduces to a polynomial equation of degree 7. The phenomenology is thus much richer than in Kerr's case. In particular, some photon trajectories can have more than one radial turning point. This is illustrated in Fig. 4.12 below. The central shaded region of the right panel is particularly striking: photons with energy E_0 ,

angular momentum L_0 and a Carter constant \mathcal{Q}_0 can oscillate back and forth between two radial turning points, around $r = 0$.

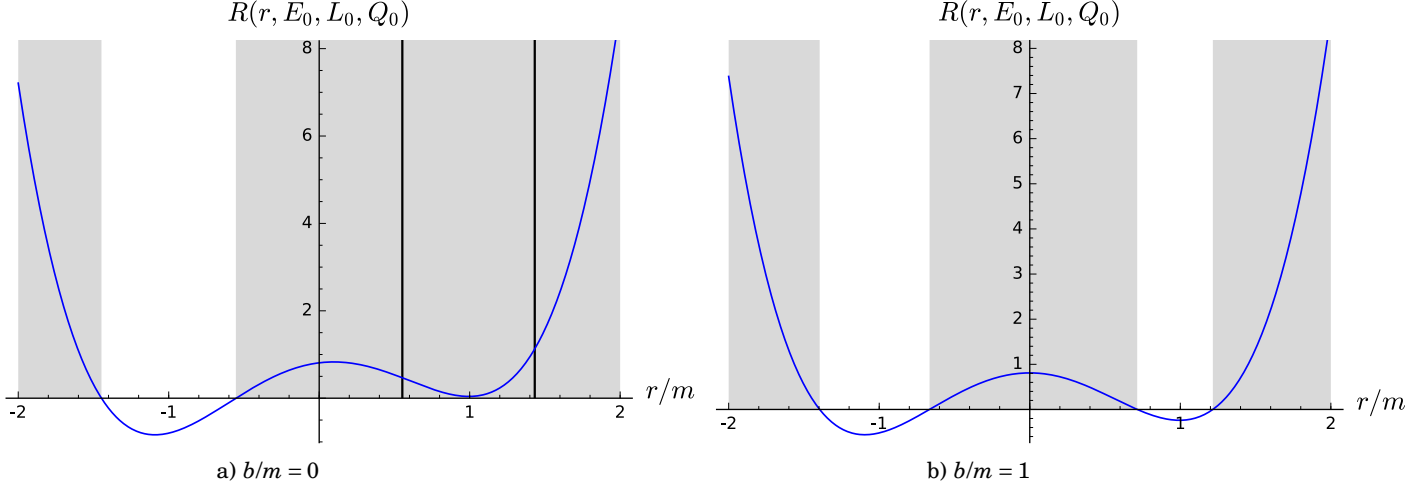


Figure 4.12: Plot of \mathcal{R} as a function of the radial coordinate r/m . The shaded regions represent the allowed regions for a photon with $E_0/m = 1$, $L_0/m = 2$, $\mathcal{Q}_0/m^2 = -1$, in the case of a rotating Hayward black hole with $a/m = 0.9$ and $b/m = 0$ (a) (the black lines denote the outer and inner horizons) and of a naked rotating wormhole with $b/m = 1$ (b).

This analysis, using the inequality (4.112), also allows us to understand the behaviour of photons travelling into the region with $r < 0$ before reaching an observer on Earth, whose trajectories will be studied in detail in Sec. 3.2.2 of Chap. 5. Fig. 4.13 shows the allowed region for a photon with $E_1/m = 1$, $L_1/m = -2$, $\mathcal{Q}_1/m^2 = -1$ in two different cases: $b/m = 0$ (left) and $b/m = 1$ (right), while $a/m = 0.9$. One can see that in both cases, a photon going from $r > 0$ to $r < 0$ has a radial turning point and goes back to the region with positive radial coordinate. However, in the case $b/m = 0$ where a trapped region is located between the two trapping horizons (black vertical lines), this photon cannot cross the inner horizon and thus reach the observer. When $b/m = 1$ no horizon is present, which allows a photon from the accretion torus to travel towards the region $r < 0$, reach a turning point and then an observer on Earth.

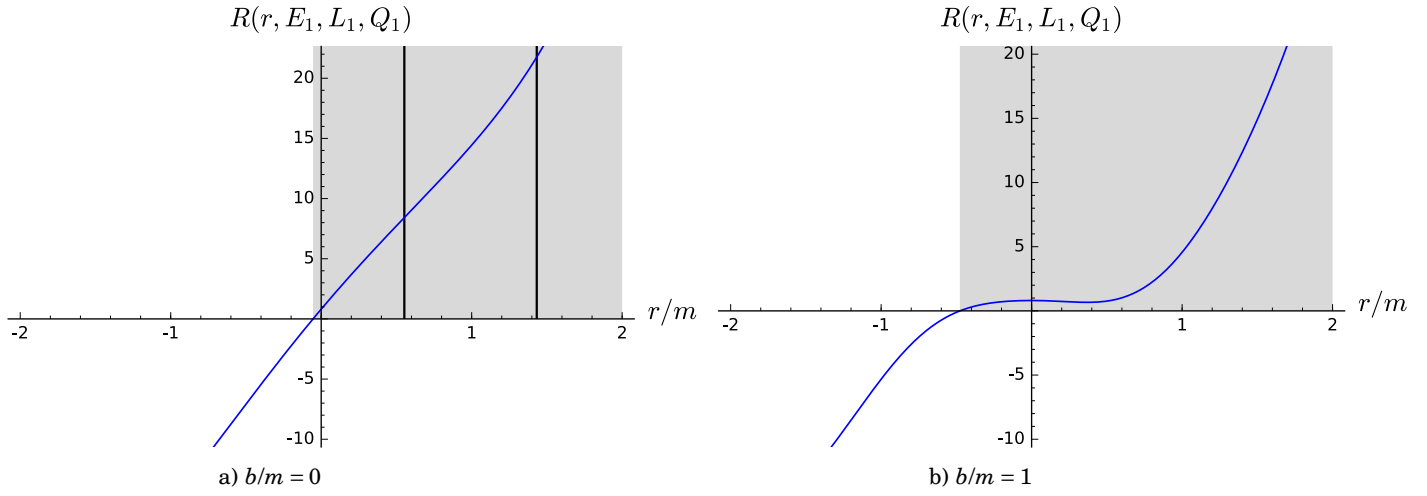


Figure 4.13: Plot of \mathcal{R} as a function of the radial coordinate r/m . The shaded regions represent the allowed regions for a photon with $E_1/m = 1$, $L_1/m = -2$, $\mathcal{Q}_1/m^2 = -1$, in the case of a rotating Hayward black hole with $a/m = 0.9$ and $b/m = 0$ (a) (the black lines denote the outer and inner horizons) and of a naked rotating wormhole with $b/m = 1$ (b).

SIMULATING A ROTATING NON-SINGULAR BLACK HOLE AT THE CENTER OF THE GALAXY



j~n=j mjn m dr.w 3h.t p.t

“C’est des confins de l’horizon du ciel que je suis venu ici.”

(*Textes des Sarcophages* VII, 313d, B2L [30, 43].)

This chapter aims at presenting the numerical results we obtained with E. Gourgoulhon, T. Paumard and F. Vincent in [80]. These results concern ray-traced images of the regular rotating Hayward model introduced in Chap. 4, surrounded by an accretion torus playing the role of the light source. A ray-traced image is defined as a set of pixels, each corresponding to a photon with given specific intensity and whose null geodesic is integrated backward in time. Both the regular rotating black hole and naked rotating wormhole regimes will be investigated in Sec. 3. Before that, we will explain the general features of black hole images, which stem from the properties of the spherical photon orbits around the hole, all located inside the *photon region* whose shape will be examined (Sec. 1). Of the uttermost importance will be the *shadow*, delineated in the numerical computations by a *photon ring*, which is a central dark region that light rays never reach due to their capture by the black hole. To make connections with the observations, and in particular the forthcoming results of the Event Horizon Telescope, the simulations are performed with an astrophysical model compatible with the known data on Sagittarius A* (Sgr A*), the black hole at the center of the Milky Way, that we present in Sec. 2 along with the ray-tracing code GYOTO used for the numerical simulations. A special emphasis is put on the the *Hayward plugin* I specifically developed in my thesis to describe our regular rotating Hayward model.

Contents

1	General features of black hole images	132
2	Astrophysical and numerical set-up	141
3	Images of the regular rotating Hayward model	149

1 General features of black hole images

1.1 First approach

Before showing the first ray-traced images of a black hole, let us anticipate on what one should expect to see. Since a black hole (e.g., Kerr’s black hole) possesses a trapped region from which light rays cannot escape, one should expect that some of the light rays emitted by a source behind the black hole will never reach an observer located on the other side of the hole. The *shadow* is precisely the region, in an observer’s sky, that would receive light solely from inside the outer trapping horizon¹ if it were to (classically) emit some [38]. In other words, performing a backwards ray-tracing computation, all photons on the shadow will cross the horizon.

From this definition, we are almost led to think that the shadow is merely the image of the outer horizon on the observer’s sky. Actually, that would amount to considering a black hole only as an absorbing sphere in flat spacetime, which it is not. Indeed, one should not forget that a black hole significantly curves spacetime in its neighbourhood, and actually many light rays that would not have reached the horizon in a flat spacetime will be bent and eventually fall into the horizon. This curvature of spacetime reveals itself by the presence of photon orbits in Kerr’s spacetime, i.e. of trajectories with constant r . These orbits, when unstable, can lead photons to either fall into the horizon or be ejected at infinity, hence possibly reaching the observer.

It will thus be necessary to understand the properties of these photon orbits (Sec. 1.2) before explaining the main features of a typical black hole image, and in particular of its shadow (Sec. 1.3).

1.2 Photon region

1.2.1 Definition

The existence of photon orbits can be inferred from the study of null geodesics, whose equations were first given by Carter [32] for Kerr’s metric. They also apply for a more general metric, where we allow M to depend on r : $M \rightarrow M(r)$ (see [115] for instance). It is precisely for this metric that we will investigate the shape of the photon sphere, so that we can apply it both to Kerr’s spacetime and to our rotating Hayward model.

The r -motion of a null geodesic is governed by

$$\left(\frac{\Sigma}{E}\right)^2 \left(\frac{dr}{d\lambda}\right)^2 = \mathcal{R}(r) \equiv [(r^2 + a^2) - a\varphi]^2 - \Delta [(a - \varphi)^2 + \mathcal{Q}] , \quad (5.1)$$

¹in this Chapter, it will be referred as outer horizon without ambiguity. We choose not to call it an event horizon, since the latter notion requires the knowledge of the full spacetime.

which corresponds to eq. (4.109) with a massless particle ($m_0 = 0$), and where we have defined the dimensionless angular momentum and Carter constant $\varphi = \frac{L}{E}$, $\mathcal{Q} = \frac{Q}{E^2}$.

Besides, the θ -motion is governed by

$$\left(\frac{\Sigma}{E}\right)^2 \left(\frac{d\theta}{d\lambda}\right)^2 = \Theta(\theta) \equiv \mathcal{Q} + \left(a^2 - \frac{\varphi^2}{\sin^2 \theta}\right) \cos^2 \theta. \quad (5.2)$$

Let us focus on the *spherical orbits*² of photons, which have a constant radius r . At this radius, one must then have

$$\mathcal{R}(r) = \mathcal{R}'(r) = 0. \quad (5.3)$$

This leads to the following two equations

$$\mathcal{R}(r) = 0 \iff \mathcal{Q} = \frac{[(r^2 + a^2) - a\varphi]^2}{\Delta} - (a - \varphi)^2 \quad (5.4)$$

$$\mathcal{R}'(r) = 0 \iff \mathcal{Q} = \frac{4r[(r^2 + a^2) - a\varphi]}{\Delta'} - (a - \varphi)^2. \quad (5.5)$$

Combining eqs. (5.4) and (5.5), a first solution is

$$\begin{cases} \varphi = \frac{r^2 + a^2}{a} \\ \mathcal{Q} = -\frac{r^4}{a^2}, \end{cases} \quad (5.6)$$

However, as in Kerr's case this solution is unphysical since it leads to $\dot{\theta}^2 < 0$ (see [107] for details). Let us then consider the other solution, obtained for $\varphi \neq \frac{a^2 + r^2}{a}$:

$$\begin{cases} \varphi_0 = \frac{r^2 + a^2}{a} - \frac{4r\Delta}{a\Delta'} \\ \mathcal{Q}_0 = \frac{16r^2\Delta}{\Delta'^2} - (a - \varphi)^2, \end{cases} \quad (5.7)$$

Let us now study the θ -motion described by eq. (5.2), which can also be written

$$\left(\frac{\Sigma}{E}\right) \dot{\theta}^2 = \mathcal{Q} + (a - \varphi)^2 - \frac{(a \sin^2 \theta - \varphi)^2}{\sin^2 \theta}. \quad (5.8)$$

Plugging the expressions (5.7) in eq. (5.8), and requiring that the θ -motion be allowed ($\dot{\theta}^2 \geq 0$), yields after a straightforward calculation

$$16r^2 a^2 \Delta \sin^2 \theta \geq (4r\Delta - \Sigma\Delta')^2 \quad (5.9)$$

This inequality defines the *photon region* \mathcal{K} in which a spherical orbit goes through every point (r, θ) .

Note that we recover the results of Teo [107] in the limit $M = \text{cst}$. This result is also consistent with Grenzebach's, applying to a more general class of spacetimes (eq. (3.7) in [65]). Finally, we

²Rigorously, the term "spherical orbits" is specific to Kerr's black hole. The more general *fundamental photon orbits* can be defined in stationary and axisymmetric spacetimes [39], and reduce to spherical orbits in Kerr's spacetime

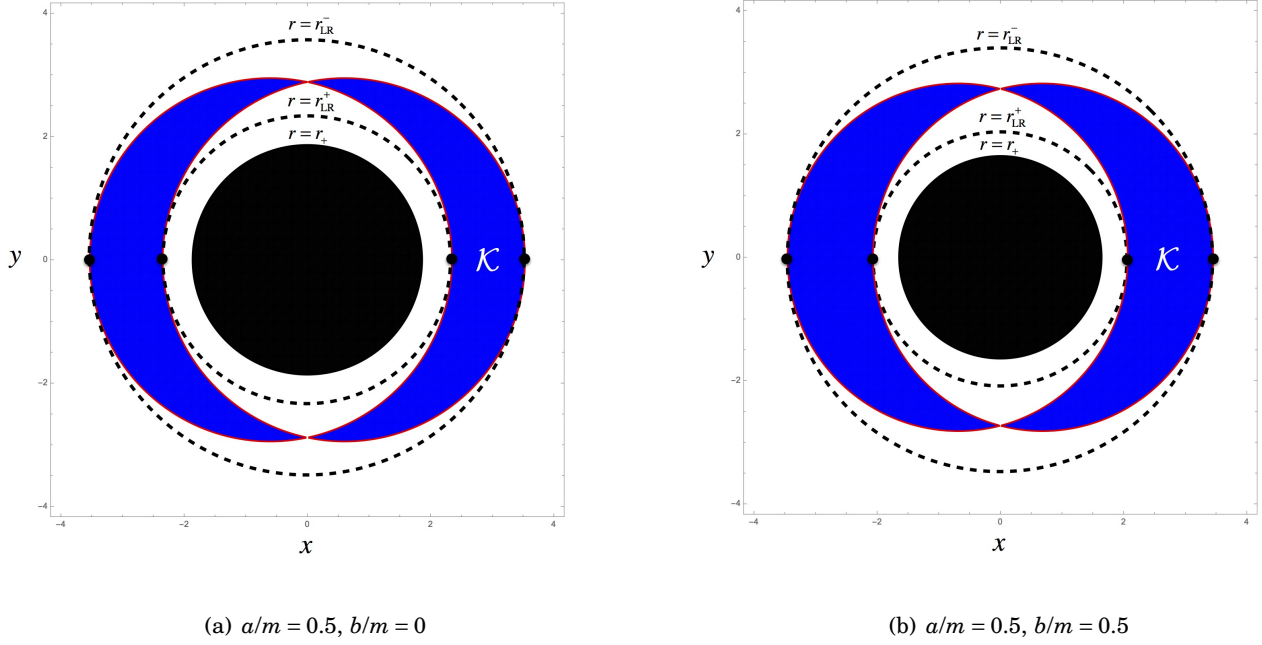


Figure 5.1: Plot of the photon region \mathcal{K} for two configurations of the parameter b corresponding to regular rotating Hayward black holes, on meridional sections of the black hole. The coordinates satisfy $x^2 + y^2 = r^2$ and $x = r \cos \theta$, and the trapped region below the photon region is represented as a black disk.

should recover the photon sphere of Schwarzschild's spacetime in the limit $a = 0$ and $M = M_0$. Indeed, eq. (5.9) becomes

$$(2r(r^2 - 2M_0r) - (r - M_0)r^2)^2 \leq 0 \quad (5.10)$$

This must thus be an equality, which yields $r = 3M_0$: the well known radius of the photon sphere in Schwarzschild's spacetime.

The photon region \mathcal{K} for a Kerr spacetime with $a/M = 0.5$ is plotted in blue in Fig. 5.1(a). Spherical orbits correspond to arcs of circle of constant r inside the photon region (blue crescent). The motion along θ occurs along this arc of circle, while the motion along φ is to be imagined in the plane perpendicular to the Figure.

All photon orbits satisfy $r_{\text{LR}}^+ \leq r \leq r_{\text{LR}}^-$, where r_{LR}^- and r_{LR}^+ are actually two circular orbits in the equatorial plane, called *light rings*. This property of the light rings is evident from Fig. 5.1(a), where they are represented by black dots. Indeed, the only photon orbits in region \mathcal{K} that cannot move along the θ direction are the ones at the crossing of the equatorial plane and the boundary of \mathcal{K} (i.e. the black dots), which must then stay confined in the equatorial plane. More formally, this can be shown easily by writing down the conditions for the orbit to be at the crossing of the

equatorial plane and the boundary of \mathcal{K} :

$$\begin{cases} \theta = \frac{\pi}{2} \\ 16r_{\text{LR}}^{\pm 2} a^2 \Delta = \left(4r_{\text{LR}}^{\pm} \Delta - r_{\text{LR}}^{\pm 2} \Delta' \right)^2, \end{cases} \quad (5.11)$$

It is then straightforward to show, from eq. (5.7),

$$\mathcal{Q} \left(r = r_{\text{LR}}^{\pm}, \theta = \frac{\pi}{2} \right) = 0. \quad (5.12)$$

Hence, from eq. (5.2), we immediately get $\dot{\theta} = 0$: the photon orbit is indeed confined to the equatorial plane.

One may wonder why there are two circular photon orbits in Kerr's spacetime, while there is only one circular photon orbit (in the equatorial plane) in Schwarzschild's spacetime (located at $r = 3M_0$). Actually, this is due to the rotation of Kerr's spacetime, which by the property of dragging of inertial frames (see Sec. 3.1.1 of Chap. 2) facilitates the co-rotating circular orbit at $r = r_{\text{LR}}^+$ and makes it harder for a counter-rotating circular orbit ($r_{\text{LR}}^- > r_{\text{LR}}^+$).

To conclude this subsection, let us show the shapes of the photon region in our rotating regular model, described by eq. (4.34)-(4.35) of Chap. 4. In the case of the rotating regular black hole (Fig. 5.1(b)), the photon region is very similar to the one with same spin ($a/m = 0.5$) and vanishing b . The crescent shape is only slightly larger, while the radius of the outer horizon is smaller.

The naked rotating wormhole, however, provides very different examples of photon regions. Fig. 5.2 displays such photon regions in the configurations $a/m = 0.9$ and $b/m = 0.4$ (panel 5.2(a)) and $a/m = 0.9$ and $b/m = 0.7$ (panel 5.2(b)). As we will see later, part of these orbits actually are stable and might thus be a potential threat to the stability of the considered space-time.

1.2.2 Stability of photon orbits

As explained before, the study of the stability of photon orbits is of primary importance: unstable orbits can be followed by photons which then either fall into the horizon or escape to infinity, hence potentially reaching the observer and modifying the image of the black hole.

An unstable orbit at $r = r_0$ is characterized by

$$\mathcal{R}''(r) \Big|_{r=r_0} > 0, \quad (5.13)$$

where $\mathcal{R}''(r)$ is evaluated for φ and \mathcal{Q} taking their values (5.7).

in Fig. 5.3 are plotted the $r \geq 0$ meridional sections of our rotating regular model, for various values of a and b . Each figure consists in the juxtaposition of two slices of constant φ and $-\varphi$,

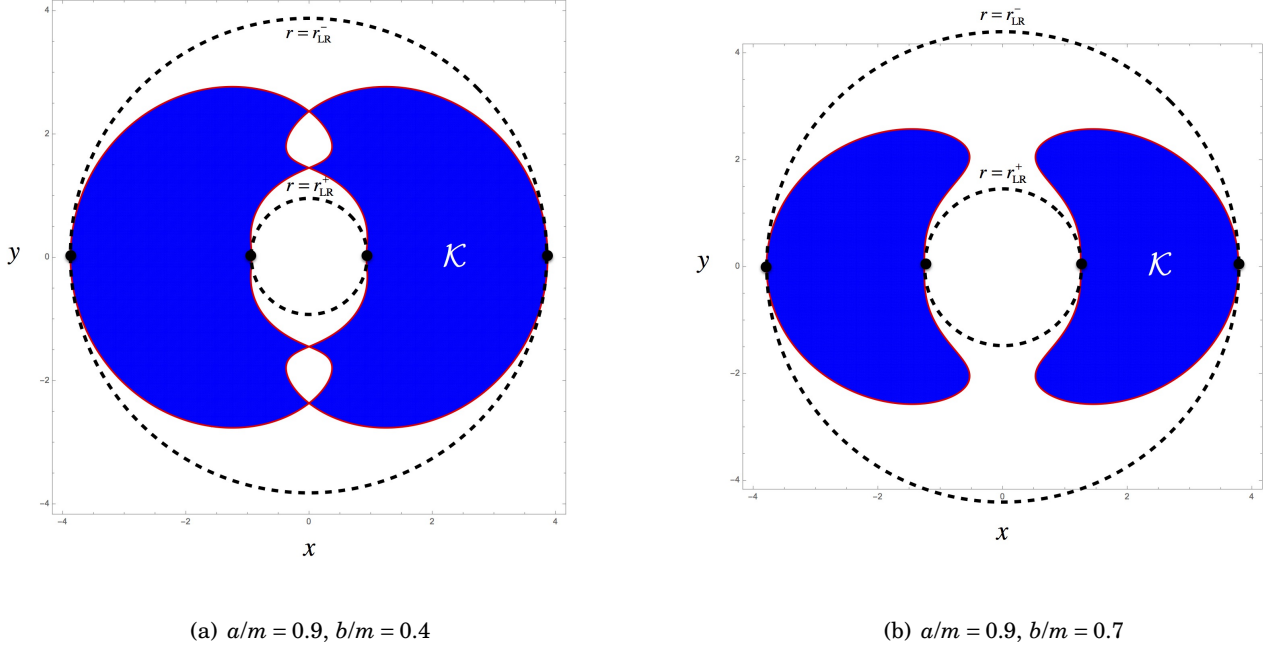


Figure 5.2: Plot of the photon region \mathcal{K} for two configurations of the parameter b corresponding to a naked rotating wormhole, on meridional sections of the wormhole. The coordinates satisfy $x^2 + y^2 = r^2$ and $x = r \cos \theta$, and no black disk is present since there is no trapped region.

separated by the vertical axis of rotation $\theta = 0$ (not represented). The photon region is pictured in blue for unstable orbits, and orange for the stable ones. When an outer horizon exists, it is depicted as a black disk preventing any communication towards the outer domain. The value of a/m increases from left to right, while that of b/m decreases from top to bottom. The bottom row corresponds to $b = 0$, i.e. to Kerr's case: we recover the well known result that spherical orbits are unstable in Kerr's spacetime [107]. It appears that for a value of b large enough so that no horizon is present, stable spherical orbits start to exist. Such a property of a spacetime often makes it unstable, since it can store and focus energy on these orbits (such as gravitational radiation).

A very characteristic phenomenon occurs for increasing values of b/m at constant a/m , i.e. in each row of Fig. 5.3 from bottom to top. First, when an outer horizon is present, the photon region intersects the axis $\theta = 0$ twice. Then, after the disappearance of the outer horizon, there are four points of intersection (two for stable orbits, two for unstable orbits). And finally, for a high enough value of b/m , the photon region does not intersect the axis $\theta = 0$ anymore. This seems to have noticeable effects on the images computed with the ray-tracing code GYOTO, as we shall see in Sec. 3.

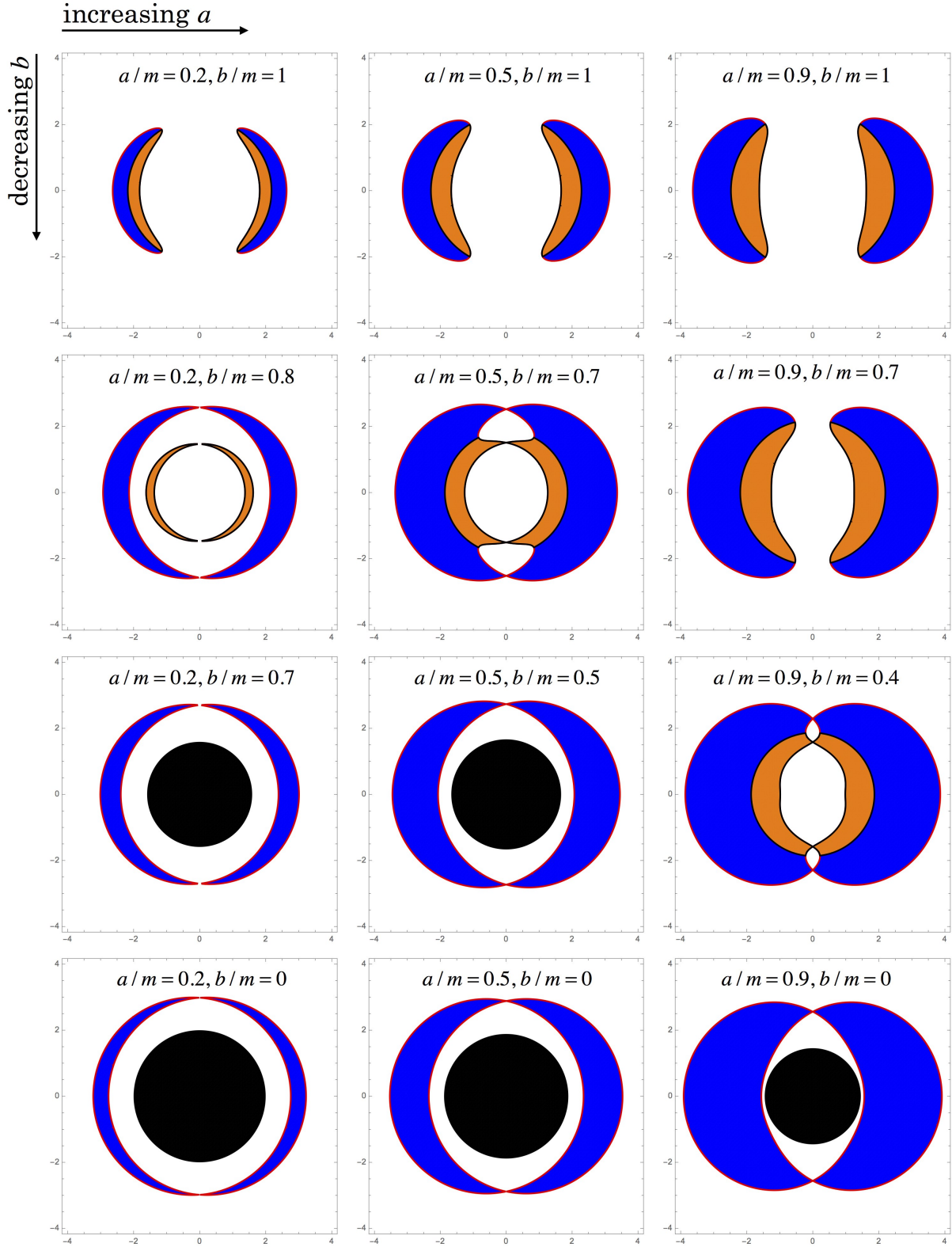


Figure 5.3: Computation of photon regions for various values of a and b . The unstable stable photon regions are represented in blue, the stable ones in orange and the trapped region as a black disk when it exists.

1.3 Structure of a typical black hole image

1.3.1 The Kerr shadow

We have spent quite some time studying the photon region, and in particular the unstable photon orbits. The reason is that the shadow of a Kerr black hole can be understood from the trajectories of photons following these unstable orbits. These photons, as soon as a perturbation occurs, will either travel towards decreasing values of r , and hence cross the horizon, or be ejected outwards, and potentially reach an observer. The boundary of the shadow is thus to be defined as the locus of points in the observer's sky associated to geodesics that barely skim the spherical photon orbits (as stated in [38]). Hence, all spherical orbits with radius $r \in [r_{\text{LR}}^+, r_{\text{LR}}^-]$ contribute to the edge of the shadow, since any of them can be approached by a null geodesic ray-traced backward in time from the observer.

Let us illustrate this with the explicit computation of Kerr's shadow, first performed by Bardeen in 1972 [12]. The edge of the shadow seen from an angle $\theta_0 = \frac{\pi}{2}$ satisfies, on a sphere with celestial coordinates (α, β) , the parametric equations

$$\begin{cases} \alpha(r) = -\varphi_0(r), \\ \beta(r) = \pm \sqrt{\mathcal{Q}_0(r)}, \end{cases} \quad (5.14)$$

where $\varphi_0(r)$ and $\mathcal{Q}_0(r)$ are the constants of motion for particles inside the photon region, and are thus defined only for $r \in [r_{\text{LR}}^+, r_{\text{LR}}^-]$. The edge of Kerr's shadow can then be obtained on a parametric plot with axes $(\alpha(r), \beta(r))$, while r goes from r_{LR}^+ to r_{LR}^- .

The plot of the shadow's edge is shown in Fig. 5.4. The blue curve represents the solution $\beta(r) = +\sqrt{\mathcal{Q}_0(r)}$ and the yellow one the solution $\beta(r) = -\sqrt{\mathcal{Q}_0(r)}$. The parametric plot starts at $r = r_{\text{LR}}^+$ (left black dot) and ends at $r = r_{\text{LR}}^-$ (right black dot), hence following the direction of the arrows. Otherwise, a given value of $r \in]r_{\text{LR}}^+, r_{\text{LR}}^-[$ is associated with two distinct points of the shadow's edge. Hence, the whole photon region contributes to the shadow's edge.

Let us now propose a more precise description of the link between the photon region and the edge of Kerr's shadow. This viewpoint is summarized in Fig. 5.5, displaying the photon region (left) and the shadow's edge of a Kerr black hole with spin $a/m = 0.5$ seen by an observer from an angle $\theta_0 = \pi/2$. On the photon region (in blue, with a red boundary), 5 different classes of spherical photon orbits are shown. From left to right, the light ring with $r = r_{\text{LR}}^-$ is the first counter-rotating³ orbit. It is represented by the points 7 and 7', at which the orbiting photon is moving perpendicularly to the plane of the image and respectively away from or towards the reader.

The next class of orbit corresponds to the black arc of circle and is again counter-rotating. The

³i.e., with $\dot{\varphi} < 0$.

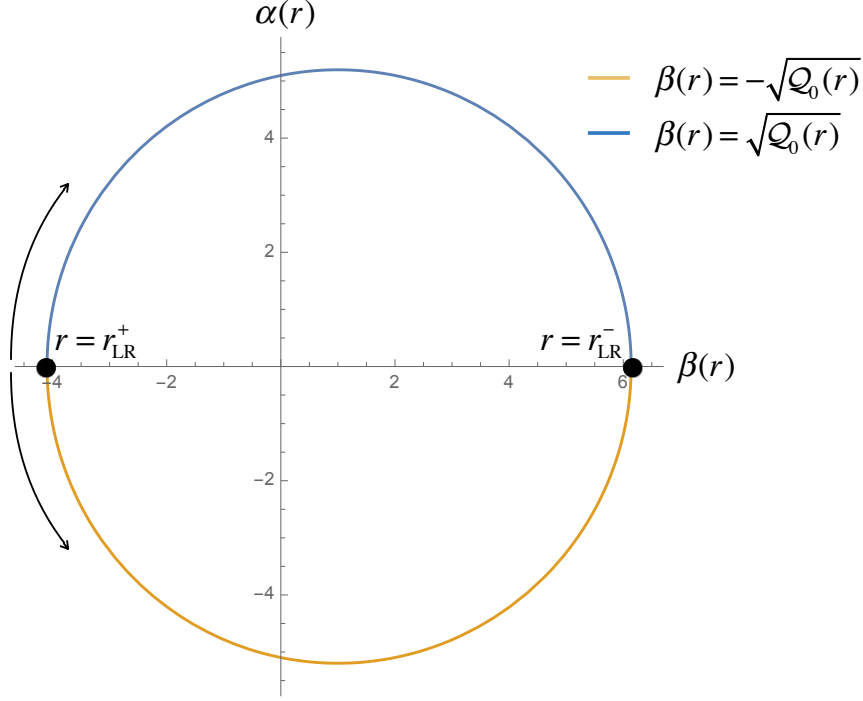


Figure 5.4: Parametric plot of Kerr's shadow computed from Bardeen's formula.

photons belonging to this class have a maximal (resp. minimal) angle θ determined by the points 5 and 5' (resp 6 and 6').

The following grey class of orbit is neither counter- nor co-rotating: it has $\dot{\varphi} = 0$, and contains the only orbit going through the poles.

Then, we enter into the region of co-rotating orbits. The yellow dashed curve represents such a class of orbit, with maximal (resp. minimal) θ extension given by the points 3 and 3' (resp. 2 and 2') at the intersection of the circle of constant radius (here the dashed yellow arc of circle) and the red boundary of the photon region.

Finally, the orbit represented by the dots 1 and 1' is the co-rotating counterpart of the light ring $r = r_{\text{LR}}^-$, with $r = r_{\text{LR}}^+$.

Now, how is it that these orbits are related to the shadow's edge? What we know for sure is that each set of orbits of constant radius $r_0 \in [r_{\text{LR}}^+, r_{\text{LR}}^-]$ is associated with two points on the shadow's edge, symmetric with respect to the horizontal axis. My claim, which is also made in [39] (Fig. 2), is schematically summarized on the right of Fig. 5.5: each point on the shadow (at $r = r_0$) corresponds to a photon which asymptotically reaches, in a backwards ray-tracing computation, the intersection of the boundary of the photon region and the circle $r = r_0$. Put another way, there exist photons almost following the unstable orbit $r = r_0$ around the black

hole which will be ejected from this orbit and reach the observer. To effectively do so, if the black hole is seen from an angle $\theta = \pi/2$, they need to arrive perpendicularly to the observer, and thus initially have $\dot{\theta} = 0$.

Actually, this intersection corresponds in general to four points on the left of Fig. 5.5. But only half of them will be associated with photons coming towards the observer: for instance in the case of the co-rotating dashed yellow orbit, only photons emitted from points 3 and 2 will reach the observer, while photons emitted at points 2' and 3' will be ejected in the other direction. Counter-rotating orbits correspond to the right part of the shadow: photons are emitted towards the observer for instance at points 5' and 6'

Hence, properties of the shadow directly stem from those of the photon region. In particular, the sharp edge of the latter actually translates into a sharp edge of the former: points slightly below the shadow's edge must fall into the horizon, while those slightly above can skim orbits very close to the black hole.

In the case of spacetimes without horizon, there is a priori no reason for the existence of a shadow nor a photon ring since no photons should cross a no-return boundary⁴. Some lensing rings very similar to photon rings may nonetheless appear on ray-traced images, as we will see in 3.2.1.

1.3.2 Main features of a typical black hole image

We now have all the ingredients in order to understand the main features of a typical black hole image. As sketched before, a ray-traced image is a set of pixels corresponding each to a single photon, and to which one associates a specific intensity. Such an image is visible in Fig. 5.6, in the case of a Kerr black hole surrounded by an accretion torus, with a spin $a/m = 0.9$ and seen with an inclination angle $\theta = 90^\circ$.

Four photons emitted from the torus and reaching the observer are depicted in Fig. 5.6. Photons 1 and 4 are primary images of the torus: they correspond to bent light rays that travel above or under the torus and form a thick ring on the ray-traced image (also called Einstein ring). Inside this thick ring, there is a black gap which corresponds to the absence of light source inside the torus. Besides, the torus also emits photons (like photon 3) which do not have to go through the black hole region and directly reach the observer: they form the foreground emission on the ray-traced image. Finally, the most interesting photon to us is the second one. It corresponds to light rays which skim unstable photon orbits of the photon region, and are then ejected to infinity towards the observer. Usually in numerical computations, there exist concentric copies of lensing rings of higher and higher orders with smaller and smaller luminosity. Their limit is defined as the photon ring, which marks the innermost limit a photon can visit without falling into the

⁴We will however give a counter-example below, already studied in [74].

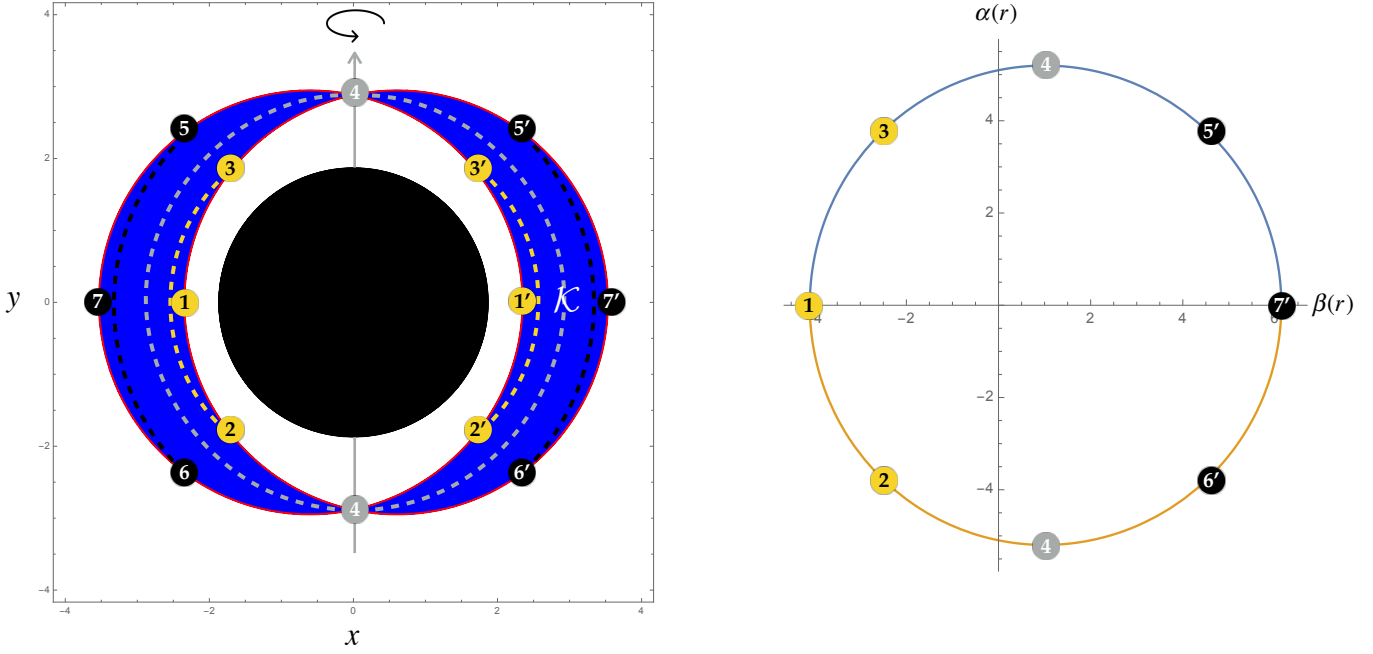


Figure 5.5: Relation between Kerr's photon region and the associated shadow.

outer horizon and delineates the shadow. A last thing that catches the eye on the ray-traced image is the asymmetry in the luminosity of the torus. The part of the accretion torus on the left of the image is actually moving towards the observer and hence produces a higher luminosity (compared to the right part of the torus) due to relativistic beaming effect.

2 Astrophysical and numerical set-up

We have seen in the previous section the main features one should expect to notice when dealing with ray-traced images. We will now explain how these images can be computed using GYOTO, taking into account the specificities of Sgr A*, before analyzing them in Sec. 3.

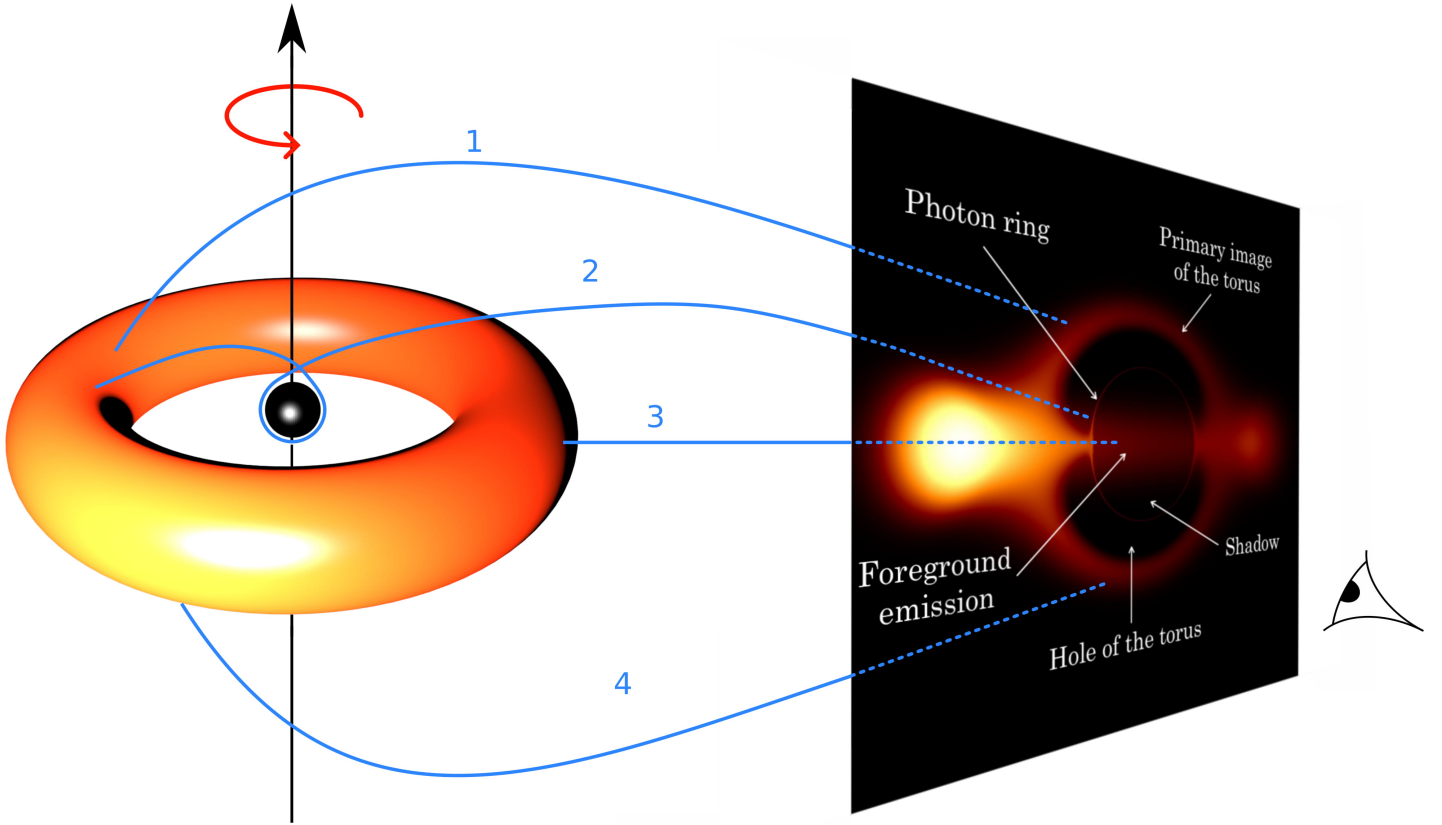


Figure 5.6: A typical ray-traced image.

2.1 Implementing regular black holes metrics in the ray-tracing code GYOTO

First things first, let us begin with the ray-tracing code `GYOTO` used to compute images of the regular rotating Hayward model presented in Chap. 4, which was developed by F. Vincent, T. Paumard, E.ourgoulhon and G. Perrin [120]. `GYOTO` stands for *General relativitY Orbit Tracer of Observatoire de Paris*, and as the authors of the code put it themselves, “it aims at computing images of astronomical objects in the vicinity of compact objects as well as trajectories of massive bodies in relativistic environments.”

To do so, it integrates the null and timelike geodesic equations in various spacetimes, which can be defined analytically (e.g., Kerr’s spacetime) or numerically. This integration runs backwards: a null geodesic equation is integrated backward in time for each pixel on a screen representing a portion of the sky as seen by an observer. If the geodesic does not reach any light source, the associated pixel will be shown dark. If it does, the pixel will be illuminated and associated with an actual photon reaching the observer. Each photon coming from a light

source, or emitter, will have a given specific intensity; the color scale on a ray-traced image is thus directly linked to the measured specific intensity at each pixel.

To determine the specific intensity of each photon, GYOTO integrates the equation of radiative transfer along the part of the geodesic that lies inside the emitting object, without taking into account the scattering effect. The specific intensity at some position s along the geodesic and for a frequency ν reads

$$I_\nu(s) = \int_{s_0}^s \exp\left(-\int_{s'}^s \alpha_\nu(s'') ds''\right) j_\nu(s') ds', \quad (5.15)$$

where α_ν and j_ν are respectively absorption and emission coefficients at a given point, specific to the astrophysical object playing the role of the emitter, and s_0 is the locus of a vanishing specific intensity. We will come back to that when considering the example of the accreting magnetized torus in Sec. 2.2.3.

On a more technical viewpoint, GYOTO is a C++ code based on several classes, which takes as input an xml file containing the parameters of the simulation and generates an output in FITS format. Three classes that will be of particular interest to us are `Gyoto::Screen`, `Gyoto::Astrobj` and `Gyoto::Metric`. The first one allows one to choose the parameters of the observation such as the distance of the studied object r_0 , the field of view of the observer, or the resolution of the image (i.e., the number of pixels). In our case, we wish to mimic the observations of Sgr A* and we will thus take $r_0 = 8.33$ kpc. The second class defines the astrophysical object we are considering as an emitting source, which will be the accretion magnetized torus of Sec. 2.2.3 for our simulations. The presence of the object is not considered to have any influence on the metric: back-reaction effects are not taken into account by GYOTO.

The metric is then fixed independently of the astrophysical object considered. In our case we have to implement the metric (4.34) of our regular rotating Hayward model, with $M_0 = M_{\text{Sgr A}^*}$. To do so I developed in the course of my thesis the *Hayward plugin*, whose associated metric class is now part of the standard distribution of GYOTO⁵. This metric class contains the coefficients of the metric (4.34) as well as the associated Christoffel symbols in order to integrate the geodesics, all reproduced in App. B.2. The creation of this plugin has actually taken a few months, due to the cumbersome expressions of the Christoffel symbols which contain rational fractions of very high powers of the distance r_0 from the observer. This distance being rather huge ($r_0 = 8.33$ kpc), I had to write the metric coefficients and Christoffel symbols under three different factorized forms, to cover the regions $r \geq 1$, $0 \leq r < 1$ and $r < 0$. This simplified the computation for GYOTO and allowed us to avoid numerical errors in the integration. The writing of a similar plugin for a regular rotating Bardeen model is currently in progress.

⁵freely available at <https://gyoto.obspm.fr>

Elément sous droit, diffusion non autorisée.

Figure 5.7: Orbits of 20 stars around Sgr A*, in the central arcsecond squared of the Milky Way. Figure taken from [61].

2.2 Mimicking an observation of Sagittarius A* in the simulations

2.2.1 Features of Sgr A*

Sagittarius A* is a compact source of radio waves at the center of galaxy, first observed by Balick and Brown in 1974 [7]. Its name stems from the fact that it is observed from Earth in the direction of the constellation Sagittarius. The * (pronounce “star”) was chosen by Brown to distinguish it from the broader Sgr A region, in reference to the presence of a cloud of ionized hydrogen surrounding it [84]. Sgr A* is thought to be the locus of a supermassive black hole. This assumption is based on the study of Keplerian stellar orbits, as the one performed by Gillessen et al. for 28 stars during 16 years [61] (see the orbits in Fig. 5.7. This figure shows a plot of 20 orbits centered on Sgr A*, representing one arcsecond squared on the sky. Gillessen et al deduced from their analysis the following mass and distance from Earth of Sgr A*:

$$\begin{cases} M_0 = 4.31 \times 10^6 M_\odot , \\ r_0 = 8.33 \text{ kpc} . \end{cases} \quad (5.16)$$

Even if there exist arguments in favor of the presence of an outer horizon (see [28]), the nature of Sgr A* is yet to be ascertained. Indeed the presence of a horizonless ultra-compact object cannot a priori be disregarded. Such objects include for instance gravastars [86], holostars [95], boson stars [119], and the naked rotating wormhole we presented in Chapter 4.

How could one then conclude in favor of the presence of a black hole at the center of the Milky Way? One way, based on a study of the electromagnetic spectrum of Sgr A*, consists in looking for the presence of a shadow, characteristic of a trapping horizon, in the observer’s sky. It is the path pursued by the Event Horizon Telescope collaboration, that we shall now describe.

Elément sous droit, diffusion non autorisée.

Elément sous droit, diffusion non autorisée.

(a) Taken from [99].

(b) Taken from [77]

Figure 5.8: Comparison of supermassive black hole candidates' angular sizes: outer horizon (left) and shadows (right).

2.2.2 Observations with the Event Horizon Telescope

The Event Horizon Telescope is an array of radiotelescopes aiming at capturing the first image of a black hole [45]. These millimeter and submillimeter wavelength telescopes are distributed all over the world, and constitute an Earth-sized very long baseline interferometry (VLBI) array.

Providing the first image of a black hole is a huge challenge which requires a good enough resolution. The first black holes one should observe must thus be those with the biggest angular sizes for shadows. From Fig. 5.8(a), which shows the opening angle (in μas) of the outer horizons of various supermassive black holes (SMBH) candidates seen from Earth, it appears that Sgr A* is the most suited one (with a horizon of $10 \mu\text{as}$). This is confirmed in Fig. 5.8(b) where the real observable, the angular diameter of the photon ring, i.e. the size of the shadow, is plotted for the same SMBH candidates. Sgr A*, if it were a black hole, should possess a shadow of width $\theta_0 \simeq 53 \mu\text{as}$.

A typical shadow of a Kerr black hole with spin $a/m = 0.9$ is shown in Fig. 5.9, where the size of the expected shadow is shown. This shadow has not yet been resolved, but some observations by the EHT at $\lambda = 1.3 \text{ mm}$ have constrained the intrinsic diameter of Sgr A*, i.e. the size of the emitting region, to $37^{+16}_{-10} \mu\text{as}$ [46].

The difficulty of resolving the shadow can be better grasped when considering that it requires the same resolution as observing, from Earth, an orange on the Moon. The angular resolution of a telescope depends on its aperture D and the observing wavelength λ :

$$\delta = \frac{\lambda}{D}. \quad (5.17)$$

Improving the resolution of an image can thus be done either by increasing the aperture of the telescope, or decreasing the observed wavelength. The first option has been explored by the EHT collaboration, since many observatories are now connected all over the world to form a very long baseline interferometry array, as illustrated in Fig. 5.10(a). The second option can be followed

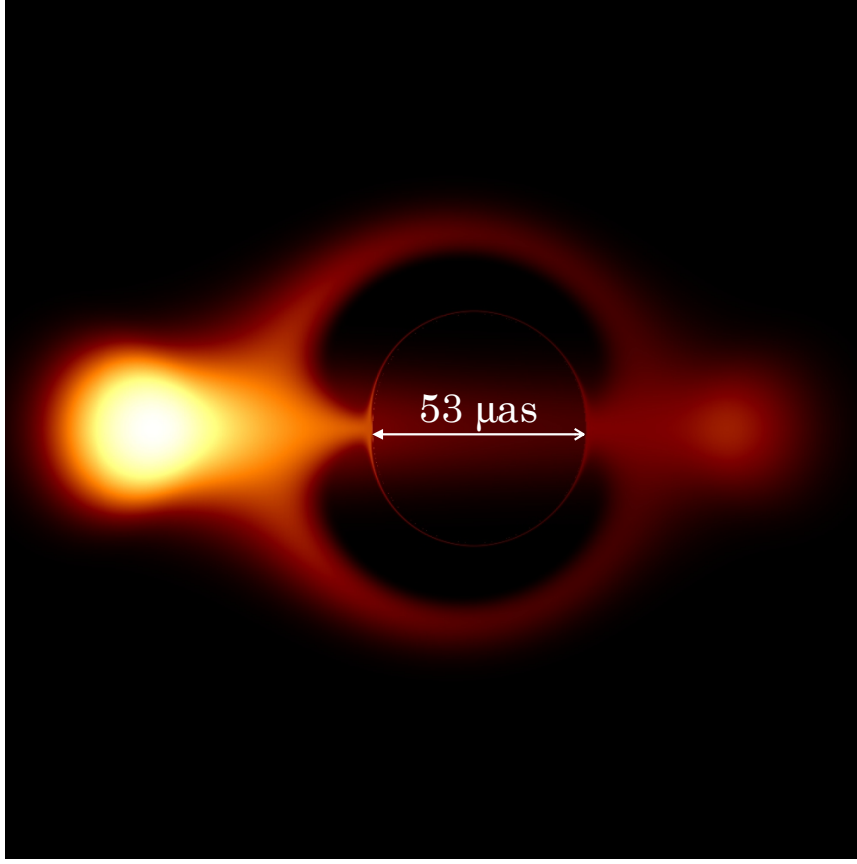


Figure 5.9: Ray-traced image of a Kerr black hole at the center of the Galaxy with $a/m = 0.5$, surrounded by a magnetized torus. The shadow’s width is of $53 \mu\text{as}$. As a matter of comparison, the Moon’s angular size is $\approx 30 \text{ as}$.

only until a certain point. As shown in Fig. 5.10(b), the terrestrial atmosphere is becoming more and more opaque to increasing frequencies of the light observed, or equivalently to decreasing wavelengths. But what really constrains the observed frequency is the fact that the millimeter and submillimeter wavelengths are those emitted closest to the black hole candidate, while the X and radio waves are emitted much farther away. The millimeter and submillimeter wavelengths are thus best suited to observe the shadow of a black hole candidate, and that is why a wavelength such as $\lambda = 1.3 \text{ mm}$ (or frequency $\nu = 230 \text{ GHz}$) was used for the first observations of the EHT [46]. It is also the one we will be using in the simulations of Sec. 3. With the current performances of the instrument, one should expect an angular resolution less than $25 \mu\text{as}$, which would in principle be enough to resolve the $50 \mu\text{as}$ -wide shadow of Sgr A*.

2.2.3 Accretion model used in the simulations

As already explained, the first observation of Sgr A* was performed by Brown & Balick [7], who reported the “detection of strong radio emission in the direction of the inner 1-pc core of the

Elément sous droit, diffusion non autorisée.

Elément sous droit, diffusion non autorisée.

(a) Taken from [45]

(b) Taken from [85]

Figure 5.10: Increasing the resolution of the Event Horizon Telescope: increasing the effective aperture of telescopes with very long baseline interferometry (left) or decreasing the observed wavelength (right).

Elément sous droit, diffusion non autorisée.

Figure 5.11: Spectral energy distribution of Sgr A*, taken from [59].

galactic nucleus”. The electromagnetic spectrum of Sgr A* is now much more documented: in its steady state⁶, Sgr A* emits $\sim 10^{36}$ erg/s essentially at radio to submillimeter wavelengths (see [59] for details), as seen on the spectral energy distribution of Fig. 5.11. This radiation essentially stems from the accretion of stellar winds from nearby stars. These flows of gas coming from the surfaces of stars spiral around Sgr A*, and hence lose gravitational energy which is converted into radiation.

There exists no direct evidence for the presence of an accretion disk around Sgr A*, but the data can be understood from analytical or numerical models. Among the analytical ones, we will be interested in *advection dominated accretion flow* (ADAF) models pioneered by Narayan et al [88], but we should also mention the existence of jet models [50]. The advection dominated flow models explain the relatively low luminosity of Sgr A* compared to other SMBH candidates: most of the energy of the spiralling accretion structure is not lost through radiation, but by

⁶Sgr A* also possesses a variable emission component, which is still not fully understood and that we will not consider in the following

transportation inside the black hole. A subclass of the ADAF models is the *radiatively inefficient accretion flow* (RIAF) model, whose latest version can be found in [27]. The RIAF model of Yuang et al. [123], for instance, reproduces very well the data as shown in Fig. 5.11. More details can be found in F. Vincent's thesis [117]

We have seen in Sec. 2.2.2 that Sgr A*, due to its angular size on the sky, is the best suited black hole candidate in order to detect the first black hole shadow. To compare the shadows of non-Kerr black holes using GYOTO to the observations of the Event Horizon Telescope, one must thus make simulations with an astrophysical environment as close as possible to the one of Sgr A*. In particular, one has to choose an accretion structure reproducing the spectral properties of Sgr A*, at least at the observed wavelength $\lambda = 1.3\text{ mm}$.

Such an accretion model precisely has been implemented in GYOTO, it is a magnetized optically thin torus developed by Vincent et al [121] and based on a paper by Komissarov [79]. This torus is composed of a non-self-gravitating perfect polytropic fluid which orbits circularly at a constant specific angular momentum l . It is thus not spiralling as one would expect, but it can nonetheless be considered as an approximation of a spiralling accreting structure at a given time. The model has already been used in simulations of Kerr black holes with scalar hair [118] and boson stars [119], and it was shown in [121] to reproduce well the spectral properties of Sgr A* in the millimeter domain. Seven parameters are required to define it: the spin of the black hole a , the inclination angle i (angle between the black hole rotation axis and the line of sight), the angular momentum l of the torus, the ratio of gas to magnetic pressures β , the polytropic index k defining the equation of state of the torus' fluid, the central density n_c and the central electron temperature T_c . From these parameters, the synchrotron absorption and emission coefficients can be computed (see [121] for details), and the equation of radiative transfer integrated by GYOTO, hence producing a map of specific intensities over a chosen field of view (i.e., an image).

Fig. 5.12(b) shows the spectrum predicted by the magnetized torus model with parameters given in Fig. 5.12(a) and its comparison with the RIAF model, which is very satisfying in the millimeter domain. The parameters we will be using in the following simulations are given on Table 5.1. They are consistent with the spectral energy distribution of Sgr A* at wavelength $\lambda = 1.3\text{ mm}$ (or frequency 230 GHz). The choices of l and of the inner radius of the torus, hence fixing the outer radius, were made so that the size of the torus be compatible with the size of the emitting region constrained to $\lesssim 37\mu\text{as}$ by the first EHT results (see Doeleman et al [46]). The outer radius varies according to the value of the spin parameter, it is for instance $r_{\text{outer}} \simeq 30 M_0$ for $a = 0.9$. The spin of Sgr A* is still not known precisely, but in the following simulations we will consider rather high values of a/m (essentially between 0.5 and 0.9). We have indeed evidence for the existence of many rapidly rotating supermassive black holes (see for instance the spin values in Table II of [8]).

Parameter	Value	
spin	a	0
inclination	i	5°
angular momentum	l	0.35
gas/magnetic pressure ratio	β	10
polytropic index	k	5/3
central density (cm^{-3})	n_c	$7.7 \times 10^6 \text{ cm}^{-3}$
central electron temperature (K)	T_c	$8.7 \times 10^{11} \text{ K}$

Elément sous droit, diffusion non autorisée.

(a) (b)

Figure 5.12: Left: Parameters of the magnetized torus whose spectrum is plotted on Fig. 5.12(b). The spin and angular momentum are expressed in units of M_0 . Right: comparison of the spectra of the RIAF model and the magnetized torus. The agreement is clear in the millimeter domain ($\nu \approx 10^{11} \text{ Hz}$)

Parameter	Value	
spin	a	0.3-0.9
inclination	i	$85^\circ - 90^\circ$
angular momentum	l	4
gas/magnetic pressure ratio	β	10
polytropic index	k	5/3
central density (cm^{-3})	n_c	6.3×10^6
central electron temperature (K)	T_c	5.3×10^{10}

Table 5.1: Parameters of the magnetized torus used in the simulations of Sec. 3. The spin and angular momentum are expressed in units of M_0 .

3 Images of the regular rotating Hayward model

Let us now describe the results obtained in [80] regarding the ray-traced images of the regular rotating Hayward model presented in Chap. 4. The regular black hole and wormhole regimes of the models will be investigated in Secs. 3.1 and 3.2.

3.1 Regular rotating Hayward black hole

In this section as in the following, the emitting astrophysical source is the magnetized torus presented in Sec. 2.2.3, with parameters of Table 5.1. The observer is located at a radial coordinate which corresponds to the distance between Earth and Sgr A* ($r_0 = 8.33 \text{ kpc}$), and the images are computed with GYOTO at a frequency of 230 GHz.

The regular rotating Hayward black hole with $a/m = 0.5$, $b/m = 0.5$ possesses an outer horizon located at $r_0 \approx 1.65m$. It is thus at a smaller value of the radial coordinate from the center than

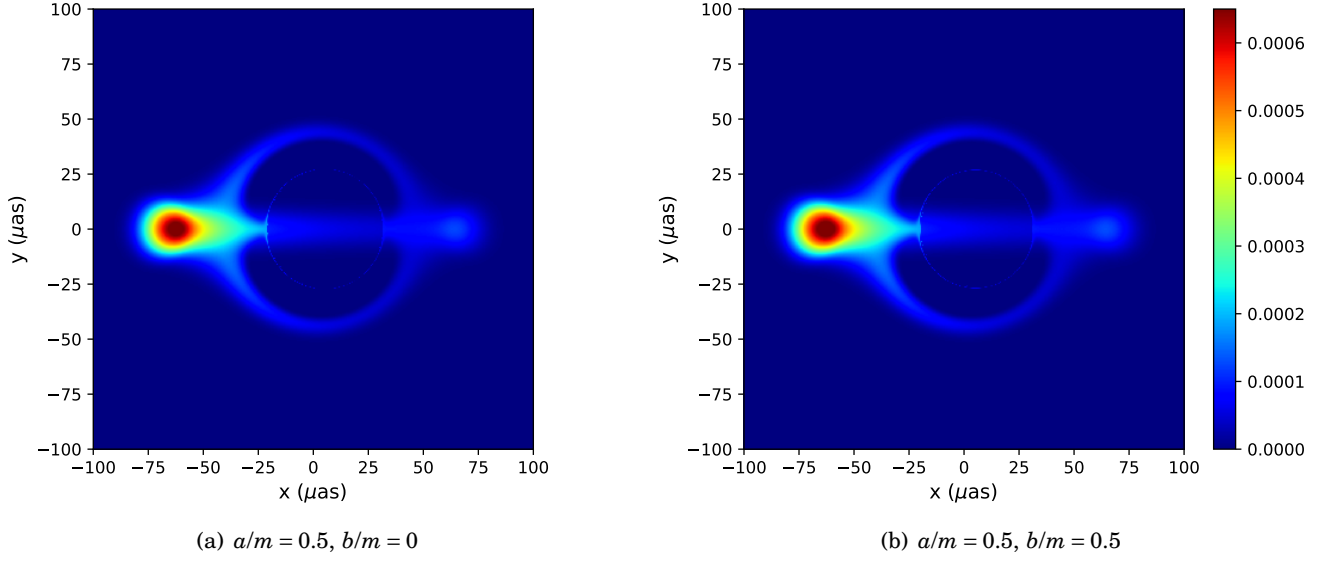


Figure 5.13: Images of an accretion torus surrounding a Kerr black hole (a) and a regular rotating Hayward black hole (b), seen from a distance of 8.31 kpc. The field of view is $200 \mu\text{as}$ and the inclination $\theta = 90^\circ$. The specific intensity I_ν is plotted in CGS units, as will be the case for the following images.

in the Kerr black hole case ($b/m = 0$), where $r_+ = m + \sqrt{m^2 - a^2} \approx 1.87m$. Hence, for a given ADM mass, the black hole radius is smaller when $b \neq 0$.

The millimeter images of these two black holes are visible in Fig. 5.13. On both panels, we observe the distorted primary image of the torus, that forms an Einstein ring. The very center of the image shows a thin photon ring delineating the black hole shadow. The differences between the millimeter images of the two black holes appear to be indistinguishable with the naked eye. However, subtracting one image from another we can distinguish the two different lensing rings (Fig. 5.14). The difference of diameter between these two rings is about $2 \mu\text{as}$ ($\approx 3\%$). This difference is out of reach for the observations in the foreseeable future, but we may hope that a telescope would be able to measure the radius of the lensing ring in a far future, or equivalently the area of the shadow, and could thus discriminate between the two black holes for a given ADM mass.

It should be noted that we considered here a macroscopic value of b ($b = 0.5m$) when computing these images. The underlying assumption is that this parameter arises because of some “macroscopic” energy-momentum tensor supporting this regular geometry, though it cannot be non-linear electrodynamics (as we have shown in Chap. 4, and contrarily to the claims of Toshmatov et al. [114]). Had we assumed that the singularity was resolved by using b as a Planckian cut-off, the difference between the images would have been invisible to any telescope even in the far future.

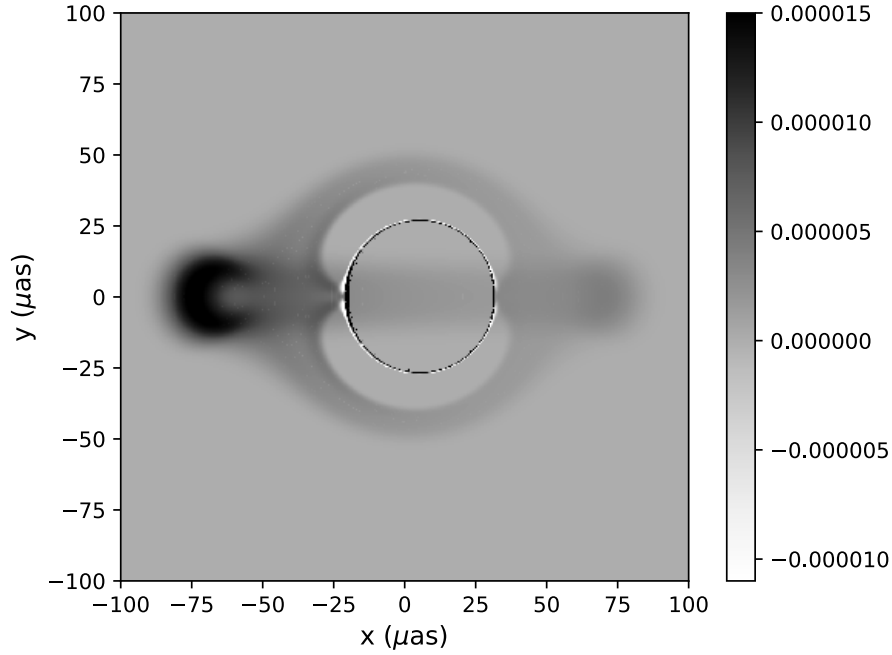


Figure 5.14: Difference of the images of Fig. 5.13. The lensing rings of the configurations $b/m = 0.5$ (black) and $b/m = 0$ (white) are visible at the centre.

3.2 Naked rotating wormhole

3.2.1 Ray-traced images

Let us now discuss the case of geometries without horizons described by the rotating Hayward metric extended to $r < 0$ (4.34), that we call naked rotating wormholes. We will first describe the results obtained with GYOTO as well as their consequences, and then explain them by studying some relevant geodesics.

The major difference in this configuration, with respect to the previous section, is the absence of horizons. Hence, the images obtained with this geometry do not contain any shadows, in the precise sense defined above. However, they do contain a central faint region showing a mixture of low-flux regions and strongly lensed contours (of increasing order from left to right, see Fig. 5.15). The shape of these contours highly depends on the value of the parameter b/m . It is thus very important to stress that observing such strongly lensed contours, which can look like a lensing ring without a good enough resolution, does not imply the existence of an event horizon, just as in the case of boson stars [119].

The two panels of Fig. 5.15 are remarkably similar to the images of accretion tori surrounding

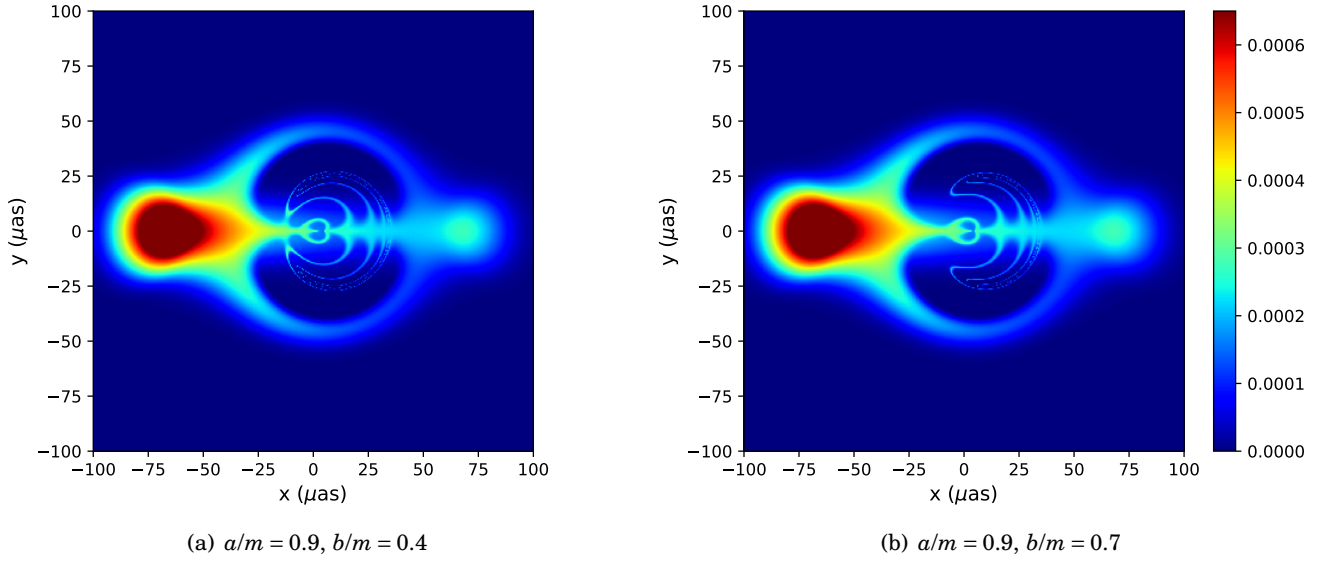


Figure 5.15: Images of an accretion torus surrounding a naked rotating wormhole with $a/m = 0.9$, $b/m = 0.4$ (a) and $b/m = 0.7$ (b). The field of view is $200 \mu\text{as}$ and the inclination $\theta = 90^\circ$.

rotating boson stars (see the middle- and lower-right panels of Fig. 5 in Ref. [119]). However, these spacetimes are completely different, those analyzed here corresponding to naked rotating wormholes, while boson stars are compact distributions of fundamental scalar fields. It is thus rather intriguing that such very different spacetimes lead to images that are difficult to differentiate. Further studies would be necessary in order to determine whether the distorted, hyper-lensed contours of Fig. 5.15 are general features of spacetimes of compact object with no event horizon and no hard surface (i.e. different from neutron stars). A first hint could probably come from the study of the photon regions of such objects. For instance, the lensing rings for the configurations $(a/m = 0.9, b/m = 0.4)$ and $(a/m = 0.9, b/m = 0.7)$ (see Fig. 5.15) are very different: the crescent shape forms a whole circle only in the first configuration, where its extremities reach the horizontal axis. This should probably be compared with the two very different photon regions for the same values of parameters (Fig. 5.3), whose meridional sections cross the vertical axis $\theta = 0$ in the first configuration but not in the second. Further analysis would be needed to explain this behaviour of the photon region and its relation to the shape of the shadow.

3.2.2 A glimpse at $r < 0$

Another interesting feature appears when the accretion torus is observed from an inclination angle θ different from 90° . In this case, the disk $r = 0$ located in the equatorial plane becomes visible. It can hardly be seen in Fig. 5.16(a), but a zoom clearly allows identifying a central dark ellipse⁷ on the image in Fig. 5.16(b). Its contour corresponds to the throat of the wormhole.

⁷It is not necessarily an ellipse in the mathematical sense.

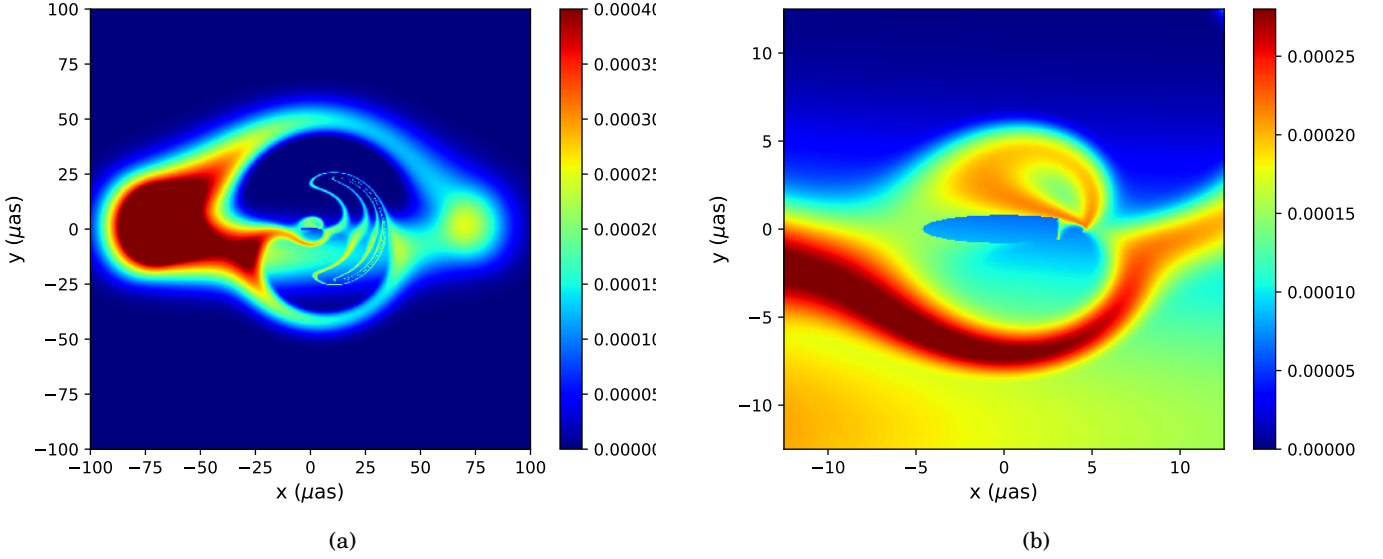


Figure 5.16: Images of an accretion torus surrounding a naked rotating wormhole with $a/m = 0.9$, $b/m = 1$. The inclination is $\theta = 80^\circ$ while the field of view is $200 \mu\text{as}$ (a) or $25 \mu\text{as}$ (b)

The blue pixels forming this ellipse-like shape (right panel) represent geodesics coming from $r \rightarrow -\infty$; a similar distorted disk also appears in the case of naked Kerr singularities [74]. These pixels are not completely black since a part of the torus, located between the throat and the observer, emits some photons directly towards the latter: it is the foreground emission visible in Fig. 5.6. However there also exists luminous (green and yellow) pixels inside the dark ellipse. All these illuminated pixels are associated with photons emitted from the torus and travelling through negative values of r back to the observer. The location of this luminous feature inside the dark ellipse highly depends on the value of b/m , as is illustrated by comparing the right panels of Figs. 5.16 and 5.17.

There exists a sharp contrast between the dark ellipse and this luminous feature, which can be studied in further detail if we consider three different geodesics (Fig. 5.18).

3.2.3 Following 3 typical geodesics

The green geodesic of Fig. 5.18 corresponds to a luminous pixel just outside the dark ellipse. This geodesic comes from $r = +\infty$, crosses the torus on its way in, approaches the $r = 0$ disk (represented by the grey sphere in Fig. 5.18) without reaching it, and escapes to the observer (crossing a second time the torus on its way out). Similarly, the blue geodesic comes from $r = +\infty$ and crosses the torus on its way in. Contrarily to the green geodesic, it enters the wormhole throat, reaching negative values of r . It also reaches a turning point and comes back to $r > 0$,

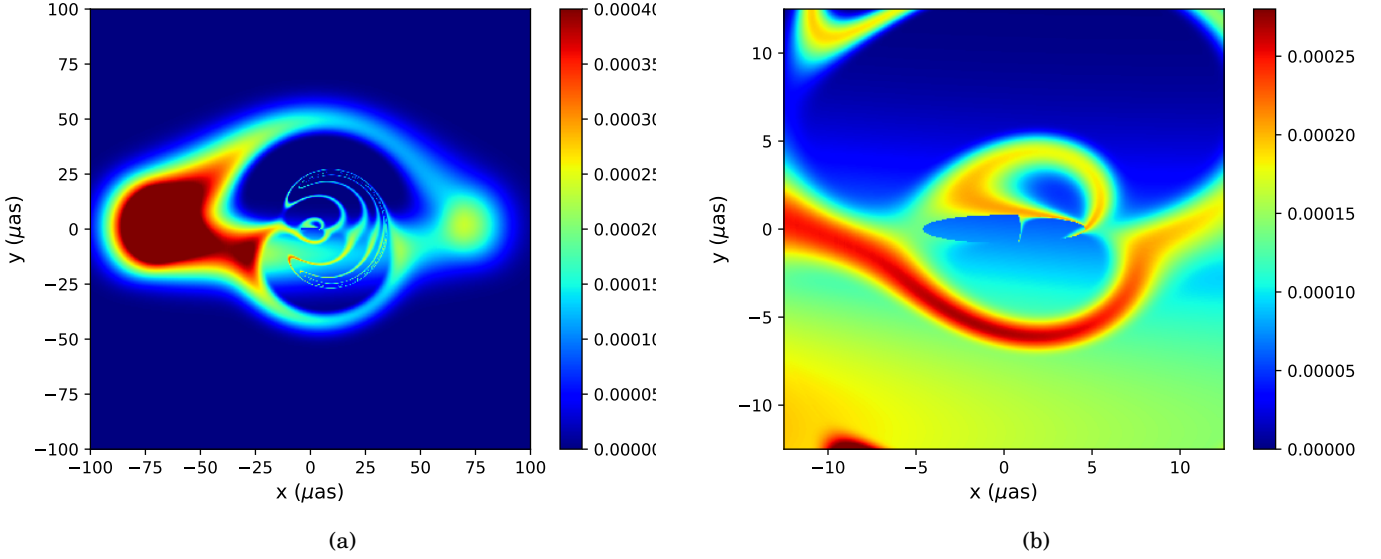


Figure 5.17: Images of an accretion torus surrounding a naked rotating wormhole with $a/m = 0.9$, $b/m = 0.5$. The inclination is $\theta = 80^\circ$ while the field of view is $200 \mu\text{as}$ (a) or $25 \mu\text{as}$ (b)

also eventually reaching the observer after having crossed the torus a second time on its way out. Finally, the red geodesic originates from $r = -\infty$. It emerges from the throat and crosses the torus only once, on its way out to the observer.

3.3 Low resolution images as seen by the Event Horizon Telescope

As a conclusion of this Chapter, we present the ray-traced images of the naked rotating wormhole, compared to Kerr's black hole, as it would be seen with the resolution of the Event Horizon Telescope. Of course, since we do not use the simulation codes of the instrument, the images we will present only give a rough picture of what the EHT would actually be able to see. As explained by Doeleman [45], the shadow of a Kerr black hole with $M_0 = M_{SgrA^*}$ at the center of Galaxy, of width $\simeq 50 \mu\text{as}$, would be visible in principle by the EHT whose resolution is $\simeq 25 \mu\text{as}$. The shadow of a Kerr black hole would thus represent 4 pixels on an image seen by the EHT, as plotted in Fig. 5.19(a). It seems extremely difficult to distinguish this image from the one of a (horizonless) naked rotating wormhole surrounded by the same accretion torus 5.19(b).

We thus wish to emphasize that the results of the Event Horizon Telescope shall be taken with caution, since the observation of a low resolution shadow does not allow one to infer the presence of an outer horizon. To end on a more optimistic note, the differences appear to be more noticeable with a twice as good resolution (Fig 5.20).

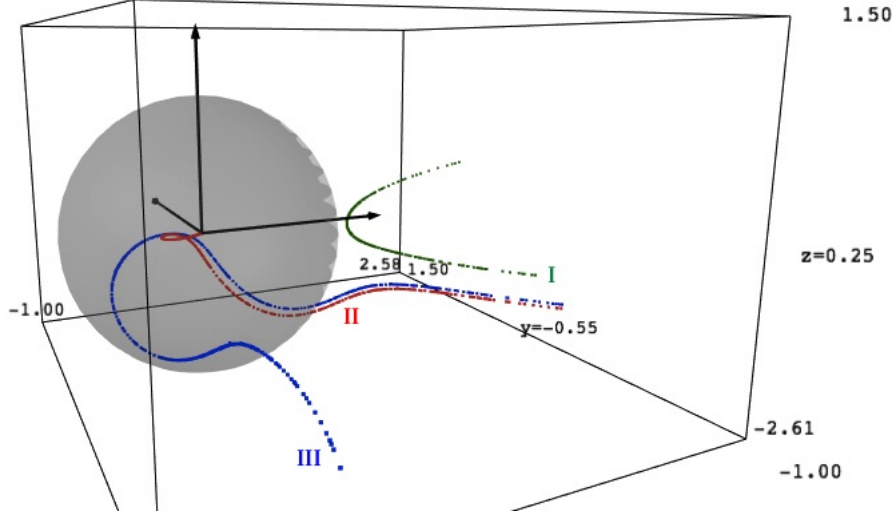


Figure 5.18: The null geodesics associated with three different pixels, starting from the accretion torus for $a/m = 0.9$, $b/m = 1$, are plotted in a frame with $x = e^r \sin \theta \cos \varphi$, $y = e^r \sin \theta \sin \varphi$, $z = e^r \cos \theta$. A frame is drawn at the origin, where $r \rightarrow -\infty$. Geodesic I (in green) has a turning point and does not enter the grey sphere of radius $r = 0$. Geodesic II (in red) has no turning point, it represents the trajectory of a photon in the central dark ellipse coming from $r \rightarrow -\infty$. Finally, geodesic III (in blue) enters the sphere of radius $r = 0$ but has a turning point inside, and goes back to an observer at $r \rightarrow +\infty$.

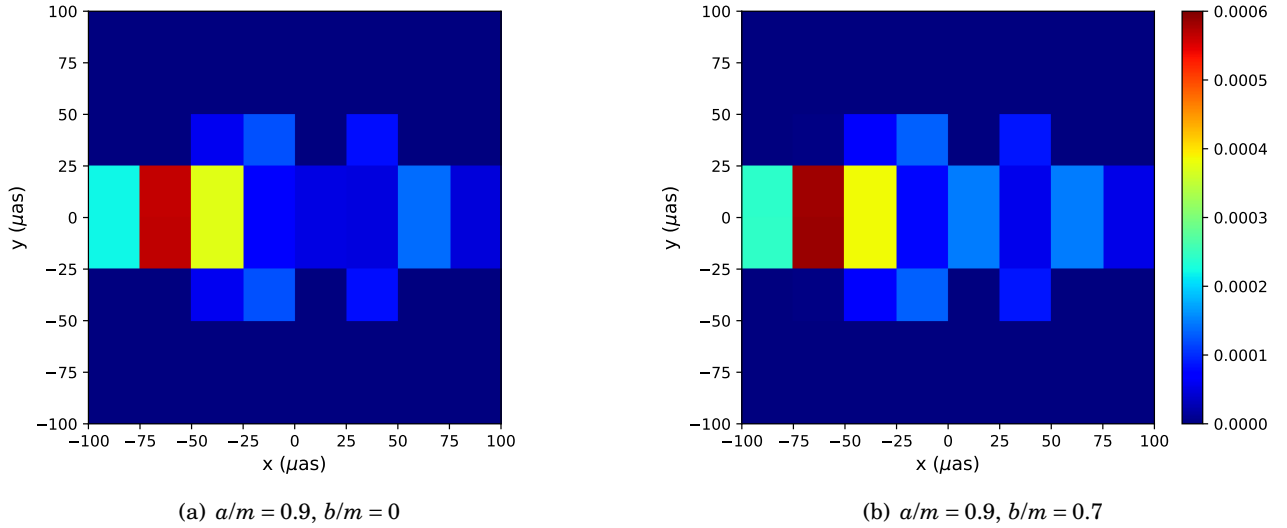


Figure 5.19: Images of an accretion torus surrounding a Kerr black hole (a) and a naked rotating wormhole (b), seen from a distance of 8.31 kpc and with a resolution of 8×8 pixels. The field of view is $200 \mu\text{as}$ and the inclination $\theta = 90^\circ$.

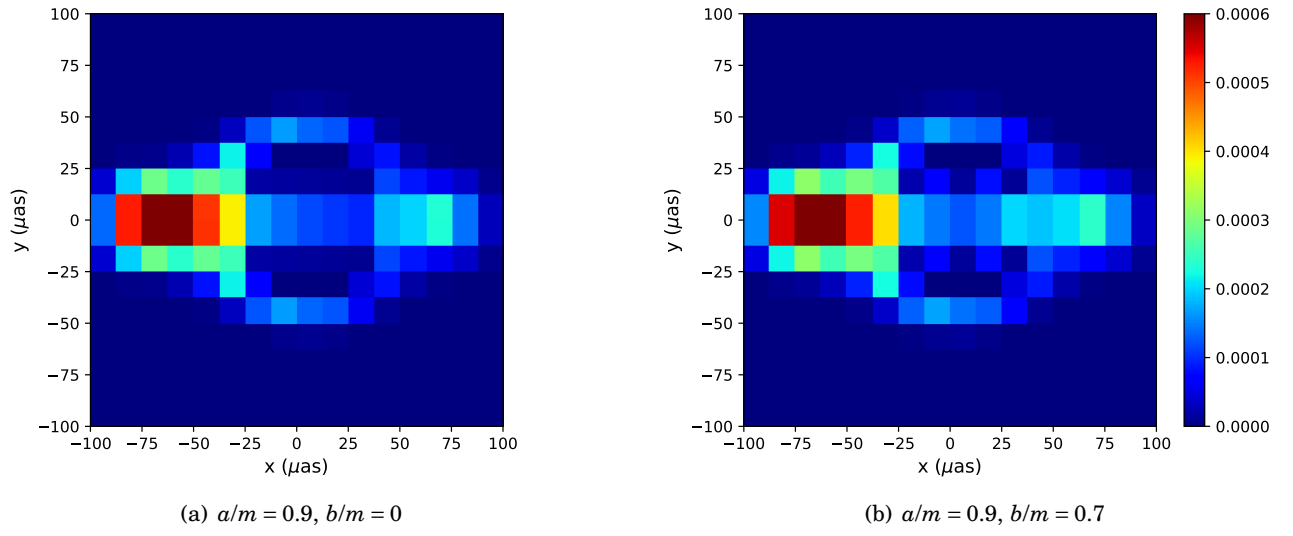


Figure 5.20: Images of an accretion torus surrounding a Kerr black hole (a) and a naked rotating wormhole (b), seen from a distance of 8.31 kpc and with a resolution of 16×16 pixels. The field of view is $200 \mu\text{as}$ and the inclination $\theta = 90^\circ$.

DYNAMICAL NON-SINGULAR BLACK HOLES



ph~n 'h.t=j 3h.t sw 3~n=j ntr.w nw.t

“Si mon vol a atteint l’horizon, c’est que j’ai dépassé les dieux du ciel.”

(*Textes des Sarcophages* II, 223b-223c, S1C^a [30, 41].)

After exploring static or stationary non-singular black holes in the previous chapters, let us now turn to dynamical ones and describe the results obtained with P. Binétruy and A. Helou in [19]. Astrophysical black holes are by essence dynamical: they are formed after a gravitational collapse (contrarily to Schwarzschild’s eternal black holes and its maximal extension presented in Sec. 1 of Chap. 2), and are also thought to radiate via Hawking’s evaporation [66]. A few solutions to Einstein’s equations describe the dynamical formation of a black hole, such as Vaidya’s metric presented in Chap. 1, but they remain classical. In this Chapter, we aim at studying effective metrics which incorporate quantum effects both near the outer horizon, to describe Hawking’s evaporation, and in the high curvature regime near $r = 0$ in order to avoid the singularity. A way of doing so consists in studying closed trapping horizons, whose dynamics can implement these two types of quantum effects. In Sec. 1 of this Chapter, we will start by deriving general conditions for the existence of singularity-free closed trapping horizons. We will then implement and study in Sec. 2 explicit models of closed trapping horizons inspired by the work of Hayward, Frolov and Bardeen, before discussing the behaviour of null geodesics in those models (Sec. 3). Finally, in Sec. 4 we solve Einstein’s equations in reverse to obtain the expression of the energy-momentum tensor for these models and analyse the weakest of energy conditions, the null energy condition (NEC). We find an explicit metric that recovers a null outgoing fluid mimicking Hawking radiation on \mathscr{J}^+ , without having to make junctions. We ultimately show that all models based on the collapse of ingoing null shells, hence (asymptotically) described by a Vaidya metric on \mathscr{J}^- , and aiming at describing Hawking’s evaporation, are doomed to violate the energy conditions in a non-compact region of spacetime.

Contents

1	Non-singular spacetimes with closed trapping horizons	158
2	Examples of closed trapping horizons: properties and limits	162
3	Behaviour of null geodesics in models with closed trapping horizons	166
4	Towards a model for the formation and evaporation of a non-singular trapped region	170

1 Non-singular spacetimes with closed trapping horizons

1.1 Motivations

A general feature of collapses leading to black holes is the formation of trapping horizons [69]. These are foliated by 2D marginally outer trapped surfaces (MOTS), which are also called apparent horizons (see App. A.3 for details). In the course of the collapse, a first MOTS will appear, and trapped surfaces will then develop. In the usual, analytic black hole spacetimes, the location of this first¹ MOTS is known. It appears at the surface in the Oppenheimer-Snyder (OS) homogeneous dust collapse (see middle panel of Fig. 6.1), in the bulk of the collapsing matter for some classes of Lemaître-Tolman-Bondi (LTB) spacetimes, or at the centre in Vaidya null-dust collapse (left panel of Fig. 6.1) as well as in some other classes of LTB spacetimes [23, 73]. When it is not formed at the centre, it immediately separates into an ingoing apparent horizon and an outgoing one, where ingoing/outgoing refers to the motion with respect to the collapsing matter (this is a hydrodynamical concept, not to be confused with the geometrical one of inner/outer trapping horizons).

The idea of closed trapping horizons was studied in [103], where it was given the general form of Fig. 6.1 (right panel). This horizon is null at four points A , B , C and D . In the classical diagrams, the apparent horizon is usually spacelike, i.e. only a portion of CB , where B is the point at which the black hole becomes isolated and the apparent horizon becomes indistinguishable from the event horizon. In some situations, one can also have a timelike inner horizon, i.e. a portion of CA [23, 73]. The reason why a classical black hole cannot produce a horizon on portion ADB is the following: in spherical symmetry, when the Null Energy Condition (NEC) is satisfied, an outer horizon is achronal while an inner horizon is timelike or null (see Theorem 2 of [69], as well as [23, 70]). Therefore we must have a violation of the NEC on portion ADB . Considerations of this portion seldom appear in the literature, although it is inherent to the widely discussed Hawking radiation of the outer horizon, which produces a timelike horizon of type BD (see Fig. 2 of [75]). Having a spacelike inner horizon of the type AD is even less considered (see, however, Fig. 2 of [13]), but it is a way to avoid the conclusions of the Penrose singularity theorem [94] by violating the NEC.

We want to stress here, in accordance with [13, 55, 71, 103], that one should not *a priori* discard any of the above behaviours for the trapping horizon. As we still do not know what happens (beyond General relativity) when the inner horizon reaches the centre of the configuration, or at the end of black hole evaporation, we think it is worth investigating these possibilities, which display a very different phenomenology from the usual classical and semi-classical picture.

In the following of this section we will investigate the conditions needed to achieve a non-singular spacetime with closed trapping horizons of the Roman-Bergmann type, before considering

¹Using the time-slice of the comoving observer [73].

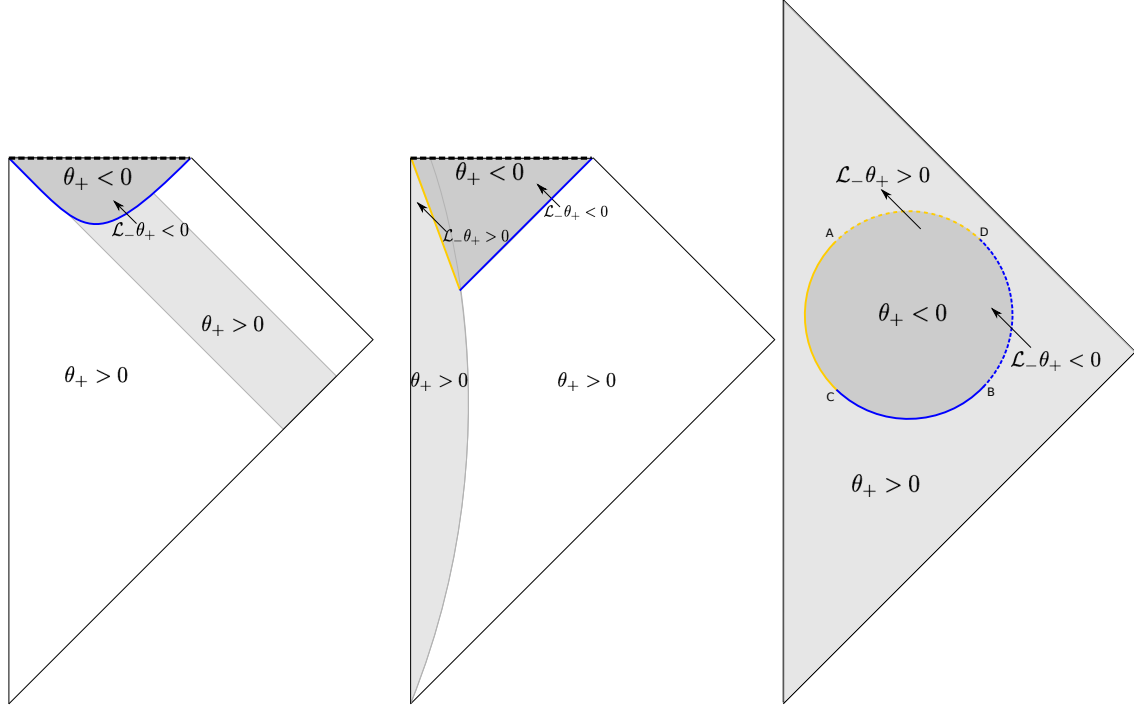


Figure 6.1: Penrose-Carter diagrams for Vaidya null dust collapse (left), Oppenheimer-Snyder homogeneous dust collapse (centre) and Roman-Bergmann closed trapping horizons [103] (right). The outer horizon is represented in blue while the inner one is shown in yellow. These are defined from [69] using the Lie derivative, along the ingoing null direction, of the expansion of outgoing null geodesic congruence θ_+ : $\mathcal{L}_-\theta_+ < 0$ for outer trapping horizons, $\mathcal{L}_-\theta_+ > 0$ for inner trapping horizons. The horizons are drawn as a solid line when the NEC is satisfied, and as a dashed line when it is violated.

some examples adapted from the literature in Sec. 2.

1.2 Existence of non-singular spacetimes with closed trapping horizons

Let us study the general conditions for the existence of a non singular spacetime containing closed trapping horizons. We will work in advanced Eddington-Finkelstein coordinates, in which the metric reads

$$ds^2 = -F(v, r)dv^2 + 2dvdr + r^2 d\Omega^2, \quad (6.1)$$

where r is the areal radius, $d\Omega^2 = d\theta^2 + \sin^2\theta d\varphi^2$, and F is a function of v and r not specified yet. This is not the most general spherically symmetric metric, whose expression will be used later (eq. (6.27)). However, as eq. (6.40) will illustrate, the additional degree of freedom of the general metric does not affect the shape of the horizons given by the metric (6.1) used in the present section.

We will assume that F can be written in the following way

$$F(v, r) \equiv 1 - \frac{2M(v, r)}{r} = 1 - 2m(v) \frac{r^{\alpha-1} + a_{\alpha-2}(v)r^{\alpha-2} + \dots + a_1(v)r + a_0(v)}{r^\alpha + b_{\alpha-1}(v)r^{\alpha-1} + \dots + b_1(v)r + b_0(v)}, \quad b_0(v) \neq 0. \quad (6.2)$$

Assuming that $F - 1$ can be written as a ratio of polynomial functions, this is the most general form one can use to recover Vaidya's limit when $r \rightarrow +\infty$ (and Schwarzschild's limit if, in addition, $m(v) = \text{cst}$). The function $m(v)$ plays the role of the Misner-Sharp mass for an observer at infinity.

1.2.1 Conditions for the existence of closed trapping horizons

The existence of closed trapping horizons requires the presence of two horizons, i.e. of one marginally outer and one marginally inner trapped surfaces, whose coordinates $r_1(v)$ and $r_2(v)$ match for at least two different values of v .

The locus of the marginally trapped surfaces is defined via the expansion of a null outgoing geodesic congruence (see App. A.3 for details):

$$\theta_+ \equiv h^{ab} \nabla_a k_b = 0, \quad (6.3)$$

where h_{ab} is the induced metric on the 2-spheres of symmetry and k_b an outgoing radial null vector.

For the metric (6.1), the expansion along the null vector $k^a = (1, \frac{F}{2}, 0, 0)$ is $\theta_+ = \frac{F}{r}$ and thus the locations of the horizons $r(v)$ are defined by

$$\theta_+ = 0 \Leftrightarrow F(v, r(v)) = 0. \quad (6.4)$$

Since the existence of a closed trapped region requires the presence of two horizons, the equation $F(v, r(v)) = 0$ should thus be of at least degree 2 in r . In this minimal case of degree 2, one has

$$F(v, r) = 1 - 2m(v) \frac{r + a_0(v)}{r^2 + b_1(v)r + b_0(v)}, \quad (6.5)$$

and

$$\begin{aligned} F(v, r) = 0 &\Leftrightarrow r^2 + (b_1(v) - 2m(v))r + b_0(v) - 2m(v)a_0(v) = 0 \\ &\Leftrightarrow r(v) = \frac{2m(v) - b_1(v) \pm \sqrt{(b_1(v) - 2m(v))^2 - 4(b_0(v) - 2m(v)a_0(v))}}{2}. \end{aligned} \quad (6.6)$$

Another condition is that there must exist two different v at which $r_1 = r_2$, so that the trapping horizons be closed. It is thus entirely possible to choose $a_0(v)$, $b_1(v)$ and $b_2(v)$ in order to construct closed trapping horizons. However such a spacetime cannot be singularity-free, as we shall now see.

1.2.2 Conditions for the absence of singularities

In order to investigate the presence of a singularity in our spacetime, we need to verify that no curvature scalar diverges at any point of spacetime. We will thus compute the Ricci and Kretschmann scalars, which will give us constraints on the parameter α in eq. (6.2). They read

$$\begin{cases} R = g_{\mu\nu}R^{\mu\nu} = -\frac{r^2 \frac{\partial^2 F}{\partial r^2} + 4r \frac{\partial F}{\partial r} + 2F(v,r) - 2}{r^2} \\ K = R_{\mu\nu\rho\sigma}R^{\mu\nu\rho\sigma} = \frac{r^4 \left(\frac{\partial^2 F}{\partial r^2}\right)^2 + 4r^2 \left(\frac{\partial F}{\partial r}\right)^2 + 4F(v,r)^2 - 8F(v,r) + 4}{r^4} \end{cases} \quad (6.7)$$

Let us focus on the Ricci scalar first. One has to ensure that the expression

$$\frac{r^2}{2} \frac{\partial^2 F}{\partial r^2} + 2r \frac{\partial F}{\partial r} + F(v,r) - 1 ,$$

is of at least degree 2 in r to avoid the presence of a singularity.

First of all one notices that $b_0(v) \neq 0$ so that F does not diverge when $r \rightarrow 0$. This implies that $\frac{\partial^2 F}{\partial r^2}$ will contain no divergence, and $\frac{r^2}{2} \frac{\partial^2 F}{\partial r^2}$ will be at least of degree 2.

Then, one can show that

$$2r \frac{\partial F}{\partial r} + F(v,r) - 1 = \frac{-2m(v)}{(r^\alpha + \dots + b_0)^2} [\dots + r^2(5a_2b_0 + a_1b_1 - 3a_0b_2) + r(3a_1b_0 - b_1a_0) + a_0b_0] , \quad (6.8)$$

where the dots denote higher order terms in r . Since $b_0 \neq 0$, one must have $a_0 = 0$ and $a_1 = 0$ so that the expression in brackets be of at least degree 2. This means that the first nonzero coefficient must be a_2 , which implies

$$\boxed{\alpha \geq 3} . \quad (6.9)$$

A similar reasoning with the Kretschmann scalar leads to the same result, $\alpha \geq 3$.

1.2.3 Minimal form of F

This draws us to the conclusion that the simplest form of F describing a spacetime without singularities and containing closed trapping horizons, as well as allowing to recover Vaidya's solution when $r \rightarrow +\infty$, will have the general, minimal form

$$F(v,r) = 1 - 2m(v) \frac{r^2}{r^3 + b_2(v)r^2 + b_1(v)r + b_0(v)} . \quad (6.10)$$

Since we are interested only in the asymptotic behaviours, we can choose for simplicity $b_1(v) = b_2(v) = 0$. Then, by writing $b_0(v)$ as $b_0(v) = 2m(v)b^2$, we get

$$F(v,r) = 1 - \frac{2m(v)r^2}{r^3 + 2m(v)b(v)^2} , \quad (6.11)$$

where we recover Hayward's metric [71] when we set $b(v) = b = \text{cst}$. This metric has the interesting property of exhibiting a de Sitter limit when $r \rightarrow 0$, on top of the Vaidya limit when $r \rightarrow +\infty$. The constant parameter b plays the role of a de Sitter radius, and is interpreted as a Planckian cutoff [13, 71].

2 Examples of closed trapping horizons: properties and limits

For now, we have argued that the form of F given by eq. (6.11) is the most simple way of building a singularity-free spacetime with closed trapping horizons while recovering Vaidya and de Sitter limits (provided $b(v) = \text{cst}$ for the latter one). Let us then get more specific and obtain the coordinates of the horizons from eq. (6.11), before discussing the details of specific models.

2.1 Location of the trapping horizons

The location of the horizons is by definition

$$\theta_+ = 0 \Leftrightarrow F(v, r(v)) = 0, \quad (6.12)$$

which, with our expression (6.11) of F , boils down to a polynomial equation in r

$$r^3 - 2mr^2 + 2mb^2 = 0. \quad (6.13)$$

Using Cardan's method, one gets the discriminant $\Delta = 4m^2b^2(16m^2 - 27b^2)$. The equation admits at least two distinct real solutions if $\Delta > 0$, and two degenerate real solutions if $\Delta = 0$. One has

$$\Delta \geq 0 \Leftrightarrow m \geq \frac{3\sqrt{3}}{4}b. \quad (6.14)$$

The starting point and endpoint of the trapping horizons in a (r, v) diagram are thus defined by $m = \frac{3\sqrt{3}}{4}b$. Provided $m \geq \frac{3\sqrt{3}}{4}b$, one finally gets three solutions for a given value of v

$$r_j = \frac{4m}{3} \cos \left(\frac{1}{3} \arccos \left(1 - \frac{27b^2}{8m^2} \right) + \frac{2(j-1)\pi}{3} \right) + \frac{2m}{3}, \quad j = 1, 2, 3 \quad (6.15)$$

r_1 and r_3 are the only positive solutions, describing the outer and inner trapping horizons respectively. In the case where $b \ll m$ (e.g. when b is a Planckian cutoff), expanding these solutions in terms of b/m leads to

$$\begin{cases} r_1 = 2m - \frac{b^2}{2m} + o\left(\frac{b^2}{m}\right), \\ r_3 = b + \frac{b^2}{4m} + o\left(\frac{b^2}{m}\right). \end{cases} \quad (6.16)$$

r_1 will play the role of the future outer trapping horizon, reducing to Schwarzschild's event horizon when $b = 0$ and $m = \text{cst}$. r_3 is actually a future inner trapping horizon. As seen in the case of Reissner-Nordström black hole (Sec. 2 of Chap. 2), the presence of an inner horizon, hence preventing the existence of a trapped region between it and $r = 0$, is not enough to avoid a singularity. That is why we have chosen carefully the form (6.11).

2.2 Hayward-like model

Hayward presented in [71] a simple model describing the formation and evaporation of a trapped region, relying on the form (6.11) of the metric with a constant Planckian cutoff b . He chose a symmetric function $m(v)$ containing a plateau that describes similarly the formation and the evaporation phases. We have here used the following form for $m(v)$ and b

$$m(v) = r_0 \exp \left\{ \left(- \frac{(v - v_0)^2}{\sigma^2} \right) \right\}, \quad (6.17)$$

$$b = \frac{r_0}{5}, \quad (6.18)$$

which is plotted in Fig. 6.2(a) and where $r_0 = 100$, $v_0 = 1000$, $\sigma = 400$. Here we chose a macroscopic value for b solely for pedagogical reasons, so that the inner horizon be distinguishable from the horizontal axis in Fig. 6.2(b). This model, although it displays closed trapping horizons and no singularity, suffers from certain limitations in its physical interpretation.

First of all, let us consider the NEC along the ingoing radial null direction l^μ :

$$T_{\mu\nu} l^\mu l^\nu = - \frac{1}{32\pi r} \frac{\partial F}{\partial v} = \frac{1}{16\pi} \frac{m'(v)r^4}{(r^3 + 2m(v)b^2)^2} \geq 0, \quad (6.19)$$

where $T_{\mu\nu}$ is the energy-momentum tensor. We see that the NEC is violated when $m'(v) < 0$, which happens along lines of constant $v \geq v_0$, v_0 being the time when the outer horizon starts shrinking. This allows circumventing Penrose's singularity theorem 1.3, but remains problematic since it would imply a violation of the NEC in regions arbitrarily far from the collapsed body (e.g. $v = \text{cst}$, $r \rightarrow +\infty$). In Sec. 4, we will show that this limitation is inherent to the black hole models asymptotically constructed out of ingoing Vaidya shells.

Another limitation in the physical interpretation is the symmetry in the outer trapping horizon growing and shrinking. The increase in horizon radius physically comes from the inflow of matter or radiation into the trapped region, while its decrease must come from Hawking radiation. These two effects have no reasons to show the same scaling, which they do in Hayward's model (see Fig. 6.2(b)).

Moreover, the reason why the inner trapping horizon is quantum mechanically held at a fixed distance from the centre is not clear, and this feature appears to be quite artificial. Lastly, as noticed in [44], this model does not allow for a time delay between the centre of the cloud and infinity since $F \rightarrow 1$ when $r \rightarrow 0$ as well as $r \rightarrow +\infty$.

We will call Hayward-like models those that exhibit symmetric phases of formation and evaporation whilst their inner horizon's radius remains at a Planckian distance from the centre $r = 0$.

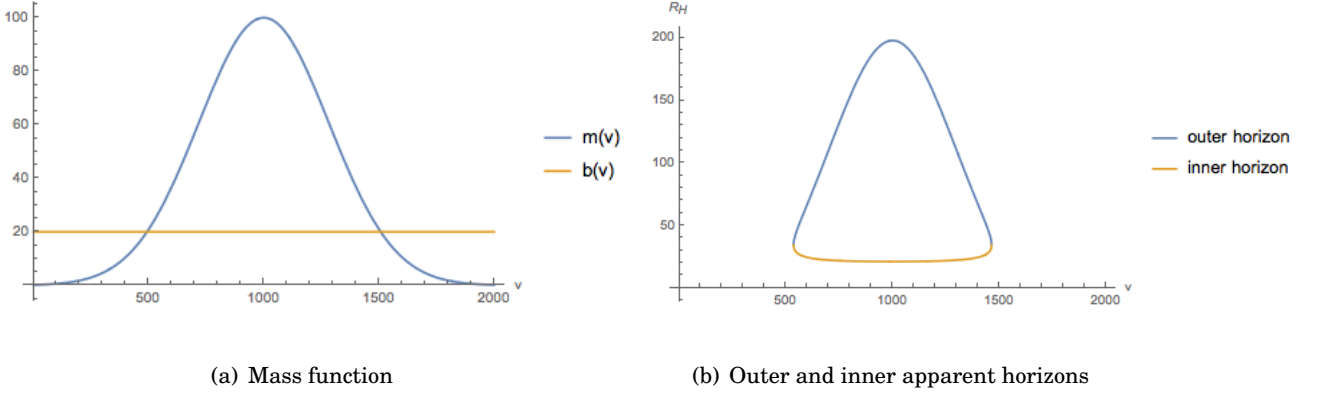


Figure 6.2: Hayward-like model

2.3 Frolov's model

Frolov's construction [53] aims at modeling the Hawking evaporation, and thus introduces an asymmetry between the formation and the evaporation phases. F has the same form as in Hayward's model, but here the mass function is defined by parts

$$\begin{cases} -\infty < v < v_0 & : m(v) = 0, \\ v_0 < v < 0 & : m(v)/b = (m_0/b)^3 + v/b, \\ 0 < v < v_1 & : (m(v)/b)^3 = (m_0/b)^3 - v/b, \\ v_1 < v < +\infty & : m(v) = 0, \end{cases} \quad (6.20)$$

where v , $m(v)$ and $m_0 = 4$ are expressed in units of b . The form of $m(v)$ during the evaporation phase ($0 < v < v_1$) is chosen so that one recovers the correct scaling for the mass loss \dot{m} due to Hawking radiation, i.e.

$$\dot{m} \sim -C \left(\frac{m_{Pl}}{m} \right)^2, \quad (6.21)$$

where C is a coefficient depending on the details of the emitted particles, and m_{Pl} is the Planck mass. This gives a more realistic description of the evaporation process than the symmetric model of Hayward. The obtained shapes for the parameter functions and for the horizons are shown in Fig. 6.3.

However, this model still displays some important limitations from the point of view of the physical interpretation: the violation of the NEC at infinity when the outer trapping horizon starts shrinking, the constancy of the inner trapping horizon radius, and the absence of time delay between the centre and infinity.

2.4 Bardeen-like model

In the two previous models, we have noticed that the inner horizon almost stays at a constant and small radius r . This actually results directly from the expansion (6.16), which implies that the inner horizon radius is essentially given by the constant Planckian cutoff b .

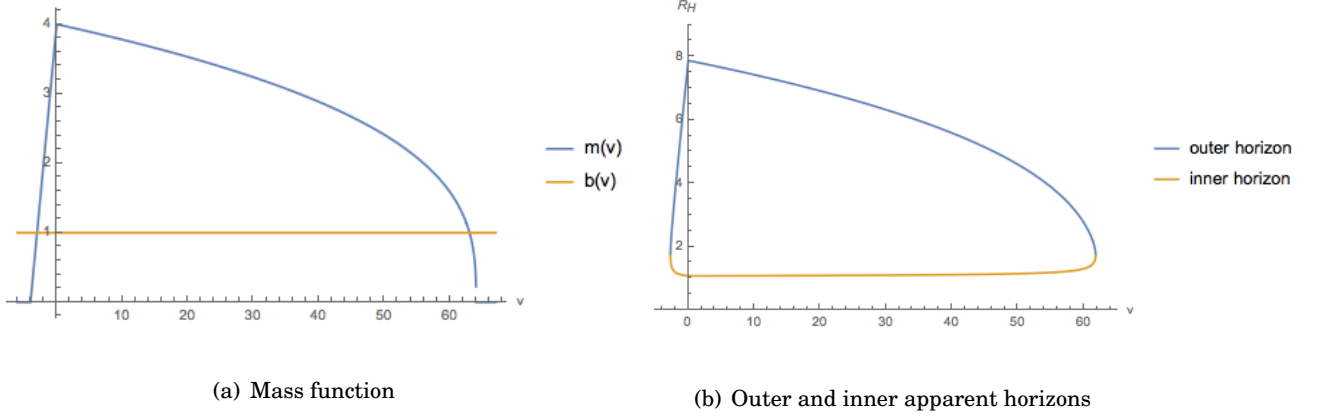


Figure 6.3: Frolov's model

However, one of Bardeen's main points in [13] consists in giving a dynamics to the inner horizon. More precisely, Bardeen argues that some Hawking pairs will be created at the inner horizon, which will begin to grow due to Bousso's covariant entropy bound [24] and finally reach the outer horizon at macroscopic scales. We will thus call Bardeen-like models those which exhibit such a property of the inner horizon (Fig. 6.4(b)). We have tried to explicitly recover this model with the following parameter functions, plotted in Fig. 6.4(a)

$$m(v) = r_0 \exp \left\{ \left(- \frac{(v - v_0)^2}{\sigma^2} \right) \right\}, \quad (6.22)$$

$$b(v) = r_0 \exp \left\{ \left(- \frac{(v - v'_0)^2}{\sigma'^2} \right) \right\} + b_0, \quad (6.23)$$

where $r_0 = 100$, $v_0 = 1000$, $v'_0 = 800$, $\sigma = 400$, $\sigma' = 200$, $b_0 = 5$.

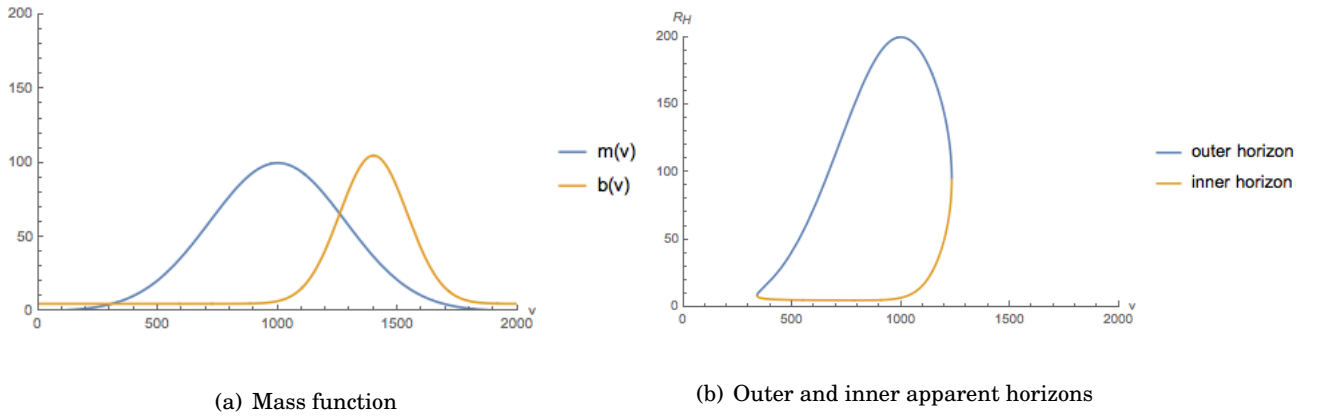


Figure 6.4: Bardeen-like model

Once again, this model possesses important limitations in its physical interpretation: the NEC is violated in a non-compact region as soon as the outer trapping horizon starts shrinking, and the time-delay between the centre and an asymptotic clock is absent.

Another model of non-singular black hole, based on the metric (6.1) with a function $F(v, r)$ given by eq. (6.11), and known as Planck stars, is free from some of these limitations: the NEC is violated in a compact neighbourhood of the source and the time-delay in the core is present [44]. However, this model is static, with fixed values for the radii of the outer and inner trapping horizons, and therefore cannot describe the dynamics of the formation and evaporation of a closed trapped region.

Before presenting in Sec. 4 our attempt to answer the aforementioned limitations of the models that are found in the literature, let us investigate in more detail in Sec. 3 some properties shared by all these models.

3 Behaviour of null geodesics in models with closed trapping horizons

The above models do not possess any event horizon since they are dynamical and aim at describing a trapped region that will eventually be fully evaporated, leaving no region of spacetime causally disconnected from future null infinity. It is nonetheless of interest to study the relevant geodesics of such spacetimes.

3.1 Null geodesic flow

The radial null geodesics for metric (6.1),

$$ds^2 = -F(v, r)dv^2 + 2dvdr + r^2 d\Omega^2, \quad (6.24)$$

are given by

$$ds^2 = 0 \Leftrightarrow \begin{cases} dv = 0, \\ \frac{dr}{dv} = \frac{F(v, r)}{2}. \end{cases} \quad (6.25)$$

In the case of Minkowski spacetime, $F = 1$ and the radial null geodesics are trivial since the lightcone is the same at each point of spacetime. In a (v, r) diagram, ingoing radial null geodesics are $v = \text{cst}$ lines while outgoing ones are lines of slope 1/2; this is the behaviour we will recover far from the trapped region.

When the metric is not trivial, the outgoing radial null geodesics will differ from straight lines in the (v, r) diagram. This can be seen in Fig. 6.5(a), where we have plotted these geodesics for a Schwarzschild metric (with $M = 1$). Visualizing the outgoing geodesics reveals the existence of an event horizon: the lightcone prevents any matter or light from the region $r < 2$ from escaping, and this is the case for all v . Therefore there exists a region of spacetime that cannot communicate with \mathcal{I}^+ , and this region is by definition bounded by an event horizon.

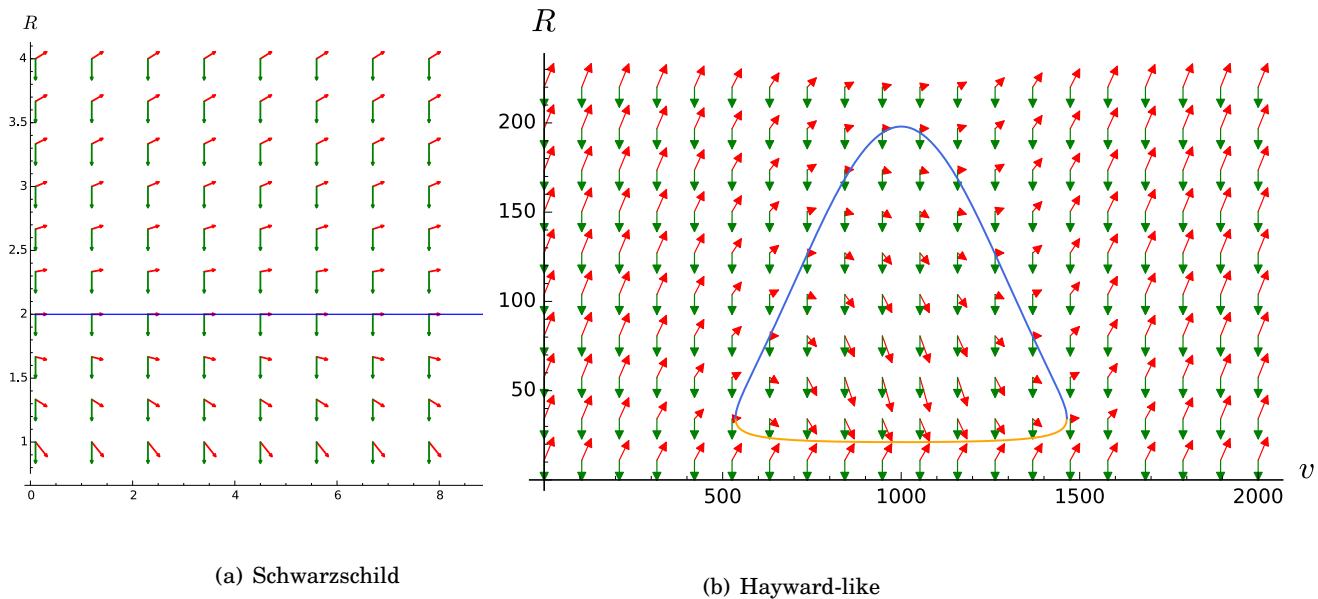


Figure 6.5: Plot of the outgoing (in red) and ingoing (in green) null vectors depicting the lightcone of Schwarzschild (a) and Hayward-like (b) spacetimes. In Schwarzschild’s case there is only one horizon (in blue), which is a null hypersurface for all v hence called *event horizon*. As regards the Hayward-like geometry, the outer (in blue) and inner (in yellow) *trapping horizons* are successively timelike, null and spacelike.

In our models (e.g. the Hayward-like model, Fig. 6.5(b)), no event horizon appears. However trapping horizons develop, and are not necessarily tangent to the lightcones. Indeed, trapping horizons are dynamical and can be spacelike, null or timelike [69].

3.2 Frolov’s separatrix and quasi-horizon

In spite of the absence of a region causally disconnected from future null infinity, there is still a non-trivial behaviour of the radial null outgoing geodesics due to the trapped region, which is interesting to investigate. In particular, since the apparent horizon can now be timelike and therefore traversable, we may want to look for an alternative surface that would not be traversable from the inside. This surface is easily found to be the one generated by the radial null outgoing geodesic which passes through the last trapped sphere, i.e. point D of Fig. 6.1. It is the last radial null outgoing geodesic to leave the trapped region (in terms of time v , see Fig. 6.6), and we may call it the D -geodesic. This boundary of the no-escape region (a region which has finite lifetime here) is dubbed “quasi-horizon” in [54]: it traps all the matter it contains until the final evaporation of the trapped region.

It was also suggested in [54] to use the separatrix of the null outgoing radial vector field, defined by the vanishing of $\frac{d^2 r}{dv^2}$ for the geodesics of eq. (6.25), $\frac{dr}{dv} = \frac{F}{2}$. This yields

$$\frac{\partial_v F}{2} + \frac{dr}{dv} \frac{\partial_r F}{2} = \frac{\dot{F}}{2} + \frac{FF'}{4} = 0 \quad \Leftrightarrow \quad 2\dot{F} + FF' = 0, \quad (6.26)$$

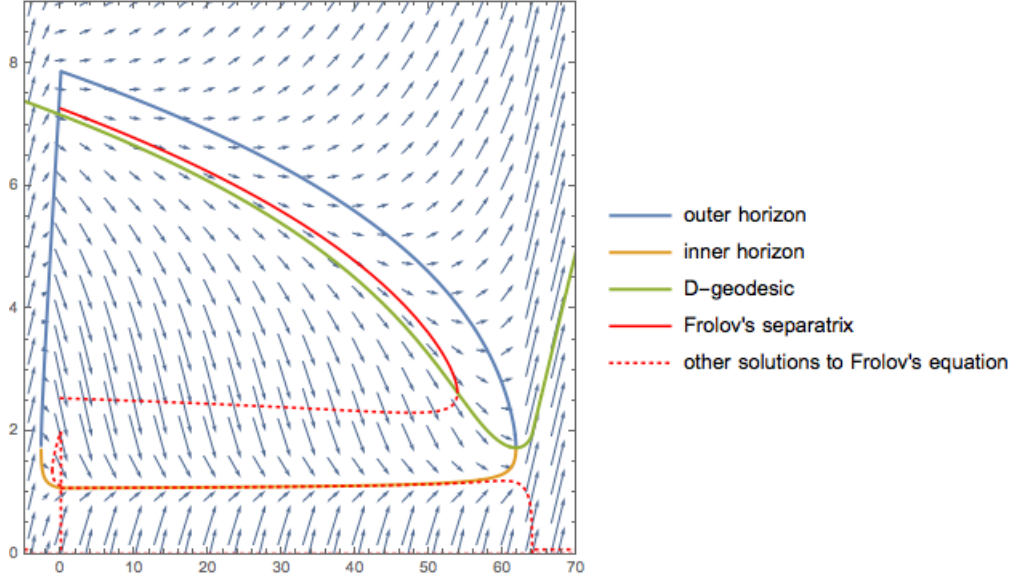


Figure 6.6: Example of separatrix (in red) and D -geodesic (in green) for Frolov's model with $b = 1$, $m_0^3 = 4$. The field of outgoing null vectors (blue arrows) illustrates that the separatrix is traversable by outgoing null or timelike matter, while the D -geodesic is not.

where a dot (resp. prime) denotes a derivative with respect to v (resp. r). This surface characterizes the strength of the trapping of light rays inside the trapped region: on one side of the separatrix the light rays are more and more trapped, whereas they are less and less so on the other side. When this surface is a null outgoing geodesic in the trapped region, it is not possible for light rays to cross it from inside to outside, and they are doomed to become evermore trapped. This is the case with the Schwarzschild black hole, where $F = 1 - 2M/r$ and M is a constant. Then eq. (6.26) yields $r = 2M$ and the separatrix coincides with the apparent horizon which, in this case, is also an event horizon (and of course also a quasi-horizon).

However, in general, the separatrix is not lightlike but can be timelike, and therefore null outgoing geodesics may traverse it. This is visible in Fig. 6.6, where all the solutions to eq. (6.26) have been plotted in red. In this case it cannot coincide with the D -geodesic (or “quasi-horizon”), and we consider the latter notion to be the relevant one in the study of the region of non-escaping matter and radiation.

In [54], closed trapping horizons are built, with the separatrix and D -geodesic taken as synonymous, most certainly because the separatrix is close to being null in this particular case. We nevertheless stress the fact that in general, the two notions are distinct.

3.3 Relevant null geodesics for closed trapping horizons

We defined above the D -geodesic, called quasi-horizon by Frolov, which enables us to divide all particles located in the trapped region into two categories: those exiting this region through the

outer horizon, and those exiting by the inner one.

Other regions are relevant for the study of models of closed trapping horizons, and can be defined by using radial null outgoing geodesics going through not only D but also points A , B , and C of Fig. 6.1. The A -geodesic goes through the last point (in terms of v) at which the inner horizon is null. This curve thus bounds from above the region of spacetime whose content is causally prevented from going into the trapped region. The B -geodesic goes through the first point (in terms of v) at which the outer horizon is null. It represents the first geodesic (in terms of v) able to escape from the trapped region. Finally, it may also be interesting to define the C -geodesic as the geodesic going through the point of formation of the two horizons. It divides massless outgoing particles located in the trapped region into two categories: those which entered via the outer horizon, and those entered via the inner horizon.

These geodesics allow to define (at least) two zones of the spacetime which have a physical significance:

- (i) all massless outgoing particles of the trapped region which do not exit by the outer horizon must belong to a zone bounded by the A -geodesic and the D -geodesic.
- (ii) all Hawking particles emitted from the outer horizon must belong to a zone bounded by the B -geodesic and A -geodesic.

The A and D -geodesics are plotted below for the three different models. In each model these two geodesics quickly tend towards those of Minkowski's spacetime (slope 1/2) after the disappearance of the trapped region. They delineate a corridor whose largest version is associated with the Bardeen-like case.

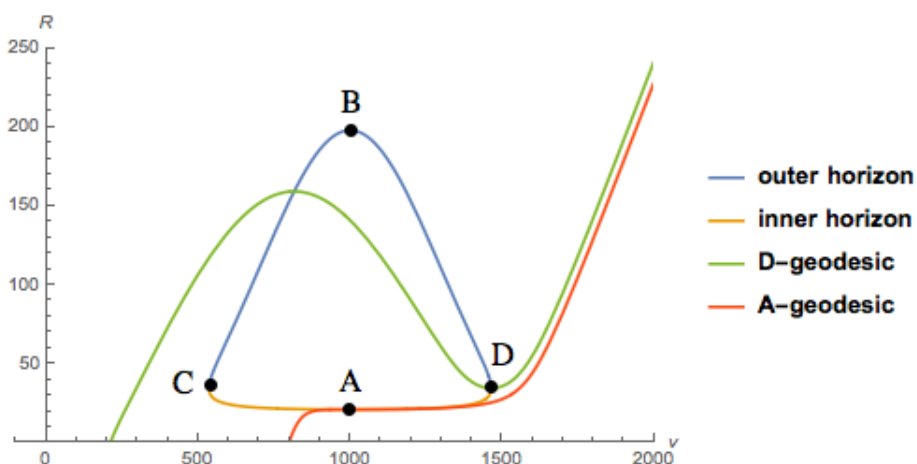


Figure 6.7: Hayward-like model

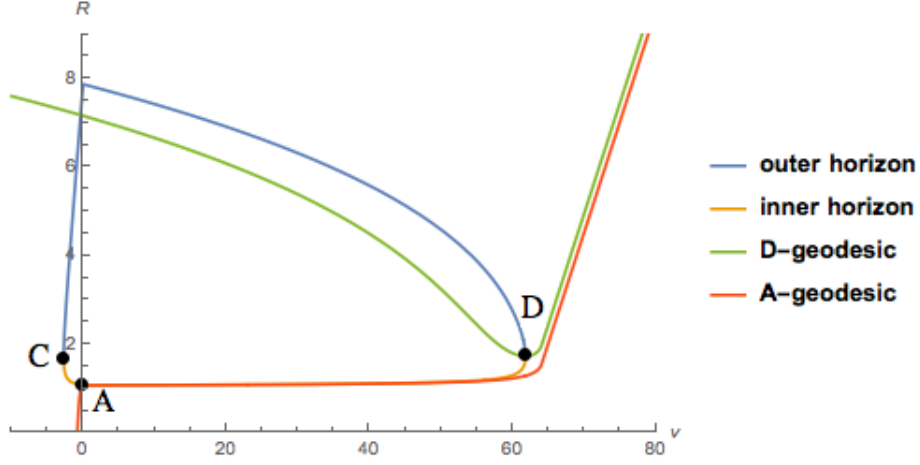
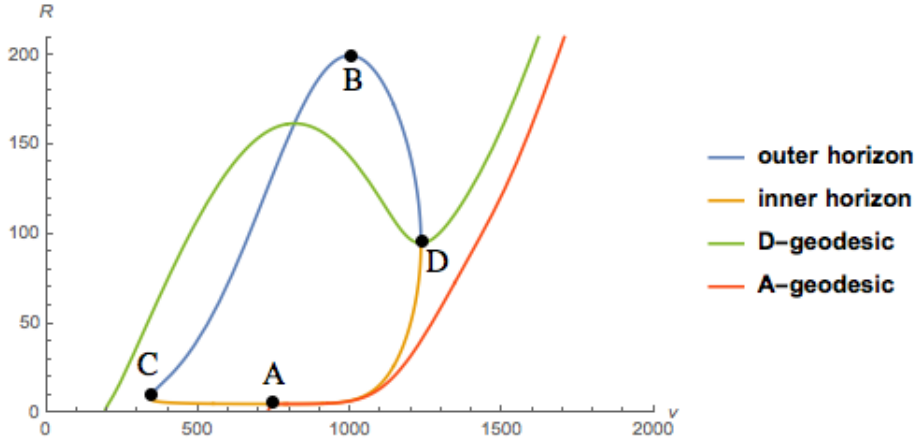

 Figure 6.8: Frolov's model. There is no point B since $m(v)$ is not differentiable.


Figure 6.9: Bardeen-like model

4 Towards a model for the formation and evaporation of a non-singular trapped region

Until now we have provided a geometry describing the formation and evaporation of closed trapping horizons without singularity, while requiring solely that we recover the appropriate Vaidya limit on \mathcal{I}^- and the de Sitter limit at the center. It is now necessary to study the associated energy content, given by the Einstein tensor via Einstein's equations, in order to check whether this content is physical.

4.1 A form of the metric constrained by the energy-momentum tensor

Let us start with the most general spherically symmetric metric in advanced Eddington-Finkelstein coordinates, encoding a new degree of freedom through function ψ :

$$ds^2 = -F(v, r)e^{2\psi(v, r)} dv^2 + 2e^{\psi(v, r)} dv dr + r^2 d\Omega^2. \quad (6.27)$$

This form will prove to be useful later on, since we will show that no evaporation can occur without a dynamical ψ , and that this ψ is also necessary not to violate the null energy condition on \mathcal{J}^- . By virtue of Einstein's equations, the energy-momentum tensor can be written as

$$\mathbf{T} = T_{vv} \mathbf{d}v \otimes \mathbf{d}v + T_{vr} (\mathbf{d}v \otimes \mathbf{d}r + \mathbf{d}r \otimes \mathbf{d}v) + T_{rr} \mathbf{d}r \otimes \mathbf{d}r + T_{\theta\theta} (\mathbf{d}\theta \otimes \mathbf{d}\theta + \sin^2 \theta \mathbf{d}\varphi \otimes \mathbf{d}\varphi), \quad (6.28)$$

with

$$\begin{cases} 8\pi T_{vv} = -\frac{1}{r^2} \left(rF(v, r) e^{2\psi(v, r)} \frac{\partial F}{\partial r} + F(v, r)^2 e^{2\psi(v, r)} + r e^{\psi(v, r)} \frac{\partial F}{\partial v} - F(v, r) e^{2\psi(v, r)} \right), \\ 8\pi T_{vr} = \frac{1}{r^2} \left(r e^{\psi(v, r)} \frac{\partial F}{\partial r} + F(v, r) e^{\psi(v, r)} - e^{\psi(v, r)} \right), \\ 8\pi T_{rr} = \frac{2}{r} \frac{\partial \psi}{\partial r}, \\ 8\pi T_{\theta\theta} = \frac{1}{2} \left[2r^2 F(v, r) e^{\psi(v, r)} \left(\frac{\partial \psi}{\partial r} \right)^2 + 2r^2 F(v, r) e^{\psi(v, r)} \frac{\partial^2 \psi}{\partial r^2} + r^2 e^{\psi(v, r)} \frac{\partial^2 F}{\partial r^2} + 2r e^{\psi(v, r)} \frac{\partial F}{\partial r} \right. \\ \left. + 2r^2 \frac{\partial^2 \psi}{\partial v \partial r} + (3r^2 e^{\psi(v, r)} \frac{\partial F}{\partial r} + 2r F(v, r) e^{\psi(v, r)}) \frac{\partial \psi}{\partial r} \right] e^{-\psi(v, r)}. \end{cases} \quad (6.29)$$

In the following, we will attempt to compare our energy content to the one of a pure Vaidya spacetime. Indeed, the collapse of an ingoing null shell described by an ingoing Vaidya metric is a natural candidate for the formation phase of the trapped region written in (v, r) coordinates. Moreover, the Hawking radiation associated with the evaporation phase can be described at first order by a flux of outgoing photons, hence the use of an outgoing Vaidya metric. To that purpose, let us write our energy-momentum tensor as follows

$$\mathbf{T} = T_{kk} \mathbf{k} \otimes \mathbf{k} + T_{ll} \mathbf{l} \otimes \mathbf{l} + T_{kl} (\mathbf{k} \otimes \mathbf{l} + \mathbf{l} \otimes \mathbf{k}) + T_{\theta\theta} (\mathbf{d}\theta \otimes \mathbf{d}\theta + \sin^2 \theta \mathbf{d}\varphi \otimes \mathbf{d}\varphi), \quad (6.30)$$

where \mathbf{l} and \mathbf{k} are two independent null covectors, respectively ingoing and outgoing. Notice that it is always possible to write the energy-momentum tensor under this form under the assumption of spherical symmetry; the coefficients T_{kk} , T_{ll} and T_{kl} depend solely on the non-spherical components of the metric.

To get to the form (6.30), one needs the expressions of the outgoing and ingoing radial null covectors \mathbf{k} and \mathbf{l}

$$\begin{cases} \mathbf{k} = -\frac{F}{2} e^{2\psi} \mathbf{d}v + e^{\psi} \mathbf{d}r, \\ \mathbf{l} = -2 \mathbf{d}v, \end{cases} \quad (6.31)$$

where the normalization $\mathbf{k} \cdot \mathbf{l} = -2$ has been chosen.

One then obtains

$$\begin{cases} \mathbf{d}v = -\frac{1}{2}\mathbf{l} , \\ \mathbf{d}r = e^{-\psi}\mathbf{k} - \frac{Fe^\psi}{4}\mathbf{l} . \end{cases} \quad (6.32)$$

Plugging (6.32) into (6.28) finally leads to

$$\begin{cases} 8\pi T_{kk} = 8\pi T_{rr}e^{-2\psi} = \frac{2e^{-2\psi(v,r)}\frac{\partial\psi}{\partial r}}{r} , \\ 8\pi T_{ll} = 8\pi \left(\frac{T_{vv}}{4} + \frac{Fe^\psi}{4}T_{vr} + \frac{F^2e^{2\psi}}{16} \right) = \frac{F(v,r)^2e^{2\psi(v,r)}\frac{\partial\psi}{\partial r} - 2e^{\psi(v,r)}\frac{\partial F}{\partial v}}{8r} , \\ 8\pi T_{kl} = 8\pi \left(-\frac{e^{-\psi}}{2}T_{vr} - \frac{F}{4}T_{rr} \right) = -\frac{rF(v,r)\frac{\partial\psi}{\partial r} + r\frac{\partial F}{\partial r} + F(v,r) - 1}{2r^2} . \end{cases} \quad (6.33)$$

As we have already mentioned in Sec. 2, models of trapped region with closed horizons require a violation of the null energy condition on the interval ADB of Fig. 6.1. When the NEC is violated, so are all the energy conditions. It is thus of interest to verify that this violation occurs in a region of finite size, i.e. that the violation is confined to a compact region of spacetime. Recall that the NEC reads, for all null vector n^μ ,

$$T_{\mu\nu}n^\mu n^\nu \geq 0 . \quad (6.34)$$

Using the covectors l and k as long as equations (6.30) and (6.33), the NEC then reads

$$\begin{cases} T_{\mu\nu}k^\mu k^\nu = T_{kk} = \frac{2e^{-2\psi(v,r)}\frac{\partial\psi}{\partial r}}{8\pi r} \geq 0 , \\ T_{\mu\nu}l^\mu l^\nu = T_{ll} = \frac{F(v,r)^2e^{2\psi(v,r)}\frac{\partial\psi}{\partial r} - 2e^{\psi(v,r)}\frac{\partial F}{\partial v}}{64\pi r} \geq 0 . \end{cases} \quad (6.35)$$

Let us now focus on the cases of the models developed above, namely the Hayward, Frolov and Bardeen-like models. In this case, $\psi(v, r) = 0$ and the conditions (6.35) boil down to

$$\begin{cases} T_{kk} = 0 \geq 0 , \\ T_{ll} = -\frac{1}{32\pi r}\frac{\partial F}{\partial v} \geq 0 . \end{cases} \quad (6.36)$$

A necessary condition for the NEC to be satisfied is thus: $\partial_v F \leq 0$. Considering the form of F (see eq. (6.11)) and taking $r \rightarrow +\infty$, one recovers the standard ingoing Vaidya metric $F = 1 - \frac{2M(v)}{r}$. This means that the NEC is violated at infinity as soon as M becomes a decreasing function of v . Using the previous calculations for various models, one sees in fact that there exists a line dividing the whole spacetime into a NEC-satisfying and a NEC-violating region (see Fig. 6.10, where the NEC line represents $\partial_v F = 0$).

4.2 Explicit energy-momentum tensor

4.2.1 Conditions on the energy-momentum tensor

The requirements on the energy-momentum tensor for obtaining a transition from the collapse of a null ingoing Vaidya shell to a Hayward-like non-singular trapped region, which then evaporates forming a null outgoing Vaidya shell on \mathcal{I}^+ , are the following:

$$\begin{aligned} T_{ll} &\gg T_{kk}, T_{kl}, T_{\theta\theta} \text{ on } \mathcal{I}^- , \\ T_{kk} &\gg T_{ll}, T_{kl}, T_{\theta\theta} \text{ on } \mathcal{I}^+ . \end{aligned} \quad (6.37)$$

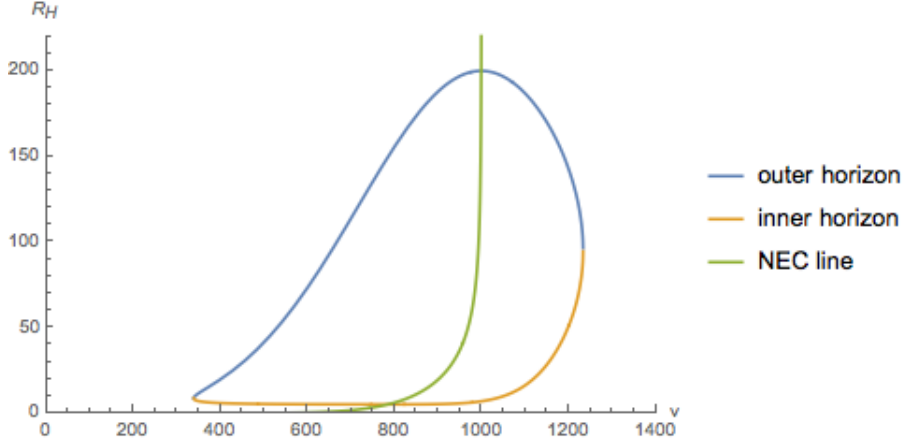


Figure 6.10: NEC violation in Bardeen-like model

We also demand that the null energy condition be satisfied up to infinity, thus:

$$T_{ll}, T_{kk} \geq 0 \text{ on } \mathcal{I}^- \text{ and } \mathcal{I}^+ . \quad (6.38)$$

The \mathcal{I}^+ and \mathcal{I}^- limits are characterized by $v \rightarrow +\infty$ and $u \rightarrow -\infty$, where $u = v - 2r$. We can define all functions in terms of u and v , which gives

$$\begin{cases} T_{kk} = -\frac{e^{-2\psi(u,v)} \partial_u \psi}{2\pi(v-u)} , \\ T_{ll} = -\frac{F(u,v)^2 e^{2\psi(u,v)} \partial_u \psi + e^{\psi(u,v)} \frac{\partial F}{\partial v}}{32\pi(v-u)} , \\ T_{kl} = \frac{F(u,v) \partial_u \psi + \partial_u F + \frac{F(u,v)-1}{v-u}}{8\pi(v-u)} . \end{cases} \quad (6.39)$$

In order to obtain an explicit energy-momentum tensor describing the formation and evaporation of a non-singular trapped region, we will have the freedom to choose ψ . Indeed, this function will not affect the form of the horizons:

$$\theta_+ = \frac{F(v,r) e^{\psi(v,r)}}{r} = 0 \Leftrightarrow F = 0 . \quad (6.40)$$

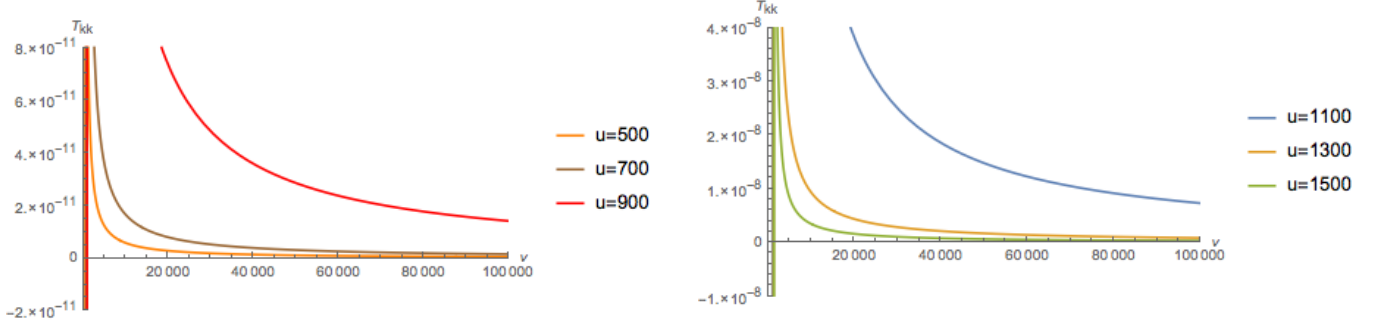
We can thus look for a function ψ to model the gravitational collapse and Hawking radiation while keeping the horizons of the Hayward, Frolov or Bardeen cases; this is the purpose of the next two subsections.

4.2.2 Generating a Hawking flux on \mathcal{I}^+

Let us start by describing the phase of evaporation of the trapped region, mimicking the Hawking radiation by the energy-momentum tensor of an outgoing Vaidya metric. The component that must dominate all others is

$$T_{kk} = -\frac{e^{-2\psi(u,v)} \partial_u \psi}{\pi(v-u)} . \quad (6.41)$$

It is thus clear that ψ must not be a constant in order to obtain a flux of Hawking radiation on \mathcal{I}^+ . For simplicity we can choose ψ of the form $\psi = \psi(u)$. This allows us to avoid a violation of


 Figure 6.11: Plots of T_{kk} as a function of v for $u = 500, 700, 900, 1100, 1300, 1500$.

the NEC on \mathcal{I}^+ , as well as to recover Minkowski's metric there (up to a rescaling of the advanced time v). Furthermore, with the intensity of the Hawking flux being driven by T_{kk} , hence by $\partial_u \psi$, we are looking for a function ψ with an important slope for a given interval of u (the phase of Hawking radiation) and that tends towards a constant value for large u . The following function meets all the above criteria:

$$\psi(u) = \arctan(1000 - u) . \quad (6.42)$$

This leads to

$$\begin{aligned} T_{kk} &= \frac{\exp(-2 \arctan(1000 - u))}{\pi(1 + (v - u)^2)(v - u)} , \\ T_{ll} &= -\frac{\exp(\arctan(1000 - u))}{32\pi(v - u)} \left[\partial_v F - \frac{\exp(\arctan(1000 - u))F^2}{1 + (1000 - u)^2} \right] . \end{aligned} \quad (6.43)$$

On \mathcal{I}^+ , $v \rightarrow +\infty$ and we immediately have $T_{kk} \rightarrow 0^+$. As concerns T_{ll} , $\partial_v F \rightarrow 0$ and the second term thus dominates in the bracket. Hence, $T_{ll} \rightarrow 0^+$ on \mathcal{I}^+ as well.

In Fig. 6.11, one can see that for large positive values of v , the biggest values of T_{kk} are centered around $u = 1000$.

Finally, it can be seen in Fig. 6.12 that abruptly after $u = 1000$ and at large v , T_{kk} dominates the other components of the energy-momentum tensor. This outgoing Vaidya-like behaviour mimics the beginning of Hawking's radiation.

4.2.3 Avoiding the NEC violation on \mathcal{I}^-

We will now focus on the choice of ψ on \mathcal{I}^- , giving three necessary conditions that must be fulfilled in order to recover Vaidya's metric without a NEC violation on \mathcal{I}^- (eq. (6.47)). As explained in Sec. 4.1, choosing $\psi = 0$ leads to a violation of the NEC on all $v = \text{cst}$ slices as soon as m begins to decrease ($v > 1000$ in the Hayward-like model). In order to avoid this violation of the NEC on \mathcal{I}^- , one has to carefully study the sign of the following components of the

4. TOWARDS A MODEL FOR THE FORMATION AND EVAPORATION OF A NON-SINGULAR TRAPPED REGION

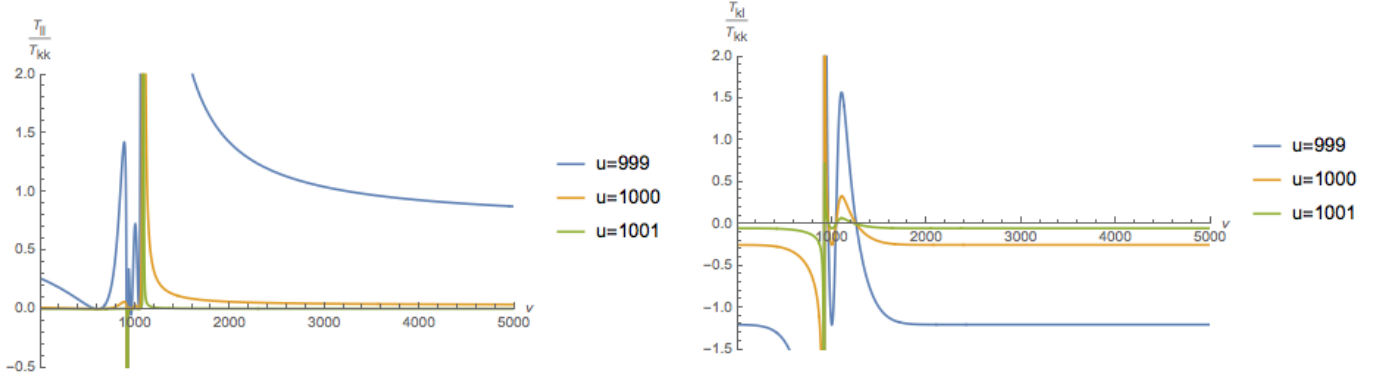


Figure 6.12: Plots of $\frac{T_{ll}}{T_{kk}}$ (left) and $\frac{T_{kl}}{T_{kk}}$ (right) as a function of v for $u = 999, 1000, 1001$.

energy-momentum tensor:

$$\begin{cases} T_{kk} = -\frac{e^{-2\psi(u,v)}\partial_u\psi}{\pi(v-u)}, \\ T_{ll} = -\frac{e^{\psi(u,v)}}{32\pi(v-u)} [F^2 e^{\psi(u,v)}\partial_u\psi + \partial_v F] . \end{cases} \quad (6.44)$$

First of all, choosing a function ψ such that $\partial_u\psi \leq 0$ for $u \rightarrow -\infty$ ensures that T_{kk} is non negative on \mathcal{I}^- (this translates into condition ii) in eq. (6.47)). As concerns T_{ll} , the term inside the brackets must be negative for $u \rightarrow -\infty$. Let us study the sign of $\partial_v F$, assuming a form for F boiling down to an ingoing Vaidya metric near \mathcal{I}^- :

$$\begin{cases} F(v,r) = 1 - \frac{2M(v,r)}{r}, \\ \lim_{\substack{v=\text{cst} \\ r \rightarrow +\infty}} M(v,r) = m(v). \end{cases} \quad (6.45)$$

Since $r = (v - u)/2$, the leading term of $\partial_v F$ on \mathcal{I}^- is

$$\partial_v F \simeq \frac{4\partial_v m(v)}{u}. \quad (6.46)$$

Therefore, as long as $m(v)$ is increasing, $T_{ll} \rightarrow 0^+$ on \mathcal{I}^- assuming that we keep the value of ψ such that $\partial_u\psi \leq 0$.

However, as soon as $m(v)$ begins to decrease, this leads to $\partial_v F \rightarrow 0^+$ on \mathcal{I}^- . Since $\partial_u\psi \leq 0$, we have to study carefully the sign of T_{ll} . On \mathcal{I}^- , $F \rightarrow 1$ and we require that $e^{\psi(u,v)} \rightarrow \text{cst}$ so that we recover Vaidya's metric there: this is our condition i) in eq. (6.47) below. Hence, the study of the sign of T_{ll} comes down to the comparison of the dominant terms of $\partial_u\psi$ and $\partial_v F \simeq \frac{4\partial_v m(v)}{u}$ (condition iii) below). Ultimately, finding $\psi(u,v)$ boils down to satisfying simultaneously the three following conditions:

$$\begin{aligned} \text{i) } & \lim_{u \rightarrow -\infty} \psi(u,v) = a, a \in \mathbb{R}. \\ \text{ii) } & \lim_{u \rightarrow -\infty} \partial_u\psi(u,v) = b, b \in \mathbb{R}^-. \\ \text{iii) } & \partial_u\psi \leq \frac{1}{u} \text{ for large enough } |u|, \text{ with } u < 0. \end{aligned} \quad (6.47)$$

It appears that conditions i) and iii) are incompatible. Indeed, after integrating iii) we get:

$$c_0 - \psi(u, v) \leq c_1 - \log(-u) , \quad (6.48)$$

where c_0 and c_1 are integration constants. Hence,

$$\psi(u, v) \geq \log(-u) + c_0 - c_1 \xrightarrow{u \rightarrow -\infty} +\infty . \quad (6.49)$$

$\psi(u, v)$ can thus be made arbitrarily large in absolute value, in contradiction with i).

Finally, we have shown that every spacetime equipped with a metric of the ingoing Vaidya form (6.45) near \mathscr{I}^- , hence satisfying i), will violate condition iii) and thus the NEC in a non-compact region as soon as $m(v)$ decreases. This applies, in particular, to the models of Hayward, Frolov and Bardeen, which mimic the Hawking evaporation through a decreasing function $m(v)$.

CONCLUSION

This dissertation aimed at presenting the various projects I conducted during my thesis, which all fall under the scope of non-singular black holes. From static to dynamical models, from theoretical to observational aspects, numerous dimensions of non-singular black holes have been covered.

The project on rotating regular black holes is certainly the one which best illustrates this variety of approaches. We began by proposing the so-called regular rotating Hayward model, which is in some regime the first model of a fully regular rotating black hole and reduces to Hayward's metric in the absence of rotation. We then showed that its matter content could not be matched to a non-linear electrodynamics source, contrarily to the static Hayward black hole. We nonetheless kept studying the phenomenological aspects of this model, in particular by computing the images it would produce if it were at the center of the galaxy, surrounded by an accretion structure similar to the one of Sgr A*. We obtained with GYOTO some images in the regular rotating Hayward black hole regime (where an outer trapping horizon is present), which are extremely close to images of a Kerr black hole in the same configuration: the size of the two shadows differs by only a few percents. In this case, distinguishing a non-singular black hole from a Kerr one is for now out of reach of observations.

Some images in the horizonless regime of this model have also been computed. They emphasize the results already obtained with other horizonless ultra-compact objects, namely that the central faint region appearing in the images can be confused with the standard shadow structure of Kerr black holes observed at low resolution. They should thus encourage us to take the claims of observation of black hole shadows and horizons with caution, all the more so as we currently await the forthcoming results of the Event Horizon Telescope.

The same phenomenological approach was employed to study the formation and evaporation of a non-singular trapped region. In this dynamical case as in the previous rotating one, we imposed a form of the metric, defined on the whole spacetime without any junctions, and then looked at the corresponding energy-momentum tensor. As regards the dynamical non-singular trapped region, we managed to match the energy-momentum tensor with an outgoing Vaidya one on \mathcal{I}^+ and an ingoing Vaidya one on \mathcal{I}^- , but showed that with such limits the null energy condition was doomed to be violated on a non-compact region of spacetime.

The last results obtained in this thesis follow the other, complementary approach which consists in considering modifications of gravity to reproduce the known Hayward and Bardeen static non-singular black holes. Generalizing the tensor-scalar theory of mimetic gravity, we

wrote down the field equations for a static spherically symmetric metric encompassing Hayward's and Bardeen's ones. They are in principle solvable, but we did not manage to find solutions yet. Finally, we used the Hamiltonian formulation of General Relativity to implement quantum corrections to the constraint algebra, following the spirit of loop quantum gravity. We managed to solve Einstein's equations for a general class of deformations depending on a single function parametrized by one phase space variable. The deformation parametrizing Hayward and Bardeen black holes can then be defined implicitly by an integral, which we evaluated numerically.

Ultimately this thesis opens up some new perspectives, that further research shall try to address. First of all, the striking similarities shared by ray-traced images of horizonless ultra-compact objects, such as the naked rotating wormhole presented in this thesis, are to be examined further. Computing ray-traced images from other ultra-compact objects, such as Bardeen's metric in the horizonless regime, could confirm this behaviour. If so, it will then have to be properly understood. The study of the features of photon regions, and of their link with the lensing rings appearing on the ray-traced images, might be a key to this understanding.

As regards the formation and evaporation of a non-singular trapped region, it is now clear that a Vaidya collapse without junctions is not enough to describe a physically relevant model. One should then reproduce our analysis for more general collapses, trying to limit the violation of the null energy condition to a compact region of spacetime and describing again Hawking evaporation with an outgoing Vaidya metric on \mathcal{J}^+ .

The starting point of this thesis was to consider that, in lack of a quantum theory of gravity supposed to cure singularities, one was led to study non-singular black holes from an effective viewpoint. It should be stressed that this fruitful approach might be two-way: investigating the common features of quantum-inspired deformations of the constraint algebra that lead to non-singular black holes could for instance give us some hints about the properties of a quantum theory of gravity.



TYPOLOGY OF HORIZONS

1 Killing horizon

A Killing vector ξ is defined by the following Killing equation:

$$\nabla_a \xi_b + \nabla_b \xi_a = 0 \quad (\text{A.1})$$

This equation is actually tantamount to

$$\mathcal{L}_\xi g_{ab} = 0, \quad (\text{A.2})$$

where \mathcal{L} denotes the Lie differentiation. The Lie derivative of a vector \mathbf{A} along a vector \mathbf{u} is defined as

$$\mathcal{L}_u A^\alpha = \nabla_\beta A^\alpha u^\beta - \nabla_\beta u^\alpha A^\beta. \quad (\text{A.3})$$

The Lie differentiation satisfies a very nice property (see [96] for details): in a given coordinate system, the Lie derivative of a tensor along a vector $u^\alpha = \delta_0^\alpha$ vanishes if the components of this tensor do not depend on the coordinate x^0 . Hence, by eq. (A.2), Killing vectors characterize the symmetries of the metric tensor: if its components do not depend on a coordinate x^0 , the vector with components $\xi^\alpha = \delta_0^\alpha$ will be a Killing vector.

Killing vectors are of great use when searching for constants of motions along a geodesic. Taking a geodesic parametrized by λ with \mathbf{u} as a tangent vector, one can indeed show that $u^\alpha \xi_\alpha$ is constant along this geodesic:

$$\begin{aligned} \frac{d}{d\lambda} (u^\alpha \xi_\alpha) &= \nabla_\beta (u^\alpha \xi_\alpha) u^\beta \\ &= \nabla_\beta u^\alpha u^\beta \xi_\alpha + \nabla_\beta \xi_\alpha u^\alpha u^\beta \\ &= 0 \end{aligned} \quad (\text{A.4})$$

A Killing horizon associated with a Killing vector ξ can then simply be defined as a null hypersurface to which ξ is normal, and hence on which its norm vanishes.

2 Event horizon

The event horizon \mathcal{H} of a black hole is a null hypersurface separating, in a given spacetime, what will fall into the black hole from what will reach future and null infinity.

Technically, given a manifold \mathcal{M} with future null infinity \mathcal{I}^+ , it is defined as a boundary:

$$\mathcal{H} = \partial \mathcal{B} , \quad (\text{A.5})$$

where the black hole region \mathcal{B} represents the part of a \mathcal{M} causally disconnected from \mathcal{I}^+ :

$$\mathcal{B} = \mathcal{M} \setminus (J^-(\mathcal{I}^+) \cap \mathcal{M}) . \quad (\text{A.6})$$

The event horizon is teleological: it requires the knowledge of the whole spacetime to be drawn on a Penrose diagram. Hence, it is a global concept which is not relevant astrophysically.

3 Trapping and apparent horizons

The trapping horizons are particularly well suited to astrophysical contexts, since they provide, as stated in [69], an operational definition of a black hole allowing observers to detect it.

3.1 Definition

The notion of (future) trapped surface was the object of Def. 1.26 in Sec. 4.2.1 of Chap. 1: it is a 2-surface Σ on which the expansion of the congruence of both outgoing (+) and ingoing (−) null geodesics, orthogonal to Σ , is negative: $\theta_+ < 0$ and $\theta_- < 0$. Put another way, any particle belonging to such a surface will go towards decreasing values of the radial coordinate r in the future.

On the contrary, on a normal surface outgoing particles evolve towards increasing values of r and ingoing ones towards decreasing values of r . A *marginally trapped* surface is the limit case between normal and trapped surfaces: one of the expansions vanishes, here θ_+ . This marginal surface is called an *apparent horizon*. The *trapping horizons* are merely 3-surfaces foliated by the two-dimensional apparent horizons.

Let us define the trapped (resp. normal) region of spacetime as the set of points belonging to a trapped (resp. normal) surface. There are two types of trapping horizons associated with the future trapped surface defined above: one for which the normal region surrounds the trapped region, and the other for which it is the trapped region that surrounds the normal region. The former corresponds to the familiar black hole situation, with a central trapped region delimited by a *future outer trapping horizon* (FOTH). Following an ingoing null geodesic, one goes from a trapped region ($\theta_+ > 0$) to ($\theta_+ < 0$). Hence, the Lie derivative of θ_+ along the ingoing direction is: $\mathcal{L}_- \theta_+ < 0$.

The latter corresponds to a contracting cosmology, with a central observer whose normal region is delimited by a *future inner trapping horizon* (FITH). In this case, $\mathcal{L}_- \theta_+ > 0$.

Then, one can also define past trapped surfaces. These are 2-surfaces on which the expansion of the congruence of both outgoing and ingoing null geodesics is positive: $\theta_+ > 0$ and $\theta_- > 0$. The associated apparent horizons are such that $\theta_- = 0$. In this case, any particle belonging to such a surface will go towards increasing values of r in the future and decreasing values in the past. As before, let us consider two configurations of the trapped and normal regions.

When the trapped region is surrounded by the normal region, one is faced to a *past outer trapping horizon*. It is associated with a white hole spacetime, and one has $\mathcal{L}_+ \theta_- < 0$.

Finally, when the trapped region surrounds the normal region, this describes an expanding cosmology. The associated horizon is a *past inner trapping horizon*, on which $\mathcal{L}_+ \theta_- > 0$.

We can thus summarize the properties of the future/past outer/inner horizons as follows:

- FOTH: $\theta_+ = 0$ and $\mathcal{L}_- \theta_+ < 0$
- FITH: $\theta_+ = 0$ and $\mathcal{L}_- \theta_+ > 0$
- POTH: $\theta_- = 0$ and $\mathcal{L}_+ \theta_- < 0$
- PITH: $\theta_- = 0$ and $\mathcal{L}_+ \theta_- > 0$

More details can be found in [69, 72].

3.2 Dynamical spherically symmetric metric

As a first exemple, let us compute the ingoing and outgoing expansions for a spherically symmetric metric written in the ingoing Eddington-Finkelstein form

$$ds^2 = -F(v, r) e^{2\psi(v, r)} dv^2 + 2e^{\psi(v, r)} dv dr + r^2 d\Omega^2. \quad (\text{A.7})$$

The null outgoing (l) and ingoing vectors (k) read

$$\begin{cases} [l^\mu] = \left(1, \frac{F e^\psi}{2}, 0, 0\right) \\ [k^\mu] = (0, -e^{-\psi}, 0, 0) \end{cases}, \quad (\text{A.8})$$

with $k_\mu l^\mu = -1$. The outgoing and ingoing expansions finally read

$$\begin{cases} \theta_+ = h^{\mu\nu} \nabla_\mu l_\nu = \frac{F e^\psi}{r} \\ \theta_- = h^{\mu\nu} \nabla_\mu k_\nu = -\frac{2e^{-\psi}}{r} \end{cases}. \quad (\text{A.9})$$

This result will be extensively used in the following. Let us state another results, for the outgoing version of the metric (A.10)

$$ds^2 = -F(u, r) e^{2\psi(u, r)} du^2 - 2e^{\psi(u, r)} du dr + r^2 d\Omega^2. \quad (\text{A.10})$$

The expansions then read

$$\begin{cases} \theta_+ = \frac{2e^{-\psi}}{r} \\ \theta_- = -\frac{Fe^\psi}{r} . \end{cases} \quad (\text{A.11})$$

3.3 Stationary axisymmetric metric

As a second and last example, let us compute the ingoing and outgoing expansions for a generalized Kerr metric, where $M \equiv M(r)$. The original metric reads

$$ds^2 = -\left(1 - \frac{2rM(r)}{\Sigma}\right)dt^2 - \frac{4arM(r)\sin^2\theta}{\Sigma}dt d\varphi + \frac{\Sigma}{\Delta}dr^2 + \Sigma d\theta^2 + \sin^2\theta \left(r^2 + a^2 + \frac{2a^2rM(r)\sin^2\theta}{\Sigma}\right)d\varphi^2, \quad (\text{A.12})$$

And in its ingoing version:

$$\begin{aligned} ds^2 = & -\left(1 - \frac{2rM(r)}{\Sigma}\right)dv^2 + 2dv dr - \frac{4arM(r)\sin^2\theta}{\Sigma}dv d\psi - 2a\sin^2(\theta)dr d\psi + \Sigma d\theta^2 \\ & + \sin^2\theta \left(r^2 + a^2 + \frac{2a^2rM(r)\sin^2\theta}{\Sigma}\right)d\psi^2, \end{aligned} \quad (\text{A.13})$$

where

$$\begin{cases} v = t + \int \frac{r^2 + a^2}{\Delta} dr, \\ \psi = \varphi + \int \frac{a}{r} dr. \end{cases} \quad (\text{A.14})$$

The curves of $(v, \theta, \psi) = \text{cst.}$ represent null ingoing geodesics, with decreasing r as time increases. The null ingoing vector field (\mathbf{k}) tangent to these curves, as well as the null outgoing one orthogonal to them (\mathbf{l}) can be written

$$\begin{cases} \mathbf{k} = -\frac{a^2 + r^2}{\Sigma} \partial_r, \\ \mathbf{l} = \partial_v + \left(\frac{1}{2} - \frac{rM(r)}{a^2 + r^2}\right) \partial_r + \frac{a}{a^2 + r^2} \partial_\psi, \end{cases} \quad (\text{A.15})$$

where the normalization of \mathbf{k} has been chosen so that $\mathbf{k} \cdot \mathbf{l} = -1$.

We can then define as follows an induced metric \mathbf{h} on the hypersurfaces $r = \text{cst.}$, to which \mathbf{k} and \mathbf{l} are orthogonal:

$$\mathbf{h} = \mathbf{g} + \mathbf{l} \otimes \mathbf{k} + \mathbf{k} \otimes \mathbf{l}. \quad (\text{A.16})$$

The outgoing and ingoing expansions finally read

$$\begin{cases} \theta_+ = h^{\mu\nu} \nabla_\mu l_\nu = \frac{r\Delta}{(a^2 + r^2)\Sigma} \\ \theta_- = h^{\mu\nu} \nabla_\mu k_\nu = -\frac{2r(a^2 + r^2)}{\Sigma^2}. \end{cases} \quad (\text{A.17})$$

Similarly, one can consider the outgoing version of metric (A.12):

$$\begin{aligned} ds^2 = & -\left(1 - \frac{2rM(r)}{\Sigma}\right)du^2 - 2du dr - \frac{4arM(r)\sin^2\theta}{\Sigma}du d\psi' - 2a\sin^2(\theta)dr d\psi' + \Sigma d\theta^2 \\ & + \sin^2\theta \left(r^2 + a^2 + \frac{2a^2rM(r)\sin^2\theta}{\Sigma}\right)d\psi'^2, \end{aligned} \quad (\text{A.18})$$

where

$$\begin{cases} u = t - \int \frac{r^2 + a^2}{\Delta} dr, \\ \psi' = \varphi - \int \frac{a}{r} dr. \end{cases} \quad (\text{A.19})$$

Taking the following null ingoing and outgoing vectors:

$$\begin{cases} \mathbf{k} = 2(a^2 + r^2)\partial_u - \Delta\partial_r + 2a\partial'_\psi, \\ \mathbf{l} = \frac{1}{2\Sigma}\partial_r, \end{cases} \quad (\text{A.20})$$

the outgoing and ingoing expansions finally read

$$\begin{cases} \theta_+ = h^{\mu\nu}\nabla_\mu l_\nu = \frac{r}{\Sigma^2} \\ \theta_- = h^{\mu\nu}\nabla_\mu k_\nu = -\frac{2\Delta}{\Sigma}. \end{cases} \quad (\text{A.21})$$

4 Cauchy horizon

Let us illustrate the Cauchy horizon defined in Sec. 2.4 of Chap. 1 with the exemple of Reissner-Nordström's spacetime.

On Fig. A.1, we show a section of the maximal extension of this spacetime as well as a (partial) Cauchy surface Σ . Let us recall that the future domain of dependence of Σ is the set of all points $p \in \Sigma$ such that every past inextendible causal curve through p intersects Σ . This domain is shown in blue on Fig. A.1: it has a future boundary since, for instance, any point $p \in \mathcal{M}_{\text{III}}$ lies on some causal curves emerging from $r = 0$. This boundary is the future Cauchy horizon \mathcal{C} .

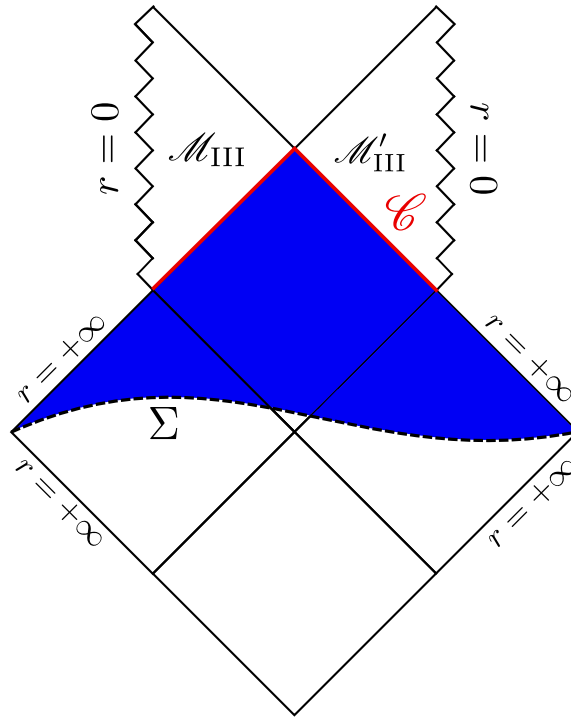


Figure A.1: Section of the maximal extension of Reissner-Nordström's spacetime, drawn in the compactified Kruskal coordinates of Chap. 2. The domain of dependence of the partial Cauchy surface Σ is shown in blue. It possesses a boundary, which is the future Cauchy horizon \mathcal{C} .

TENSORIAL COMPUTATIONS

1 General spherically symmetric metric

Any spherically symmetric metric can be cast in the form

$$\mathbf{g} = -F e^{(2\psi)} \mathbf{d}t \otimes \mathbf{d}t + \frac{1}{F} \mathbf{d}r \otimes \mathbf{d}r + r^2 \mathbf{d}\theta \otimes \mathbf{d}\theta + r^2 \sin(\theta)^2 \mathbf{d}\phi \otimes \mathbf{d}\phi, \quad (\text{B.1})$$

where $F \equiv F(t, r)$ and $\psi \equiv \psi(t, r)$. The Christoffel symbols computed out of this metric are

$$\begin{aligned} \Gamma^t_{tt} &= \frac{2F \frac{\partial \psi}{\partial t} + \frac{\partial F}{\partial t}}{2F} \\ \Gamma^t_{tr} &= \frac{2F \frac{\partial \psi}{\partial r} + \frac{\partial F}{\partial r}}{2F} \\ \Gamma^t_{rr} &= -\frac{e^{(-2\psi)} \frac{\partial F}{\partial t}}{2F^3} \\ \Gamma^r_{tt} &= F^2 e^{(2\psi)} \frac{\partial \psi}{\partial r} + \frac{1}{2} F e^{(2\psi)} \frac{\partial F}{\partial r} \\ \Gamma^r_{tr} &= -\frac{\frac{\partial F}{\partial t}}{2F} \\ \Gamma^r_{rr} &= -\frac{\frac{\partial F}{\partial r}}{2F} \\ \Gamma^r_{\theta\theta} &= -rF \\ \Gamma^r_{\phi\phi} &= -rF \sin(\theta)^2 \\ \Gamma^\theta_{r\theta} &= \frac{1}{r} \\ \Gamma^\theta_{\phi\phi} &= -\cos(\theta) \sin(\theta) \\ \Gamma^\phi_{r\phi} &= \frac{1}{r} \\ \Gamma^\phi_{\theta\phi} &= \frac{\cos(\theta)}{\sin(\theta)} \end{aligned} \quad (\text{B.2})$$

The Ricci tensor then reads

$$\begin{aligned} \mathbf{R} = & -\frac{1}{2rF^3} \left\{ 2rF^4 e^{(2\psi)} \left(\frac{\partial \psi}{\partial r} \right)^2 + 2rF^4 e^{(2\psi)} \frac{\partial^2 \psi}{\partial r^2} + rF^3 e^{(2\psi)} \frac{\partial^2 F}{\partial r^2} + 2F^3 e^{(2\psi)} \frac{\partial F}{\partial r} - rF \frac{\partial F}{\partial t} \frac{\partial \psi}{\partial t} - 2r \frac{\partial F^2}{\partial t} \right. \\ & + rF \frac{\partial^2 F}{\partial t^2} + \left(3rF^3 e^{(2\psi)} \frac{\partial F}{\partial r} + 4F^4 e^{(2\psi)} \right) \frac{\partial \psi}{\partial r} \left. \right\} e^{(-2\psi)} \frac{\partial}{\partial t} \otimes \mathbf{d}t + \frac{e^{(-2\psi)} \frac{\partial F}{\partial t}}{rF^2} \frac{\partial}{\partial t} \otimes \mathbf{d}r - \frac{\frac{\partial F}{\partial t}}{r} \frac{\partial}{\partial r} \otimes \mathbf{d}t \\ & - \frac{1}{2rF^3} \left\{ \left(2rF^4 e^{(2\psi)} \left(\frac{\partial \psi}{\partial r} \right)^2 + 3rF^3 e^{(2\psi)} \frac{\partial F}{\partial r} \frac{\partial \psi}{\partial r} + 2rF^4 e^{(2\psi)} \frac{\partial^2 \psi}{\partial r^2} + rF^3 e^{(2\psi)} \frac{\partial^2 F}{\partial r^2} + 2F^3 e^{(2\psi)} \frac{\partial F}{\partial r} \right. \right. \\ & \left. \left. - rF \frac{\partial F}{\partial t} \frac{\partial \psi}{\partial t} - 2r \frac{\partial F^2}{\partial t} + rF \frac{\partial^2 F}{\partial t^2} \right) \right\} e^{(-2\psi)} \frac{\partial}{\partial r} \otimes \mathbf{d}r - \frac{rF \frac{\partial \psi}{\partial r} + r \frac{\partial F}{\partial r} + F - 1}{r^2} \left(\frac{\partial}{\partial \theta} \otimes \mathbf{d}\theta + \frac{\partial}{\partial \phi} \otimes \mathbf{d}\phi \right), \end{aligned}$$

and the Ricci scalar is

$$\begin{aligned} R = & -\frac{1}{r^2 F^3} \left\{ \left(2r^2 F^4 e^{(2\psi)} \frac{\partial}{\partial r} \psi^2 + 2r^2 F^4 e^{(2\psi)} \frac{\partial^2}{(\partial r)^2} \psi + r^2 F^3 e^{(2\psi)} \frac{\partial^2}{(\partial r)^2} F + 4rF^3 e^{(2\psi)} \frac{\partial}{\partial r} F + 2F^4 e^{(2\psi)} \right. \right. \\ & \left. \left. - r^2 F \frac{\partial}{\partial t} F \frac{\partial}{\partial t} \psi - 2F^3 e^{(2\psi)} - 2r^2 \frac{\partial}{\partial t} F^2 + r^2 F \frac{\partial^2}{(\partial t)^2} F + \left(3r^2 F^3 e^{(2\psi)} \frac{\partial}{\partial r} F + 4rF^4 e^{(2\psi)} \right) \frac{\partial}{\partial r} \psi \right) e^{(-2\psi)} \right\}. \end{aligned}$$

Finally, the Einstein tensor reads

$$\begin{aligned} \mathbf{G} = & \left(\frac{r \frac{\partial F}{\partial r} + F - 1}{r^2} \right) \frac{\partial}{\partial t} \otimes \mathbf{d}t + \frac{e^{(-2\psi)} \frac{\partial F}{\partial t}}{rF^2} \frac{\partial}{\partial t} \otimes \mathbf{d}r - \frac{\frac{\partial F}{\partial t}}{r} \frac{\partial}{\partial r} \otimes \mathbf{d}t + \left(\frac{2rF \frac{\partial \psi}{\partial r} + r \frac{\partial F}{\partial r} + F - 1}{r^2} \right) \frac{\partial}{\partial r} \otimes \mathbf{d}r \\ & + \frac{1}{2rF^3} \left\{ \left(2rF^4 e^{(2\psi)} \left(\frac{\partial \psi}{\partial r} \right)^2 + 2rF^4 e^{(2\psi)} \frac{\partial^2 \psi}{\partial r^2} + rF^3 e^{(2\psi)} \frac{\partial^2 F}{\partial r^2} - 2r \frac{\partial F^2}{\partial t} + 2F^3 e^{(2\psi)} \frac{\partial F}{\partial r} \right. \right. \\ & \left. \left. - rF \frac{\partial F}{\partial t} \frac{\partial \psi}{\partial t} + \left(3rF^3 e^{(2\psi)} \frac{\partial F}{\partial r} + 2F^4 e^{(2\psi)} \right) \frac{\partial \psi}{\partial r} \right) e^{(-2\psi)} + rF \frac{\partial^2 F}{\partial t^2} \right\} \left(\frac{\partial}{\partial \theta} \otimes \mathbf{d}\theta + \frac{\partial}{\partial \phi} \otimes \mathbf{d}\phi \right) \end{aligned}$$

2 Regular rotating black hole

Let us consider the following axisymmetric and stationary metric:

$$\begin{aligned} \mathbf{g} = & \left(\frac{2rM(r)}{\Sigma} - 1 \right) \mathbf{d}t \otimes \mathbf{d}t - \frac{2arM(r)\sin(\theta)^2}{\Sigma} \mathbf{d}t \otimes \mathbf{d}\phi + \frac{\Sigma}{\Delta} \mathbf{d}r \otimes \mathbf{d}r + \Sigma \mathbf{d}\theta \otimes \mathbf{d}\theta \\ & - \frac{2arM(r)\sin(\theta)^2}{\Sigma} \mathbf{d}\phi \otimes \mathbf{d}t + \left(\frac{2a^2rM(r)\sin(\theta)^2}{\Sigma} + a^2 + r^2 \right) \sin(\theta)^2 \mathbf{d}\phi \otimes \mathbf{d}\phi, \end{aligned} \quad (\text{B.3})$$

where

$$\Sigma \equiv r^2 + a^2 \cos^2 \theta, \quad \Delta \equiv r^2 - 2M(r)r + a^2. \quad (\text{B.4})$$

Eq. (B.3) reduces to the metric of our regular rotating Hayward model for

$$M(r) \equiv m \frac{|r|^3}{|r|^3 + 2mb^2}, \quad (\text{B.5})$$

and to the metric a regular rotating Bardeen model (still under investigation) for

$$M(r) \equiv m \frac{r^2}{(r^2 + g^2)^{\frac{3}{2}}}. \quad (\text{B.6})$$

Denoting the derivatives with respect to r (resp. θ) as primes (resp. dots), the Christoffel symbols used to write the Hayward.C extension of GYOTO read

$$\begin{aligned}
 \Gamma^t_{tr} &= \frac{(a^2 + r^2)\Sigma M(r) - (a^2 r + r^3)M(r)\Sigma' + (a^2 r + r^3)\Sigma M'(r)}{2a^2 r \Sigma \cos(\theta)^2 M(r) + 2r^3 \Sigma M(r) - (a^2 + r^2)\Sigma^2} \\
 \Gamma^t_{t\theta} &= -\frac{4a^2 r^2 \cos(\theta) M(r)^2 \sin(\theta) + (a^2 r + r^3)M(r)\dot{\Sigma}}{2a^2 r \Sigma \cos(\theta)^2 M(r) + 2r^3 \Sigma M(r) - (a^2 + r^2)\Sigma^2} \\
 \Gamma^t_{r\phi} &= -\frac{((a^3 - ar^2)\Sigma M(r) - (a^3 r + ar^3)M(r)\Sigma' + (a^3 r + ar^3)\Sigma M'(r)) \sin(\theta)^2}{2a^2 r \Sigma \cos(\theta)^2 M(r) + 2r^3 \Sigma M(r) - (a^2 + r^2)\Sigma^2} \\
 \Gamma^t_{\theta\phi} &= \frac{4a^3 r^2 \cos(\theta) M(r)^2 \sin(\theta)^3 + (a^3 r + ar^3)M(r) \sin(\theta)^2 \dot{\Sigma}}{2a^2 r \Sigma \cos(\theta)^2 M(r) + 2r^3 \Sigma M(r) - (a^2 + r^2)\Sigma^2} \\
 \Gamma^r_{tt} &= \frac{r\Delta M(r)\Sigma' - r\Delta \Sigma M'(r) - \Delta \Sigma M(r)}{\Sigma^3} \\
 \Gamma^r_{t\phi} &= -\frac{(ar\Delta M(r)\Sigma' - ar\Delta \Sigma M'(r) - a\Delta \Sigma M(r)) \sin(\theta)^2}{\Sigma^3} \\
 \Gamma^r_{rr} &= -\frac{\Sigma\Delta' - \Delta\Sigma'}{2\Delta\Sigma} \\
 \Gamma^r_{r\theta} &= \frac{\dot{\Sigma}}{2\Sigma} \\
 \Gamma^r_{\theta\theta} &= -\frac{\Delta\Sigma'}{2\Sigma} \\
 \Gamma^r_{\phi\phi} &= -\frac{r\Delta\Sigma^2 \sin(\theta)^2 - (a^2 r \Delta M(r)\Sigma' - a^2 r \Delta \Sigma M'(r) - a^2 \Delta \Sigma M(r)) \sin(\theta)^4}{\Sigma^3} \\
 \Gamma^\theta_{tt} &= \frac{rM(r)\dot{\Sigma}}{\Sigma^3} \\
 \Gamma^\theta_{t\phi} &= \frac{2ar\Sigma \cos(\theta) M(r) \sin(\theta) - arM(r) \sin(\theta)^2 \dot{\Sigma}}{\Sigma^3} \\
 \Gamma^\theta_{rr} &= -\frac{\dot{\Sigma}}{2\Delta\Sigma} \\
 \Gamma^\theta_{r\theta} &= \frac{\Sigma'}{2\Sigma} \\
 \Gamma^\theta_{\theta\theta} &= \frac{\dot{\Sigma}}{2\Sigma} \\
 \Gamma^\theta_{\phi\phi} &= -\frac{4a^2 r \Sigma \cos(\theta) M(r) \sin(\theta)^3 - a^2 r M(r) \sin(\theta)^4 \dot{\Sigma} + (a^2 + r^2)\Sigma^2 \cos(\theta) \sin(\theta)}{\Sigma^3} \\
 \Gamma^\phi_{tr} &= -\frac{arM(r)\Sigma' - ar\Sigma M'(r) - a\Sigma M(r)}{2a^2 r \Sigma \cos(\theta)^2 M(r) + 2r^3 \Sigma M(r) - (a^2 + r^2)\Sigma^2} \\
 \Gamma^\phi_{t\theta} &= -\frac{arM(r) \sin(\theta) \dot{\Sigma} + 2(2ar^2 M(r)^2 - ar\Sigma M(r)) \cos(\theta)}{(2a^2 r \Sigma \cos(\theta)^2 M(r) + 2r^3 \Sigma M(r) - (a^2 + r^2)\Sigma^2) \sin(\theta)} \\
 \Gamma^\phi_{r\phi} &= \frac{2r^2 \Sigma M(r) - r\Sigma^2 + (a^2 r M(r)\Sigma' - a^2 r \Sigma M'(r) - a^2 \Sigma M(r)) \sin(\theta)^2}{2a^2 r \Sigma \cos(\theta)^2 M(r) + 2r^3 \Sigma M(r) - (a^2 + r^2)\Sigma^2} \\
 \Gamma^\phi_{\theta\phi} &= \frac{1}{(2a^2 r \cos(\theta)^2 M(r) + 2r^3 M(r) - a^2 \Sigma - r^2 \Sigma) \Sigma \sin(\theta)} [4a^2 r^2 \cos(\theta) M(r)^2 \sin(\theta)^2 - a^2 \Sigma^2 \cos(\theta) \\
 &\quad - 4a^2 r \Sigma \cos(\theta) M(r) \sin(\theta)^2 + a^2 r M(r) \sin(\theta)^3 \dot{\Sigma} + 2a^2 r \Sigma \cos(\theta) M(r) + 2r^3 \Sigma \cos(\theta) M(r) - r^2 \Sigma^2 \cos(\theta)] ,
 \end{aligned}$$

SAGEMATH WORKSHEETS

1 Rotating non-singular black holes

Computation of geometric quantities relative to the metric (4.34)-(4.35) have been performed by means of the free computer algebra system SageMath [2], thanks to its tensor calculus part (SageManifolds [1]). The corresponding worksheets are available at the following url's.

1.1 Curvature

- Curvature of the naively extended rotating Hayward metric [Eq. (4.32)]:
https://cocalc.com/projects/09367c7f-3a39-4079-9d4d-cd59ebdca289/files/Rotating_Hayward_metric_curvature.ipynb
- Curvature of the regular rotating Hayward metric (4.34) extended to the region $r < 0$ [Fig. 4.2(a) & 4.2(b)]:
https://cocalc.com/projects/09367c7f-3a39-4079-9d4d-cd59ebdca289/files/rotating_Hayward_metric_ext.ipynb

1.2 Null energy condition

- Null energy condition in the regular rotating Hayward metric (4.34) extended to the region $r < 0$ [Fig. 4.6]:
https://cocalc.com/share/09367c7f-3a39-4079-9d4d-cd59ebdca289/Locally_nonrotating_frames_and_NEC.ipynb?viewer=share

1.3 Geodesics

- Expressions of the energy, angular momentum and angular velocity of a test particle in the regular rotating Hayward metric (4.34) extended to the region $r < 0$; comparison with Toshmatov et al. [113] and Bardeen et al. [14]:
https://cocalc.com/share/09367c7f-3a39-4079-9d4d-cd59ebdca289/Comparison_of_E_L_and_Omega.ipynb?viewer=share

- Stable circular orbits in the regular rotating Hayward metric (4.34) extended to the region $r < 0$ [Table 4.1]:

https://cocalc.com/projects/09367c7f-3a39-4079-9d4d-cd59ebdca289/files/Stable_circular_orbits.ipynb

1.4 Energy-momentum tensor from nonlinear electrodynamics

- Inconsistencies in the solution to Maxwell's and Einstein's equations proposed by Toshmatov et al. [113]

https://cocalc.com/projects/09367c7f-3a39-4079-9d4d-cd59ebdca289/files/Inconsistencies_EMT_Toshmatov_et_al.ipynb

- Exact solution of nonlinear Maxwell's equations as well as Einstein's equations with the electromagnetic field proposed by Toshmatov et al. [113]

https://cocalc.com/projects/09367c7f-3a39-4079-9d4d-cd59ebdca289/files/EMT_Toshmatov_et_al_Kerr_Newman.ipynb

BIBLIOGRAPHY

- [1] *SageManifolds*: sagemanifolds.obspm.fr.
- [2] *SageMath*: sagemath.org.
- [3] B. E. A. ABBOTT, *Observation of gravitational waves from a binary black hole merger*, Phys. Rev. Lett., 116 (2016), p. 061102.
- [4] R. ARNOWITT, S. DESER, AND C. W. MISNER, *Dynamical structure and definition of energy in general relativity*, Phys. Rev., 116 (1959), pp. 1322–1330.
- [5] E. AYON-BEATO AND A. GARCIA, *The Bardeen model as a nonlinear magnetic monopole*, Physics Letters B, 493 (2000), pp. 149 – 152.
- [6] J. BAEZ AND J. P. MUNIAIN, *Gauge fields, knots and gravity*, 1995.
- [7] B. BALICK AND R. L. BROWN, *Intense sub-arcsecond structure in the galactic center*, The Astrophysical Journal, 194 (1974), pp. 265–270.
- [8] C. BAMBI, *Testing black hole candidates with electromagnetic radiation*, Rev. Mod. Phys., 89 (2017), p. 025001.
- [9] C. BAMBI AND L. MODESTO, *Rotating regular black holes*, Physics Letters B, 721 (2013), pp. 329 – 334.
- [10] C. BARCELO AND M. VISSER, *Twilight for the energy conditions?*, International Journal of Modern Physics D, 11 (2002), pp. 1553–1560.
- [11] J. BARDEEN, in Abstracts of the 5th International Conference on Gravitation and the Theory of Relativity (Tbilisi, USSR), T. U. P. V.A. Fock *et al.*, ed., Sept. 1968, p. 174.
- [12] J. M. BARDEEN, *Timelike and null geodesics in the Kerr metric*, in Proceedings, Ecole d’Eté de Physique Théorique: Les Astres Occlus: Les Houches, France, August, 1972, 1973, pp. 215–240.
- [13] J. M. BARDEEN, *Black hole evaporation without an event horizon*, (2014).
- [14] J. M. BARDEEN, W. H. PRESS, AND S. A. TEUKOLSKY, *Rotating Black Holes: Locally Nonrotating Frames, Energy Extraction, and Scalar Synchrotron Radiation*, The Astrophysical Journal, 178 (1972), pp. 347–370.
- [15] C. BARRABES, W. ISRAEL, AND E. POISSON, *Collision of light-like shells and mass inflation in rotating black holes*, Classical and Quantum Gravity, 7 (1990), pp. L273–L278.

- [16] M. BARTUSIAK, *Black Hole: How an Idea Abandoned by Newtonians, Hated by Einstein, and Gambled on by Hawking Became Loved*, Yale University Press, New Haven London, Apr. 2015.
- [17] J. BEN ACHOUR, F. LAMY, H. LIU, AND K. NOUI, *Non-singular black holes and the limiting curvature mechanism: a hamiltonian perspective*, Journal of Cosmology and Astroparticle Physics, 2018 (2018), p. 072.
- [18] ———, *Polymer Schwarzschild black hole: An effective metric*, arXiv:gr-qc/1803.01152, (2018).
- [19] P. BINÉTRUY, A. HELOU, AND F. LAMY, *Closed trapping horizons without singularity*, arXiv:1804.03912 [gr-qc, physics:hep-th], (2018).
- [20] N. BODENDORFER, A. SCHFER, AND J. SCHLIEMANN, *On the canonical structure of general relativity with a limiting curvature and its relation to loop quantum gravity*, (2017).
- [21] M. BOJOWALD, S. BRAHMA, AND J. D. REYES, *Covariance in models of loop quantum gravity: Spherical symmetry*, Phys. Rev., D92 (2015), p. 045043.
- [22] M. BOJOWALD AND R. SWIDERSKI, *Spherically symmetric quantum geometry: Hamiltonian constraint*, Classical and Quantum Gravity, 23 (2006), p. 2129.
- [23] I. BOOTH, L. BRITS, J. A. GONZALEZ, AND C. V. D. BROECK, *Marginally trapped tubes and dynamical horizons*, Classical and Quantum Gravity, 23 (2006), p. 413.
- [24] R. BOUSSO, *A covariant entropy conjecture*, Journal of High Energy Physics, 1999 (1999), p. 004.
- [25] S. BRAHMA, *Spherically symmetric canonical quantum gravity*, Phys. Rev. D, 91 (2015), p. 124003.
- [26] O. BRAUER, H. A. CAMARGO, AND M. SOCOLOVSKY, *Newman-Janis algorithm revisited*, International Journal of Theoretical Physics, 54 (2015), pp. 302–314.
- [27] A. E. BRODERICK, V. L. FISH, M. D. JOHNSON, K. ROSENFELD, C. WANG, S. S. DOELEMAN, K. AKIYAMA, T. JOHANNSEN, AND A. L. ROY, *Modeling Seven Years of Event Horizon Telescope Observations with Radiatively Inefficient Accretion Flow Models*, The Astrophysical Journal, 820 (2016), p. 137.
- [28] A. E. BRODERICK, A. LOEB, AND R. NARAYAN, *The Event Horizon of Sagittarius A**, The Astrophysical Journal, 701 (2009), pp. 1357–1366.
- [29] R. CARBALLO-RUBIO, F. DI FILIPPO, S. LIBERATI, C. PACILIO, AND M. VISSER, *On the viability of regular black holes*, Journal of High Energy Physics, 2018 (2018), p. 23.

-
- [30] C. CARRIER, *Texte des sarcophages du Moyen Empire égyptien*, Champollion, Éditions du Rocher, Monaco, 2004.
 - [31] S. M. CARROLL, *Spacetime and geometry: An introduction to General Relativity*, 2004.
 - [32] B. CARTER, *Global Structure of the Kerr Family of Gravitational Fields*, Physical Review, 174 (1968), pp. 1559–1571.
 - [33] M. CHAICHIAN, J. KLUSON, M. OKSANEN, AND A. TUREANU, *Mimetic dark matter, ghost instability and a mimetic tensor-vector-scalar gravity*, JHEP, 12 (2014), p. 102.
 - [34] A. H. CHAMSEDDINE AND V. MUKHANOV, *Mimetic dark matter*, Journal of High Energy Physics, 2013 (2013), p. 135.
 - [35] ———, *Nonsingular black hole*, The European Physical Journal C, 77 (2017), p. 183.
 - [36] ———, *Resolving Cosmological Singularities*, JCAP, 1703 (2017), p. 009.
 - [37] Y. CHOQUET-BRUHAT, *General Relativity and the Einstein Equations*, Oxford Mathematical Monographs, Oxford University Press, Oxford, New York, Dec. 2008.
 - [38] P. V. P. CUNHA AND C. A. R. HERDEIRO, *Shadows and strong gravitational lensing: a brief review*, General Relativity and Gravitation, 50 (2018), p. 42.
 - [39] P. V. P. CUNHA, C. A. R. HERDEIRO, AND E. RADU, *Fundamental photon orbits: black hole shadows and spacetime instabilities*, Phys. Rev., D96 (2017), p. 024039.
 - [40] A. DE BUCK, *The Egyptian Coffin Texts 1: Texts of Spells 1-75*, Oriental Institute Publications 34, University of Chicago Press, Chicago, IL, United States, 1935.
 - [41] ———, *The Egyptian Coffin Texts 2: Texts of Spells 76-163*, Oriental Institute Publications 49, University of Chicago Press, Chicago, IL, United States, 1938.
 - [42] ———, *The Egyptian Coffin Texts 4: Texts of Spells 268-354*, Oriental Institute Publications 67, University of Chicago Press, Chicago, IL, United States, 1951.
 - [43] ———, *The Egyptian Coffin Texts 7: Texts of Spells 787-1185*, Oriental Institute Publications 87, University of Chicago Press, Chicago, IL, United States, 1961.
 - [44] T. DE LORENZO, C. PACILIO, C. ROVELLI, AND S. SPEZIALE, *On the effective metric of a Planck star*, General Relativity and Gravitation, 47 (2015), p. 41.
 - [45] S. DOELEMEN, *Seeing the unseeable*, Nat. Astron., 1 (2017), p. 646.
 - [46] S. S. E. A. DOELEMEN, *Event-horizon-scale structure in the supermassive black hole candidate at the Galactic Centre*, Nature, 455 (2008), pp. 78–80.

- [47] S. P. DRAKE AND P. SZEKERES, *Uniqueness of the Newman–Janis algorithm in generating the Kerr–Newman metric*, General Relativity and Gravitation, 32 (2000), pp. 445–457.
- [48] I. DYMNIKOVA, *Vacuum nonsingular black hole*, General Relativity and Gravitation, 24 (1992), pp. 235–242.
- [49] A. EINSTEIN, *Die Feldgleichungen der Gravitation (The Field Equations of Gravitation)*, Sitzungsberichte der Königlich Preußischen Akademie der Wissenschaften (Berlin), Seite 844-847., (1915).
- [50] H. FALCKE AND S. MARKOFF, *The jet model for Sgr A*: Radio and X-ray spectrum*, Astronomy & Astrophysics, 362 (2000), pp. 113–118.
- [51] Z.-Y. FAN AND X. WANG, *Construction of regular black holes in general relativity*, Physical Review D, 94 (2016), p. 124027.
- [52] L. H. FORD, *The classical singularity theorems and their quantum loopholes*, International Journal of Theoretical Physics, 42 (2003), pp. 1219–1227.
- [53] V. P. FROLOV, *Do Black Holes Exist?*, in Proceedings, 18th International Seminar on High Energy Physics (Quarks 2014): Suzdal, Russia, June 2-8, 2014, 2014.
- [54] ———, *Information loss problem and a 'black hole' model with a closed apparent horizon*, JHEP, 05 (2014), p. 049.
- [55] V. P. FROLOV AND G. A. VILKOVISKY, *Quantum gravity removes classical singularities and shortens the life of black holes*, in The Second Marcel Grossmann Meeting on the Recent Developments of General Relativity (In Honor of Albert Einstein) Trieste, Italy, July 5-11, 1979, 1979, p. 0455.
- [56] V. P. FROLOV AND A. ZELNIKOV, *Introduction to Black Hole Physics*, Oxford University Press, Oxford, UK, 2015.
- [57] G. GALLOWAY, *Topology and general relativity*, Erwin Schrödinger International Institute for Mathematics and Physics, Vienna, Austria., 2017, Summer school: between Geometry and Relativity.
- [58] R. GAMBINI AND J. PULLIN, *A first course in loop quantum gravity*, 2011.
- [59] R. GENZEL, F. EISENHAUER, AND S. GILLESSEN, *The galactic center massive black hole and nuclear star cluster*, Rev. Mod. Phys., 82 (2010), pp. 3121–3195.
- [60] R. GEROCH, *What is a singularity in general relativity?*, Annals of Physics, 48 (1968), pp. 526 – 540.

-
- [61] S. GILLESSEN, F. EISENHAUER, S. TRIPPE, T. ALEXANDER, R. GENZEL, F. MARTINS, AND T. OTT, *Monitoring stellar orbits around the Massive Black Hole in the Galactic Center*, *Astrophys. J.*, 692 (2009), pp. 1075–1109.
 - [62] E. GOURGOULHON, *3+1 formalism and bases of numerical relativity*, (2007).
 - [63] E. GOURGOULHON, *Geometry and physics of black holes*, Institut d’Astrophysique de Paris, France., 2016.
 - [64] P. GRANDET AND B. MATHIEU, *Cours d’Égyptien hiéroglyphique*, Éditions Khéops, Paris, France, 2003.
 - [65] A. GRENZEBACH, *The Shadow of Black Holes: An Analytic Description*, SpringerBriefs in Physics, Springer International Publishing, 2016.
 - [66] S. W. HAWKING, *Particle creation by black holes*, *Communications in Mathematical Physics*, 43 (1975), pp. 199–220.
 - [67] S. W. HAWKING AND G. F. R. ELLIS, *The Large Scale Structure of Space-Time*, Cambridge Monographs on Mathematical Physics, Cambridge University Press, 1973.
 - [68] S. W. HAWKING AND R. PENROSE, *The singularities of gravitational collapse and cosmology*, *Proceedings of the Royal Society of London A: Mathematical, Physical and Engineering Sciences*, 314 (1970), pp. 529–548.
 - [69] S. A. HAYWARD, *General laws of black-hole dynamics*, *Phys. Rev. D*, 49 (1994), pp. 6467–6474.
 - [70] ———, *The disinformation problem for black holes (conference version)*, arXiv:gr-qc/0504037, (2005).
 - [71] ———, *Formation and Evaporation of Nonsingular Black Holes*, *Physical Review Letters*, 96 (2006), p. 031103.
 - [72] A. HELOU, *Beyond the trapping horizon: the apparent universe and the regular black hole*, PhD thesis, Université Paris Diderot., 2015.
 - [73] A. HELOU, I. MUSCO, AND J. C. MILLER, *Causal Nature and Dynamics of Trapping Horizons in Black Hole Collapse*, *Class. Quant. Grav.*, 34 (2017), p. 135012.
 - [74] K. HIOKI AND K. MAEDA, *Measurement of the Kerr spin parameter by observation of a compact object’s shadow*, *Physical Review D*, 80 (2009), p. 024042.
 - [75] W. A. HISCOCK, *Models of evaporating black holes. I.*, *Phys. Rev. D*, 23 (1981), pp. 2813–2822.

- [76] M. P. HOBSON, G. P. EFSTATHIOU, AND A. N. LASENBY, *General relativity: An introduction for physicists*, 2006.
- [77] T. JOHANNSEN, D. PSALTIS, S. GILLESSEN, D. P. MARRONE, F. OZEL, S. S. DOELEMAN, AND V. L. FISH, *Masses of Nearby Supermassive Black Holes with Very-Long Baseline Interferometry*, *Astrophys. J.*, 758 (2012), p. 30.
- [78] R. P. KERR, *Gravitational field of a spinning mass as an example of algebraically special metrics*, *Phys. Rev. Lett.*, 11 (1963), pp. 237–238.
- [79] S. S. KOMISSAROV, *Magnetized tori around kerr black holes: analytic solutions with a toroidal magnetic field*, *Monthly Notices of the Royal Astronomical Society*, 368 (2006), pp. 993–1000.
- [80] F. LAMY, E. GOURGOULHON, T. PAUMARD, AND F. H. VINCENT, *Imaging a non-singular rotating black hole at the center of the galaxy*, *Classical and Quantum Gravity*, 35 (2018), p. 115009.
- [81] D. LANGLOIS, M. MANCARELLA, K. NOUI, AND F. VERNIZZI, *Mimetic gravity as DHOST theories*, (2018).
- [82] T. LEE, *An introduction to loop quantum gravity and its application to black holes*, Master’s thesis, Imperial College London, 2014.
- [83] H. LIU, K. NOUI, E. WILSON-EWING, AND D. LANGLOIS, *Effective loop quantum cosmology as a higher-derivative scalar-tensor theory*, (2017).
- [84] G. W. M., B. R. L., AND L. K. Y., *The discovery of sgr A**, *Astronomische Nachrichten*, 324, pp. 497–504.
- [85] R. MAIOLINO, *Prospects for AGN studies with ALMA*, *New Astron. Rev.*, 52 (2008), p. 339.
- [86] P. O. MAZUR AND E. MOTTOLA, *Gravitational condensate stars: An alternative to black holes*, (2001).
- [87] C. W. MISNER, *Taub-NUT space as a counterexample to almost anything*, *Tech. Rep.* 529, Nov. 1965.
- [88] R. NARAYAN, I. YI, AND R. MAHADEVAN, *Explaining the spectrum of Sagittarius A* with a model of an accreting black hole*, *Nature*, 374 (1995), pp. 623–625.
- [89] E. T. NEWMAN, R. COUCH, K. CHINNAPAREDDI, A. EXTON, A. PRAKASH, AND R. TORRENCE, *Metric of a Rotating, Charged Mass*, *J. Math. Phys.*, 6 (1965), pp. 918–919.
- [90] E. T. NEWMAN AND A. I. JANIS, *Note on the Kerr spinning particle metric*, *J. Math. Phys.*, 6 (1965), pp. 915–917.

-
- [91] P. NICOLINI, *Noncommutative nonsingular black holes*, Bled Workshops Phys., 6 (2005), pp. 79–87.
 - [92] B. O’NEILL, *Semi-Riemannian Geometry With Applications to Relativity, Volume 103*, Academic Press, San Diego, 1 edition ed., July 1983.
 - [93] B. O’NEILL, *The geometry of Kerr black holes*, A.K. Peters, Wellesley (MA), 1995. Reprinted by Dover, Mineola (NY), 2014.
 - [94] R. PENROSE, *Gravitational collapse and space-time singularities*, Phys. Rev. Lett., 14 (1965), pp. 57–59.
 - [95] M. PETRI, *The Holostar: A Selfconsistent model for a compact selfgravitating object*, (2003).
 - [96] E. POISSON, *A Relativist’s Toolkit: The Mathematics of Black-Hole Mechanics*, May 2004.
 - [97] E. POISSON AND W. ISRAEL, *Inner-horizon instability and mass inflation in black holes*, Phys. Rev. Lett., 63 (1989), pp. 1663–1666.
 - [98] E. POISSON AND W. ISRAEL, *Internal structure of black holes*, Phys. Rev. D, 41 (1990), pp. 1796–1809.
 - [99] D. PSALTIS AND T. JOHANNSEN, *Sgr A*: The Optimal Testbed of Strong-Field Gravity*, J. Phys. Conf. Ser., 283 (2011), p. 012030.
 - [100] R. A. REMILLARD AND J. E. MCCLINTOCK, *X-Ray Properties of Black-Hole Binaries*, Annual Review of Astronomy and Astrophysics, 44 (2006), pp. 49–92.
 - [101] J. REYES, *Spherically Symmetric Loop Quantum Gravity: Connections to Two-Dimensional Models and Applications to Gravitational Collapse*, PhD thesis, Penn State U., 2009.
 - [102] M. E. RODRIGUES AND E. L. B. JUNIOR, *Comment on “Generic rotating regular black holes in general relativity coupled to nonlinear electrodynamics”*, Physical Review D, 96 (2017), p. 128502.
 - [103] T. A. ROMAN AND P. G. BERGMANN, *Stellar collapse without singularities?*, Phys. Rev., D28 (1983), pp. 1265–1277.
 - [104] K. SCHWARZSCHILD, *Über das Gravitationsfeld eines Massenpunktes nach der Einsteinschen Theorie*, Phys.-Math. Klasse 1916, 189 (1916).
 - [105] J. M. M. SENOVILLA AND D. GARFINKLE, *The 1965 Penrose singularity theorem*, Class. Quant. Grav., 32 (2015), p. 124008.
 - [106] K. TAKAHASHI AND T. KOBAYASHI, *Extended mimetic gravity: Hamiltonian analysis and gradient instabilities*, (2017).

- [107] E. TEO, *Spherical photon orbits around a Kerr black hole*, General Relativity and Gravitation, 35 (2003), pp. 1909–1926.
- [108] T. THIEMANN, *Modern Canonical Quantum General Relativity*, Cambridge University Press, Oct. 2007.
- [109] R. TIBREWALA, *Spherically symmetric Einstein-Maxwell theory and loop quantum gravity corrections*, Class. Quant. Grav., 29 (2012), p. 235012.
- [110] ———, *Inhomogeneities, loop quantum gravity corrections, constraint algebra and general covariance*, Class. Quant. Grav., 31 (2014), p. 055010.
- [111] R. TORRES, *Non-singular quantum improved rotating black holes and their maximal extension*, General Relativity and Gravitation, 49 (2017), p. 74.
- [112] R. TORRES AND F. FAYOS, *On regular rotating black holes*, General Relativity and Gravitation, 49 (2016), p. 2.
- [113] B. TOSHMATOV, Z. STUHLÍK, AND B. AHMEDOV, *Generic rotating regular black holes in general relativity coupled to nonlinear electrodynamics*, Physical Review D, 95 (2017), p. 084037.
- [114] ———, *Note on the character of the generic rotating charged regular black holes in general relativity coupled to nonlinear electrodynamics*, arXiv:1712.04763 [gr-qc], (2017).
- [115] N. TSUKAMOTO, *Black hole shadow in an asymptotically flat, stationary, and axisymmetric spacetime: The Kerr-Newman and rotating regular black holes*, Phys. Rev. D, 97 (2018), p. 064021.
- [116] P. VAIDYA, *The Gravitational Field of a Radiating Star*, Proc. Natl. Inst. Sci. India, A33 (1951), p. 264.
- [117] F. VINCENT, *Simulations d’observations du centre galactique par l’instrument GRAVITY*, theses, Observatoire de Paris, July 2011.
- [118] F. H. VINCENT, E. GOURGOULHON, C. HERDEIRO, AND E. RADU, *Astrophysical imaging of Kerr black holes with scalar hair*, Physical Review D, 94 (2016), p. 084045.
- [119] F. H. VINCENT, Z. MELIANI, P. GRANDCLÉMENT, E. GOURGOULHON, AND O. STRAUB, *Imaging a boson star at the Galactic center*, Classical and Quantum Gravity, 33 (2016), p. 105015.
- [120] F. H. VINCENT, T. PAUMARD, E. GOURGOULHON, AND G. PERRIN, *GYOTO: a new general relativistic ray-tracing code*, Classical and Quantum Gravity, 28 (2011), p. 225011.

- [121] F. H. VINCENT, W. YAN, O. STRAUB, A. A. ZDZIARSKI, AND M. A. ABRAMOWICZ, *A magnetized torus for modeling Sagittarius A* millimeter images and spectra*, *Astronomy & Astrophysics*, 574 (2015), p. A48.
- [122] R. M. WALD, *General relativity*, Chicago Univ. Press, Chicago, IL, United States, 1984.
- [123] F. YUAN, E. QUATAERT, AND R. NARAYAN, *Nonthermal electrons in radiatively inefficient accretion flow models of Sagittarius A**, *Astrophys. J.*, 598 (2003), pp. 301–312.